University of Southampton
Faculty of Physical Sciences and Engineering
School of Electronics and Computer Science

Microfluidic control of oxygen for long-term maintenance of tissues on chip

Fernando Carlos García García

fcgg1g17@soton.ac.uk
https://orcid.org/0000-0003-0539-5884

Thesis for the degree of Doctor of Philosophy

April 2023

Abstract

Faculty of Engineering and Physical Sciences

School of Electronics and Computer Sciences

Doctor of Philosophy

Microfluidic control of oxygen for long-term maintenance of tissues on chip

By

Fernando Carlos Garcia Garcia

Current *in vitro* models are not able to accurately replicate the *in vivo* architectures, morphologies, cell diversity and the communications and interactions between the cells and their microenvironments. Culturing whole tissue explants presents many advantages, the most remarkable one being that they preserve the original three-dimensional architecture, cell types and extracellular matrix of the tissues *in vivo*. However, this field as not been yet widely explored and still presents many challenges. The aim of this project is the development of new technologies for extending the viability of tissue biopsies *in vitro*. This project seeks to study how the oxygen concentration affects the survival *ex vivo* of tissues to optimise the culture conditions and increase our understanding of the behaviour of the samples outside the body.

A microfluidic platform able to control oxygen concentrations inside culture chambers, with an integrated electronic oxygen sensor to monitor *in situ* and in real time the gaseous microenvironment has been developed. The results demonstrate the ability of the system to obtain four oxygen concentrations with a microfluidic gradient generator to control the gaseous conditions of four cell culture chambers. An integrated optical oxygen sensing detector was built to monitor the oxygen levels in real time during the experiments without disturbing the culture. The results showed that the platform was able to culture HeLa cells for up to 48 h and maintain the oxygen levels constant for the duration of the hypoxic challenge (24h). We observed a 12.3- and 2.73-fold increase in the hypoxia-related genes *CA9* and *VEGF*, evidencing the suitability of this system to be integrated with conventional biological assays to study the response of the cells or tissues to changes in the gaseous microenvironment.

Table of content

Table of figures

List of Accompanying Materials

Data sets associated with the thesis have been deposited in the University of Southampton's Institutional repository (Pure) and are accessible via the following DOI:

https://doi.org/10.5258/SOTON/T0060

Research Thesis: Declaration of Authorship

Print name: Fernando Carlos Garcia Garcia

Title of thesis: *Microfluidic control of oxygen for long-term maintenance of tissues on chip*

I declare that this thesis and the work presented in it are my own and has been generated by me as the result of my own original research.

I confirm that:

1) This work was done wholly or mainly while in candidature for a research degree at this University;

2) Where any part of this thesis has previously been submitted for a degree or any other qualification at this University or any other institution, this has been clearly stated;

3) Where I have consulted the published work of others, this is always clearly attributed;

4) Where I have quoted from the work of others, the source is always given. With the exception of such quotations, this thesis is entirely my own work;

5) I have acknowledged all main sources of help;

6) Where the thesis is based on work done by myself jointly with others, I have made clear exactly what was done by others and what I have contributed myself;

7) Parts of this work have been published as:
Garcia-Garcia, F. C., Candarlioglu, P. L., Porter, J. D., Davies, D. E., Swindle, E. J., and Morgan, H., 2022, "Microfluidic Technologies for Ex Vivo Tissue Biopsies: A Review," Organs-on-a-Chip, **4**(March), p. 100020.

Signature: Date: 07/06/2024

Acknowledgments

In first place I would like to thank Prof Hywel Morgan for giving me the opportunity to work in such an exciting project, and for his help and guidance through these challenging years. I would also like to thank Dr Emily J. Swindle for her support and her patience, and for listening to my struggles during the toughest times. I would like to give a special mention to everyone in the CHB lab: Roel, Jon, Victor, Raúl, Nikita, João, Ric and everyone else that has been around and helped me to get here, whether that is by helping directly in the lab when I felt lost, listening to my complains during the lunch times, or the breaks at Stags. My biggest thank you goes, of course, to my sister Maria, my most ruthless critic, my most important support, and my biggest inspiration. I would like to recognise my parents for their unwavering encouragement and for giving me the chance to have the best education possible, even if that means moving to a different country. To all my family for their faith in me, especially my godmother Beatriz and my grandparents, the ones still here and the ones watching me from above. To the swim team, for giving me an escape to burn out the stress and the frustration and giving me unbelievable memories of these years in Southampton, and to my friends in Spain, Ayelén, María, Rita, Bea and Marta for their love and understanding.

I would also like to acknowledge the work of others in this thesis. The colleagues at the Brooke Lab for providing me with the cells for the project and other materials and reagents, especially Anna Willis for always being happy to help me, no matter how many times my cells died. The colleagues at the University ECS Workshop, Mark Long, James Chalk, and Anthony Gardner for helping with the 3D printed moulds, the PMMA micromilled gradient generators and their crucial input to fabricate the chip holders. Dr Yihua Wang and his student Siyuan Wang for their help with the RNA extraction and teaching me how to perform PCRs, and for providing me with the primers for my experiments. Finally, I would like to thank GlaxoSmithKline (Pelin Candarlioglu, James Porter, Wendy Rowan and Theresa Pell) for their contribution and support to this project.

Abbreviations

ACTB	β-actin
ADME	Absorption, Distribution, metabolism, and excretion
ATP	Adenosine triphosphate
CA9	Carbonic anhydrase IX
cDMEM	Complete Dulbecco's modified eagle medium
cDNA	Complementary DNA
cL-15	Complete Leibovitz medium
cMEM	Complete Minimum Essential medium
C_T	Threshold cycle
dH_2O	Deionised water
DMEM	Dulbecco's modified eagle medium
DNA	Deoxyribonucleic acid
DO	Dissolved oxygen
dsDNA	Double-stranded DNA
ECM	Extracellular Matrix
EDTA	Ethylenediaminetetraacetic acid
EGFR	Epidermal growth factor receptor
ELISA	Enzyme-linked immunosorbent assay
Ex/Em	Excitation/Emission
FBS	Foetal bovine serum
FDA	Food and Drug Administration
FET	Field-effect transistor
HBSS	Hank's Balanced salt solution
HEPES	4-(2-hydroxyethyl)-1-piperazinetanesulphonic acid
HIF	Hypoxia inducible factor
HKG	Housekeeping gene
HNSCC	Head and neck squamous cell carcinoma
HPRT1	Hypoxanthine-guanine phosphoribosyltransferase 1
HSPC3	Heat shock protein HSP90-β
IBD	Inflammatory bowel disease
IM-MS	Ion mobility mass spectrometry
iPSC	Induced pluripotent stem cell
L-15	Leibovitz L-15 medium
LDH	Lactate dehydrogenase
LED	Light-emitting diode
LOXL2	Lysyl oxidase-like 2
MEA	Microelectrode array
MEM	Minimum essential medium
MPS	Microphysiological system
mRNA	Messenger RNA
MSC	Microbiological Safety Cabinet
MTT	(3-(4,5-dimethylthiazol-2-yl)-2,5-diphenyl-2H-tetrazolium bromide)),
NAD+	Nicotinamide adenine dinucleotide (oxidised)

NADH	Nicotinamide adenine dinucleotide (reduced)
NEEAs	Non-essential aminoacids
NVB	Non-volatile buffers
PBS	Phosphate buffered saline
PCB	Printed circuit board
PCR	Polymerase chain reaction
PCTS	precision cut tissue slices
PDMS	Polydimethylsiloxane
Pe	Péclet number
PMMA	Polymethylmethacrylate
PTFE	Polytetrafluoroethylene
PdTFPP	Palladium(II) meso-tetra(pentafluorophenyl)porphyrin
PtTFPP	Platinum(II) meso-tetra(pentafluorophenyl)porphyrin
R&D	Research and Development
Re_c	Reynolds number
RNA	Ribonucleic acid
ROS	Reactive oxygen species
RPS18	Ribosomal protein S18
RT-qPCR	Reverse transcription quantitative polymerase chain reaction
$Ru(BPY)_3$	Tris(2,2′-bipyridyl) dichlororuthenium(II) hexahydrate
sccm	Standard cubic centimetre per minute
SD	Standard deviation
SDHA	Subunit A of succinate dehydrogenase complex
SEM	Standard error of the mean
VEGF	Vascular endothelial growth factor

Chapter 1. Overview and context

1.1 Introduction

The human body is an extraordinarily complex system composed of cells, tissues, and organs. Organs are formed by several tissues and these, in turn, contain an abundance of different cell types. Cells are connected to each other by intercellular junctions and are located within a specialised extracellular matrix (ECM). Each organ possesses a specific architecture and functions. They are functionally interdependent and are integrated to perform organ-specific functions. Understanding the intricate network of pathways, signals and interactions between cells and their microenvironment is key for the advancement of biology and medicine. Human anatomy has been studied for centuries, and it was already well known at the microscopic level from the beginning of the twentieth century. However, it is yet not fully understood at the cellular and molecular level, and there are still many open questions, for instance, or how cells change during disease [1,2].

Mammalian tissues and organs are relatively difficult to access for experimentation, manipulation, or observation. Additionally, tissues and organ functions are highly interdependent, and isolating the components to study their individual roles can be very complex and lead to inconsistent results. Non-human animals have been widely used in scientific research and current techniques rely greatly on animal experimentation. Since the publication in 1959 of "*Principles of humane experimental techniques*", scientific progress has been guided by the 3Rs framework: Replacement, Reduction and Refinement. This report highlights the need to replace, reduce and refine the use of animals for biomedical and pharmaceutical research by developing new methods and models that are more human-relevant [3]. Hence, *in vitro* models and culture techniques have become necessary. *In vitro* cultures at different levels of physiological relevance can give insight on the morphology of the different cell types, their primary functions, behaviours, migration, and proliferation mechanisms, as well as their gene expression and regulation. More complex models can yield information on processes such as tissue formation and organisation, on the role and function of cells, tissues and organs and the communication and interactions between them, and their responses to stimulus such as mechanical stress, hormonal fluctuations, or drug exposure.

The major goal of *in vitro* models used in biomedical research is to translate our understanding of the fundamental principles that govern biological systems to improve patient outcomes. A deeper understanding of human physiology and pathology can lead to better prognosis and diagnosis methods and novel or improved treatments, as well as to guide the selection of therapies and to help healthcare professionals make more informed decisions [4]. Opportunities arise to use the patient's own tissue to obtain individualised predictive or prognostic

information, leading to patient-specific or population-specific treatments and even to the development of tissues *ex vivo* that can be transplanted in the patient to repair or replace damaged tissues.

1.1.1 Models for pharmaceutical research

The pharmaceutical industry and biomedical progress are strongly linked. Pharmaceutical research aims to turn the fundamental research advances into innovative treatments for patients. These improvements have led to a decrease in mortality, control and management of diseases, and improved quality of life. In the past century, life expectancy has increased globally from 30 to 73 years [5], and the pharmaceutical industry has played a crucial role with the discovery and market approval of many drugs such as aspirin or antibiotics [6]. Besides the impact in the health of the population, the pharmaceutical industry is a key part of the world's economy. The world pharmaceutical market was worth an estimated €845,235 million in 2018 [7]. The pharmaceutical and biotechnology sector amounts to 18.9% of total business research and development (R&D) expenditure worldwide and, as of 2017, it directly employed 760,000 people just in Europe [7]. However, the pharmaceutical industry is in an unprecedented situation. Environmental issues, major revenue losses due to patent expirations, escalating R&D costs and increasingly demanding regulatory requirements are putting the industry under growing pressure. Since the sequencing of the human genome in 2004, the number of compounds in development has increased 62%, and R&D expenditures have doubled, yet the number of drugs approved per year has not significantly increased since the 1990s. Amongst the contributing factors are the higher regulatory efficacy hurdles, commercial and financial decisions driving to project termination, and the increased complexity and costs of clinical trials [8]. Nevertheless, more recent studies show an upward trend since 2013, potentially due to an improvement in the potential failure identification by the companies, the use of biomarkers for better targeted drugs, or a new wave of medical breakthroughs, especially in immunotherapies [9].

1.1.1.1 The drug discovery process

The drug discovery process begins in laboratories, where thousands of potential candidate compounds are screened. These candidates are discovered through new insights into a disease process, or by testing many molecular compounds to find possible beneficial effects against a large number of diseases. Additionally, some compounds previously discovered can be repurposed, from existing treatments with unanticipated effects; or even through new technologies that provide new ways to target medical products [10]. Once a promising candidate is found, investigations are carried out to gather information on pharmacokinetics (what the body does to

the drug) and pharmacodynamics (what the drug does to the body). When the new drug candidates have been selected, they undergo preclinical studies. Researchers need to obtain detailed information on absorption, distribution, metabolism, and excretion (ADME), as well as on safety, dosing, and toxicity levels prior to testing them in humans. Drug development must establish the physicochemical properties of the new candidate (chemical composition, solubility, stability, etc) together with examining if the product is suitable for packaging (tablets, capsules, aerosols, injectables, etc). At this stage, tests are performed using *in vitro* methods, mainly two-dimensional cell cultures, and animal models. After the new compound has successfully passed the previous tests, it undergoes clinical trials. Clinical trials are powerful experimental techniques for assessing the effectiveness of a new drug or intervention in humans (medical device, surgical procedure, etc). They are divided into four phases [11]:

Phase I: attempts to estimate tolerability and characterise drug pharmacokinetics and pharmacodynamics. It is usually performed in small groups (~10-20) of healthy individuals. It provides a first assessment of the drug activity and serves to estimate the maximum dose before it shows unacceptable levels of toxicity. It also gives information on how the drug should be administered.

Phase II: aims to evaluate whether the drug has any biological activity or effect. It is performed in larger groups (up to 100) of individuals with the targeted condition. It is used to get an initial estimation of efficacy (ability of the drug to show effectiveness for the indicated disorder) and is usually tested against a placebo or control group.

Phase III: is designed to determine the safety and efficacy of the new drug in large numbers of patients (hundreds to thousands) with the targeted disease. It is also used to assess the effectiveness of the new drug compared to pre-existing treatments. If the drug is successful, the investigators can then apply for approval.

Phase IV: drug approvals in phase III are based on relatively short-term and group size-limited studies, compared to the years or decades the drugs may be used in practice and the millions of people that would use them. This means that the drugs are released with incomplete information on the clinical outcomes and could have adverse effects after a few years. Thus, phase IV is a long-term surveillance study after regulatory agency approval, also known as post-market safety monitoring. If problems are observed, the regulatory agencies can add cautions to the dosage or usage, and even consider more serious measures.

The drug discovery and development process is long, risky, and expensive. The stages of the pipeline and the approximate timelines are represented in Figure 1.1. From the first synthesis or isolation of a compound in the laboratory until its market release, it takes an average of 12-13

years and an approximated cost of €1,926 million (figure from 2014) [7]. On average, out of every 10,000 substances that start the process, only one or two will make it successfully to the market. In a thorough survey on clinical trials success made in 2014 by Hay *et al.*, it was found that 1 out of every 10 development paths entering phase I clinical trials ended up being approved by the Food and drug administration (FDA). It was observed that ~64% transition from phase I to phase II, only ~32% of the remaining candidates are successful in phase II and move on to phase III, and around 60% of these are submitted for approval. Even at this stage, only 83% of the applications are approved by regulatory bodies [8]. This means that after all the trials and the documentation for submission have been completed (a process that takes more than 10 years) one in four compounds are rejected, incurring the full discovery and development costs.

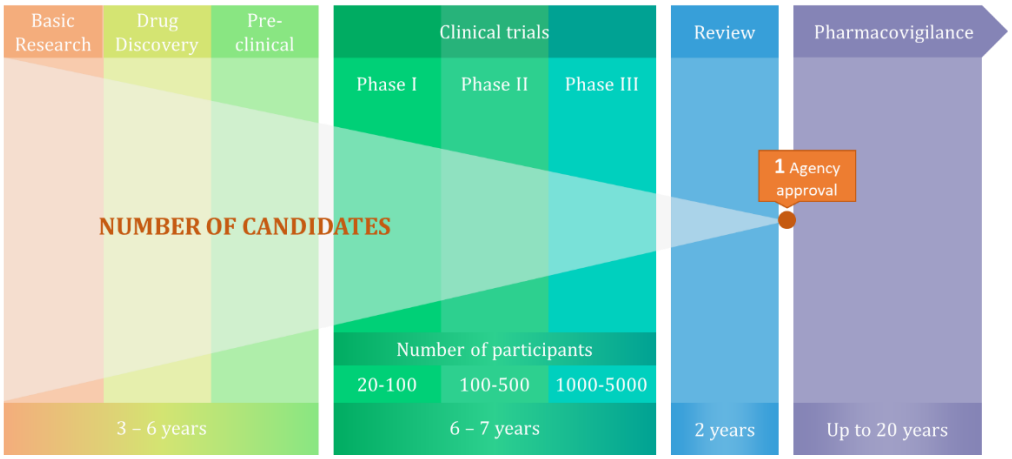

Figure 1.1: Drug discovery and development process. Adapted from https://www.efpia.eu/publications/data-center/innovation/research-and-development-process/

This makes the whole process very inefficient and costly. From the data shown in the mentioned report, it can be easily concluded that the biggest attrition rate occurs in phases II and III of the clinical trial. In a study by Arrowsmith *et al.*, 2013 on the causes of failure, it was observed that up to 80% of the candidates failed due to efficacy and safety causes (Figure 1.2) [12]. And yet, 50% of the R&D investment in the drug discovery process is allocated to clinical trials, mainly to phases II and III [7]. This clearly evidences the poor prediction power of the methods used in the preclinical stage to evaluate the pharmacokinetic properties and toxicity of the compounds in the human body (Figure 1.3).

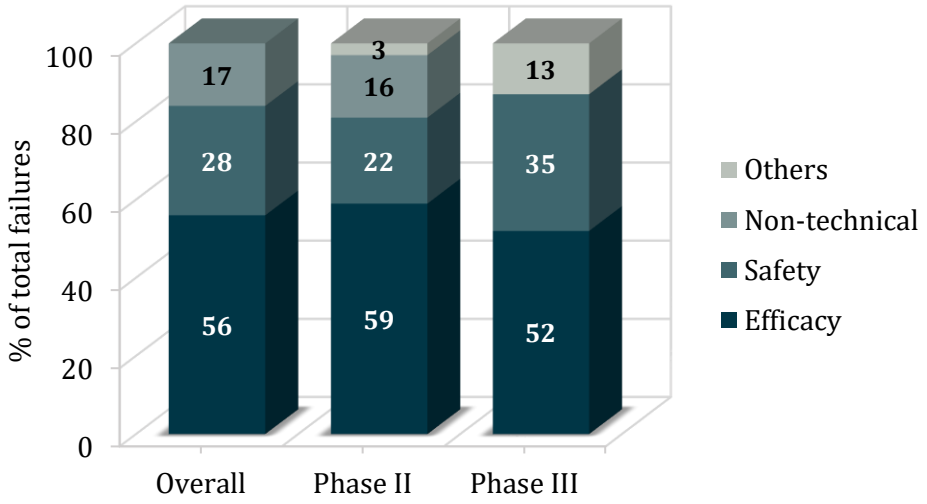

Figure 1.2: Causes of failure in the drug development pipeline for the overall process and for phase II and III clinical trials [12].

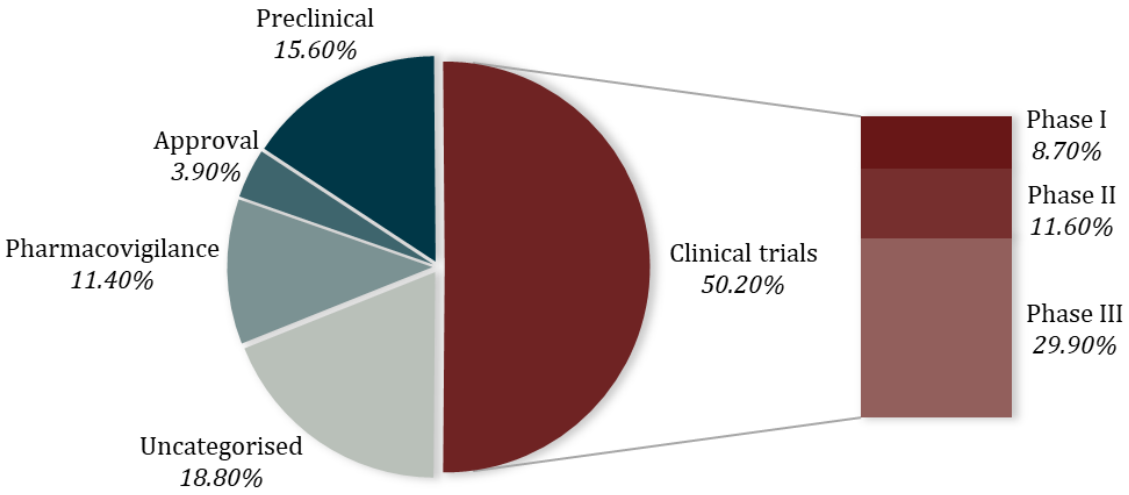

Figure 1.3: Allocation of the investment in Research and Development in the different steps of the process made by the pharmaceutical industry in the year 2017. Note how clinical trials involving human subjects get over half of the funding and how the cost of human trials increases with the number of participants. Data obtain from EFPIA, The Pharmaceutical Industry in Figures 2019 [7].

Paul *et al.*, 2010 did an analysis of the relative contribution to the overall success of the drug development process of each step. They concluded that a key aspect for improving the R&D efficiency and productivity was the reduction of the attrition in Phases II and III. To do that, two approaches were proposed to reduce technical uncertainty early in the development, i.e., whether or not the compound engages the target and has the desired effect in humans: 1) improve the target selection, i.e., select more validated and druggable targets; and 2) pursue early proof-of-

concept clinical trials to detect activity and toxicity issues in humans much earlier in the pipeline[13]. It is therefore crucial for the industry to develop new paradigms and methodologies that are more predictive to identify risks preclinically. Since most of the candidates are destined to fail inevitably, the aim should be to get them to fail sooner and less expensively. Even though the scenario may look pessimistic, localising and pinpointing the root of the problem is the first step towards the solution. As an example, in 1991, the main reason for failure (~40%) was adverse pharmacokinetics and bioavailability. In 2000, these factors only accounted for 10%, which evidences the power of the industry to identify and put a remedy to the issues that are involved in the attrition of the new drugs [6].

1.1.1.2 Personalised medicine

When it comes to the real application of medicine to patients, one size does not fit all. Current practice consists usually of the prescription of therapies based on population averages. However, treatments that have proven to be effective in some, are ineffective for others and can cause different adverse effects in different individuals. According to the Personalised Medicine Coalition, 75% of cancer drugs are ineffective, and so are 70% of Alzheimer's drugs and 50% of arthritis drugs [14]. After the launch of a new HIV treatment (abacavir), it was found that a rare but serious side effect was increased risk for myocardial infarction. This was not observed in clinical trials as this risk is only present in patients with an already high risk of cardiovascular disease, that were excluded from the trial because of this same reason, and thus the side effect was not detected [15]. Personalised, stratified, precision or individualised medicine is an emerging field in which physicians use different diagnostic tests to help determine which medical treatment will work best for each patient. Nevertheless, the concept of personalised medicine is not new. When patients present fever, for example, the underlying cause is studied to identify if it is bacterial or viral, and the treatment is selected accordingly. Similarly, individuals are divided by blood type (A, B, AB and O) for blood transfusions or organ transplants. With the completion of the Human Genome Project in 2003, individuals can now get their genome sequenced. This genetic information yields an enormous amount of information on the patient's health such as how likely they are to suffer a condition, detect the risk or presence of the disease before symptoms appear, or predict how they will respond to a specific treatment. For example, cytochrome P450 is involved in the metabolism of drugs. Mutations in the genes coding these drug-metabolising enzymes can cause drugs to be metabolised faster than normal, eliminating the drugs before they had any effect; or slower than normal, struggling to inactivate and eliminate the drug, leading to toxicity[16]. Combining the genetic information with the individual's medical records, circumstances and habits, personalised medicine allows clinicians to develop targeted treatments and prevention plans, shifting the health care away from the current trial-and-error approach (Figure

1.4). The detailed knowledge of the genetic material of an individual can help determine appropriate dosages and create maximum efficacy with prescription drugs. Using genetic diagnosis, the presence of a pathogenic mutation can be detected, and a treatment or prevention plan can be established early on, reducing the need to repeat testing for signs of the disease, relieving the individual of the burden of uncertainty, and saving the time and money of unnecessary testing. Additionally, this approach could also be used to stratify or segment populations, grouping the patients presenting specific sets of gene mutations and targeting therapies to those groups rather than to only individuals or the whole population. This can change the dynamics of drug development and the practice of medicine. Exclusion and inclusion criteria in clinical trials can be decided using this information and would help identify who will benefit the most from the clinical trial. It would increase safety, reduce adverse outcomes, and improve the efficiency of the process, as drugs previously deemed to be ineffective for the larger population can be beneficial for that specific subpopulation group. In summary, personalised medicine presents many benefits such as the shift from reactive to preventive medicine, help the selection of optimal therapies, reduce adverse reactions, increase patients' adherence to treatments and, overall, improve their quality of life. Moreover, it would reveal additional or alternative uses for drug candidates that were perceived as failures, controlling the overall cost of the drug development process and the health care system [17,18].

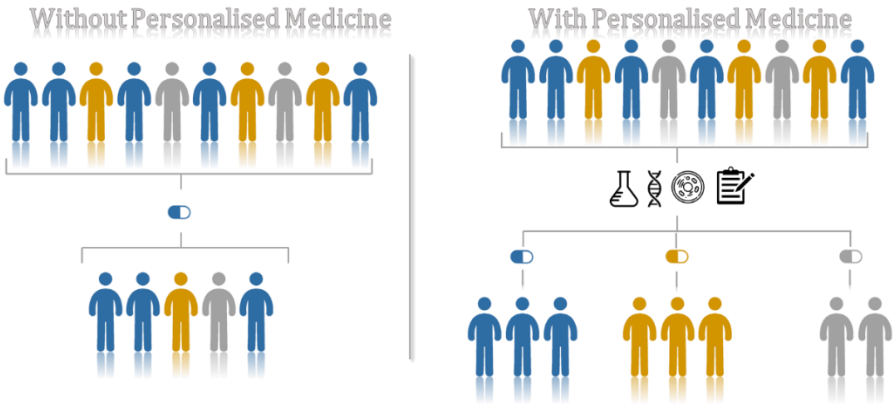

Figure 1.4: Without personalised medicine all patients receive the same treatment, however, only a few will benefit from it. With personalised medicine, the additional testing and individual diagnostic allow for each patient to receive the right therapy, increasing the number of patients that get a benefit. From The personalised medicine report 2017 [14].

There are many obstacles facing precision medicine, for example, regulatory hurdles, lack of reimbursement strategies or the need for a wider clinical adoption. One of the key challenges is to gather all the health-related data of a patient obtained from genomics, imaging, biomarkers, and biometrics and link this information to functional outcomes in their response to treatments. *In vitro* models could help bridge this gap, by reproducing the physiological environment outside

of the body and giving relevant read-outs to drug tests, they offer the possibility to generate representations of patients and apply the treatments directly to the patient's samples in the clinic, informing decisions on strategies for treatment and prevention [19]. These models have the potential to be used in parallel to link the gene variations of single patients or specific populations to their responses to treatments, generating an extensive health-database that can be used for the benefit of all.

1.2 In vitro models

The aim of any model is to simplify experimental variables to isolate different components for their study under controlled conditions. *In vitro* models in biomedical research try to mimic organs or organ structures at different levels (whole organ, tissues, cellular or molecular) (Figure 1.5). *In vitro* cell culture models have been a very valuable tool for the study of physiological and pathological cellular processes for over a century. They have made possible the study of cell biology, tissue morphology, disease mechanisms, protein production and gene expression, and also drug action and toxicity investigations in preclinical research. In this section, the current *in vitro* models recapitulating the *in vivo* situation at increasing degrees of complexity are discussed with their benefits and drawbacks.

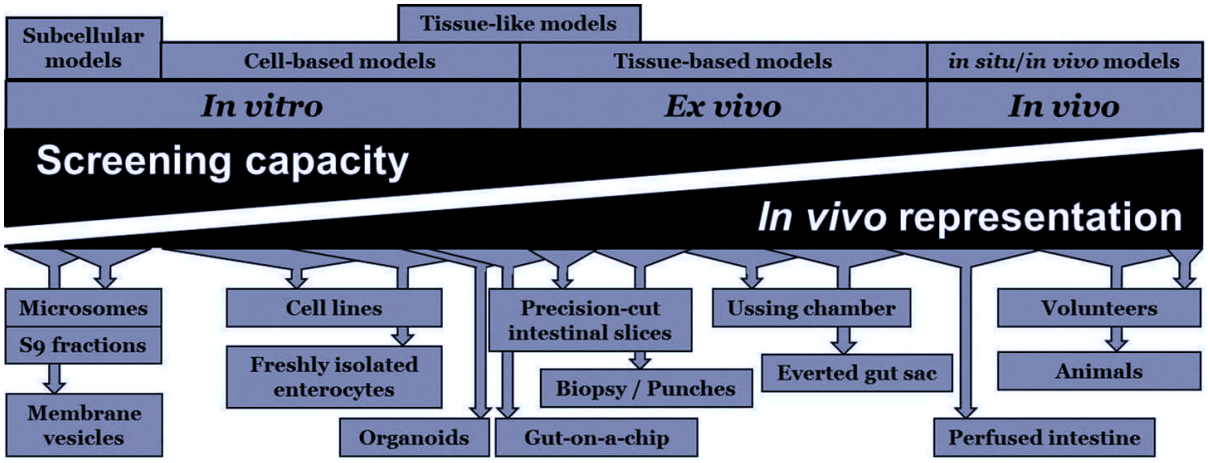

Figure 1.5: Classification of the current models in order of complexity. Note that the more physiologically-relevant the model is, the more complex it becomes and the capacity of high-throughput screening is reduced. From Li et al., 2016 [20].

1.2.1 2D culture models

Cell culture refers to the removal of cells from a tissue and their incubation in a favourable artificial environment. The first publications describing cell dissociation of explanted cells for cell culture were over a century ago [21]. Two-dimensional cell culture on plastic surfaces has been the basis of much of our cellular biology knowledge and is still the mainstay for biomedical and pharmacological research. It presents many advantages such as ease of cell maintenance and manipulation, lower cost compared to other models, the possibility for high-throughput screening and the potential for genetic manipulation. Because of its wide use throughout the years, there are a large number of commercialised cell lines and products for maintenance and assessment and established reproducible and reliable culture techniques [22,23].

Nonetheless, cells cultured in monolayers on a plastic flat surface fail to mimic the *in vivo* physiological conditions. Two-dimensional culture does not recapitulate the cell-cell, cell-matrix, or cell-extracellular environment interactions. These interactions, such as cell communication or

signalling pathways, play a key role in cell differentiation, proliferation, activity, gene and protein expression and many other vital cell functions [24]. Also, 2D methods fail to mimic the architecture and morphology of the tissues and the variety of cell types present in those tissues. Moreover, cells are usually cultured in high glucose media and without any mechanical, chemical stimuli or fluctuation hormones and other signalling molecules. The media is refreshed in batches, meaning that the concentration of nutrients decrease over time while cytotoxic metabolic products build-up, meaning that the cells are starving and slowly suffocating until the media is changed [25]. It is because of these reasons that researchers have started to look into other *in vitro* models, with the aim of obtaining models able to mimic the *in vivo* environment more closely and obtain more physiologically relevant results. One of the key parameters that influence the results, and the success of these models is the origin of the cells and the tissues used [1,26].

1.2.1.1 Primary cells

These are obtained directly from harvesting the tissues from the individual, followed by disaggregation, separation and/or purification using mechanical, enzymatic or chemical methods. These cells preserve their phenotype, unadulterated nature which results in a better preservation of the structural and biochemical complexity found *in vivo*, closely mimicking the physiological state of the cells in the organism, which allows for the generation of more biologically-relevant data. Thus, they are usually the chosen model to validate data obtained *in vitro* or in immortalised cells, as well as in research comparing specific characteristics of the donors, such as diseases, age or smoking. Several cell types are frequently used in research as primary cells, such as fibroblasts, epithelial cells, endothelial cells, hematopoietic cells, or mesenchymal cells. However, once isolated, primary cells begin to de-differentiate within a short time of culture in a process difficult to control, requiring continuous host tissue isolation and major planning of the experiment. Moreover, because they are directly derived from fresh tissue, it is difficult to obtain homogenous populations, which is often reflected in higher experimental variability. They are also sensitive to passaging (subculture into a new vessel/plate) which results in altered phenotypes (observable characteristics such as morphology, behaviour, developmental processes and biochemical properties), slow proliferation and metabolic rates [27,28].

1.2.1.2 Immortalised cell lines

These originate from primary cells that have undergone deliberate genetic modification. These modifications are aimed to overcome the challenges posed by primary cells mentioned above. Immortalisation can be achieved by selective gene mutation, introducing oncogenes, viral vectors or introducing telomerase reverse transcriptase [29]. This enables rapid proliferation,

resistance to de-differentiation, improved passaging, and greater resilience in culture. Immortalised cell lines are easy to maintain and can be easily expanded and stored. They have been widely used in the research community and have become the models for many experimental designs, due to the reproducibility of the data obtained from them (although there are different opinions on this topic [30]), and the fact that they are cost-effective, work-friendly and can run many passages compared to primary cells. In this work, HeLa cells have been used. HeLa cells are the first immortal human cells grown in culture and have been used for countless scientific experiments. They were isolated in 1951 from the epithelium of a 31-year old female patient with cervical carcinoma. These calls were infected with human papilloma virus 18 [31] and report a low expression of the oncogene P53 (reported to help prevent the development of tumours) [32]. These cells are easy to manipulate and expand, making them an attractive model, given that there is an almost unlimited supply.

However, due to the genetic manipulations, immortalised cells are no longer primary cells, and have lost their original phenotype. There is a growing number of publications showing examples of the changes in cell behaviour upon immortalisation compared to the homologous primary cells: altered genomic content, abnormal expression of intracellular proteins, deterioration of key morphological features and loss of cellular polarity amongst others [27]. Therefore, there is a need for validation of the models with primary cells, induced pluripotent stem cells or animals, to assess the physiological relevance of the data obtained.

1.2.1.3 Induced pluripotent stem cells

These are obtained by reprogramming of differentiated somatic cells to an embryonic-like state. These induced pluripotent stem cells (iPSCs) are comparable to human embryonic stem cells in morphology, proliferation, surface markers, gene expression and differentiation potential [33,34]. The resulting cells can self-renew virtually indefinitely and can be differentiated into any cell type, offering a versatile, improved, standardised, personalised and virtually unlimited source of cells for tissue engineering, therapeutic discovery and modelling of diseases. Nevertheless, this is still an emerging field, and many challenges exist in directing iPSCs differentiation with high efficiency and reliability, but their potential is undeniable.

1.2.2 3D culture models

As presented above, the two-dimensional culture of dissociated cells poses a number of limitations in the recapitulation and prediction of cellular responses. The addition of a third dimension has the potential to fulfil the gaps in research and open avenues to a better and deeper understanding of physiological and pathological processes. Three-dimensional models are *in*

vitro cultures where immortalised cell lines, primary cells, stem cells or whole tissue explants are placed within a matrix or scaffold that mimics the *in vivo* cell microenvironment. This allows the growth and interaction of the cells with their surroundings in all dimensions, which in turn enables the study of cellular processes not possible in 2D models, such as cellular organisation, cancer propagation and metastasis, inflammatory pathways or angiogenesis. 3D cultures show improved viability, proliferation, differentiation, responses to stimuli, cell-cell communication, cell polarisation and, overall, more physiological relevance. On the other hand, they are more difficult to obtain and reproduce as the generation of the construct is complex and laborious, and they have limitations in performance and compatibility with high-throughput screening technologies [26].

1.2.2.1 3D constructs

Three-dimensional culture constructs are usually made by suspending cells in biocompatible hydrogels that can be cross-linked *in vitro*, or by seeding cells on solid support matrices with high porosity or other non-planar surfaces. There are many examples in the literature that use these methods to engineer tissues from different organs. For example, Tobita *et al.*, 2006 engineered cardiac tissue to investigate myocardial growth, differentiation and maturation by mixing isolated cells with Matrigel™ into culture plates with a silicone membrane that was subsequently deformed using vacuum pressure to form a trough. After culture and incubation, a cylindrical-shaped construct was obtained, to which mechanical stretch forces could be applied [35]. Bokhari *et al.*, 2007 opted for a different approach in which hepatic cells were seeded in a highly porous scaffold. Compared to the 2D culture counterparts, the constructs showed better morphological characteristics and improved function and viability and also were less susceptible to cell death when exposed to a toxin [36]. This same scaffold was more recently used to mimic the architecture of bone and was seeded with stem cells to recapitulate the bone marrow niche microenvironment. This platform allowed for prolonged maintenance of haematopoietic stem and progenitor cells, which can be a useful cell source for other studies as well as for the study of the investigation of haematopoiesis and serves as a first step for the use of this scaffold for the culture and manipulation of other types of stem cells [37]. More sophisticated techniques have been used to recapitulate specific architectures present *in vivo*. For example, Sung *et al.*, 2011 produced a 3D hydrogel using microchip fabrication techniques to obtain villi-like structures and seeded them with intestine epithelial cells to mimic the intestinal architecture [38].

A technique more widely used for the 3D reconstruction of epithelial barriers is the Transwell® technology. It consists of a two-compartment culture-well separated by a semipermeable membrane. Cells can be seeded and co-cultured on one or both sides of the membrane to

replicate epithelial barriers such as the airway epithelium, the intestinal epithelium, or the epidermis. Because the cells in each compartment are separated, cells on each side can be subjected to different environments, to mimic for example an air-liquid interface, or exposed to different substances and treatments. This type of culture has gained popularity in the scientific community in the past decades and there are now many commercialised epithelial barrier constructs such as EpiSkin® (L'Oreal), EpiDerm™ (MatTek) or MucilAir™ (Epithelix).

Even though 3D culture models entail a significant increase in the capability to mimic the physiological setup, they still have some drawbacks in that they are seeded with a limited number of cell types, and the scaffolds and matrices do not completely replicate the *in vivo* ECM. For example, Matrigel™ is a tumour-derived ECM that has several characteristics highly dissimilar to *in vivo* ECM in terms of composition (the mixture of proteins, growth factors, etc) and of structure and organisation. Additionally, it has a significant batch-to-batch variation, which complicates the interpretation and extrapolation of the results. Furthermore, the most common way of validation of the biological relevance of 3D models is only through direct comparison with 2D models in terms of cell adhesion, proliferation, and viability.

1.2.2.2 Organoids and spheroids

Organoids and spheroids are self-assembled clusters of cell colonies which can be generated from one or several cell types and are formed by taking advantage of the tendency of cells to aggregate. The main difference between organoids and spheroids is that organoids use organ-specific progenitor cells that self-organise whilst spheroids are formed from cancer cell lines or tumour-derived cells. There are many different approaches for organoid formation (hanging drop, rotating culture, centrifugation pellet culture, etc.) reviewed in Lin *et al.* [39] (Figure 1.6). Organoids can serve as *in vitro* platforms for the study of cell interactions, migration, tissue development and toxicology. Their use has increased significantly in the last years and to the point where there are now commercial methods for the consistent generation of organoids. Different generation techniques have been used to produce equivalents of intestinal [40], cerebral [41] or testicular [42] tissue using stem cells to mimic early development of these organs and for the generation of disease models related to congenital defects. In other studies, organoids have been used as a method for expansion of liver stem cells and bipotent progenitor liver cells, which can be a useful tool as a source of human liver material for other studies [43].

They have had their widest application in cancer research, as they provide an excellent platform to mimic the tumour environment. Organoids usually represent avascular tissue or tumour masses, in which the transport of nutrients, oxygen and waste products is governed by

diffusion. This means that for organoids above a certain size, the supply of nutrients is insufficient, resulting in a necrotic core with a proliferating outer layer.

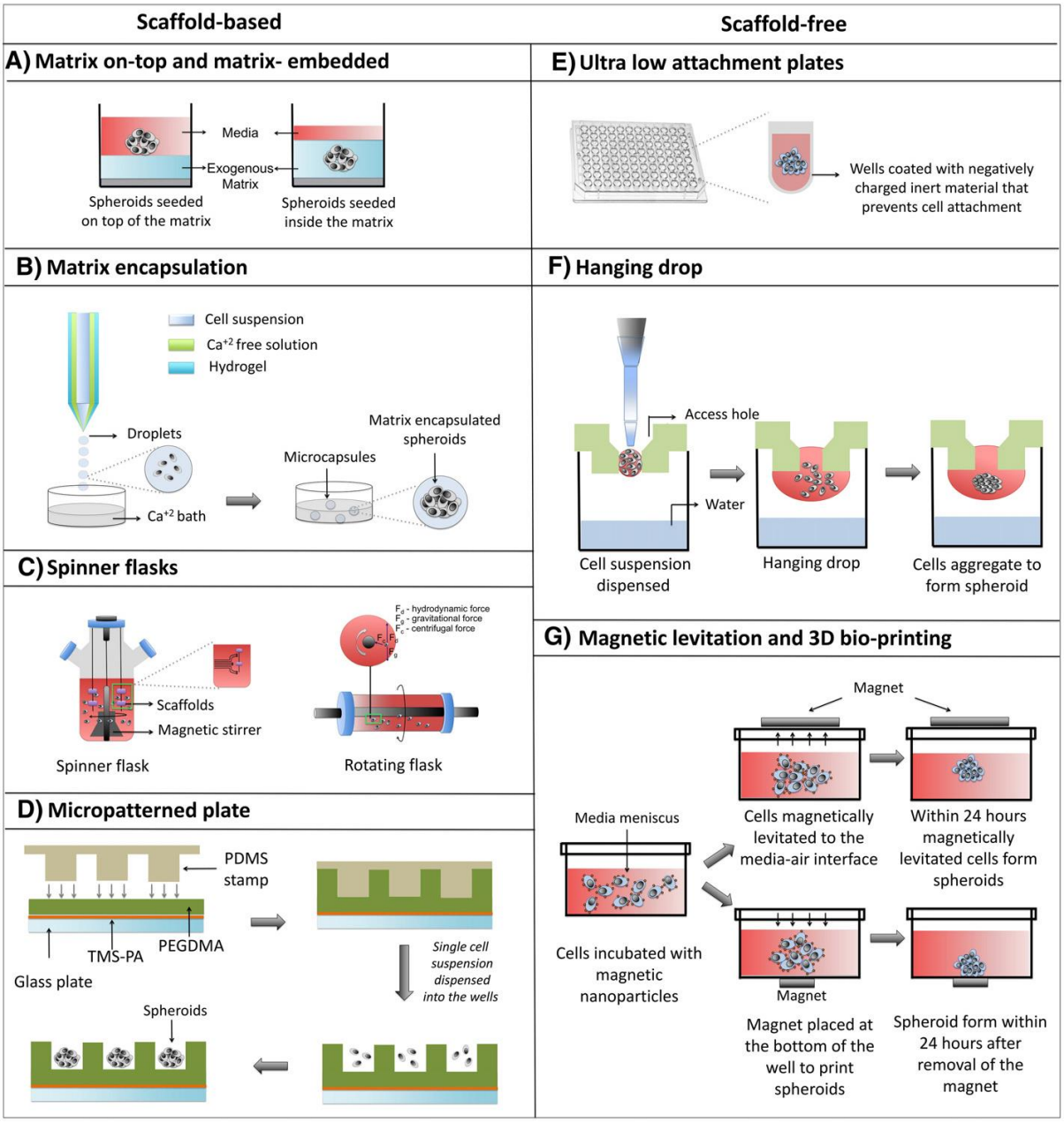

Figure 1.6: Most common methods to generate organoids and spheroids. Cells are brought together using scaffolds to promote adherence to other cells and to the scaffold that acts as support (left) or without scaffolds using external forces (right) [44].

1.2.2.3 Tissue explants

Organ culture preserves the whole or partial architecture of a surgically removed organ or biopsy. This type of culture presents many advantages in that it is the most accurate recapitulation of the situation *in vivo* as it preserves cell diversity, architectures, and ECM. However, it presents many drawbacks such as their elevated cost, limited availability, difficulty for long-term maintenance, and low applicability for high-throughput screenings. Tissue explants include

whole organ extraction and investigation *ex vivo* [45], decellularised and reseeded scaffolds [46], punched biopsies [47] and tissue slices [48]. Tissue slices present certain advantages compared to whole organ explants as they combine the 3D architecture and multicellularity preservation with better operability and viability. However, their poor reproducibility and long-term viability hinder their wider application. Recent technological advances allow the obtention of precision-cut tissue slices (PCTS) that allow for more reliable and reproducible samples. Standardised procedures and protocols for their culture have been established [49], resulting in an increase in operability and viability, making them more suitable for assessment methods such as visual analysis, immunochemistry or live imaging. PCTS can be a simpler, faster, and more reliable *ex vivo* model for biological and drug research than current *in* vitro models and have the potential to be a link in the *in vitro-in vivo* extrapolation[50]. PCTS for investigation have been obtained from several body organs such as liver [51,52], intestines [48,53] or lungs [54]. As an example to illustrate their potential as candidates to link in the translation *in vitro-in vivo*, some reports have proven their ability to be kept viable for at least five days in the case of liver slices [55], up to 15 days for lung slices [54,56], and even some reports have claimed to maintain brain slices for several months [57,58].

However, they have some limitations. Typically, the tissue slices are submerged in culture medium, exposing the whole sample to the same environment. This can present some problems for tissues such as intestines or lungs that constitute epithelial barriers, and each side is subjected to a different microenvironment *in vivo*. This comes as part of the loss of physiological context when the tissue is extracted and loses its possibility to communicate with other tissues and organs and lacks physiological signals and cues such as hormones, stress and growth factors, and cytokines.

1.2.2.4 Bioreactors

Bioreactors are devices that sustain biological and chemical processes under highly controlled environment and operating conditions, such as temperature, oxygen tension, pH or nutrient supply, as well as mechanical stimulation. They enable the culture of tissue 3D constructs *in vitro* with good reproducibility, control, and automation of experimental processes [59]. However, current designs do not allow for continuous interrogation and sampling and are not compatible with high-throughput screening techniques. Moreover, even though feedback and automation loops strategies have been developed, adjustments into bioreactor designs and integration systems able to respond to *in vivo* conditions have not yet been completely exploited.

1.2.3 Disease modelling

One of the aims of biomedical research is the obtention of deeper and more insightful knowledge of the human body in healthy and diseased states in order to develop new and more effective methods of diagnosis, prevention and intervention. Diseases are extremely complex and very difficult to model. Typically, animal models are used to replicate human diseases as they show similar manifestations and phenotypes [4]. However, animals are not the best representation of the complex gene-environment interactions that occur in many chronic human diseases, and the underlying mechanisms vary greatly between species. In some cases, the species used do not experience the human condition modelled, and thus it has to be artificially generated in the animal [60,61]. Hence, investigators have started to build *in vitro* models of human diseases using the techniques discussed above.

For example, cardiac tissue and liver tissue have been generated in two dimensions using micropatterning techniques where a monolayer of cells is grown on top of a patterned substrate. Chang *et al.*, 2009 used this method to mimic myocardial infarcted regions to study the re-entry cardiac rhythm dynamics after healing [62], whereas Beauchamp *et al.*, 2012 used it to replicate the ventricular myocardium to study arrhythmogenesis [63] and March *et al.*, 2013 used it as a liver platform to study the effects of malaria infection on the liver [64].

Three-dimensional models have also been developed to simulate human diseases. For example, 3D scaffolds have been used to engineer cartilage tissue to model osteoarthritis [65], or the cylindrical-shaped cardiac constructs explained above have been used to study hypertrophic cardiomyopathy [66]. The Transwell® barrier models discussed previously have been used to study asthma [67], chronic obstructive pulmonary disease [68], inflammatory bowel disease [69] or psoriasis [70], amongst many other conditions. Moreover, other more sophisticated methods have been reported like the three-dimensional bronchiole model developed by Miller *et al.*, 2010, in which a bioreactor was designed to culture cylindrical-shaped bronchioles constructed from different cells lines, that allows the application of radial forces. This model enables the study of airway remodelling components such as subepithelial fibrosis, smooth muscle hyperplasia and hypertrophy or epithelial cell metaplasia [71]. There are also reports of modelling diseases using tissue slices like the one presented by Duff *et al.*, 2002, where brain slices from transgenic mice overexpressing Alzheimer's-relevant genes were cultured to mimic the disease [57]. Spheroids have had a major impact in the modelling of diseases, especially in the cancer research field, given their unique capability to mimic the complexity of solid tumours and the tumour environment. Tumour organoids can be generated from a wide variety of cell types to study metabolic alterations during tumour progression, cancer cells invasion and migration, the tumour

microenvironment and gain insight in the tumour generation, progression and chemotherapy resistance [44].

iPSCs can play an important role in the modelling of diseases as they can virtually differentiate into any cell type and offer an almost unlimited supply of cells. For example, they have been used to model inherited metabolic liver disorders [72], arrhythmogenic syndromes such as long QT syndrome [73] or familial dilated cardiomyopathy [74]. Even though these advances have greatly contributed to our understanding of disease states, they still present the limitations inherent to the culture models used. It is, therefore, crucial to keep exploring new possibilities and paradigms and improving the current systems to drive the investigations towards more realistic and physiologically-relevant representations.

1.3 Microphysiological systems

Microphysiological systems are *in vitro* platforms created with microchip manufacturing methods that recapitulate many structural, biological, and functional properties of tissues in a small scale. They are able to overcome many of the issues of the conventional 2D and 3D culture models discussed above and have the potential to serve as a bridge between them and the complexity of humans *in vivo*. MPS technology arises from the convergence of two other technologies: microfluidics and tissue engineering.

1.3.1 Introduction to microfluidics

Microfluidics is the science of the behaviour, control and manipulation of small volumes of fluid (10^{-9} to 10^{-18} litres) and particles on the scale of tens to hundreds of micrometres [75]. Fluids at this scale behave differently. The fluid flow in microchannels is characterised by a low Reynolds number (Re_c) which is a dimensionless parameter that describes the ratio between the inertial and viscous forces in a fluid.

$$Re_c = \frac{\rho U D_h}{\mu} \qquad (1.1)$$

Here ρ is the fluid density, U the fluid velocity, D_h the hydraulic diameter of the channel ($D_h = 2hw/(h+w)$, where w is the width and h the height of the channel cross section) and μ the dynamic viscosity. When the Re_c is low, viscous forces dominate over inertial forces. The fluid flows parallel to the channel walls and is referred to as laminar flow, i.e., there is no turbulence, and mixing occurs only through diffusion. For values above ~2300, the flow is considered turbulent, and its study is much more complex. In the human body, the Reynolds number varies widely from the large arteries such as the aorta with an average Re_c around 3000, which means turbulent flow, all the way down to 150 for veins, or as low as 0.002 for the capillaries [76]. This property makes microfluidics a really interesting technology, as it is possible to predict and control the behaviour of the fluids in laminar flow, resulting in excellent spatial and temporal regulation of solute concentrations, and therefore could be a useful tool for mimicking the behaviour of the fluids in the body. Microfluidics has a wide range of applications across many fields and holds many advantages compared to conventional macroscale platforms such as reduced sample and reagent volumes, faster processing, higher sensitivity, lower cost and improved portability. It also allows for automation and integration with other technologies, reducing human intervention and errors [77].

In the biomedical and pharmaceutical research fields, microfluidics is also an interesting tool. In addition to the properties mentioned above, microfluidic devices have high surface-to-

volume ratio. This can be exploited to provide a biomimetic environment for cell and tissue culture. Compared to traditional methods, microfluidic devices allow for a continuous flow of fresh media. Laminar flow replicates the normal fluid flow within the body, supplying nutrients continuously, removing waste and facilitating mass transport of solutes, with a tight control of the culture conditions (oxygen tension, pH, temperature, etc.) therefore generating more *in vivo*-like environments [78,79]. The high control over the fluid irrigating the sample also translates in the possibility of a highly spatiotemporally controlled exposure to xenobiotics, gradients, and relevant physiological cues within the culture chamber, taking a step further in the simulation of the cellular microenvironment. One of the most relevant properties of MPS is their possibility to be self-contained, i.e., the operation of the system does not require external fluid or gas loops, and functional measurements can be performed through non-invasive, non-destructive approaches [80]. Besides the living tissue and the network of microstructures to host and irrigate it, MPS can also integrate sensors and actuators. These features make MPS the cornerstone of future biomedical and pharmaceutical research, as they provide means for miniaturisation and automation of the systems, increase the *in vitro-in vivo* relevance, allow for biological sampling and challenging, reduce the experimental duration, and increase the throughput, sensitivity, and accuracy of the measurements.

MPS such as organ-on-chip, multiorgan-on-chip, or tissue-on-chip, are poised to be the paradigm shift the research community needs. These novel platforms can serve as tools for mechanistic investigation, preclinical safety screening and drug disposition. MPS can offer new opportunities to recapitulate unique physiology, increase disease understanding, discover new biomarkers of toxicity, and facilitate rapid assessment of on- and off-target mechanisms. They can be used for determination of ADME profiles, predict human pharmacodynamics, and have a major impact in the predictive capacity, speed and cost of preclinical research [81]. Additionally, these systems allow for the interconnection of more than one tissue type or organ, providing an unprecedented physiological accuracy for the study of organ-organ and organ-drug interaction. They also present many potential applications in regenerative medicine, synthetic biology, and environmental sciences.

1.3.2 Organ-on-chip

An organ-on-chip is a microfluidic device for the culture of cells and tissues continuously perfused in micrometre-sized chambers with the goal of building the minimal functional unit that recapitulates tissue or organ-level functions. Organ-on-chips allow for an exceptional level of control of the positioning of the cells in a well-defined microarchitecture, and the culturing

conditions, enabling the replication of distinct functional units of organs, enhancing differentiation, functions, and long-term survival, and facilitating the computational modelling of the interactions of gases, metabolites and cells within the devices [82]. They hold the potential for investigating the basic mechanisms of organ physiology and disease. The most famous organ-on-chip is the lung-on-chip developed by Dr Ingber's group at Harvard University. This device consists of two channels separated by a semipermeable membrane, on the top of which alveolar epithelial cells are cultured and subjected to flowing air, and on the other side, vascular endothelial cells are cultured in the presence of flowing media (Figure 1.7a). Additionally, the device contains two empty chambers on each side that are subjected to pressure changes, to generate expansion and contraction movements in the central channel, mimicking the respiration motion in the alveolus *in vivo*. This system recapitulates the alveolar-capillary interface and is able to simulate nanoparticulate uptakes and inflammatory responses [83]. Stucki *et al.*, 2018 have also attempted to reproduce the air-liquid interface, mimicking the breathing movements by deflecting a membrane into a microcavity by applying vacuum cyclically and including trans-epithelial electrical resistance measurements with a chopstick electrode to assess the barrier integrity as a result of it [84] (Figure 1.7b). The group from Harvard used the same concept of their lung-on-chip to produce a gut-on-chip, lining the top side of the membrane with intestinal epithelial cells in this case. Their system allowed to generate movement that mimics the physiological peristaltic motion of the bowel. Normal intestinal microbes were included in the luminal side to mimic the microbiome and an improvement of the barrier function was observed [85]. This group also presented a kidney proximal tubule-on-a-chip using the two microchannels design for the study of drug transport and nephrotoxicity [86]. The concept of separating the media from the cells, via endothelial cells, a membrane or ECM is explored for many organ models. For example, Lee *et al.*, 2007 recreated a liver sinusoid by seeding primary hepatocytes into a cell culture chamber that was connected to the bulk flow of media by microchannels mimicking the endothelial barrier [87] (Figure 1.7c), and Booth *et al.*, 2012 used it to model the blood-brain barrier, flowing two channels perpendicularly, mimicking the luminal and abluminal sides of a neurovascular unit [88] (Figure 1.7d). Many other systems and designs have been presented for a wide variety of organs and tissues. Here, only a few relevant reports on the major organs have been mentioned to illustrate the great potential this technology holds. There are many extensive reviews focused on the progress of organ-on-chip technology that can be found elsewhere [89–91].

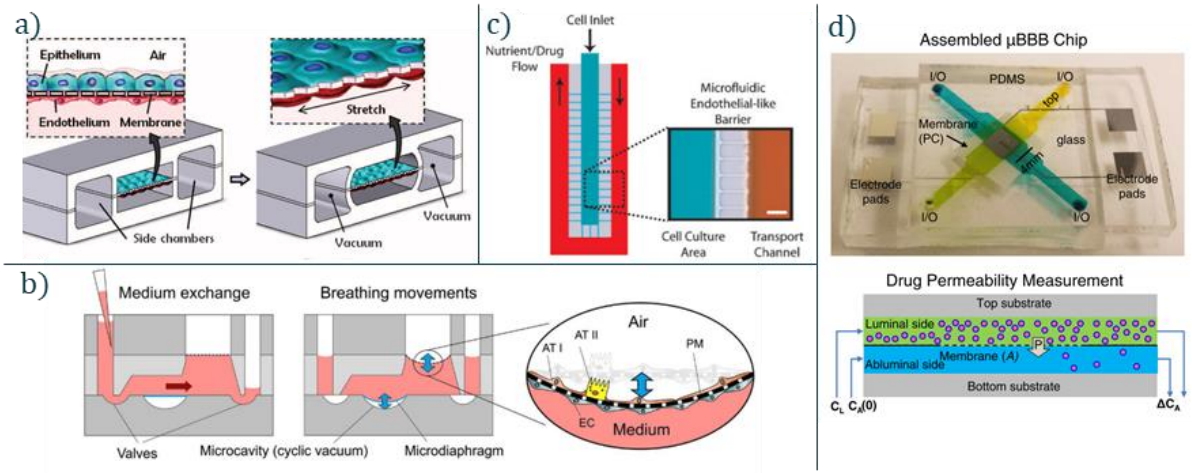

Figure 1.7: Examples of organ-on-chip technology. Microfluidic devices are designed to provide the cells with an environment that mimics the human physiology, for example, culturing endothelial and epithelial cells on opposite sides of a membrane to replicate: the alveolar wall (a and d [83,84]*), the liver (c* [87]*) or the blood-brain barrier (d* [88]*).*

1.3.2.1 Multiorgan-on-chip

The human body is composed of several organ systems that interact with each other and influence each other's behaviours. These interactions also alter the pharmacokinetic processes of ADME of exogenous compounds. Single organ-on-chip fail to include these interactions and thus are not able to predict correctly the effects of the substance in the body. In more recent years, multiorgan-on-chip have been presented, aiming to shorten the drug development pipeline, reduce the use of animals and inform regulatory and therapeutic decisions. Multiorgan-on-chips are multiple single organ-on-chip interconnected in parallel and/or in cascade. Maschmeyer *et al.*, presented a multiorgan system containing skin, intestine, liver and kidney surrogates with two separated flow circuits (blood flow and excretions flow) to mimic the ADME processes [92] (Figure 1.8a). Other efforts have been focused on the recapitulation of a single organ system, adding several of the tissues composing the system, for example, the female tract platform presented by Xiao *et al.* In this system, surrogates of the ovary, the fallopian tube, the uterus, the cervix and the liver (for metabolism purposes) were co-cultured to study the hormone regulation and homeostasis during the menstrual cycle [93]. More recently, platforms with higher complexity have been developed, like the one presented by Edington *et al.*, connecting up to 10 organ equivalents [94] (Figure 1.8b), or the integrated human organ-on-chip patented by Wikswo *et al.*, that recapitulates 3D tissues in a mechanically active micro-environment, with electrical and chemical stimulation and complex organ functions such as breathing lung, beating heart, or peristaltic gut. It also includes instrumentation for physiological and pharmacological analysis [95]. The integration of several organ equivalents into a multiorgan-on-chip or body-on-chip is an emerging field gaining recognition worldwide and there are still many challenges to overcome but in the past

decade, numerous programmes and initiatives have been brought up for the advancement of these body-on-chips [96].

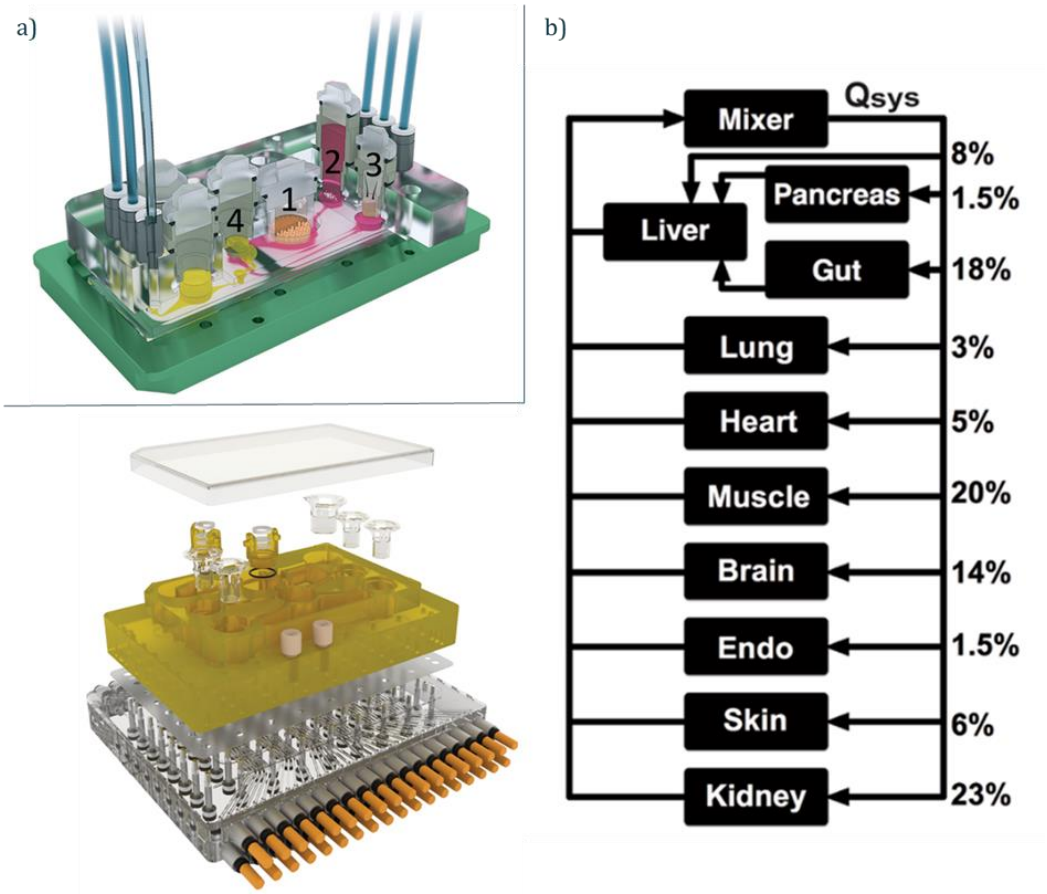

Figure 1.8: Multiorgan-on-chip systems. The platforms include circuit flows and pumps that allow the recirculation of the media to distribute the secreted factors to the rest of the organ surrogates. a) Four organ-chip co-culturing intestine (1), liver (2), skin (3) and kidney (4) tissues [92] *and b) Schematic of 10-organ system with the specific flow partition (percentages) for each organ type to simulate cardiac output* [94].

1.3.3 Tissue-on-chip

Organ-on-chips have proven to be very important and useful tools for the recapitulation of organ and tissue functions. They have provided new investigation methods, offering tools to do experiments that were not possible before and giving new insights into physiological and pathological mechanisms [97]. However, the prediction of *in vivo* responses remains limited, as the cells exist within an artificial architecture, without a native ECM and its unique architecture nor the cell type diversity found *in vivo.* Culturing tissue slices and biopsies provides a further step in the complexity of organ-on-chip models, as they preserve the original architecture, morphology, ECM, and cell heterogeneity [98]. It is known that culturing tissue samples with continuous perfusion improves circulation in and around the tissue biopsies, improving mass transfer into the tissues, and increasing the viability of the samples compared to static (no-flow) models [99,100]. Schumacher *et al.*, 2007 cultured liver slices in conventional static culture and with continuous perfusion. The improvement in culture conditions extended viability for dynamic

compared to static culture, seen through the reduction in protein markers expression after 24 h for no-flow conditions (Figure 1.9).

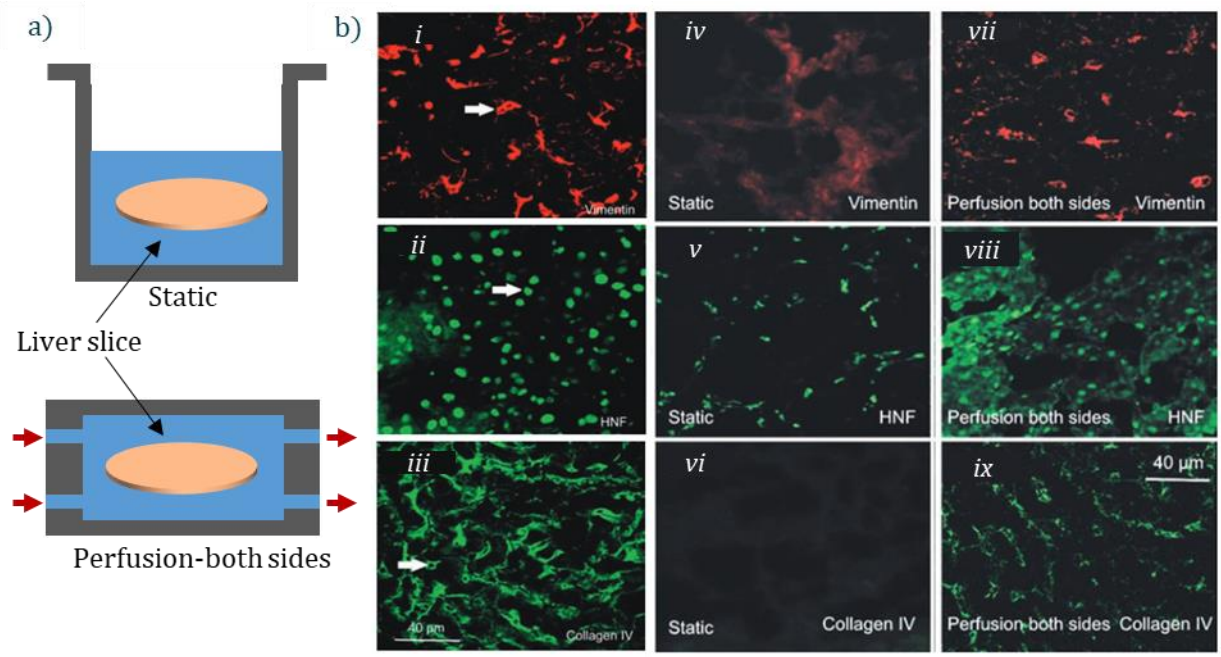

Figure 1.9: a) Comparison of static and dynamic culture (sample continuously perfused). b) Images i), ii) and iii) correspond to freshly isolated liver slices. iv), v) and vi) are liver slices after 24 h with no-flow and vii), viii) and ix) with continuous perfusion (after 24 h). The reduction in protein expression in static cultures indicates the loss of function, changes in phenotype and degradation of ECM, compared to dynamic cultures. Figure adapted from [101].

Microfluidic technology provides an ideal means of perfusing the samples, improving nutrient and oxygen supply and removal of waste. The integration of tissue explants into microfluidic chip (or tissue-on-chip) offers the possibility of extending the sample viability, controlling the microenvironment, delivering chemicals and treatments with high spatiotemporal resolution, and allowing for probing, analysing, and monitoring responses. This platform could be the most accurate model to the *in vivo* situation, providing an outstanding tool for physiological and pathological studies and the prediction of responses in the body. Nevertheless, the culture of tissue explants has proven difficult, and the life span of the biopsy samples is generally very limited. This is due to many reasons, predominantly the lack of vascularisation caused by the extraction of the tissue from the body: nutrient and oxygen supply and waste removal occur only through diffusion. Thus, the inner layers do not receive enough nutrients, reducing the viability of the sample [102].

1.3.3.1 Oxygen and nutrient delivery

The culture of tissue slices gained scientific recognition after the early work of Henry McIlwain. In 1957 his group developed a conical glass chamber in which a piece of brain tissue sat at the interface between air and saline solution providing a means of electrical recording and

stimulation [103]. Resting membrane potentials were recorded for the first time from cortical slices *in vitro*. Since then, the standard for brain slice culture was set by Haas *et al.*, in 1979. A tissue slice sits on a nylon mesh where a medium flows by capillarity from the inlet into the slice and out of the device [104]. This work was probably the first example of continuous perfusion, long before the advent of microfluidic technology. The first integration of a brain slice into a microfluidic device was reported by Passeraub *et al.*, where the nylon mesh of the Haas chamber was substituted for an array of microposts (400 μm high) on top of which the tissue sat with cell medium flowing between the posts. Brain tissue slices could be kept viable for 5 h, enough time to record spontaneous activity [105]. However, the short-term viability restricted the number and type of experiments that could be performed, and long-term conditions could not be investigated. Building on this work, Blake *et al.,* developed a device in which a slice was held between two sets of microposts (top and bottom), allowing perfusion from both surfaces simultaneously (Figure 1.10a) [106]. The device subjected different regions of the slice to various environments. However, the tissue only remained viable for 3 h, which may have been due to the thickness of the slice (530-700 μm), which is critical when nutrient and oxygen supply is controlled solely by diffusion. Other approaches for continuous perfusion of submerged tissue samples include a system where the tissue sits bathed in media that is continuously refreshed by perfusion and withdrawal of the fluid using microchannels [107–109] (Figure 1.10b and c).

To improve the viability of *ex vivo* tissue slices and increase their lifespan, new methodologies have been developed such as PCTS. PCTS can be obtained as thin as a few tens of micrometres but to preserve tissue architecture, while ensuring adequate diffusion of nutrients and oxygen, thicknesses of 200-300 μm are more commonly used. de Graaf *et al.,* established a standardised protocol for the culture of liver and intestinal slices *in vitro* [49], and in 2010 they described a microfluidic system for the maintenance of liver slices to study metabolic activity over extended periods. The device consisted of a droplet-shaped chamber with an inlet at the bottom and an outlet at the top, with the flow directed perpendicular to the surface of the slice. The slices were held in the chamber with polycarbonate filters that also distributed the fluid flow velocity more uniformly (Figure 1.10d). The behaviour of slices cultured under continuous perfusion was comparable to standard cultures in static well plates [[110]. To extend the lifespan of the slices, they were embedded in a hydrogel to avoid disaggregation and attachment to the polycarbonate filters, reducing damage to the tissue. In this manner, the viability of the slices was maintained for 72 h, and even though the metabolic rate decreased over time, it was less pronounced than in static cultures [[111]. Although an improvement, it still could not be used to observe the long-term effects of treatments.

To extend the life of thicker (>300 µm) tissue slices, different perfusion methods have been proposed. Choi *et al.,* developed an intra-perfusion system, in which 400 µm thick brain tissue slices were pinned to an array of microneedles that served as microjets, infusing media directly into the tissue rather than around it (Figure 1.10e). They observed that after 4 h, the viability of the static model was almost non-existent while in the perfused sample it was largely intact [112]. Using the same approach, Khong *et al.*, maintained the viability of liver tissue slices of up to 1 mm thick for 3 days [113]. The difference in lifespan could be due to the viability assessment methods, the length of the experiments or the sensitivity of the different organs to disruptions and *ex vivo* culture. The slices maintained their metabolic activity with albumin and urea production at values significantly higher than for traditional static cultures. Even though the technique was promising, enlarged interstitial spaces were observed after 3 days of culture, indicating tissue dissociation following injection of media through the needles. Rambani *et al.,* proposed a different strategy using what they called "interstitial perfusion". The tissue was placed on top of a gold grid in a chamber the exact size of the slice, and fluid was infused from the bottom, forcing it through the tissue and into the top chamber, where the medium was collected (Figure 1.10f). 700 µm-thick brain slices could be kept viable for up to 5 days [114].

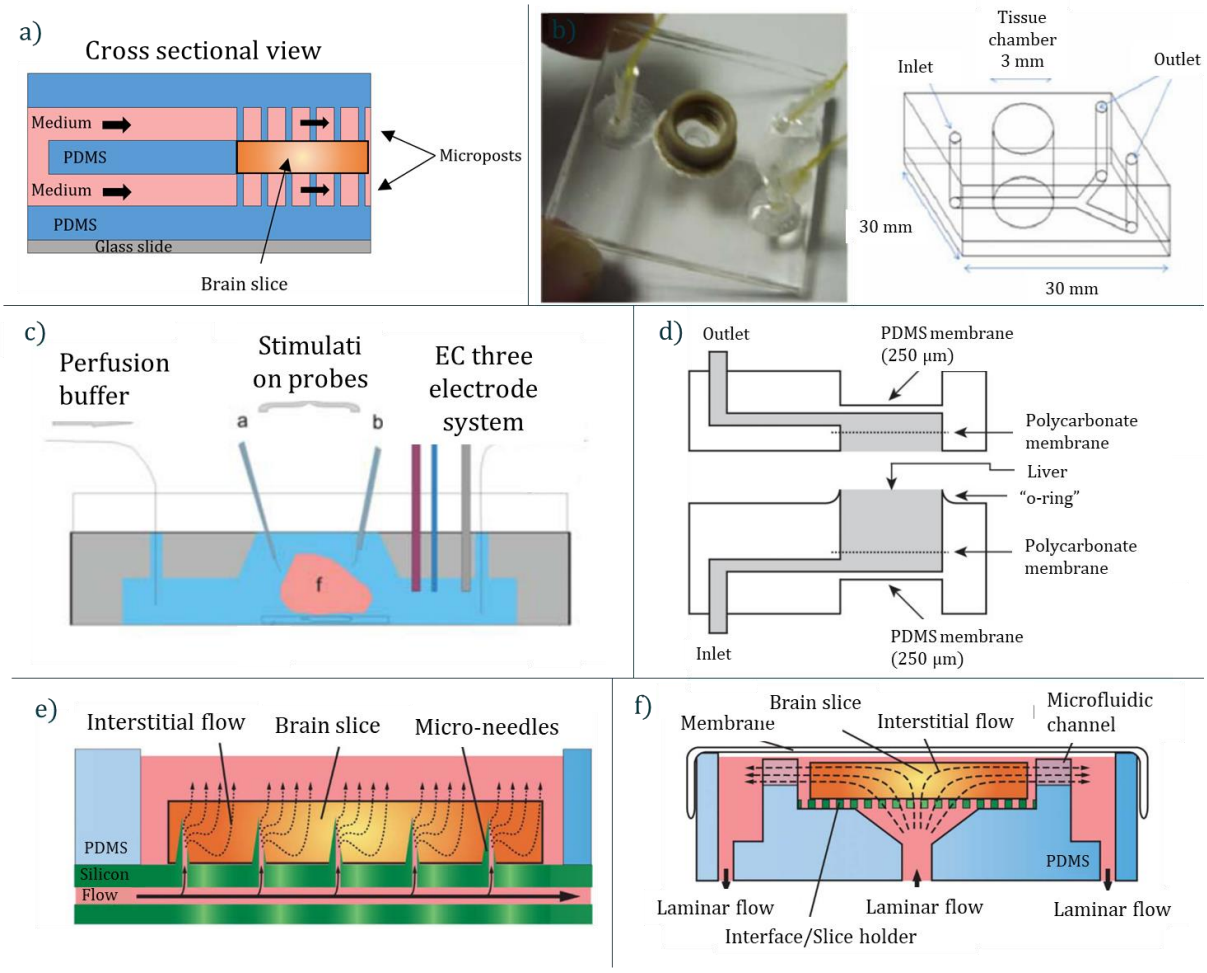

Figure 1.10: Microfluidic devices for continuous perfusion of whole tissue samples. a) This device holds a slice between microposts and the media flows continuously around the top and bottom surfaces [106]. *The devices in b) and c) have an inlet and an outlet that provide and remove the media to and from the chamber in which the sample sits* [107,115]*d) Perfusion design in which the tissue slices are placed perpendicular to the flow direction. This technique enhances the nutrient and oxygen delivery to inner cells* [110]. *e) Intra-perfusion device, where the tissue is pinned into the port needles and the media is delivered directly inside the sample, instead of around it. f) Interstitial perfusion device. The media is forced to flow through the slice, flowing from the bottom into a chamber the exact size of the sample slide and exiting from the top* [116].

Some tissues in the body constitute physiological barriers in which each side is exposed to a different environment, for example, the skin, the airways, the intestine, or the kidneys. This poses particular challenges when replicating a multiplicity of environments. In the case of the intestine, punch biopsies have been inserted into a chamber the exact size of the biopsy so that each side of the intestine is perfused separately, with different media irrigating the serosal and luminal sides (Figure 1.11a)[117–119]. An interphase system similar to a Transwell® integrated within microfluidic channels has also been used for continuous perfusion (Figure 1.11b)[120–122]. Yissachar *et al.*, cultured whole gut segments by separately perfusing the sample internally and externally by sewing the excised piece to input and output ports (Figure 1.11c)[123]. Other approaches to extend the viability of tissue slices include reducing the temperature to reduce metabolic activity and using UV light to sterilise the medium before perfusion to reduce the presence of bacteria and slow bacterial growth [124]. Other more creative solutions include air-propelled fluid circulation [125] or maintaining the slice in a perfused droplet [126]. However, none of the devices reported to date has had a major impact on the field. Tissue-on-chip technology is still emerging and most of these devices are still in the developmental stage, not ready for scalability and commercialisation. Furthermore, every design uses different tissues or tissue regions, from different species and with different thicknesses and sizes. Each assesses the viability with different protocols making it very difficult to directly compare performances and outcomes.

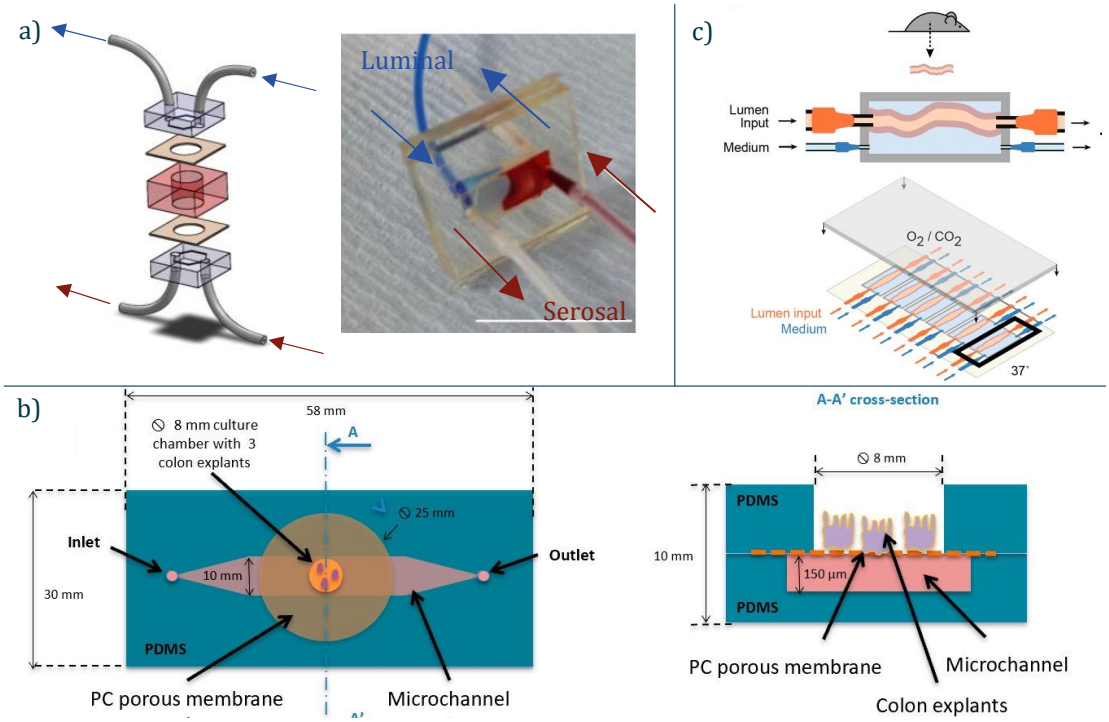

Figure 1.11: Microfluidic devices for the culture of tissue explants of physiological barriers, providing specific environments to each side. a) Intestinal biopsy punch subjected to dual flow. The luminal (blue) and serosal (red) sides are continuously perfused with different media [117]. *b) culture of colon biopsies at an air-liquid interface, with continuous perfusion to the bottom of the sample, maintaining the stratified architecture of the epithelium* [120]. *c) Culture of whole intestinal segments. The lumen is threaded and fixed to connection ports that introduce molecules or microbes into the lumen, and the sample is submerged in media that is continuously refreshed* [123].

1.3.3.2 Control of the microenvironment

The ability to deliver compounds spatiotemporally and thus control the microenvironment can add value to MPS platforms. In the device described above (Figure 1.10a), Blake *et al.*, exploited the laminar flow characteristics of their microfluidic device to expose different regions of a brain slice to different microenvironmental conditions, such as Na^+-free or ice-cold solutions, in order to block rhythmic activity in selected regions [106] (Figure 1.12a). Similar devices have been presented in [127–129]. In these platforms, relatively large regions are exposed to a specific condition. Other reports have subjected the samples to gradients across the tissue samples [130]. However, in some cases, the delivery of compounds is required in much more localised regions. To achieve this, Mohammed *et al.*, presented a system for controlled and localised delivery of factors to the brain slices that could be used as an "add-on" to commercial electrophysiology chambers, expanding their capabilities (Figure 1.12b). The design consisted of four microchannels running underneath an "off-the-shelf" perfusion chamber, with ports to deliver fluid from the microchannels into the chamber. This device allowed delivery of factors such as dopamine, while still maintaining viability and allowing electrophysiological measurements. The device provided a new way of controlling the microenvironment and delivering compounds to specific regions of the brain [131–133]. Tang *et al.*, developed a similar system but with additional suction

ports that held the tissue slice in place without the need for mechanical forces enabling better control of the jets through the ports and improving the spatial resolution of drug delivery [134,135]. In these devices, the tissues are placed manually and exact alignment with the fluidic ports with the regions of interest is difficult and time-consuming, therefore the experimental reproducibility is poor (Figure 1.12b). To circumvent this and increase throughput, Catterton *et al.*, presented a variation of the previous port delivery system by creating mobile ports beneath the tissues to supply the components to the desired locations [136]. A different approach was presented by Chang *et al.*, in which they placed a brain slice on a removable membrane on top of an array of parallel open channels. The permeable membrane allowed simultaneous perfusion of the slices and exposure to multiple substances in localised regions (Figure 1.12c). The compounds could be easily and rapidly changed, and the membrane rotated so that orthogonal exposures could be achieved, enabling several treatments and combinations to be tested on the same piece of tissue [137–139].

van Midwoud *et al.*, sequentially connected two chambers containing an intestinal and a liver slice that directed metabolites produced in the intestine into the liver for further metabolism [140]. This replicated the homeostasis of bile acid, with potential for exploration of ADME-Tox studies. Recirculating media through multiple tissue chambers or devices provides homogenous and continuous exposure of the tissue to various factors within the media. The EVATAR™ system (Figure 1.12d) developed by Xiao *et al.*, replicated a human 28-day menstrual cycle hormone profile by interconnecting up to five different tissues from the female reproductive tract [93]. TissUse HUMIMIC® Chip model combined reconstructed small intestine, liver spheroids, kidney proximal tubules and a skin biopsy with two separated recirculating flows (blood surrogate and excretory). They maintained homeostasis and functionality of the four organs for over 28 days, showing the potential of this platform for the generation of ADME profiles [92].

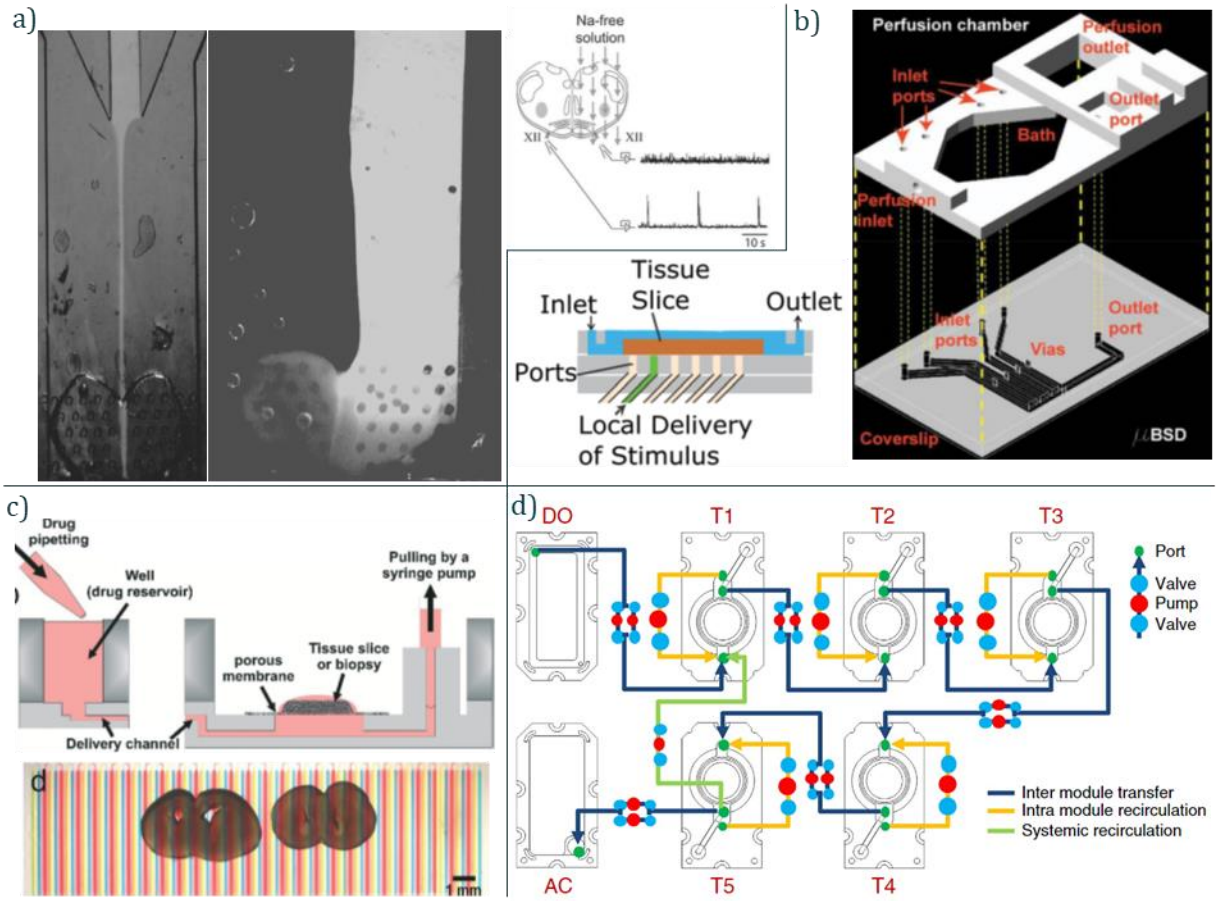

Figure 1.12: Mechanisms for the manipulation and control of the microenvironment during tissue slice cultures. The design in a) takes advantage of the properties of laminar flow to perfuse the same sample with two different media [106]*, while b) and c) used techniques that allow a higher spatial delivery control through the use of ports* [131,133] *and open channels* [137] *respectively. d) is a diagram of the EVATAR system, connecting up to 5 chambers containing different tissues interconnected to allow recirculation and homogeneous mixing of secreted factors* [93].

MPS technologies provide ways of controlling the microenvironment including temperature[124] and dissolved gas concentrations [141]. Oxygen is one of the most important factors for the survival of tissues, and tissue explants in microfluidic devices are usually cultured with standard incubator oxygen concentrations (atmospheric N_2 and O_2 and 5% CO_2). However, this level of oxygen is not physiologically relevant in most *in vivo* tissues where the partial pressure of oxygen is much lower and varies from tissue to tissue [142]. High oxygen concentrations during culture could lead to oxidative stress and other deleterious effects [143] which is removed from physiological conditions. Although microfluidic technology offers the possibility for fine spatial control of oxygen and for the generation of gradients, and there have been many reports of using disaggregated cells [144–146], to the best of our knowledge, only a couple of groups has integrated oxygen control with tissue explants in microfluidic devices [141,147]. To achieve this, they designed microfluidic systems consisting of a channel and a gas-permeable membrane on top of which sat a perfusion chamber for the tissue samples. By supplying gas with the desired oxygen concentration to the microfluidic channel, the gas diffused through the membrane and brain slices

were cultured at specific oxygen tensions. This is an important line of investigation and could provide important insight into the optimal conditions for tissue culture *ex vivo* or on the effect of hypoxia on tumours, for example. However, neither of these platforms integrated oxygen sensors within the system to monitor the exact oxygen concentration at which the samples were cultured and obtaining intermediate oxygen concentrations required expensive and bulky equipment.

Culture method	Sample type	Tissue	Refs
Static	Slices	Brain	[147–149]
		Liver	[100]
Full immersion	Explant	Liver	[150–152]
		Gut	[98]
		Heart	[148]
		Tumour	[149–156]
		Female reproductive system	[157]
	Slices	Brain	[158–160]
		Liver	[101]
		Lymph	[161,162]
		Tumour	[163–165]
Single side flow	Explant	Adipose	[166]
		Gut	[167]
	Slice	Brain	[168–170]
Dual side flow	Explant	Gut	[171–174]
		Artery	[175,176]
	Slice	Brain	[177–180]
Flow through	Slice	Brain	[181–183]
		Liver	[184–189]
		Tumour	[164,165]

Table 1: Summary of culture methods for different sample types and tissues.

1.3.3.3 Tissue interrogation

Microfluidic devices for analysing tissue explants should include methods for optical analysis, sampling of molecules, and chemical or electrical stimulation and recording. This means that access to the sample is an important factor in the design process. For example, electrophysiological measurements for neurological investigations are usually performed by inserting electrodes into a brain slice. Blake *et al.*, modified their system (described in Figure 1.10a) to allow access to the top and side for insertion of electrophysiological probes (Figure 1.13a). This design allowed measurements from the top and from the edges of the brain slice using multi-electrode probes. Multi-site measurements were simultaneously obtained with continuous perfusion of the sample[129]. These open chambers are of great advantage since they can be used with instruments and probes that already exist in most laboratories. Non-invasive techniques of recording from

electroactive cells are generally via microelectrode arrays (MEA) [190] which support the tissue, provide electrical contact to the bottom surface and allow perfusion with medium. However, MEAs can only record activity from neural cells from the surface in contact with the electrodes, which is often compromised due to poor perfusion or injury suffered during the slicing process. MEAs also do not give any information on the spread of signals throughout the entire thickness of the slice. To increase the viability of the bottom surface of a slice, Killian *et al.*, integrated a perforated MEA (pMEA) into the interstitial flow chamber developed by Rambani *et al.,* (Figure 1.10f), to replace the gold grid sustaining the brain slice (Figure 1.13b). This allowed recording of spontaneous and evoked electrical activity and stimulation of the slice. The device provided oxygen and nutrients to the bottom surface [191], improving tissue viability by up to 5 days. Other modifications of the MEAs include three-dimensional features in the form of tip-shaped protrusions to record from deeper tissue[192], or integrating the recording electrodes with microfluidic ports that are inserted into the sample[193]. Scott *et al.,* presented a method that combined multi-site electrical recording with multi-site localised chemical stimulation. Their device was based on the same fluid port concept presented previously (Figure 1.12b), using ports for stimulation (chemical and electrical) and recording [194]. Optical methods have also been used to record brain activity, using fast voltage-sensitive dye and laser photostimulation. Ahrar *et al.*, presented a device to culture brain slices while generating two distinct chemical environments: with or without the presence of caged glutamate (an excitatory neurotransmitter) or Ca^{2+} (a key signalling cation in synaptic activity). The sample was laser photostimulated resulting in evoked neuronal activity at the point of exposure, measured with voltage-sensitive dyes. This tool enabled visualisation of neural dynamics over a larger surface of the brain, not restricted to the site where the electrode is inserted, and also fine spatial control of the microenvironment and signal initiation and propagation (Figure 1.13c) [127]. Although promising, the method has limitations due to fluorescence photobleaching or disturbance of the signal due to the fluid flow.

For assessment of viability or functionality of tissue, the most widely used technique is the analysis of effluents. Continuous perfusion means that any secretions can be continuously collected. This provides a way of continuous monitoring markers of cell death or cell metabolism. Another important benefit of using microfluidics is the reduction in sample volumes, which minimises dilution of the metabolites or target compounds, so that their presence can be detected and quantitatively measured. van Midwoud *et al.*, observed that the production of metabolites was similar in static well plates to continuously perfused chips, but because of the reduction of volume in the chip, the concentration in the latter case was 4.3 times higher [110]. This evidences the potential of microfluidic miniaturisation to increase the physiological relevance of the models when cytokines and other factors are used to elicit responses in neighbouring tissues.

Very simple devices have been developed by Hattersley *et al.*, to maintain tissue biopsies. The devices consist of a chamber with one inlet and two outlets, in which a liver tissue biopsy of approximately 4 mm^3 is continuously perfused. The tissue could be maintained and monitored for 70h, with cell effluent collected periodically to measure lactate dehydrogenase (LDH) release to assess cell damage, and albumin and urea to evaluate hepatocyte function. Cell viability was assessed using fluorescent markers (Calcein AM and Propidium Iodide) [107]. They used this system to study the toxicity induced in the liver by ethanol and observed a concentration-dependent response to increasing concentrations of ethanol in tissue viability via a cell proliferation assay (WST-1 (water-soluble tetrazolium salt)) and tissue functionality measuring albumin and urea secretions[195]. They also explored the potential for personalised medicine, using the device as a tool to assess and guide therapeutical treatment decisions exposing head and neck squamous cell carcinoma (HNSCC) samples to chemotherapeutic drugs for 7 days [196], using LDH release as the marker for tumour cell death. The longer lifespan of these samples could be due to the reduction in sample volume (3 mm^3) or because tumour cells viability is not affected by a necrotic core. The effect of radiotherapies was also examined with this platform by irradiating the samples with a photon beam while being cultured in the microfluidic device [197,198] Although they did not observe an increase in LDH release after treatment, their results showed an increased apoptotic rate and a concentration-dependent reduction in Ki-67 expression (proliferation marker) following irradiation [198]. A similar perfusion system was used to stimulate cardiac tissue with changes in reactive oxygen species (ROS) monitored electrochemically [199]. More recently, a newer version of this system has been described with a user-friendly "plug-and-play" interface for maintenance of precision-cut slices of HNSCC. The devices allowed irradiation treatments and off-chip analysis combining radiotherapy with chemotherapeutics [200,201]. In their latest work [200–202], they used human samples, showing the applicability of these platforms for personalised medicine and translation of tissue-on-chip methods into the clinic.

MPS provide a platform for investigations that are too difficult or cumbersome with traditional methods. For example, Günther *et al.,* presented an "artery-on-chip" for routine assessment of artery structure and function. The traditional methods used for these studies are complicated, laborious and require skilled personnel as well as being non-scalable. Their microfluidic system trapped a whole artery segment and subjected it to varying conditions on the outer walls (e.g. stepwise increases in drugs such as phenylephrine or acetylcholine), and even to different conditions on either side of the arterial wall [203,204] (Figure 1.13d). They observed virtually identical vasoconstriction in mouse mesenteric arteries following phenylephrine stimulation compared to results using conventional pressure myography and highly localised responses to challenges that do not spread to the non-stimulated sides, in agreement with previous findings. This system caused less damage to the tissue, and reduced the technical demand for

preparation, increasing the ease of use and scalability, which should allow for higher throughput screenings.

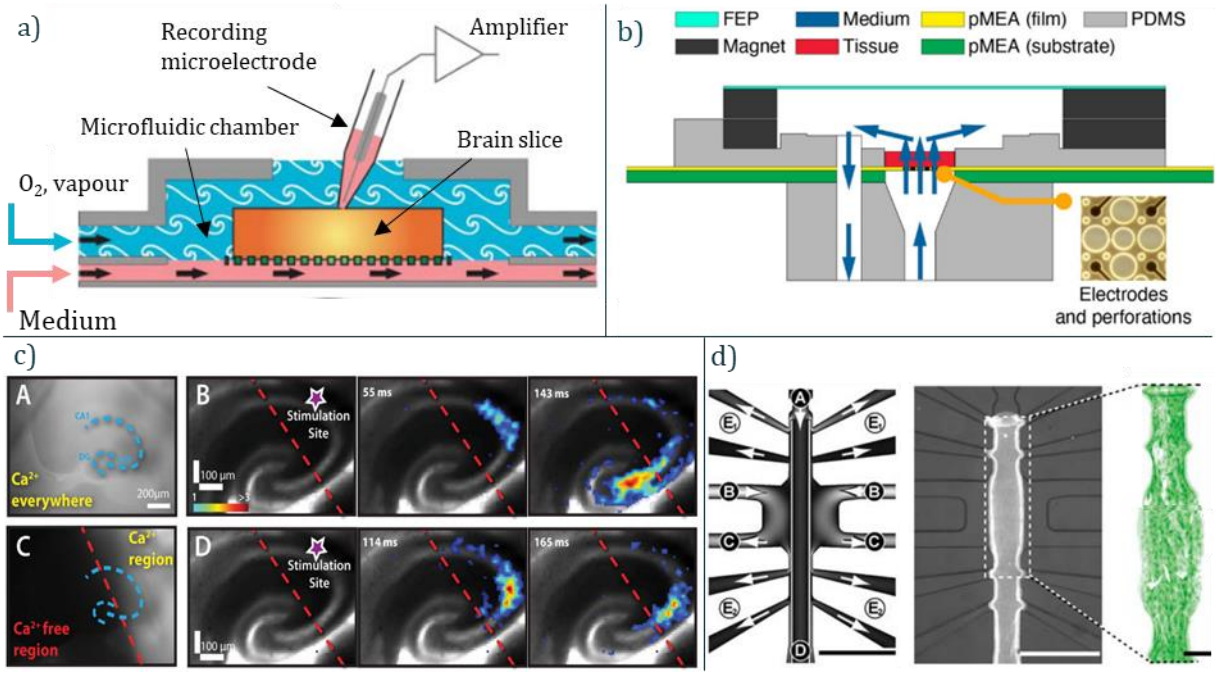

Figure 1.13: Examples of methods for interrogation of tissue samples. (a) Electrophysiological measurements using microelectrodes for recording electrical brain activity [116]*. Non-invasive techniques have also been developed, such as microelectrode arrays (b)*[191] *or optical methods based on fast voltage-sensitive dyes (c)* [127]*. d) The artery-on-chip platform in which the artery segment is fixed and the inner and outer walls are subjected to different conditions* [203]*.*

Diseases are complex and very difficult to model. Using primary disease tissue would give more accurate and predictive responses and could help researchers gain more insight into the healthy and diseased states. A tissue-on-chip system can also have a significant impact on disease modelling. Some skin conditions are particularly difficult to recreate and using platforms like the aforementioned TissUse could allow disease tissue biopsies to be studied. Dawson *et al.,* extracted tissue from inflammatory bowel disease (IBD) patients and cultured them on-chip to study differences in the intestinal wall permeability between healthy and diseased samples [117]. They showed that the system preserves inflammation throughout the experiment. This potential has also been explored in cancer research by trapping tumour biopsies obtained directly from patients in MPS. These samples maintained the *in vivo* cell heterogeneity inherent in tumours and allowed different treatment strategies to be used to assess chemosensitivity [205–208]. For example, Astolfi *et al.*, observed variability in the response to the same treatment for samples from different individuals but also for samples from the same patient [205], a trend also observed by Cheah *et al.,* [198]. This could be due to the high heterogeneity of cancer tumours inter and intra-patients, and highlights the importance of personalised medicine, as different patients respond differently to the same treatments and universal treatments are not always the most effective.

Tissue	Challenge type	Recording method	Refs
Brain	Chemical stimulation	Electrode	[169,177,178,180]
		MEA	[182,183,209]
		Optical	[209–212]
		Biological assays	[170]
	Electrical stimulation	MEA	[159,160,209,213]
		Optical	[209]
	Hypoxia		[212]
Liver	Chemical st.	Biological assays	[157,185–188,214,215]
Gut			[171,172,187]
	Hypoxia		[98,174]
Heart	Electrical st.	Electrodes	[148,216]
		Biological assays	
Tumour	Chemical st.		[149,150,152–155,164,165]
	Radiotherapy		[149,150,164,165]
Artery	Chemical st.	Optical	[175,176]
Lymph		Biological assays	[161,162]
Female reproductive system			[157]

Table 2: Challenges and recording methods presented in the literature for tissue-on-chip devices for multiple organ tissues.

1.3.4 Limitations and challenges

To date, no organ-on-chip or tissue-on-chip has been fully incorporated into the drug discovery pipeline or established as a complete validated model for biomedical research and drug development. MPS need to overcome hurdles before becoming widely accepted and utilised as validated and clinically relevant research tools. MPS technologies are generally challenging to fabricate and use by non-experts, material biocompatibility of the chip is important, and experimental issues such as the presence of bubbles or damage to the tissues during handling remain. The models used to mimic organ or tissue function have to recapitulate the *in vivo* physiological environment as closely as possible but increasing the level of complexity of the model also makes the system more difficult to use. Thus, it is important to identify the minimal functional unit that has an acceptable level of complexity for the context of use and focus on replicating that only. This raises questions on which physiological cues or other native components should be included, and whether the systems are designed to address a very specific question (only "fit-for-purpose"), or more broadly to mimic the whole organ function and finally the "body-on-chip" system. Once a piece of tissue is isolated, it requires external intervention to provide adequate biomechanical cues, soluble factors, metabolic cues, etc. Which of these are necessary to sustain the minimal

functional unit needs to be established, along with how these can be incorporated, or even replaced with computational models [217]. Some of the factors needed to sustain tissue functions originate in other organs, thus connecting two or more organ units could help overcome this problem and improve prediction.

One of the main drawbacks specific to tissue-on-chip is the biological low throughput, particularly given the difficulty in sourcing human samples – this limits the number of replicate experiments. Another major hurdle is the culture media. Most cell cultures use customised media specially designed to enhance the survival and functionality of a particular cell type. If different cell types use different customised media, which media is most appropriate when multiple organ units/tissues are cultured together?

MPS can be used as research tools to gain insight into (patho)physiological processes but can also be applied in the pharmaceutical field for target identification and validation, efficacy testing and physiological response prediction. Thus, MPS not only need to recapitulate the *in vivo* physiology of the tissue, but also provide a means to deliver and distribute the drugs of different modalities into the tissue in a physiologically-relevant manner. There is a wealth of ADME-Tox data available on thousands of compounds that have already been thoroughly studied. There is detailed information on metabolism, persistence, efficacy, dosing, expected and adverse effects and other outcomes. Using this database, the feasibility and reliability of MPS could be evaluated and established by mimicking these known effects. There is also a need to establish analytical performance standards in order to evaluate the qualification of these platforms for their context of use, such as reliability and reproducibility and their features, such as throughput, inter- and intra-laboratory reproducibility, integration, and compatibility with other existing laboratory processes. For example, the Emulate lung-on-a-chip has already demonstrated a well-defined domain of validity by recapitulating human pulmonary oedema and they have shown clinical translatability that is human [83] or species-specific [77]. Another important bottleneck against wider adoption by end-users is the lack of qualification of these MPS models for regulatory acceptance. MPS face obstacles in productisation and commercialisation, especially when comparing their costs to traditional 2D models in the larger scales. Full acceptance by the scientific community will occur when MPS are used routinely with user-friendly features, extended shelf life and at a cost-effective price. The field is moving rapidly but to accelerate uptake the scientific community will have to collaborate with the industry and regulatory agencies for these systems to reveal their full potential and benefits to society.

1.4 Control of relevant microenvironment parameters

Cells *in vivo* are constantly subjected to a plethora of signals and stimuli from other cells and their surroundings while producing responses and generating other signals simultaneously. Cells actively control and modify their intra and extra-cellular microenvironments. In this way, homeostasis is maintained, and the functions of the body are regulated and synchronised. This continuous feedback control by the cells complicates the study of cellular physiology and the influence of individual ambient factors. Therefore, it is crucial in cell culture to monitor and control physiological parameters, for example, the oxygen tension, pH, temperature, glucose, lactate, growth factors, hormones, as well as mechanical, chemical, and electrical stimulations [218–220]. In this section, the most relevant microenvironmental parameters will be discussed along with the most used techniques to control and measure them.

1.4.1 Homeostatic factors

1.4.1.1 Physicochemical

One of the key parameters every researcher needs to take into account when culturing cells or tissues is the oxygen tension. Humans can live up to one month without food and up to two weeks without water but cannot survive more than 10 minutes without oxygen. Oxygen is vital for living cells and plays a crucial role in metabolism, development, migration, or apoptosis, amongst others. Due to the lack of vascular network, it is of utmost importance that the correct oxygenation is delivered to the tissues, a delicate balance between oxygen availability and oxygen consumption. Both hyperoxia and hypoxia trigger biological responses. Thus, tight control and continuous monitoring are essential in any experimental setup. There are several approaches for the control of oxygen within culture chambers. The most widely used are hypoxic chambers and hypoxic workstations that generate an atmosphere with the desired oxygen tension in which the device is hosted. These stations, however, are bulky and expensive, and only provide one oxygen level at a time, requiring long times of equilibration during changes. Other techniques include the control of oxygen at a local level. This can be achieved by diffusion from a fluid source or by generating or scavenging oxygen by chemical reactions [221] (Figure 1.14). In the first approach, the region where the cells are cultured is separated by a thin, gas-permeable membrane that allows the diffusion from a source or control channel. In this control channel, a fluid with a defined oxygen tension is flushed. This fluid can be an equilibrated liquid, whose oxygen tension has been established off-chip; or a gas or mixture of gases [141,222]. The latter approach allows for a faster diffusion and equilibration on-chip and allows for fast changes. However, it is prone to produce evaporation. Modulation of oxygen on-chip through chemical reactions that either consume or

generate oxygen is another common method. It avoids the need of pre-equilibration of the fluids or bulky gas cylinders, but it requires a careful study of the reaction kinetics and it consumes reagents [223,224].

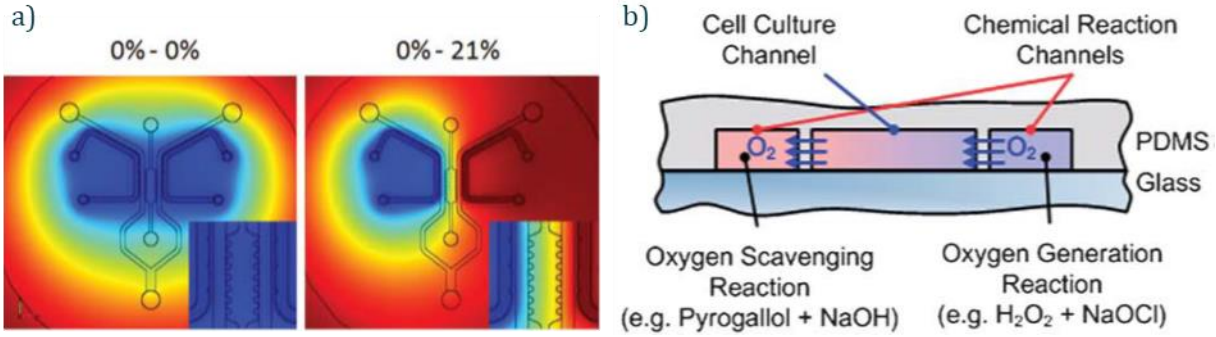

Figure 1.14: Oxygen modulation in microchannels exploiting diffusion in the device through a permeable membrane. The medium in the culture chambers equilibrates with the oxygen level of the adjacent channels, generating uniform or gradient concentrations. The oxygen levels in the adjacent channels can be obtained using pre-equilibrated gas mixtures with specific oxygen concentrations (a) or chemical reactions that remove or produce oxygen (b). Adapted from [222] *and* [223] *respectively.*

Most importantly, these methods allow for the generation of oxygen tension gradients across the tissue, simulating the gradients present *in vivo* [144,225]. As well as a tight control of the oxygen tension, it is also crucial to incorporate methods for the measurement and monitoring of the oxygen in the devices. The most common method for measuring oxygen concentration is the Winkler titration. In this test, an excess of manganese (II), iodide and hydroxide ions are added to water, and the precipitate is oxidised by the oxygen present, changing the colour of the precipitate. Then, a strong acid is added, and the oxidised precipitate converts the iodide ion to iodine, which is then titrated to calculate the amount of dissolved oxygen (directly proportional relation). This method is very precise, but rather cumbersome, time-consuming, and does not allow for continuous sensing. Electroanalytical methods are also widely used for the determination of oxygen. The most known is the Clark electrode, in which a voltage is applied across the working electrode and the reference electrode, reducing oxygen at the working electrode and producing electrons (current) proportional to the amount of oxygen present. This method, however, consumes oxygen in order to measure it, which may confound the results if the sample is not stirred continuously. It also depletes the analyte, and the electrodes are subjected to fouling, meaning that they are not suitable for long-term measurements. Optical sensors have become attractive in the last years due to their lack of oxygen consumption during measurements, good precision and accuracy, they allow for non-invasive or remote sensing, and they are easy to miniaturise. Optical sensors can be designed as molecular probes, planar sensors, fibre-optic sensors or nanosensors. Luminescent probes for oxygen measurement are based on the quenching of the intensity of an oxygen-sensitive probe (usually a dye). The process involves the collision of molecular oxygen

and the probe, leading to a reduction of its intensity [226]. The relationship between the luminescence intensity and the oxygen concentration is established by the Stern-Volmer equation [221] (Figure 1.15). Typically, the oxygen sensors consist of the indicator and a matrix or host. Wang *et al.,* did a very extensive review on oxygen optical sensors discussing the properties of the different indicators and materials used in the literature. These sensors have been widely used in microfluidic systems[225,227,228].

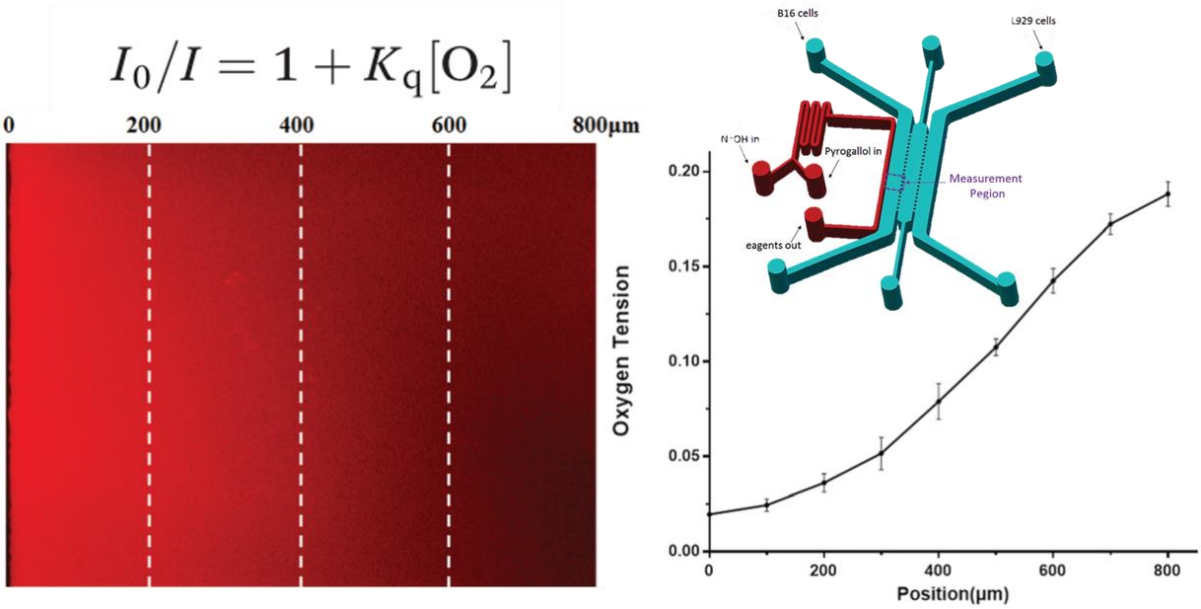

Figure 1.15: Oxygen sensing device using an oxygen-sensitive fluorescent dye. The oxygen-scavenging channel removes oxygen from the adjacent channels. On the right, the fluorescence intensity measured across the width of the microchannel. The pyrogallol reaction removes the oxygen from the left side, increasing the fluorescence intensity, while diffusion of atmospheric oxygen from the opposite side increases the oxygen concentration, reducing the fluorescence intensity. The Stern-Volmer equation converts the fluorescence intensity into oxygen tension [225].

Another fundamental variable in cell cultures is pH. Most biological processes are very sensitive to changes in acidity, thus pH must be very well controlled and defined. pH in cell culture is usually regulated by adding buffers to the perfusing media. The most physiologically relevant method is CO_2/HCO_3^- A salt of HCO_3^- is included in the medium to balance the H^+-yielding CO_2 hydration reaction. This approach provides a volatile and weak buffering at low pHs. To overcome this, exogenous non-volatile buffers (NVBs) such as HEPES, MES or PIPES have been introduced (Figure 1.16).

$$CO_2 + H_2O \xleftrightarrow{Carbonic\ anhydrase} H_2CO_3 \leftrightarrow H^+ + HCO_3^-$$

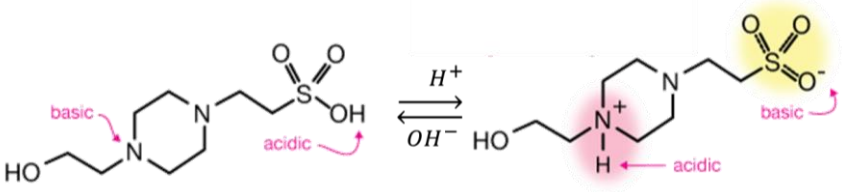

Figure 1.16: Equilibrium equations for the regulation of pH using the CO_2/HCO_3^- method (top) and using a NVB such as HEPES (bottom).

pH level is achieved by the equilibration of two opposing reactions: (1) the dissolution of CO_2 from the atmosphere that reacts with the medium and acidifies it, and (2) the equilibration between HCO_3^- ions and NVBs that alkalinise the medium. This balance is delicate and is difficult to predict, thus continuous monitoring would help in the stabilisation of the pH. The most used method for pH monitoring is using Phenol Red, a pH indicator that gradually changes from yellow to red over a range from 6.8 to 8.2. Similarly to the oxygen measuring methods, pH can also be measured using electrochemical methods [229,230] or optical sensors using luminescent indicators[231,232]. As an example of a feedback control of the pH, Welch *et al.*, 2014 presented a microfluidic device able to measure the pH using an extended-gate ion-sensitive field-effect transistor (ISFET) integrated with a system of valves with two reservoirs containing high and low pH solutions. The pH is obtained by adjusting the flow from the two inputs and controlled in real-time using the measured pH in the chamber as feedback [233]. Many have been the reports including monitoring of both parameters embedding oxygen and pH-sensitive dyes in the same polymer matrix [234,235] or adding the sensors in-line and detecting the absorption of light by the medium using photodiodes [236].

The third most important physicochemical parameter is temperature. In the human body, the temperature is tightly controlled at around 37°C. In conventional cell cultures, the cells are cultured in incubators at this temperature. Just like hypoxic chambers described above, these chambers only allow for one temperature at once, without the possibility of rapid changes or gradients. Additionally, the cells suffer a sharp change when they are extracted from the incubators for analysis, which can alter the results. In microfluidic devices, there have been many publications reporting temperature-control elements integrated into the system, using Joule effect in conductive materials [223] or ionic liquids [237]; using Peltier elements [238]; pre-heated liquids flowing next to the channels or culture chambers [239]; or endothermic or exothermic chemical reactions [240]. Common methods for determining the temperature are commercial probes such as resistance thermometers (Pt100 sensor), controlling the voltage across the heating elements [223] or using optical methods, such as temperature-dependent fluorescent dyes [241] or microwave thermometry [242]. Interestingly, luminescence-based methods use dyes that are sensitive to a particular factor while being independent of others. Hence, several dyes can be integrated into the same sensor to measure multiple parameters, such as the one presented by Borisov *et al.*, 2011, where oxygen, carbon dioxide, pH and temperature were measured simultaneously [243] (Figure 1.17).

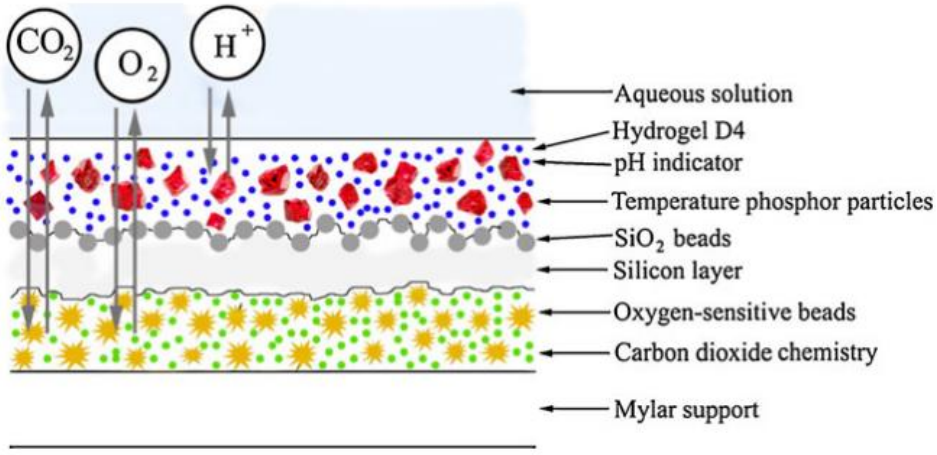

Figure 1.17: Integration of multiple fluorescent dyes for sensing multiple analytes in a single planar sensor [243].

1.4.1.2 Biochemical

The microenvironment hosting the cells and tissues is composed of a wide variety of soluble factors such as cytokines, growth factors, hormones, and other biomolecules. To characterise the MPS and obtain a closer replicate of the *in vivo* situation, these parameters should be controlled and monitored too. This is accomplished by tuning the formulation of the perfusion medium or blood surrogate (controlled concentrations of glucose, lactate, amino acids, hormones, ions, salts…) to enhance the survival of the tissues cultured. Typically, these parameters are set before the start of the experiment and are maintained constant throughout the length of it. However, for long-term cultures, this might not be the most accurate representation of the physiological situation. The human body is subjected to time-dependent fluctuations of hormone, nutrient and metabolite levels. These cyclic modulations are known as circadian rhythms. Circadian rhythms are biological rhythms that oscillate over a 24-hour period, and they are governed by internal or external stimuli such as the genetic clock or the light cycles. A well-known example of a circadian rhythm is the blood glucose levels and plasma insulin levels in response to food intake. Most MPS operate under static conditions, i.e., the levels of glucose, insulin, and other factors are maintained constant. Cyr *et al.*, 2017 proposed a microformulator to substitute a missing organ or system, in this case, the endocrine system. They suggested a device that released the necessary hormones at specific times [217]. This work is only theoretical, and they did not present an actual microformulator. However, Xiao *et al.*, 2017 did take this idea into practice. This group presented a female reproductive tract-on-chip, to which hormones were supplied externally at specific time points to simulate the hormonal cycle in the reproductive tract over 28 days to support follicular growth and maturation and ovulation [93]. The monitoring of all the factors present in the media would be of great utility and would give a great deal of information to fully characterise dynamic cellular metabolic and signalling responses. However, it is not feasible to

include sensors for every single soluble factor. Even with current clinical blood analysis, only a small number of highly concentrated biomolecules are detected. There is an impressive number of published works focused on the detection of specific molecules, such as glucose, lactate, metal ions. These parameters can be measured using amperometric techniques, for example using electrodes coated with analyte-specific enzymes (e.g. glucose oxidase or lactate oxidase) that are consumed in the presence of the analytes and the resulting hydrogen peroxide is oxidised at the working electrode, producing a measurable current [244,245]. Field-effect transistors (FETs) have also been utilised (Ion-sensitive FET (ISFET), Biosensor FET (BioFET), Chemically-sensitive FET (ChemFET)). They are based in the MOSFET (metal-oxide-semiconductor FET) structure but the gate current is generated by changes in the surface potentials induced by the binding of ions, molecules or chemicals [246]. A further modification of the ISFET was introduced by Hafeman *et al.,* with their light-addressable potentiometric sensor (LAPS), in which used light to detect the variations of the surface potentials caused by the changes in the analyte. This method allowed for laterally resolved measurements of the analyte concentrations by focusing the light beam in different spots and even permits the measurement of multiple chemical events with a single semiconductor device [247–249]. Optical techniques are also extensively used for the detection of multiple molecules. For example, Steiner *et al.,* presented a thorough review on the sensing of glucose using optical methods [250]. Luminescent sensors have also been used to measure metal ions present in the body such as sodium, potassium, calcium, magnesium, iron and zinc. These metals play critical roles in physiological processes such as osmotic regulation, metabolism or biomineralisation [251].

1.4.1.3 Other inputs

Chemical gradients exist *in vivo* and induce localised cellular responses. These gradients are an important signalling mechanism and play crucial roles in growth, migration, differentiation, or the immune response. Controlling chemical stimulation can lead to more physiologically relevant responses in the cultured tissues. Traditional gradient generation techniques include biological hydrogels, micropipettes, or the Boyden/Transwell® chambers. However, these techniques do not allow for much control over the spatiotemporal evolution of the gradient, they do not allow multi-factor gradients, and are difficult to quantify or reproduce. The recent advances in microfluidic technology have opened new opportunities to overcome these issues and allow the generation of predictable, reproducible, and easily quantifiable gradients. Keenan *et al.*, 2008, presented a review of the most relevant gradient generation methods. They divided the microfluidic gradient generation techniques in: substrate-bound gradients, in which the biomolecules are selectively absorbed to the cell culture surface; steady-state gradients, regions of constant concentrations are created exploiting the properties of fluids in

microchannels; and time-evolving gradients, that vary in space and time and have a limited lifetime, but are solely determined by the biomolecule's diffusion coefficient and the geometry of the device and thus can be predicted and characterised [252]. Microfluidics also offer the possibility to generate more than one gradient in different orientations. For example, Chang *et al.*, 2014, used a network of channels to obtain a laterally distributed chemical gradient in the direction perpendicular to the flow, and an oxygen gradient in the direction of the flow by scavenging through a polydimethylsiloxane (PDMS) membrane [253].

Mechanical stimulation in cells affects many cell functions such as motility, apoptosis, proliferation, or protein expression. Devices have been developed to examine shear stress, compression, or tension. For example, the well-known lung-on-chip by Dr Ingber's group contained two empty chambers to which different pressures were applied to expand and contract the membrane where the cells were attached. This mimicked the breathing movements in the lungs, and it was observed that with the cyclic movements, transmigration of nanoparticles across tissues was enhanced, accentuating the proinflammatory activities of the tissue and contributing to acute lung inflammation [83]. Mechanical forces have also been locally delivered through magnetic beads, laser tweezers or atomic force microscopes. These studies have greatly contributed to the understanding of the influence of mechanical stimuli on the structure and function of the cells (mechanotransduction, cytoskeleton, cells shape changes or network remodelling). Combination of multiple parameters has also been achieved, for example, in the work presented by Dou *et al.*, who established a topographical and a chemical gradients in orthogonal directions to study the synergy effects of epidermal growth factor (EGF) and the matrix stiffness in glioma cells [254].

Other possible inputs to achieve more realistic recapitulations of the *in vivo* situation include: (i) electrical stimulation, only relevant in conductive tissues such as cardiac and nervous tissues. There are diverse techniques to examine and control electrical inputs such as glass micropipette electrodes, the Campenot chamber, or microelectrodes, like the ones presented in section 1.3.3.3; (ii) Genetic inputs, that is, using genetic engineering to manipulate the expression of particular genes or (iii) optical excitation, using the light as an input activator, not as a cellular readout, to control, for example, ion channels that control electrically active cells.

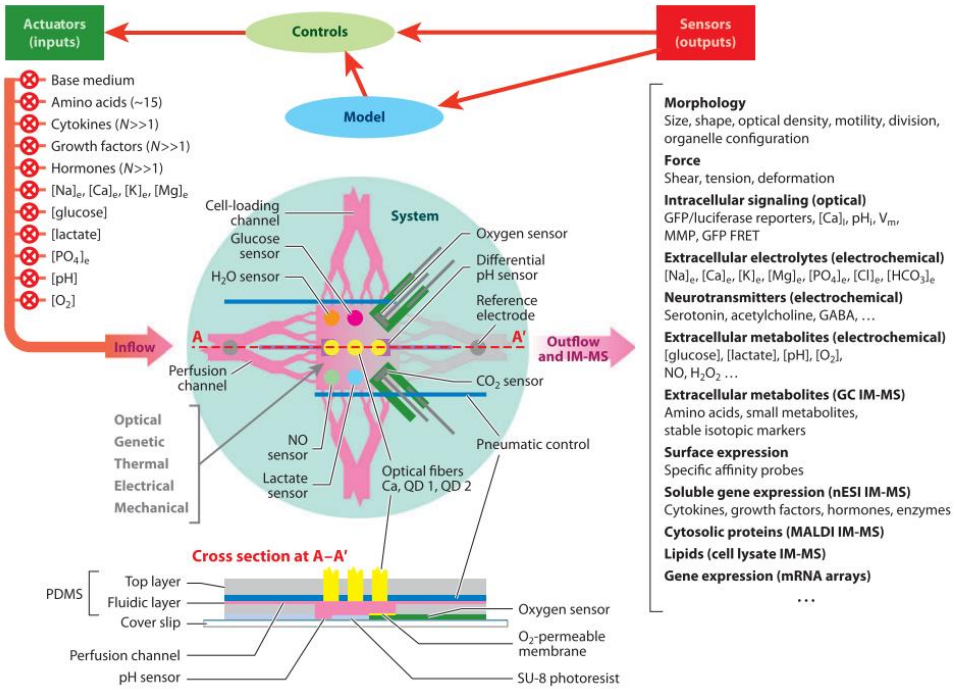

Figure 1.18: Schematic representation of a hypothetical multiple input-multiple output system proposed by LeDuc et al. [255].

1.4.2 External stimuli

All the parameters discussed above aim to replicate the *in vivo* environment in order to obtain the most physiologically relevant responses possible to study cellular behaviour. Additionally, it is also important to include external signals in a physiologically relevant manner to challenge the cells and tissues and study their responses to predict the effects of that challenge or substance in the body. In MPS, these compounds can be delivered in a wide variety of ways, taking advantage of the opportunities in fluid control that microfluidics offer. Using the properties of laminar flow, the investigators can choose the regions of the tissue that they want to subject to the treatment [106,128] or can use ports or open channels underneath the culture chamber for a more localised delivery [133,134,137,138]. More recently, microfluidic devices have been interfaced with threads, to transport fluids *via* capillary action, to achieve localised delivery with high throughput and with a significantly reduced cost of fabrication [256].

All these methods, however, are designed to expose the cells or tissues to pre-set constant concentrations of the compounds, with limited spatial or temporal control. *In vivo,* administered substances undergo ADME processes, which entail gradual changing of the pharmacokinetic concentration profiles. The concentration dynamics of the substances in the body define the exposure duration above the effective or toxic thresholds, which influence the impact of the said substance. Constant concentration, thus, do not recreate realistic *in vivo* situations, and new methods need to be developed [257]. Currently, there are two approaches to address this issue: integration of

several organs involved in ADME to obtain the pharmacokinetic profile, or using external devices that combine precision pumps with temporal modulation of the substances delivered in a single organ [258]. Both approaches are complex and difficult to scale for high throughput screenings. Other efforts have been focused on the generation of dynamic concentration profiles in microfluidic devices without the need for structural amendments. For example, Lohasz *et al.*, 2019 presented a microfluidic device in which the flow was gravity-driven by simply tilting the device and consisted of an asymmetric Y-junction connected to three reservoirs. The repeated tilting generated the mixing of the liquids in the reservoirs, gradually changing the substance concentration at the culture site [257]. This approach was also used by Lee *et al.*, but in this case, the height of the reservoirs was manipulated to obtain dynamic concentrations [259]. Song *et al.*, 2018 presented a device able to obtain dynamic chemical gradients to generate multiple spatio-temporal stimulation profiles [260]. As it can be deduced from all the methods and techniques here presented, and the many more that have not been included, that there is a wide range of possibilities for the study of specific tissue functions to obtain more precise and accurate systems for the determination of drug responses and cellular behaviours and interactions.

1.4.3 Viability measurements

As well as methods for the control of the parameters in which the tissues will be interrogated, it is equally important to add ways to measure the responses to those challenges and conditions. According to a survey conducted by the University of Cambridge to bioscience researchers from academia and the pharmaceutical industry, the most used analytical methods employed by biomedical researcher include western blotting, polymerase chain reaction (PCR), immunofluorescence microscopy, live-cell imaging, flow cytometry and Enzyme-linked immunosorbent assays (ELISA) [261]. Thus, for a wider application of MPS, the systems should be designed to be compatible with these analytical methods or even integrate them. Amongst the parameters that could be measured for evaluation of tissue viability and functionality include specific metabolites (lactate, albumin, urea via protein or gene expression) along with morphological changes such as size, shape, motility, or deformation. Most of these measurements are done off-chip, from samples taken from the effluents using the methods mentioned above [107]. On-chip measurements would be beneficial for the monitoring of the tissue viability and functionality in real-time and for long-term experiments. The most used non-invasive, on-chip measurement techniques include colorimetric and fluorescent staining. Stains have been used to examine cell morphology (e.g. Hematoxylin and eosin), quantify cell viability by counting live and dead cells (e.g. Propidium Iodide, Calcein AM, or MTT (3-(4,5-dimethylthiazol-2-yl)-2,5-diphenyl-2H-tetrazolium bromide)), LDH leakage, Adenosine triphosphate (ATP) levels, glycogen content, lipid accumulation or even to study hypoxia [55]. Other on-chip measurements more specific to

the function of the tissue should be included to study their functionality, to ensure that the cells are responding accordingly to the *in vivo* situation. For example, transepithelial electrical resistance (TEER) measures the impedance across the barrier to characterise the quality of the barrier function[262,263] and measurements of the electrical activity using multielectrodes can be used to assess the functionality of conductive tissues such as the brain or the heart [129,262]. Electrochemical methods are also widely used to detect soluble factors such as glucose, lactate, ions, or ROS. Furthermore, Zhang *et al.*, 2017 presented a system to fabricate label-free electrochemical immunobiosensors for detection of specific biomarkers (albumin, glutathione S-transferase α (liver markers) and creatine kinase MB (cardiac marker)). To achieve this, they designed a platform containing gold electrodes that could be functionalised with specific antibodies for biomarker binding and detection, and then washed out and regenerated upon saturation of the captured antigens for subsequent measurements [264]. Multiplexed assays collecting information on multiple parameters and analytes simultaneously can be a powerful technique for studying tissues and obtain a great deal of information on dynamic biological processes, along with providing more precise diagnostics. Schumacher *et al.,* presented the Fraunhofer ivD-platform (*in vitro* Diagnostics), a system aiming to establish a lab-on-chip that allows for a wide range of common medical assays (for example, hormones, metabolites, drugs, protein, peptides or DNA) with a high degree of integration of the sensing and pumping systems, and with potential for serial production. In this design, optical and electrochemical transducers are included for on-site analysis in short times [265]. Another promising tool for multianalyte microphysiometry is ion mobility-mass spectrometry (IM-MS). Even though this technique is off-chip, it has the potential to study complex biological samples at high speed. IM-MS consists of two steps, first, the analytes are ionised and separated and then the ions are characterised by their mass using conventional mass spectrometry analysis [266]. Low-vacuum, gas-phase electrophoresis can measure molecular cross-sections in micro- or milliseconds, followed by mass spectrometry analysis in microseconds, with a high sensitivity, allowing for the detection of thousands of molecular species almost in real time. Although promising, IM-MS instrumentation is very expensive (~$1 million) and still presents challenges such as the need for removal of salts from the medium without affecting the resolution, and the reduction of sample volumes required [267].

Most of the current work focuses on the control of one parameter, maintaining the rest constant to study its influence in the tissue survival. New technologies are advancing in the MPS field towards a multiple input-multiple output approaches, where numerous actuators and sensors are integrated and more complex studies can be performed, which has the promise of impactful breakthroughs in the biomedical and pharmaceutical fields.

1.5 Oxygen concentration effect in cell culture

Oxygen is key to life. Since oxygen started being available in the atmosphere, organisms have evolved systems to transfer the chemical energy stored in carbon bonds of molecules (such as glucose) to the high-energy phosphate bond in ATP, used to power physicochemical reactions in living cells. These reactions require the complete oxidation of glucose into CO_2 and water *via* oxidative phosphorylation, which uses oxygen as the final electron acceptor. Even though this process is much more efficient than glycolysis in terms of energy production, it generates ROS that can alter the biochemical or physical properties of macromolecules, which could lead to cell dysfunction or death. Therefore, organisms have also evolved cellular metabolic and systemic physiological systems to maintain oxygen homeostasis. Hypoxia-inducible factors (HIFs) are master regulators of oxygen homeostasis by controlling the delivery and utilisation of oxygen through complex, sensitive and cell type-specific transcriptional responses to oxygen availability variations [268]. Several members of the HIF family have been identified, including HIF-1, HIF-2, and HIF-3, with HIF-1 being the most well-known and described in the literature. The main function of HIF-1 is the regulation of metabolism. Under well oxygenated conditions, HIF-1 is under a constant and fast turnover. However, under hypoxic conditions, its degradation is inhibited, leading to its accumulation and subsequent translocation to the cell nucleus, where it triggers transcription of genes involved in adaptive responses, including the control of red blood cell production, regulation of angiogenesis, or modulation of the vascular tone. It is also responsible for the transition from oxidative to glycolytic metabolism. It is believed that this switch is essential for the prevention of excess mitochondrial generation of ROS that would otherwise occur due to the reduced efficiency of the electron transfer chain when oxygen levels are low. Extensive analysis of cultured human cells has revealed that the expression of hundreds of genes increases or decreases in response to hypoxia in a HIF-1-dependent manner, showing the pleiotropic effects of HIFs. Additionally, HIFs also play important roles in the development of diseases such as coronary artery disease, cancer, or obstructive sleep apnoea [268].

In mammals, oxygen is absorbed by the lungs, diffuses into the bloodstream in the alveoli and is circulated towards all the tissues in the body through the vascular network. Under normal conditions, each millilitre of blood carries about 0.2 mL of oxygen. In arterial blood, about 98% of this oxygen is reversibly bound to haemoglobin with the remaining 2% in a dissolved form [269]. The microvasculature provides rapid and locally optimised oxygen supply depending on the metabolic needs and functional status of each organ. This oxygen requirement ranges widely across different tissues in the body and pathological states. For example, the partial pressure of oxygen in arterial blood is 14% and in venous blood, 5% [270]; the average value in brain tissue is 4.5%, in the lungs is 5.6%, and in the kidneys 9.5% [271]. These values are altered in disease states, for

example, in brain tumours the partial oxygen pressure drops to 1.7%, in lung cancers to 2.2% and in renal cancer to 1.3% [272]. Despite oxygen being such a critical and tightly regulated parameter for both, healthy and pathological conditions, traditional *in vitro* cultures are performed at 95% air (79% N_2/21% O_2), supplemented with 5% CO_2. These conditions do not represent the physiological oxygen tension of the organs or the distinct microenvironments that define normal and diseased tissue phenotypes. This could have an impact on cell metabolism, ROS production, mitochondrial function, or even cell differentiation [142].

Cells are constantly sensing and responding to stimulation from their surroundings. Therefore, due to the regular culture conditions previously described, *in vivo* cellular functions and responses are lost or modified in conventional dish-based cell cultures, limiting their predictive capability and skewing research results. For instance, it has been noted that endothelial cells align and elongate in the presence of shear stress, and several other cell types change their morphology when experiencing substrate changes. Mimicking as closely as possible the physiological conditions is crucial to obtain accurate responses. Already in 1977, Packer and Fuehr found that low oxygen concentrations extended the lifespan of cultured human diploid cells [273]. It has also been reported that adipose tissue-derived stromal cells retain their natural phenotype when the oxygen levels of their physiological niche are maintained. Similarly, the quality of pluripotent stem cells is significantly improved when these cells are grown in an atmosphere ranging between 1 and 10% O_2 (commonly consider as hypoxic concentrations) -which is being exploited by *in vitro* fertilisation laboratories. Thus, it is important to determine and replicate the physiological oxygen levels in each tissue for their study *in vitro*. In conventional cultureware, adherent cells are cultured in a monolayer at the bottom of well plates. Thus, the only way for oxygen to reach the cells is by diffusion through the medium overlay. The speed of oxygen delivery is determined by the oxygen solubility, diffusion coefficient, medium overlay height, surface area, and the partial pressure of oxygen above the medium. If the consumption rate exceeds the oxygen delivery speed, the oxygen pressure in the cells (pericellular) would eventually equilibrate at a hypoxic value. Currently, there is no standardisation of the volume of media supplied to the cells or the attention given to the differences in oxygen demand of different cell types. There is also a discrepancy in the terminology and units used, which makes it difficult to compare the results of published material on *in vitro* hypoxia studies. For example, the terms normoxia, hypoxia and hyperoxia are somewhat arbitrary, as they refer to the composition of the headspace gas and not the actual pericellular microenvironment [274].

As mentioned previously (section 1.4.1.1), traditional methods for the study of tissue behaviour at low oxygen concentrations rely on hypoxia workstations and hypoxic chambers, which do not allow for spatial control in the microscale or rapid changes in the oxygen concentrations.

To avoid the limitation of sparse oxygen delivery, culture dishes with gas-permeable bottoms have been made available. In these devices, oxygen is delivered through the membrane, which allows to regulate the pericellular oxygen levels more closely with faster equilibration times [275]. Others have reported the use of hypoxia mimetic agents instead of controlling the oxygen availability: hypoxic conditions are simulated by increasing the availability of HIF-1, for example, through the addition of compounds, such as cobalt chloride, that compete with the iron ions necessary for the enzymatic activity of the prolyl hydroxylases (PHDs), which are crucial for degrading HIF-1 [276]. A different method to control gaseous microenvironments relies on purging or directly bubbling the gases in the culture medium, although these require large volumes of gas supply and sophisticated instruments with precise gas controllers [277]. Some published works have added chemicals into the growth medium such sodium sulphite, but this could alter the composition of the medium and affect cellular responses [278].

Thus, conventional methods do not provide the capability of controlling the gaseous microenvironments in the spatial and temporal domains. In this context, microfluidic technologies arise as an interesting alternative to overcome these challenges, as they enable the precise control of the oxygen microenvironment. Because microfluidic systems are characterised by low Re_c (>2,300) [279], no turbulent flow is present to enhance mixing within the system, and so the transport of diffusive species occurs solely by diffusion as described by the Fick's Law:

$$x^2 = 2Dt \qquad (1.2)$$

where D is the diffusion constant. The diffusion time (t) depends on the square of the mean displacement. Therefore, diffusion in the microscales is much faster than on the macroscale. The predictability of the behaviour allows for the design of bespoke devices suited for mimicking the complex and intricate physiological situation.

Some reports controlled the oxygen concentration by flushing gas with known oxygen concentrations through microchannels near the cell culture chambers. Prof Eddington's group at the University of Illinois cultured cells exposed to normoxia and hypoxia within the same chamber, which allowed for crosstalk between cells exposed to different oxygen levels. They looked at the expression of HIF-1α and examined the metabolic profiles of hypoxic cells with normoxic neighbours and found that these are similar to the ones observed for cells exposed to homogenous hypoxia [144,280]. These results suggest that cells trigger hypoxic responses if neighbouring cells are under hypoxic conditions, even if they are not themselves (hyperoxia). They observed that HIF-1α (a subunit of HIF-1) was activated only when the oxygen concentration was below 2.5%, whereas HIF-2α was seen throughout the entire spatial gradient [144]. This is an important finding in the differentiation of the roles of HIF-1 and HIF-2. Funamoto *et al.*, 2012

used a similar approach to study the migration of cancer cells under normoxic and hypoxic conditions. Hypoxia is known to promote metastasis of certain tumour cell types and enhances their invasive potential. With their design, they were able to image in real time the behaviour of cancel cells under oxygen gradients. By monitoring the migration trajectories of individual cells, they observed that the net displacement and total path length increased upon culture under hypoxic conditions. They also noticed that the speed of migration increased 1.5-fold [222].

Similarly, oxygen gradients have been achieved by generating oxygen chemical sinks by which a chemical reaction takes place and absorbs the oxygen of the surroundings through a gas-permeable membrane. In this way, they were able to generate gradients by either controlling the concentration of the reagents [224], or the position of the scavenging channel with respect to the cell culture chambers [146,253]. Li *et al.*, 2016 developed a device that consisted of multiple cell chambers, each subjected to a specific oxygen concentration. They studied the cytotoxicity of two oxygen-sensitive, anti-tumour drugs (tirapazamine (TPZ) and cisplatin). Their results showed a higher resistance to TPZ than to cisplatin at 21% oxygen tension, and the opposite happened with oxygen at ~4%, evidencing the important role of oxygen in the efficacy of the treatments [224]. Chang *et al.*, 2014 developed a microfluidic device able to generate two perpendicular gradients: one chemical and one gaseous (Figure 1.19). With this system, they studied the cell viability under combinations of TPZ and oxygen gradients, and also the migration of the cells under combinations of a chemokine (stromal cell-derived factor (SDF-1α)) and oxygen gradient. In the presence of no gradient, the cells migrated randomly without specific direction. When only the SDF-1α gradient was applied, the cells tended to migrate towards the higher chemokine concentrations and when only the oxygen gradient was applied, the cells migrated towards the low oxygen tension side. When both gradients were present simultaneously, the cells moved towards the low oxygen side, without significant movement towards the higher chemokine concentration side, suggesting that oxygen may play a more important role in guiding cell migration than SDF-1α [253].

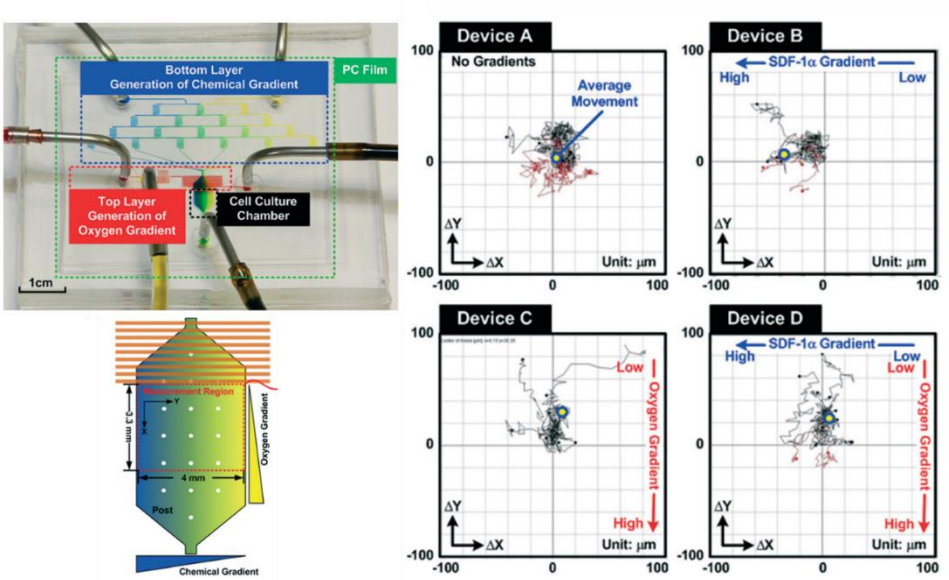

Figure 1.19: Dual-gradient generator device. Cells can be subjected simulatenously to multiple conditions. On the right, the cell migration of cancer cells under static conditions, a single gradient or a combination gradient. From [253].

Microfluidic methods to control gaseous microenvironments can also be applied to more complex models such as spheroids or the intestine-on-chip developed at the Wyss Institute. This group presented a platform able to control oxygen concentrations spatiotemporally and monitor tumour spheroid responses via microscopy in long-term. Their device consisted of a C-shaped hydrodynamic trap surrounded by hydration and gas control channels. They were able to observe that spheroids swell and shrink in response to time-varying oxygen profiles. Their results also showed that the uptake of an anticancer agent (doxorubicin) was higher under cycling hypoxia than in chronic hypoxia [281]. Jalili-Firoozinezhad *et al.*, 2019 integrated the well-known dual channel organ-on-chip lined with Caco-2 intestinal epithelial cells into an anaerobic chamber. They flushed the anaerobic chamber continuously with 5% CO_2 in nitrogen gas to maintain the low oxygen levels within the upper chamber (epithelium side). Oxygen diffused through the gas-permeable membrane from the oxygenated medium flowing in the lower chamber (endothelium side) (Figure 1.20). Compared to aerobic co-culture conditions, the hypoxia gradient increased the intestinal barrier function, and maintained a physiologically relevant level of microbial diversity [282].

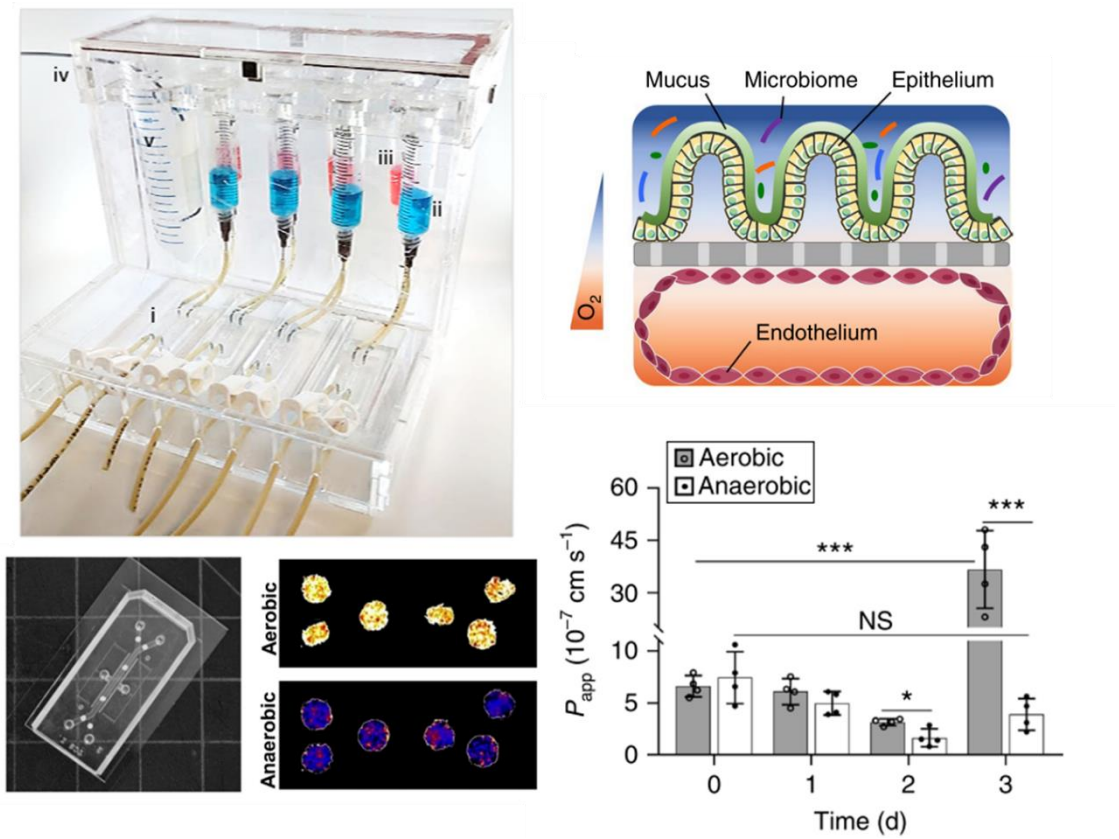

Figure 1.20: Human gut microbiome cultured in an anaerobic intestine-on-chip. On the top, the anaerobic chamber containing the devices and a cross-sectional view depiction of the chip setup. On the bottom, the modified chip with integrated oxygen sensors and the apparent permeability of the intestinal barrier under aerobic and anaerobic conditions [282].

1.6 Summary

Biomedical, pharmaceutical, and clinical research make use of *in vitro* models to study the human body in both physiological and pathological states, in order to gain insight into the functions, mechanisms, and interactions, and apply that knowledge to develop new drugs and therapies to improve our quality of life. Animal and human models provide holistic, systemic information but due to the complexity of the models, it is difficult to separate and elucidate all the factors involved and their individual roles. There are also ethical concerns around experimentation with humans and animals. Most countries have strict regulations for their use, which limits their availability and increases their cost [283].

In vitro models are simplified versions of tissues or organs-aiming to recapitulate a particular function or condition. The models are built using immortalised cell lines, primary cells or iPSCs arranged in two or three dimensions to obtain varying levels of fidelity and mimic the *in vivo* situation as closely as possible to obtain physiologically relevant information. They allow for large tests and screenings with high throughput. *In vitro* models have played a key role in the progress of life sciences in the last century. However, there is still a gap in the translation between *in vitro* and *in vivo*, as there is a lack of accuracy of the predicted responses.

With the advent of microfluidics, new *in vitro* models have emerged, holding promise to help overcome the current challenges. This technology allows for the organisation of the cells in *in vivo*-like architectures, under continuous perfusion, providing nutrients and removing cellular waste products, mimicking the role of the blood in the body. They also provide means for a tighter control of the microenvironment, and for multiple technologies to be integrated to monitor the culture conditions as well as the health and cellular responses.

An additional step in the quest for more representative *in vitro* models involves the use of whole tissue samples such as biopsies or PCTS. Culturing these samples within a microfluidic device would provide higher fidelity as the cell diversity, ECM and the tissue architectures are preserved, thus maintaining the *in vivo* phenotypes and responses. The increase in the complexity of the model also comes with more technological challenges, in particular, how to keep the samples viable and functional *ex vivo* for long enough to obtain the desired information.

Chapter 2. Research aims

Thus far, no MPS has been fully integrated in the biomedical or pharmaceutical fields. There still exists a need for technologies that fill the gap between the *in vitro* and *in vivo* situations. Tissue slices and biopsies have the potential to be the missing link. However, it is essential to obtain a better understanding of the behaviour of these models *in vitro* in order to maintain the samples viable for longer periods.

The main challenge facing the culture of tissue explants is the lack of functioning vascular network providing adequate nutrient delivery, gas supply and waste removal. Any platform aiming to culture samples for long-term will need to fulfil these requirements to ensure correct supply to the inner core of the samples. Other challenges involve the loss of physiological context of the tissue when extracted from the body. Mechanical stresses, chemical gradients, and other inherent stimuli such as growth factors, hormones and their fluctuations over time will need to be provided artificially.

The purpose of this project is to address the current limitations on the maintenance of tissue viability and functionality *in vitro:* to improve and prolong the viability and functionality of live tissues, to better understand the limiting factors that govern their survival and optimising the culture conditions to maintain the tissue. In the literature, samples are typically cultured under high-oxygen atmospheres to enhance oxygenation of the tissue, or in devices open to the atmospheric air. However, it is known that the oxygen tension within the body tissues is lower than those values and varies from organ to organ and from healthy to diseased states. This work will focus on the study of the influence of the oxygen tension in the survival of cells. This project will aim to:

1. Design, develop and optimise a new platform able to generate, control and monitor multiple oxygen concentrations within microfluidic tissue culture chambers. Including:
    1.1. Development of a microfluidic device to host tissue samples.
    1.2. An oxygen detector to monitor the oxygen levels during culture.
    1.3. An oxygen gradient generator to obtain several oxygen concentrations simultaneously without the need of bulky and expensive equipment.
2. Adapt and optimise the previously designed system for the culture of cells, subject them to an oxygen gradient and monitor their responses. Including:
    2.1. Preparation of cleaning, priming, seeding and culture protocols.
    2.2. Methods to assess the viability and functionality on-chip.
    2.3. Provide the adequate perfusion to the samples.
    2.4. Monitor the evolution of the cells in the device, and their ability to respond to changes in the oxygen levels.

Chapter 3. Development of the chip

The overall aim of this PhD is to develop a device that can maintain tissue viability and functionality long-term (generally, over 24 h is considered long-term [98,284]), and to study the effects of variations in the microenvironmental conditions and exposures to different compounds. The focus has been on the survival of cells and tissue in different oxygen tensions. Oxygen is a basic component of the microenvironment for cells. However, most *in vitro* cultures are performed under conditions that oversupply O_2, and not representative of the endogenous oxygen tension of cells in the body. Thus, the first step of this project was to develop a method to measure oxygen concentrations and to design and fabricate a system able to control the oxygen in which tissue is cultured, in order to assess the effects of these concentrations on the survival of the samples.

3.1 Oxygen sensing

As explained in Section 1.4.1.1, there are many available methods for the sensing and monitoring of the dissolved oxygen (DO) concentration. Optical methods offer many advantages such as non-invasiveness, high sensitivity, ease of miniaturisation and integration, and the fact that they do not consume oxygen for the measurements. Therefore, it was decided for this project to use an oxygen-sensitive fluorescent dye. Fluorescent probes are based on the quenching of the fluorescence intensity of the indicator. The process involves the dynamic collision between molecular oxygen and the excited probe (the dye in this case), and the transfer of energy between them (*Figure* 3.1). Collisional quenching is a photophysical process, not photochemical. This means that the process is fully reversible, and it does not alter the optical properties of the probe [226]. The relationship between the intensity of the fluorescence and the oxygen concentration is established by the Stern-Volmer equation (below) and illustrated in Figure 3.2.

$$\frac{I_0}{I} = 1 + K_{SV} \cdot [O_2] \qquad \textit{Eq. (3.1)}$$

Where I_0 is the intensity when the oxygen concentration is zero (no quencher present), I is the measured intensity at a given concentration, and K_{SV} is the quenching constant.

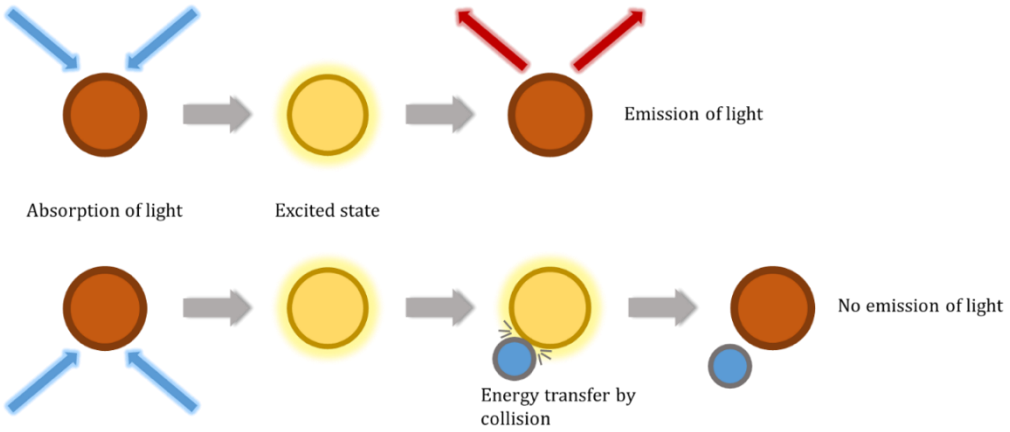

Figure 3.1: Depiction of the quenching of a fluorophore by dynamic collision. The light source excites the oxygen sensor to emit fluorescence. If the sensor encounters an oxygen molecule (blue circle), the excess energy transferred to this molecule is a non-radiative transfer, decreasing or quenching the fluorescence signal. The degree of quenching correlates to the oxygen partial pressure of the analyte. Adapted from: https://www.presens.de/knowledge/basics/detail/measurement-principle-of-chemical-optical-sensors-901

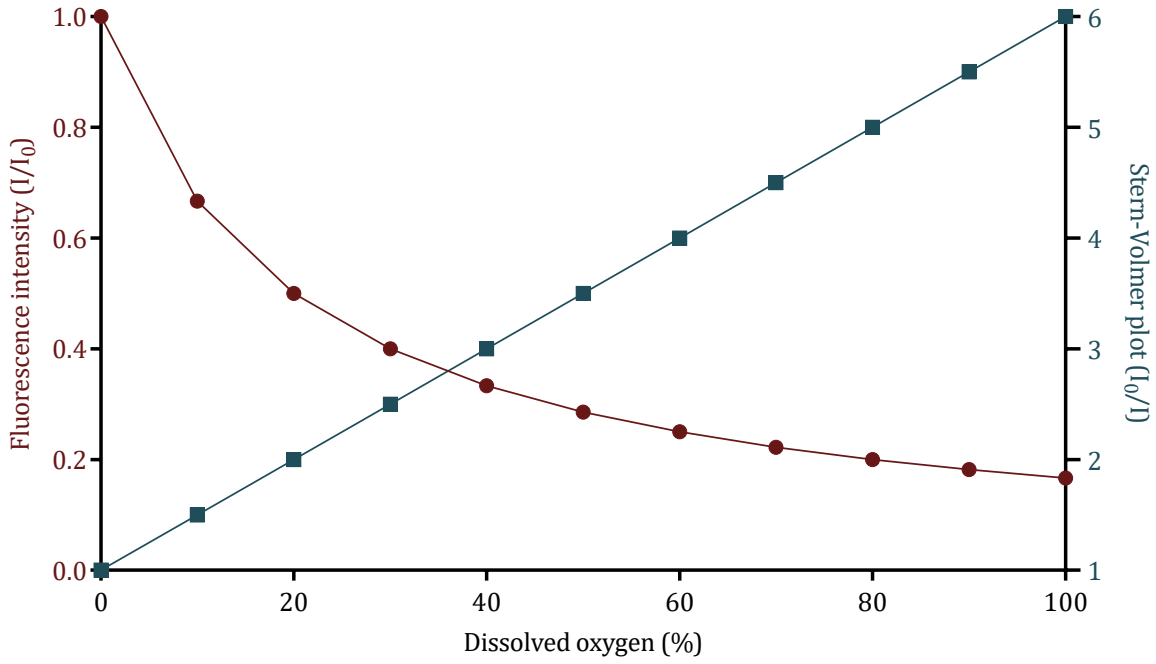

Figure 3.2: Example of a fluorescence intensity response (left axis) and its corresponding Stern-Volmer plot (right axis). The ideal optical oxygen sensor based on quenching has a linear Stern-Volmer plot with the oxygen concentration. The fluorescence decreases exponentially with the oxygen tension. 100% dissolved oxygen here is defined as the saturation concentration of oxygen in the liquid when equilibrated with atmospheric air.

Two of the most common oxygen-sensitive probes are ruthenium-based dyes and metal-loporphyrins. The first have a broad absorption band in the blue region and a large Stokes shift, whilst the latter are characterised by good chemical stability, long fluorescence lifetimes, higher sensitivity to oxygen, and are less sensitive to temperature. Specifically for this work. A ruthenium based dye called tris(2,2′-bipyridyl) dichlororuthenium(II) hexahydrate ($Ru(BPY)_3$) and a porphyrin-based dye called palladium(II) meso-tetra(pentafluorophenyl)porphyrin (PdTFPP)

were selected. $Ru(BPY)_3$ is water-soluble and exhibits good photostability while PdTFPP is not soluble in water, only in volatile solvents such as toluene or chloroform. However, they are both highly stable in polymers such as polystyrene or PDMS and are well suited for long-term continuous monitoring of oxygen. They present strong absorptions at the Soret bands (intense peak in the blue wavelength) and a large Stokes shift [226].

For the intensity characterisation of the dyes (maximum and minimum intensity corresponding to 0% and 100% DO, respectively) $Ru(BPY)_3$ was dissolved in phosphate buffered saline (PBS) at varying concentrations, and left open to equilibrate with the atmospheric air (100% DO) or mixed with sodium sulphite in excess to absorb the oxygen (0% DO). The PdTFPP dye was diluted in chloroform at 1 mg/mL then, PDMS prepolymer was added (PDMS dissolves in chloroform) at 1:1, 1:2, 1:5 and 1:10 ratios (mL dye solution:g prepolymer)., and the mixture was magnetically stirred for 1 h to mix the components and allow the solvent to evaporate, forming a homogeneous mixture. Next, the correct amount of curing agent (10:1 ratio to the amount of prepolymer added) was added and mixed manually. The mixture was degassed before it was deposited on the well plates and left to bake for 1 hour at 60°C. The 100% and 0% DO solutions prepared as previously mentioned were added on top of the cured sensors. A spectral scan was carried out for the two dyes in both oxygen concentrations using a Multimodal Microplate Reader (Clariostar Plus, BMG LABTECH). Figure 3.3 shows a comparison between the dyes. PdTFPP has a much sharper and narrower emission band, which facilitates the filtering of the wavelengths, and also shows a much larger difference in intensity between the 0% and 100% DO intensities, indicating the significantly higher sensitivity to oxygen levels of the PdTFPP dye. Figure 3.4 shows the relationship between the Stern-Volmer constant and the dye concentration. The value of the Stern-Volmer constant is a measure of the resolution of the dye (the higher the value, the better the resolution), as it is measuring the ratio between the maximum and minimum intensities. The low K_{SV} values obtained for $Ru(BPY)_3$ indicate a small difference between the 0% and 100% intensities. On the other hand, PdTFPP has a K_{SV} one order of magnitude bigger, which agrees with the results in Figure 3.3. For subsequent experiments, the concentrations with the highest K_{SV} were selected, which corresponded to 5 mg/mL for $Ru(BPY)_3$ and 1:1 ratio for PdTFPP.

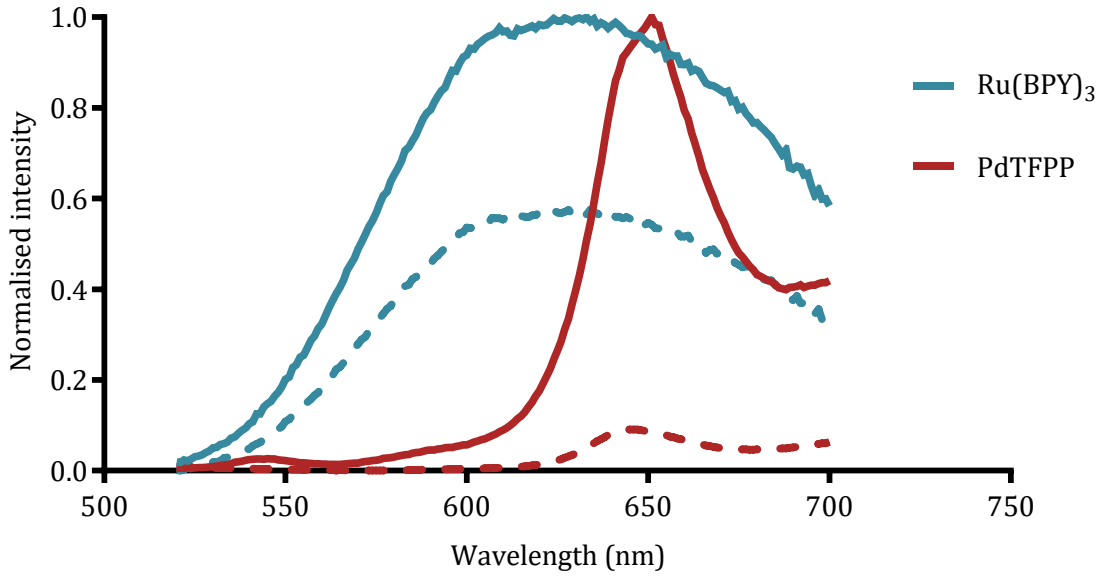

Figure 3.3: Normalised intensities of the excited dyes. Emission for $Ru(BPY)_3$ was set at 440 nm and 400 nm for PdTFPP. Continuous lines represent the 0% DO condition and the dashed lines the 100% DO. Values normalised to the maximum measured intensity for each dye for direct comparison.

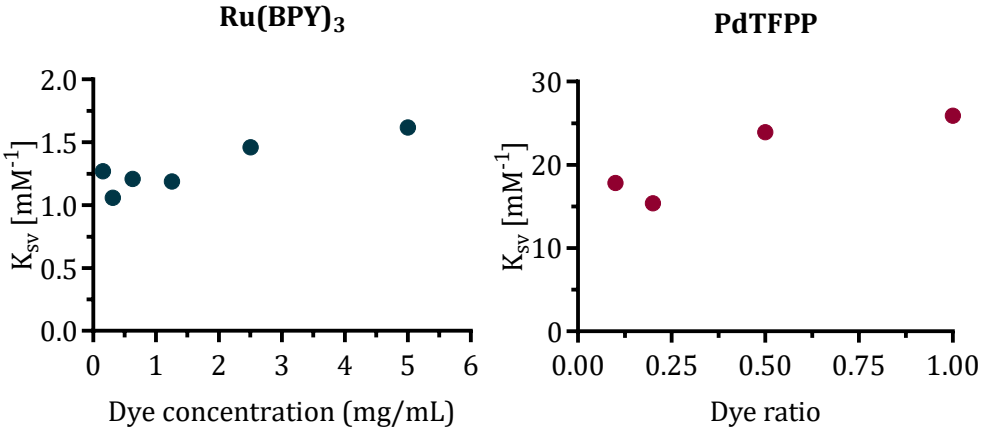

Figure 3.4: Comparison of the Stern-Volmer constants for the ruthenium-based and metalloporphyrin dyes for increasing indicator concentrations.

These oxygen-sensitive dyes cannot be used during cell culture given their toxic effects in the living cells, which limits the use of the ruthenium-based dye. For direct comparison with the porphyrin dye, the ruthenium-based dye was embedded in PDMS following the protocol explained above. However, the poor solubility of the ruthenium-based dye in the PDMS polymer was an issue and thus it was discarded in later experiments. Figure 3.5 shows a comparison between $Ru(BPY)_3$ (left) and PdTFPP (right) embedded in a PDMS membrane. It can be observed how the ruthenium-based dye clusters due to its poor solubility whereas the porphyrin-embedded membrane showed a homogeneous intensity.

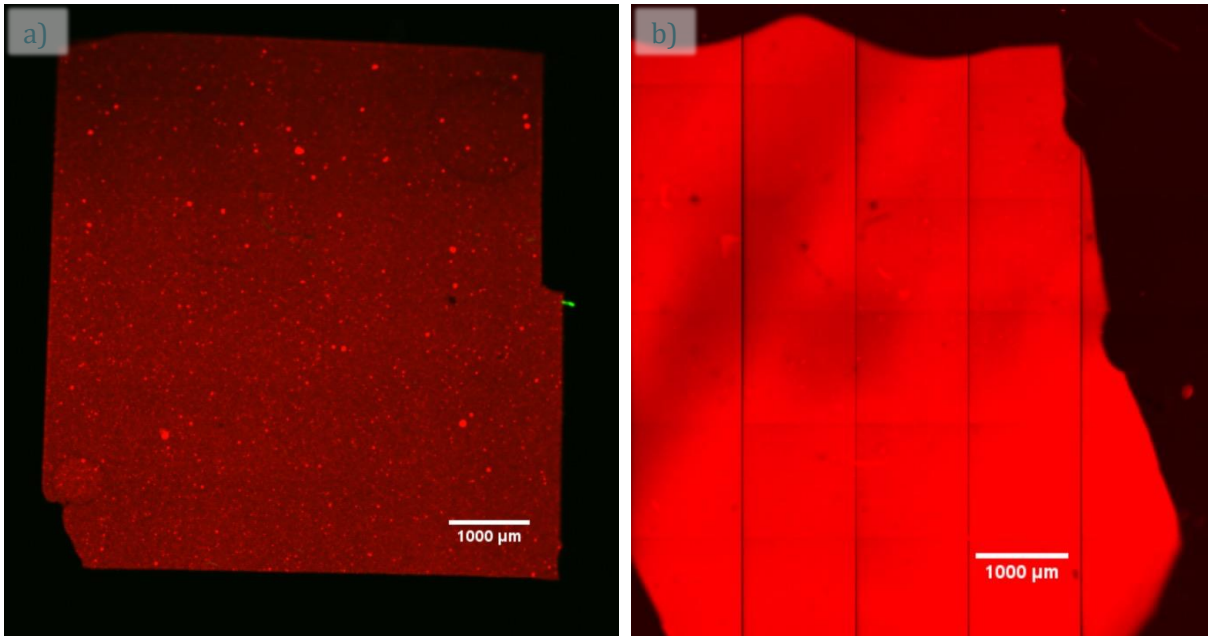

Figure 3.5: Oxygen-sensitive probes embedded in PDMS membrane 200 um thick. a) Ruthenium-based dye ($Ru(BPY)_3$), b) Palladium porphyin dye (PdTFPP) at the same dye concentration and following identical fabrication processes for direct comparison. Tile laser scan microscope images of the dye-embedded membranes immersed in oxygen depleted solutions. Images representative of triplicates for each dye. Scale bars represent 1 mm.

3.2 Device design and fabrication

The device consists of a culture chamber, the size of a 24-well cell culture plate well (ø16 mm), to hold the tissues, irrigated continuously with fresh media to provide a constant flux of nutrients and removal of cellular waste products. Figure 3.6 shows a conceptual representation of the device. To obtain the desired oxygen concentration, a chemical sink needs to be integrated (in blue). This sink consists of a chemical reaction that consumes oxygen. The reaction would be spatially confined, driving the reacting chemicals in close proximity to the flowing medium that irrigates the sample, and separating the reagents from the medium with a gas-permeable membrane to avoid contact of toxic substances with the tissues. Oxygen diffuses from the medium (red), through the membrane and into the reaction (blue). By controlling the flow rate of the chemicals and the medium, as well as the concentration of the oxygen-scavenging chemicals, a specific oxygen concentration should be obtained. The device would also incorporate an optically transparent lid to access the tissue for optical imaging.

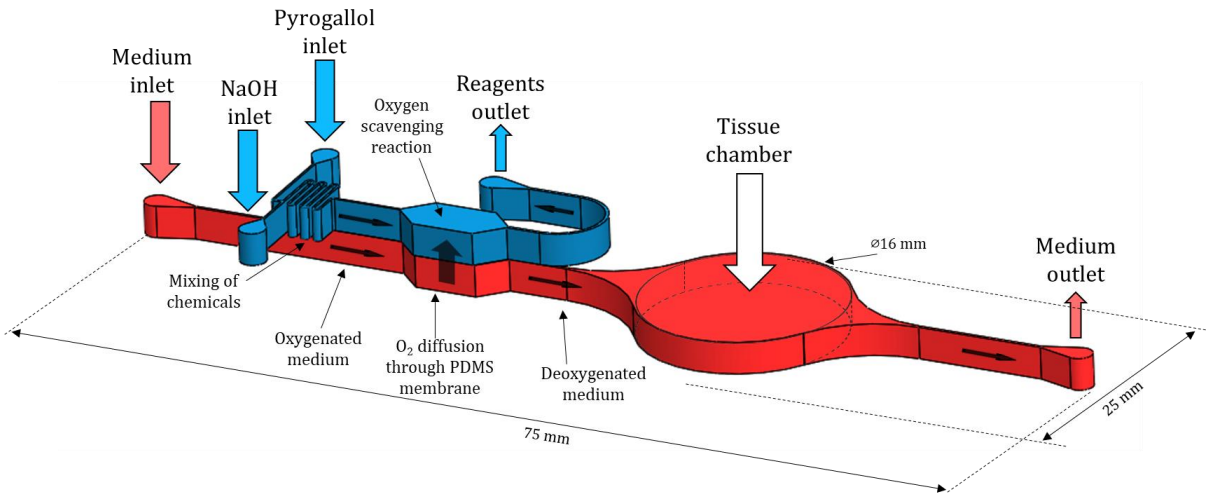

Figure 3.6: Conceptual depiction of the functioning of the prototype. The chemicals introduced in the blue channel react and absorb the oxygen from the medium flowing underneath in the red channel before it reaches the culture chamber where the tissue sits.

3.2.1 Design parameters

As previously mentioned, the oxygen concentration is controlled through a chemical sink in the microfluidic device. The oxygen sink is generated through a chemical reaction in a channel which is above the channel though which the medium flows to the sample. Over time both flows are in contact, and the reaction absorbs the oxygen from the medium before reaching the tissue (highlighted box in Figure 3.7). There are several factors that may influence the efficiency of the removal of oxygen from the medium: the channel geometry, the flow rates of the reagents and the medium, the material of the gas-permeable membrane and its thickness.

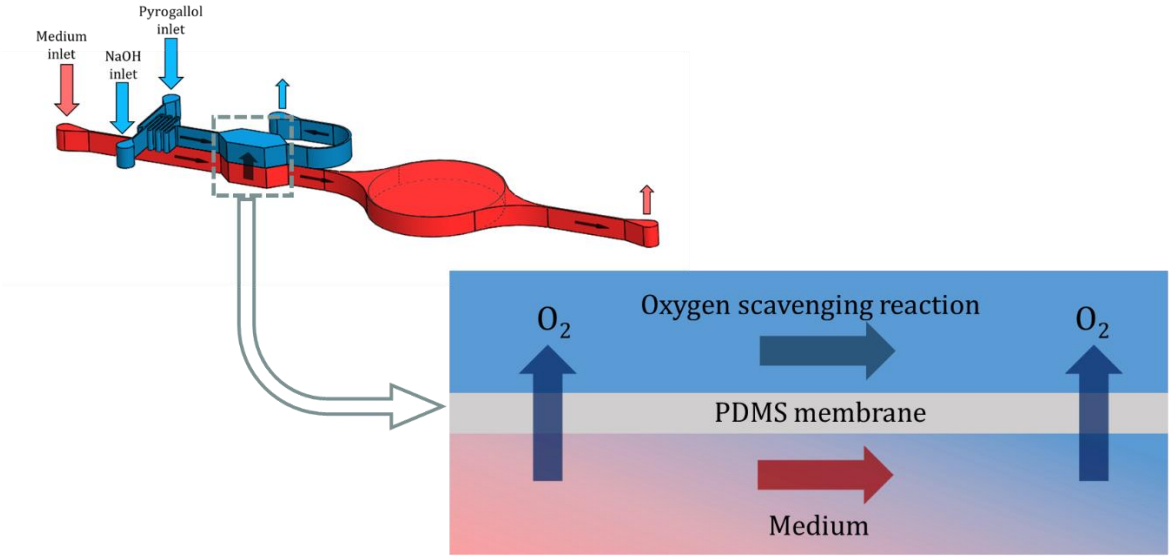

Figure 3.7: Detail of the diffusion of the oxygen from the medium channel to the scavenging reaction through the gas-permeable membrane.

Oxygen scavenging is achieved by exploiting the reduction of an organic compound, pyrogallol. Pyrogallol is a polyphenol compound, containing three hydroxyl groups, which are strong activators of aromatic systems. This turns the molecule very reactive, making pyrogallol an efficient free radical scavenger [285]. When in an alkaline solution, pyrogallol absorbs oxygen rapidly and changes colour from a colourless solution to brown (Figure 3.8). In these experiments, sodium hydroxide is mixed with the pyrogallol to catalyse the reaction. Given the speed of this reaction, the reagents are added into the device separately and mixed using a serpentine channel before reaching the region in contact with the medium, from where the oxygen is absorbed. This technique has been widely used in the literature [223,224,253].

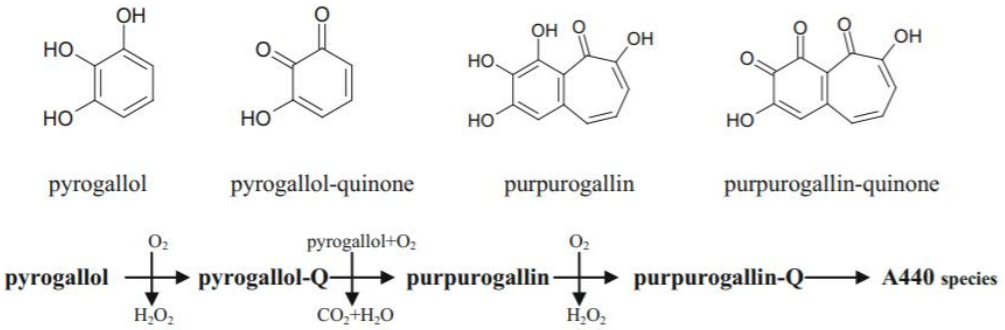

Figure 3.8: Reaction sequence of pyrogallol oxidation and its products [286].

Once in the device, the chemicals are mixed together in a serpentine mixing channel. The length of this channel was studied to ensure complete mixing before reaching the chamber where the oxygen diffusion takes place. A COMSOL simulation was carried out for this purpose. The three-dimensional model included two channels coming together in a Y junction followed by a 25

mm long serpentine channel (square channel, 250 µm-side) (Figure 3.9). A constant concentration boundary condition was applied to the inlets, one of the inlets with a concentration of 100% (representing the original pyrogallol concentration) and the second one with a concentration of 0% (representing the NaOH inlet). Measurements of the concentration were taken on each side of the channel at 1, 5, 10 and 20 mm from the junction (point A, B, C and D respectively in Figure 3.9). The mixing efficiency was calculated as:

$$mixing\ \% = \frac{1 - (C_R - C_L)}{C_{max} - C_{min}} \qquad \textit{Eq. (3.2)}$$

where C_R and C_L are the concentrations on the right and left side of the channel respectively at the measurement point, and C_{max} and C_{min} are the maximum and minimum concentration (i.e., the concentrations in the inlets). The results showed that a length of at least 20 mm was required to ensure complete mixing for any of the flow rates simulated. Based on this, a serpentine channel length of 25 mm was decided.

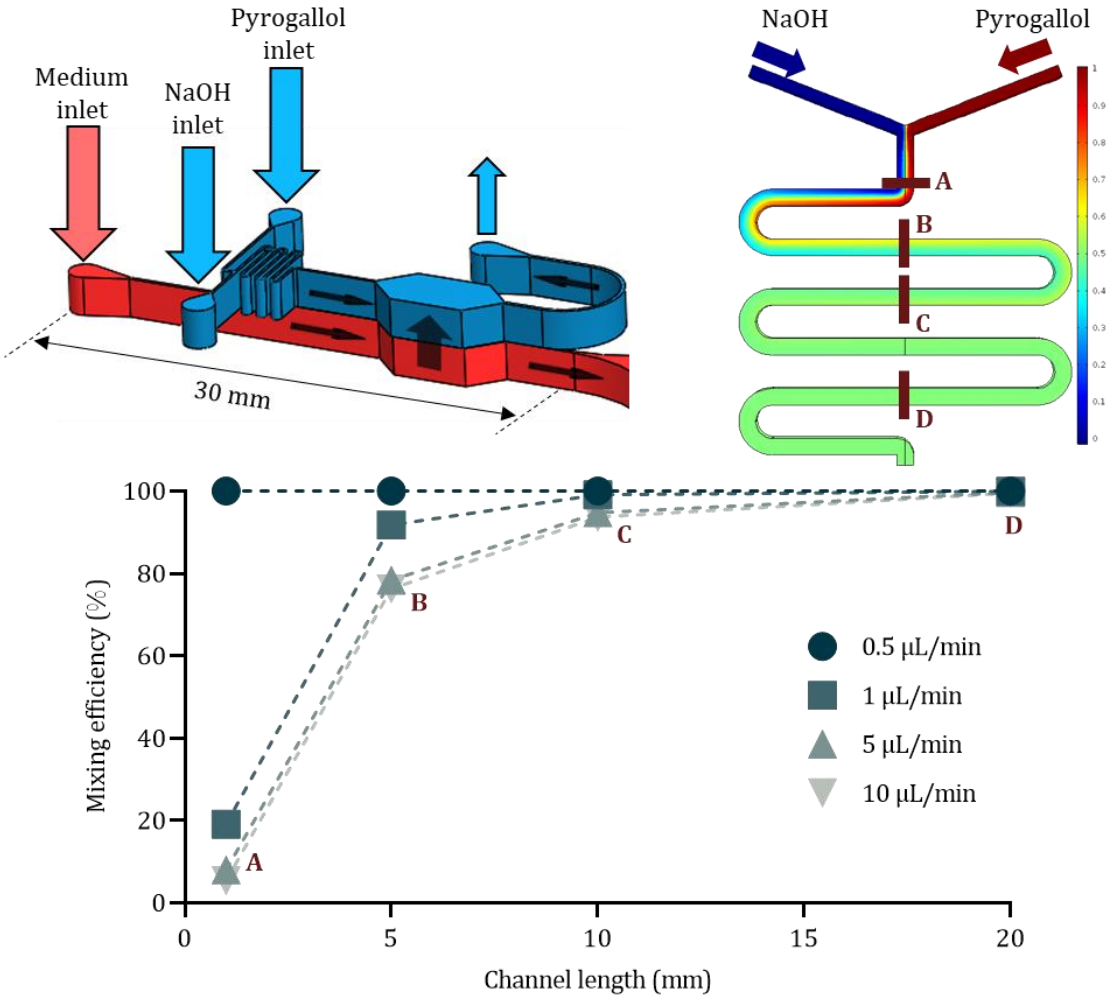

Figure 3.9: Detail of the mixing serpentine channel. The points A-D are cross-sectional cuts at different lengths of the channel where the degree of mixing is assessed (right). Below, simulation of the mixing between two fluid streams in the serpentine channel. The chemicals are mixed by diffusion, thus the mixing is more efficient for longer channels and slower flow rates that increase the time the fluid streams are flowing next to each other.

To study the effects of all the parameters on the oxygen diffusion and ensure that the equilibrium with the desired oxygen tension was achieved before the media reached the tissue, a finite element analysis was conducted using COMSOL Multiphysics 5.4 software and the Péclet number (*Pe*) used to estimate the efficiency of the diffusion. The *Pe* is the ratio of convective transfer of species in the axial direction to the diffusive flux within the channel. To compare the Pe for the different geometries used in the simulations, the factor α was introduced and defined as the geometric aspect ratio (L/H). The resulting expression is:

$$Pe/_{\alpha} = \frac{u \cdot H^2}{D \cdot L} \qquad \textit{Eq. (3.3)}$$

Where u is the velocity (m/s), H is the height (m), L is the length (m) of the channel and D is the diffusion coefficient (m^2/s). For these simulations, a three-dimensional model of two straight microfluidic channels separated by a PDMS slab was constructed, and the convection-diffusion equation was solved numerically. A chemical reaction was simulated in the domain of the scavenging channel. Assuming a reaction order of 1 for both components (pyrogallol and oxygen), the reaction rate constant was set at 5.4×10^3 $mol^{-1} \cdot m^3 \cdot s^{-1}$ [287]. The width and height of the channel were maintained constant, varying only the length of the channel and the flow rate. The results of the simulations showed a direct relationship between the dissolved oxygen tension at the end of the channel and the Pe/α number (Figure 3.10). To ensure a complete removal of dissolved oxygen (below 1%), the Pe/α number should be below 0.1. Taking into account that the only parameters modified during these simulations are the velocity of the fluid and the length of the channel, the height and the diffusion coefficient are constant. This simplification reduces the Pe/α number to u/L, i.e., the inverse of residence time, or the time that the medium and the oxygen scavenging reaction are in contact (through the membrane). Thus, a Pe/α number of 0.1 can be translated into a residence time of 3.5 minutes for this channel geometry, that is, the design of the channel, along with the flow rate of the medium have to ensure that the time the medium is in contact with the oxygen scavenging reaction is at least 3.5 minutes.

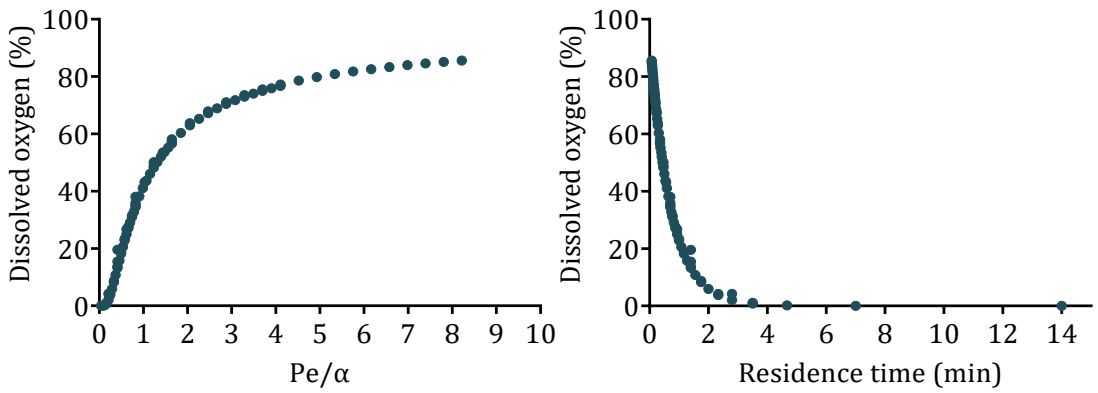

Figure 3.10: COMSOL simulation of the percentage of dissolved oxygen (100% is the equilibrium with the atmospheric air) at varying Pe/α and residence times. The dissolved oxygen concentration diminishes with decreasing Pe/α number and increasing residence times.

As a first approximation, the channel in which the oxygen diffusion takes place was designed as a 2 mm wide channel (Device v1.1; Figure 3.11a). COMSOL simulations were ran for lengths of 1, 2, 5 and 10 mm and flow rates of 0.5, 1, 5 and 10 µL/min. The simulation results in Figure 3.11b showed that at high flow rates (5 and 10 µL/min) the reaction did not have enough time to remove all the oxygen and longer channels would be required, which would increase the devices footprint. For the slower flow rates, a minimum length of 5 mm was needed to remove all the oxygen.

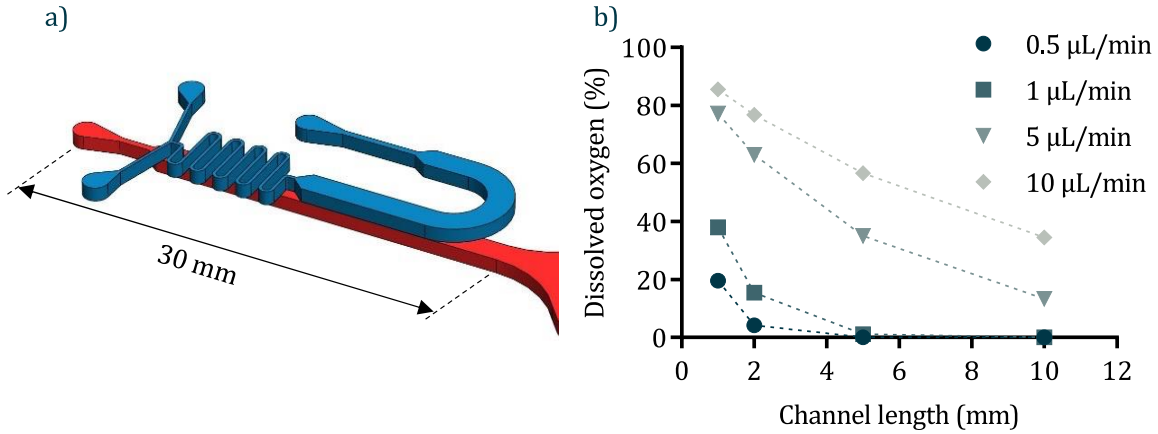

Figure 3.11: a) Detail of the gas interchange channe (Device v1.1)l. b) simulation of the dissolved oxygen concentration plotted against varying lengths of the channel in the highlighted box at different flow rates. The amount of oxygen that diffuses through the membrane is proportional to the residence time, i.e., increases directly proportional to the channel lengths and inversely proportional to the flow rate.

To reduce said footprint while maintaining or increasing the residence time, two other designs were proposed. The first design substituted the long channel with a small chamber 5 mm wide and 6 mm long to reduce the velocity of the fluids and increase the residence time (Device

v1.2; Figure 3.12a), while the second design included a serpentine channel, maintaining the fluid velocity but increasing the length of the channel and therefore the residence time (Device v1.3; Figure 3.12b). The simulations were repeated for these designs to compare the oxygen diffusion at the end of the diffusion region. The results for both designs were very similar, with a reduction of the residence time from 7 to 5 minutes for the small chamber and the serpentine channel designs (Figure 3.13). These results did not show a clear difference in the performance of these two designs and the small chamber design was decided due to its easiness of fabrication and assembly.

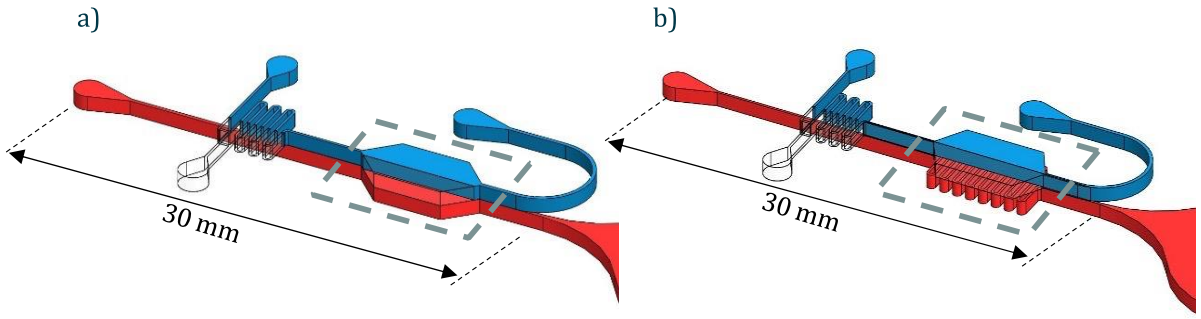

Figure 3.12: Detail of the 3D models of the gas interchange regions. In a) a small chamber (Device v1.2), and in b) a serpentine channe (Device v1.3).

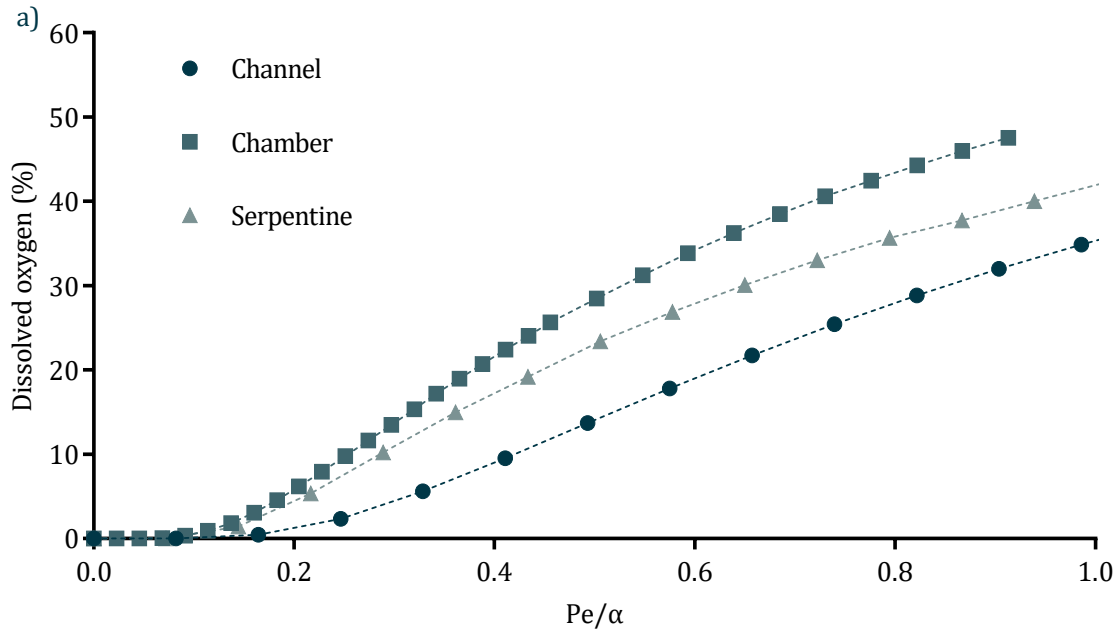

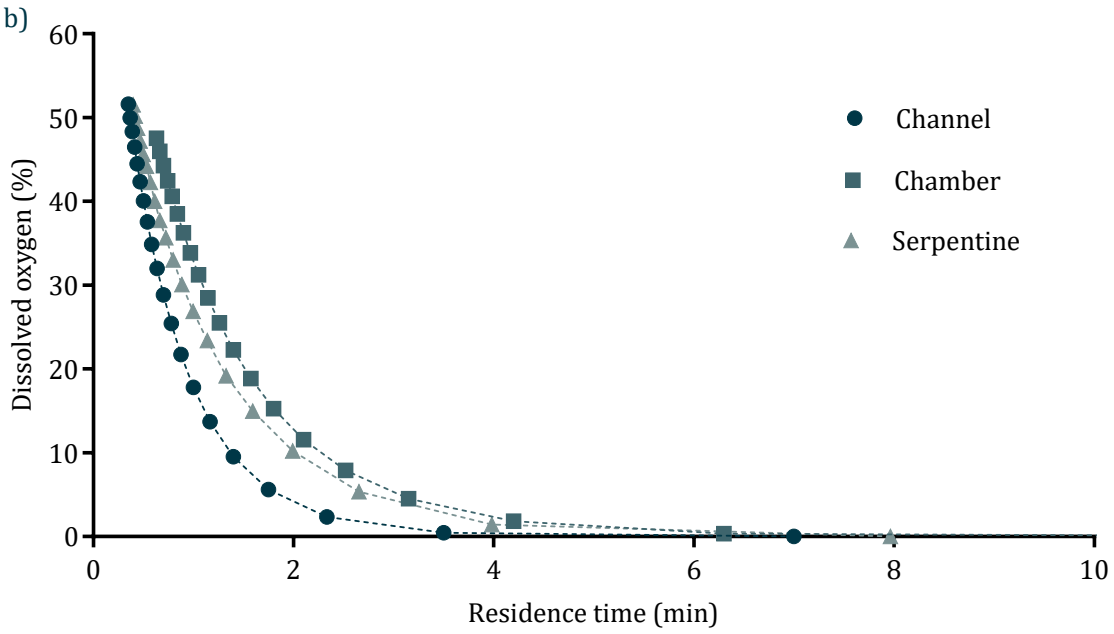

Figure 3.13: COMSOL simulation comparing the amount of dissolved oxygen diffused from the medium to the scavenging channel between different designs, including a long, straight channel, a small chamber, and a serpentine channel according to the Pe/α number (a) or the residence time (b).

These designs presented several issues. Due to the size of the culture chamber, comparatively large to the rest of the features of the design, any changes in the desired oxygen concentration within the culture chamber were very slow. This is due to the need of the new medium at the newly established oxygen tension to push the medium already present in the chamber at the previous oxygen tension (Figure 3.14). According to this simulation, the large chamber and the slow flow rate led to a refresh time above 150 min. Additionally, the design was not optimised for access to the tissue, and the height of the chamber was greater than the height of the fluidic layer. This resulted in a space between the top surface of the fluid in the chamber and the top surface of said chamber, which was filled with air, making it difficult to remove the oxygen. The design also had flaws in the fabrication and assembly process (discussed later). The rate of successful devices with no leaks was very low, and only one of the 15+ fabricated devices was able to run without leaks for 24 hours.

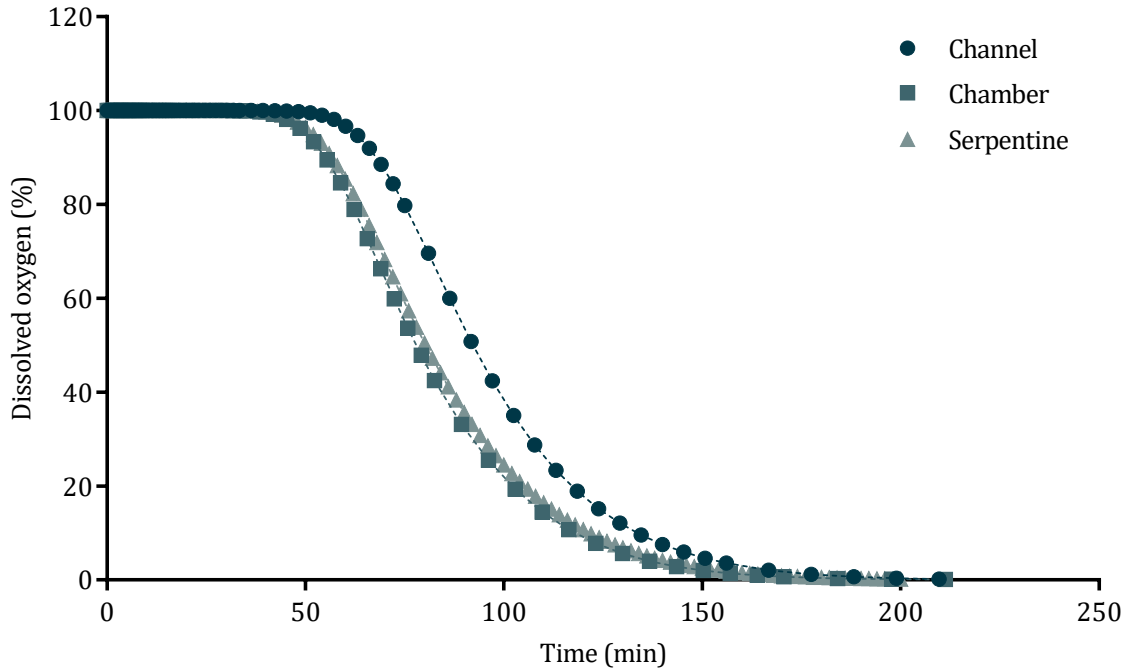

Figure 3.14: COMSOL simulation of the time for the chambers to change completely the oxygen concentration. For this simulation, laminar flow was assumed and the medium with the new concentration pushed away the old medium without mixing.

Thus, a new design was proposed, in which the whole system was fabricated in PDMS with top and bottom substrates made of glass to reduce the oxygen diffusion into the system. In this new design (Device v2) depicted in Figure 3.15a, the oxygen sink was placed right underneath the chamber holding the tissue. In this new design, the area of contact between the medium and the scavenging reaction was much larger (800 mm^2 vs 30 mm^2), and the diffusion of the oxygen was, consequently, faster. An array of microposts was included in the design of the oxygen sink layer to hold the PDMS membrane separating the fluids and avoiding the collapse of the chamber. The designs of the tissue chamber and the mixing channel were maintained. A COMSOL simulation was carried out under the same conditions to compare the diffusion time between the previous designs and the new one (Figure 3.15b)

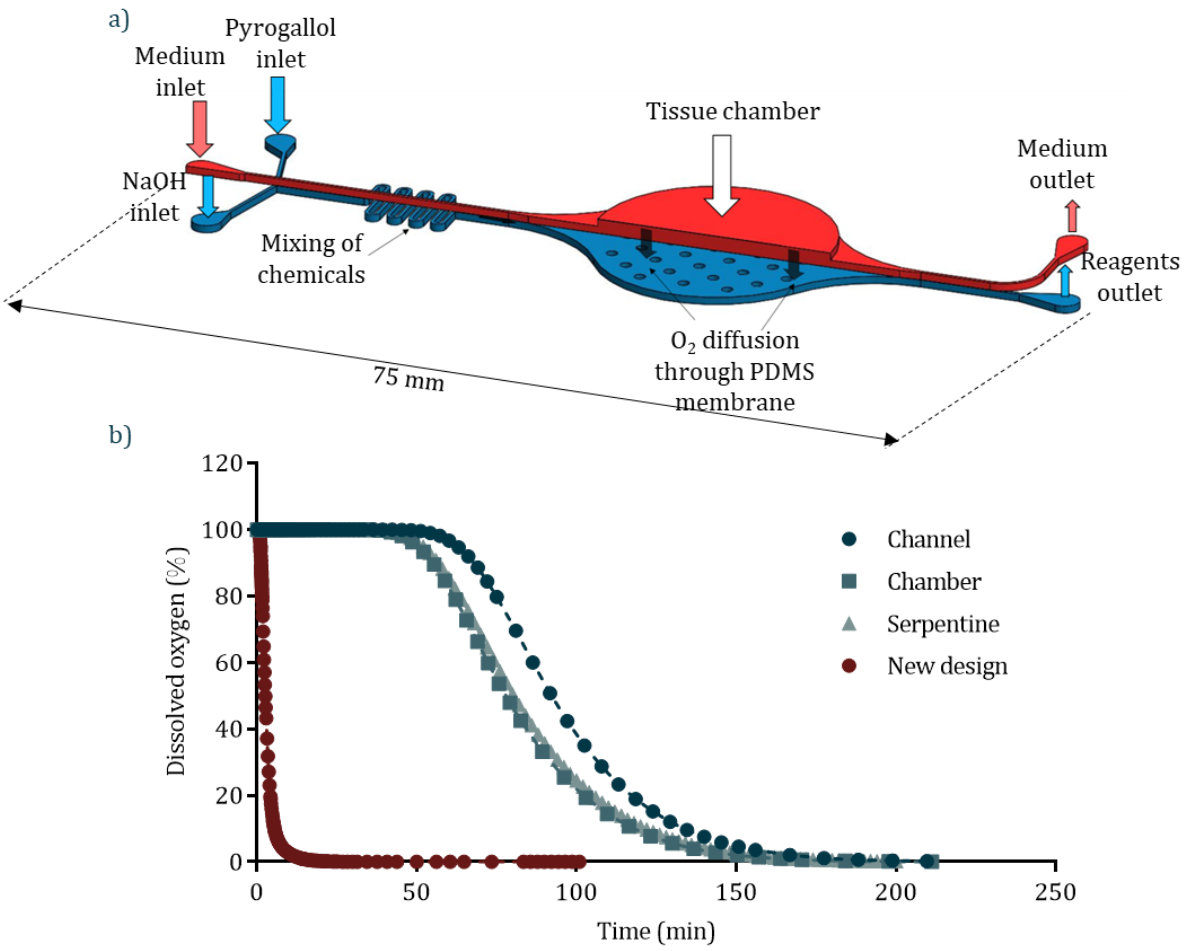

Figure 3.15: a)Depiction of Device v2. The oxygen scavenging reaction (blue) takes place directly underneath the tissue chamber. The "holes" in the bottom layer represent the microposts that hold the PDMS membrane separating the fluidic layers to avoid the collapse of the bottom chamber. b) COMSOL simulation comparing the simulated time required to remove all the oxygen from the chamber using the new design (red) compared to the previous designs.

Given that the oxygen was now removed from the chamber holding the tissue, the generation of an oxygen gradient within the chamber arose as a concern, both in the direction of the flow and in the direction perpendicular to it. A three-dimensional model of the system was created and COMSOL simulations carried out, varying the flow rate of the medium and measuring the oxygen tension at different points of the tissue chamber (Figure 3.16). For flow rates over 1 µL/min a gradient in both directions was generated, with higher concentrations of oxygen at the entrance and at the centre of the chamber. Thus, a flow rate of 1 µL/min was used for the subsequent experiments.

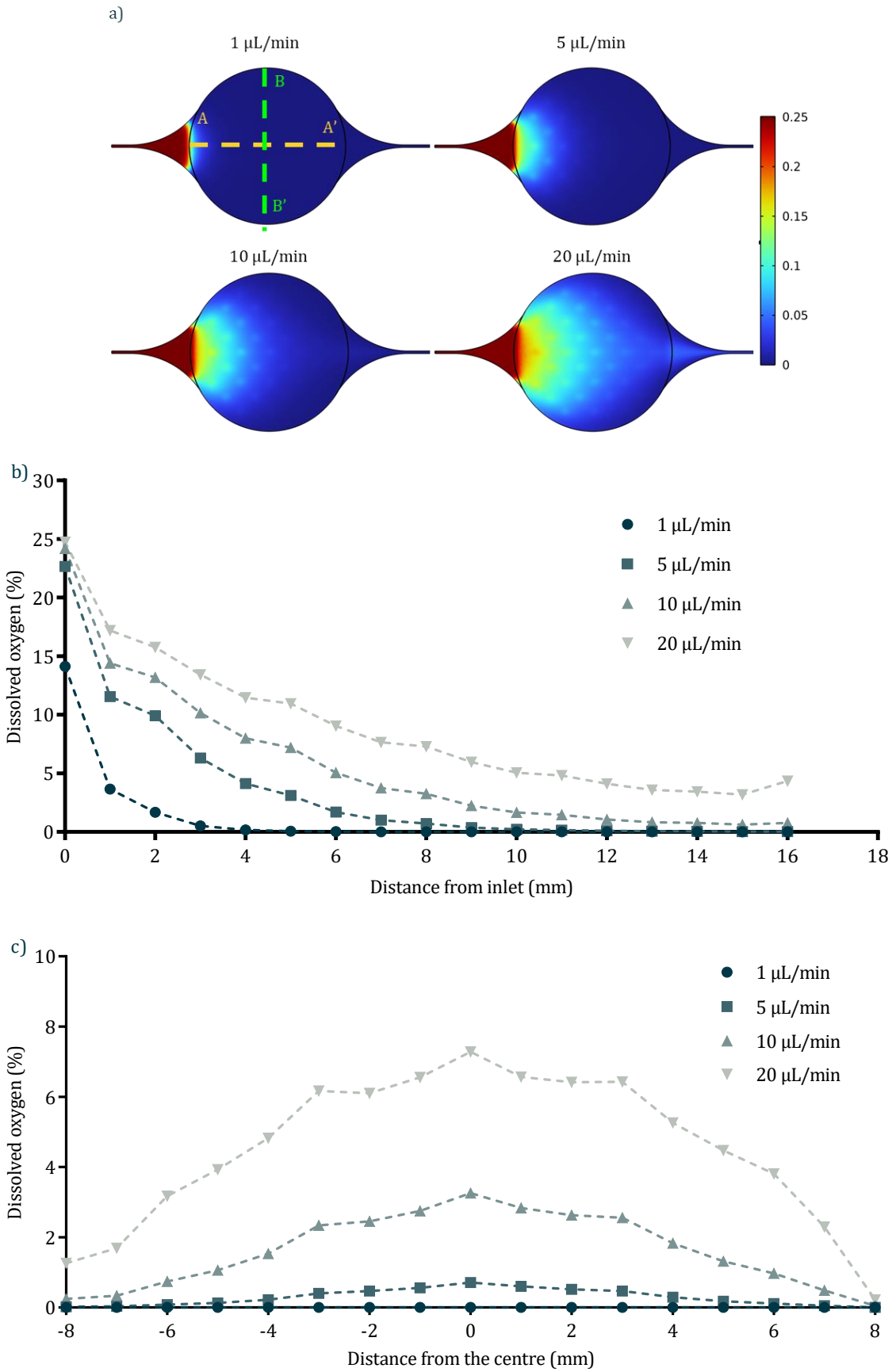

Figure 3.16: a) Simulations of the oxygen concentration distribution for increasing flow rates. B) shows the oxygen tensions simulated along the direction of the flow (line A-A') and c) along the direction perpendicular to the flow (line B-B').

3.2.2 Fabrication and assembly

The aim of this device is to control and maintain a certain oxygen concentration. Thus, the material chosen for the fabrication of the devices was polymethylmethacrylate (PMMA), which is known to be gas-impermeable (PMMA oxygen diffusion coefficient is 4.3×10^{-12} m^2/s [288]). The device consists of multiple layers, designed using AutoCAD and fabricated from PMMA of different thicknesses by laser cutting (Epilog Laser). The layers of Device v1.2 are depicted in Figure 3.17.

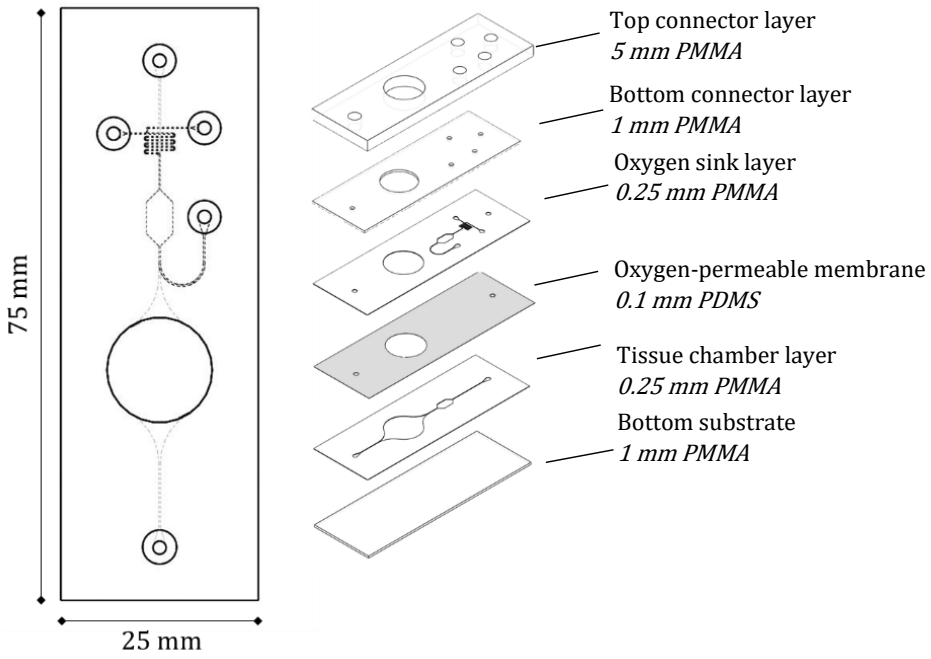

Figure 3.17: Exploded view and description of the layers for the device (Device v1.2).

The connector layer consisted of two layers of 5 mm and 1 mm thick PMMA respectively. The holes in the top layer (ø5 mm) were tapped to fit ¼"-28 threaded connectors (Kinesis Ltd) before being bonded to the 1 mm-thick layer by solvent vapour exposure [289]. For this process, 200 mL of pure chloroform (ACROS Organics™) was poured into a glass Petri dish (ø16 mm). A platform was fabricated to hold the PMMA pieces approximately 1 cm above the surface of the solvent, and the Petri dish was covered so that the vapour would evenly impregnate the surfaces that were to be bonded. The pieces were exposed for 45 minutes, before bringing them together and aligning them manually. Subsequently, the assembly was placed in a multipress (LPKF Multipress S) with a pre-press force of 80 N/cm^2 at 70°C for 30 minutes, and a press force of 160 N/cm^2 at 80°C for another 30 minutes. The fluidic layers were fabricated from 0.25 mm thick PMMA and machined by laser cutting. Prior to cutting, the PMMA films were laminated on both sides with 50 µm-thick double-sided adhesive tape (467 200MP, 3M). The PDMS membrane was fabricated by mixing PDMS precursor with curing agent with a ratio 10:1, degassed under vacuum for 30 minutes and spin-coated on a wafer for 60 seconds at 700 RPM. The membrane was then

baked for 1 h at 60°C for curing. Once the separated elements were fabricated, they were assembled as follows: first, the bottom fluidic layer was bonded to the PDMS membrane while this one was still on the wafer. The PDMS membrane was cut to fit the design and peeled off the wafer. The second fluidic layer was then bonded with double-sided tape. Finally, the assembly was bonded to the substrate followed by the connector layers. The assembled device was placed in the oven at 60°C with a 1 kg weight.

The new system (Device v2) was designed using AutoCAD software and it was decided to fabricate the fluidic layers in PDMS, with top and bottom substrates made of glass (Figure 3.18). PDMS is easier to manufacture, allowing for strong bonds between the fluidic layers and the membrane, reducing the time of fabrication, difficulty, and improving the success rate. However, it is permeable to oxygen (PDMS oxygen diffusion coefficient is 3.55x10-9 m^2/s [145]). The PDMS layers were sandwiched between glass slides to reduce the oxygen diffusion.

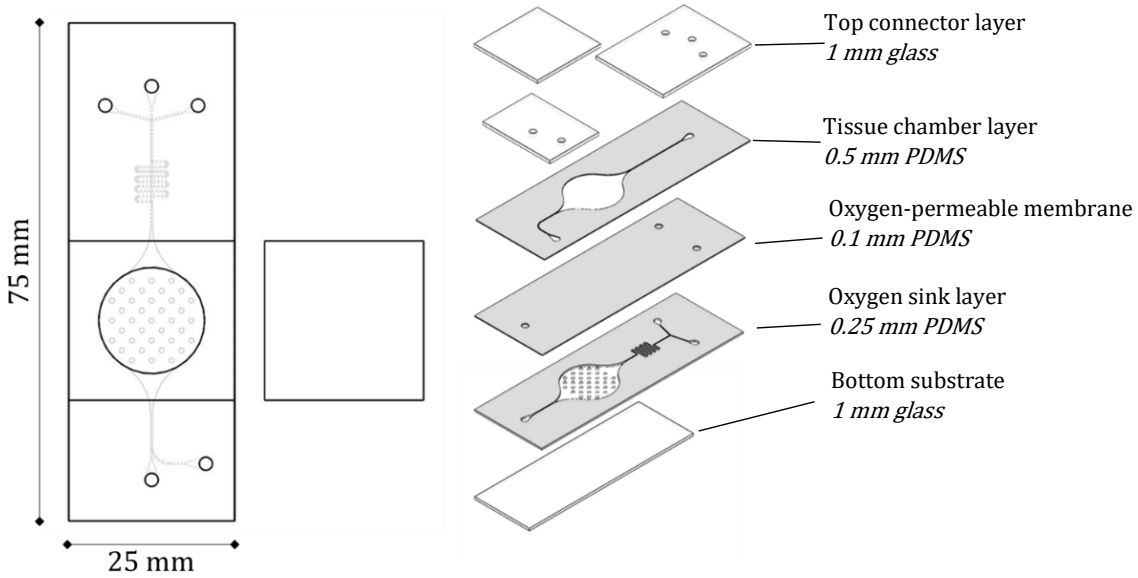

Figure 3.18: Explosion view of the layers composing the device (Device v2).

The top glass layer contained the inlets and outlets and the lid, machined using multiple passes on the laser cutter using the raster function. The PDMS channels were obtained from replica moulds manufactured by 3D printing. To fabricate the PDMS layers, the mixture of PDMS precursor and curing agent at a 10:1 ratio was degassed for 30 minutes, poured into the moulds, and degassed again for 10 minutes under vacuum. Subsequently, the excess of polymer was removed, the surface levelled, and a weight added on top to obtain the desired height in the layer (1 mm). The moulds were baked for 2 hours at 60°C. The PDMS membrane was obtained as described above. For the assembly of the layers, oxygen plasma bonding was used. First, the bottom fluidic layer was bonded to the membrane still on the wafer. The assembly was then peeled from

the wafer and bonded to the top fluidic layer. The assembly was then bonded to the bottom substrate and finally to the top glass layer (excluding the lid). The lid had the aim of facilitating the access to the tissue chamber for introducing and removing the tissue samples.

Due to the presence of leaks in the chamber lid, as well as the tubing channel interfaces, a holding platform was designed to host the device and provide the lid with access to the tissue chamber at the same time as sealing the chamber and connections (Device holder v1; Figure 3.19). This platform was designed in AutoCAD and fabricated in PMMA using a laser cutter. It consisted of a 5 mm-thick substrate, a 2 mm-thick slot for the device, and a 5 mm-thick top layer with a hole to allow microscope imaging. The hole was closed using a 1 mm-thick polycarbonate cut out. The top PMMA layer was coated with a PDMS cushion and the device was sandwiched between the two rigid PMMA slabs, held together by a set of screws and nuts tighten to provide slight compression, ensuring hydraulic tightness [264].

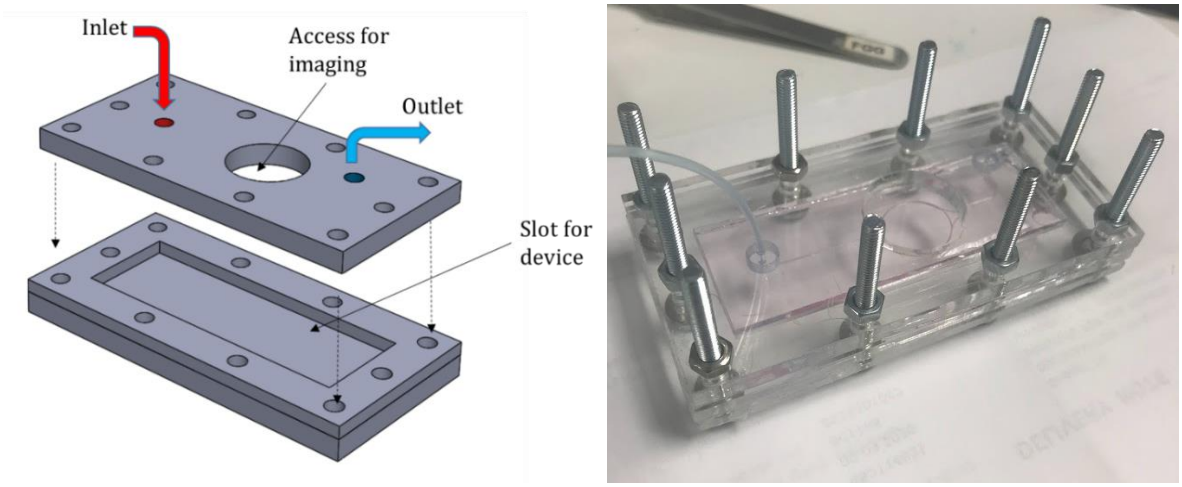

Figure 3.19: Explosion view of the platform holding the tissue chamber. The holes surrounding the slot for the device are for the nuts and bolts that will be tightened to seal the device. (Device holder v1)

3.2.3 Test and evaluation

To test the assembled device (Device v1.2), a food dye was infused into the device via the connectors using PFTE tubing. A 10 mL syringe was filled with the dye and the liquid was pushed into the system using a syringe pump. The overall success of the fabrication process was very low (1 successful device every 5 attempts). The main reason for the failure of devices was the leaks observed between the PDMS membrane and the fluidic layers, indicating a weak bond between both materials using the double-sided tape, and leaks at the connectors. These were mainly due to an incorrect sealing of the threaded connector. When the connectors were screwed in tighter to avoid leaks, the 1 mm thick PMMA layer underneath cracked due to the pressure. These cracks originated from the laser cutting process and worsened by the chloroform vapour treatment. This

resulted in a weakened material that was not able to hold the pressure (15+ attempts under different fabrication conditions).

Similar to the previous design, the new design (Device v2) was tested for leaks by infusing it with a food dye. The only source of leaks was the lid when it was not properly sealed, proving the strength of the bond between PDMS layers. The fabrication process was robust, and no devices had leaks between the fluidic layers. The devices were tested to generate and maintain an oxygen concentration. A 100 mg/mL pyrogallol solution in DI water, 1 M NaOH solution and a solution containing the oxygen-sensitive dye $Ru(BPY)_3$ at 1 mg/mL were prepared. The first two solutions were infused in the two oxygen sink inlets at 5 µL/min with a syringe pump via polytetrafluoroethylene (PTFE) tubing, while the latter solution was introduced in the top fluidic layer at 1 µL/min. The pyrogallol and NaOH solutions were then mixed in the serpentine channel before they reached the chamber underneath the tissue chamber, where the chemical reaction took place, and the oxygen was scavenged from the medium flowing through the channel on top through the PDMS membrane. The intensity of the dye was measured periodically using a confocal microscope (LSM 5 Exciter, Carl Zeiss). Results are shown in Figure 3.20. As can be observed, the system took over 2 hours to reduce the oxygen level to below 10%, which does not correlate with simulation (Figure 3.15). This could be due to diffusion of oxygen from the surroundings into the PDMS. Moreover, the system was not able to maintain that concentration for more than 20 h. This could be due to the absorption of the reaction products by the PDMS, blocking the channels and reducing the permeability of the membrane, reducing the scavenging power of the setup.

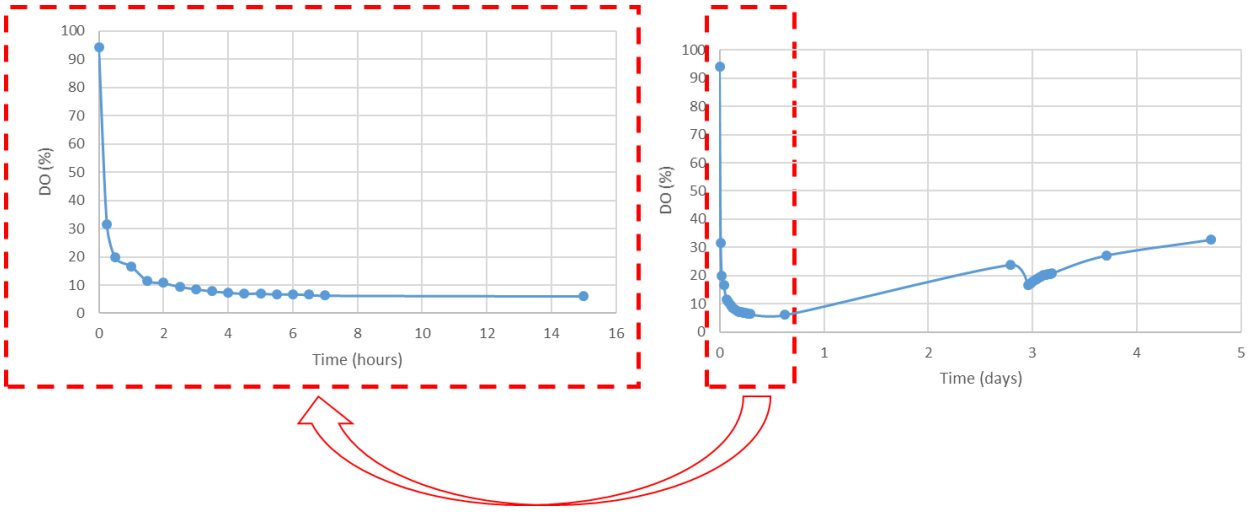

Figure 3.20: Oxygen concentration over 15 hours (left) and over 5 days (right). The oxygen is removed within 2 hours. However the concentration is not maintained constant over longer times. Best result obtained out of 13 repeats.

3.3 Multichamber device

Due to the instability of the signal, the large footprint, and the difficulty of the setup, particularly when thinking about future biological experiments where the time to seed the tissues into the devices is critical, a new way to control the oxygen levels in the culture chamber was sought. In this new system, the oxygen was not continuously removed from the chambers, instead, the desired concentration was achieved in an additional device (a gradient generator, explained in Section 3.5) placed before the tissue culture device. A gradient was generated using a network of microfluidic channels, and each outlet of the gradient generator with a specific oxygen tension was directed into a separate culture chamber. Because the oxygen was not actively removed anymore, the design did not need to include the chemical oxygen sink. This allowed for a reduction of the device's footprint and the complexity of both the design and the fabrication. However, this also meant that the setup was more sensitive to oxygen diffusion from the exterior. The materials used were chosen paying careful attention to their oxygen permeability to avoid or minimise the diffusion of oxygen into the flowing liquids. The entire device was fabricated in PMMA, the chambers were sealed with Viton O-rings, and a glass slide, and all the parts integrated within metallic holders. To direct the oxygen-specific fluid into the chambers with minimal oxygen diffusion, bespoke glass capillaries were used (see Figure 3.36).

Initially, the previous design was adapted to remove the chemical sink layer, and it was fabricated in PMMA on a glass slide substrate, using double-sided tape to bond the layers. To reduce the footprint of the device when more than one device is connected to the gradient generator, the design was modified to fit four chambers in the same surface area while maintaining the size of the chambers (Device v3). The number of layers and their thickness was optimised: when too thin, the device did not be seal properly and when too thick, the chip didn't fit in the device holder, or it cracked when the clamp was closed. To avoid cracking, the glass substrate was swapped for a PMMA substrate. However, the device warped under the pressure applied by the clamp due to the lower rigidity of the PMMA, which led to leaks. Due to the swap from glass to PMMA substrate, the size of the device was not limited to the glass slide anymore. Adjustments were made in the width of the device to allow for additional space between the inlets/outlets and the chambers for ease for handling and reduce potential leaks due to the close proximity of the features. Finally, a groove was added to the design to hold the o-ring that would provide hydraulic sealing to the chambers. The fabrication process was also reviewed due to the debris introduced by the double-sided tape. Substituting the tape for chloroform bonding produced better results as debris was reduced, there was less risk for channels getting blocked due to the glue of the tape filling the channels when under pressure, and also less risk for oxygen contamination. However,

the chloroform exposure recipe had to be optimised to avoid cracks appearing on the polymer surface. The final fabrication protocol is detailed in Section 3.3.1.

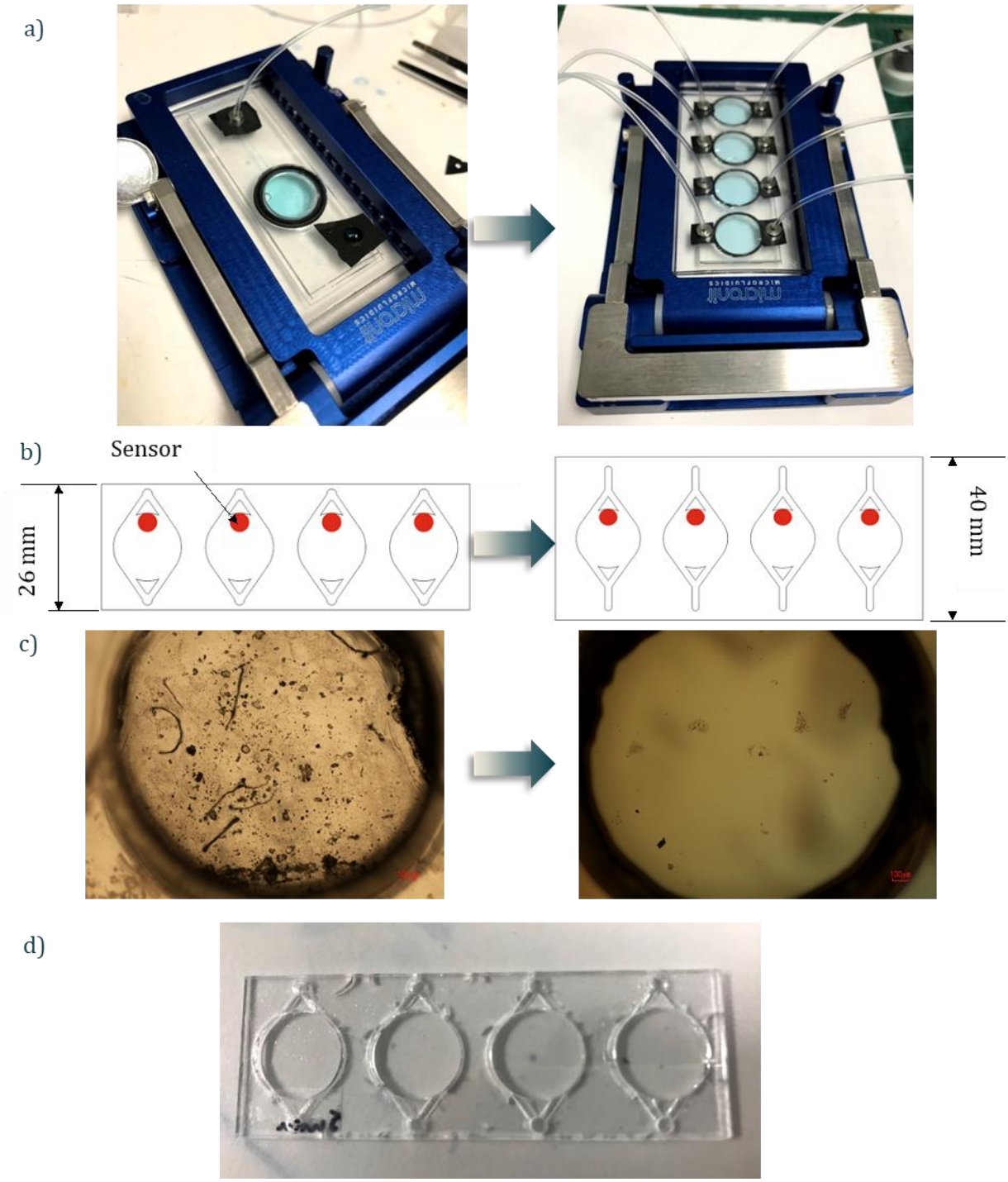

Figure 3.21: Iterations of Device v3. a) switch from one to four culture chambers with the same footprint. b) Increase in device width to increase space between features. c) Debris observed at the inlet in a device fabricated with double-sided tape (left) and a device fabricated by solvent bonding (right). d) Effect of solvent vapour exposure on the PMMA device. Overexposure leads to cracks in the material.

COMSOL simulations were carried out to assess how the changes in the chamber design changed the flow distribution. Pillars were added at the inlets and outlets of the chambers to obtain a more homogeneous distribution and irrigate the tissues more evenly (Figure 3.22).

Furthermore, a new platform in the fashion of a clamp was devised, inspired by the commercially available "Fluidic Connect Pro chip holder" from Micronit (Device holder v2; Figure 3.23). This clamp allowed for simple, fast, and reproducible sealing of the chambers, which would be of great benefit when working with living tissues.

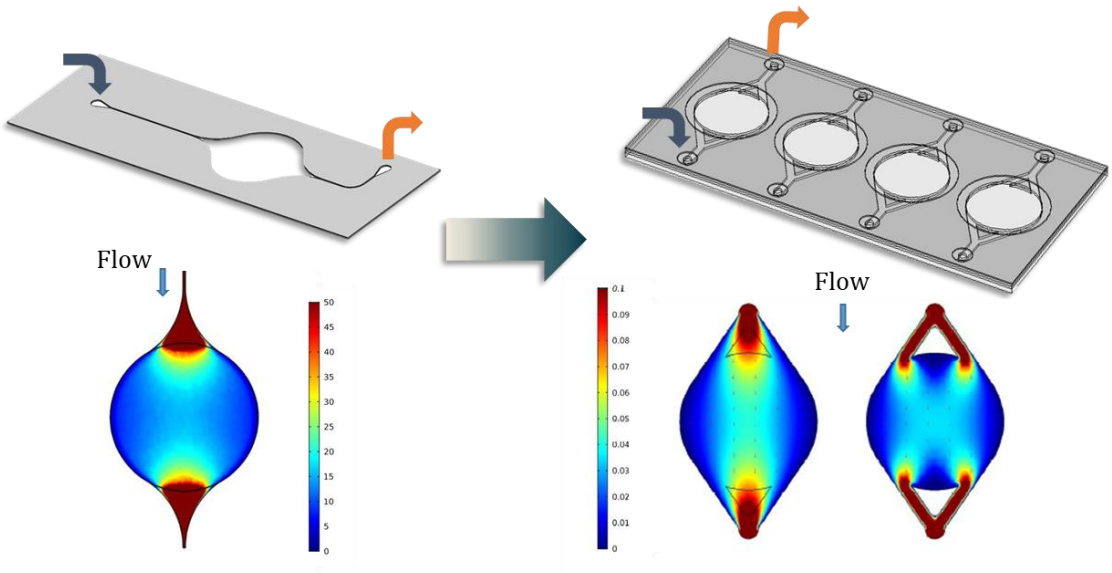

Figure 3.22: Changes in the design. Device v2 on the left and Device v3 on the right for comparison. Without significantly increasing the footprint, four chambers are fitted in the size that only fitted one in the previous design. The flow distribution was simulated to show the uniformity of the flow across the chamber.

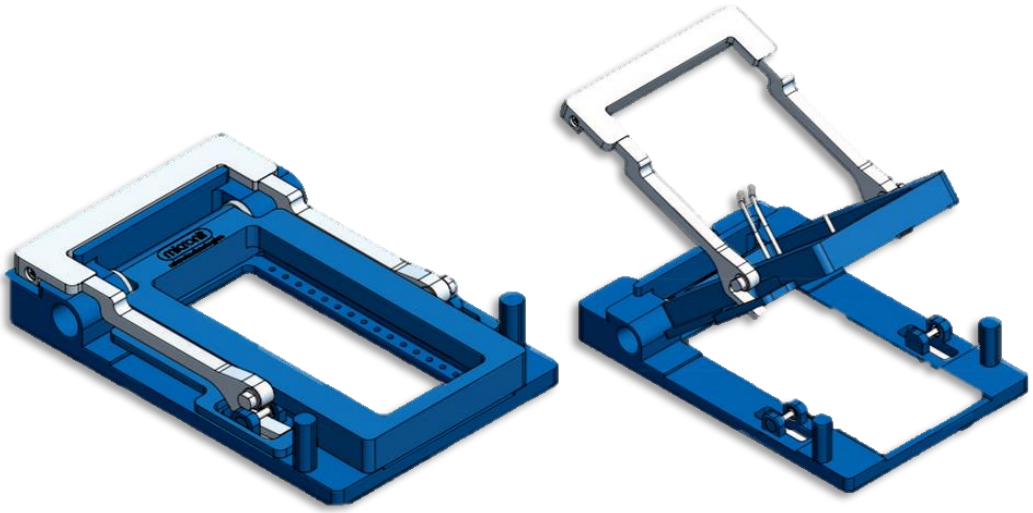

Figure 3.23: Depiction of Device holder v2. The clamp allowed for rapid and easy sealing of all the chamber simultaneously. Image taken from Micronit.

To hold and seal the device, a chip holder was designed to be integrated in the clamp platform. In this manner, the chambers are easily closed and hydraulically sealed using Viton O-rings, with even, consistent, and repeatable pressures. The holder was designed in AutoCAD and fabricated from brass by the University's Workshop. This material was selected due to its strength, to

reduce deformation when the clamp was closed, which could lead to incorrect sealing or differences in pressures between the chambers. The holder (Figure 3.24) includes holes for the inlets and outlets and a window to allow visualisation of the tissues during culture. The holes are designed to fit a PTFE/Stainless steel gripper ferrule (1/16" OD, Dibafit™, ColeParmer), a ø1 mm biopsy punch needle (Integra™ Miltex™) is fitted through and held in place using epoxy resin (Araldite, RS Components). This acts as the fluidic interface to connect the tubing that provides the fresh media to the culture chambers. It also includes a slot for a glass slide that acts as the ceiling of the chambers. The bottom part of the holder contains windows to allow the light through, as well as a groove to align the device before sealing and slots underneath to accommodate the photodiodes of the electronic oxygen detector, explained in the following section (3.4.1).

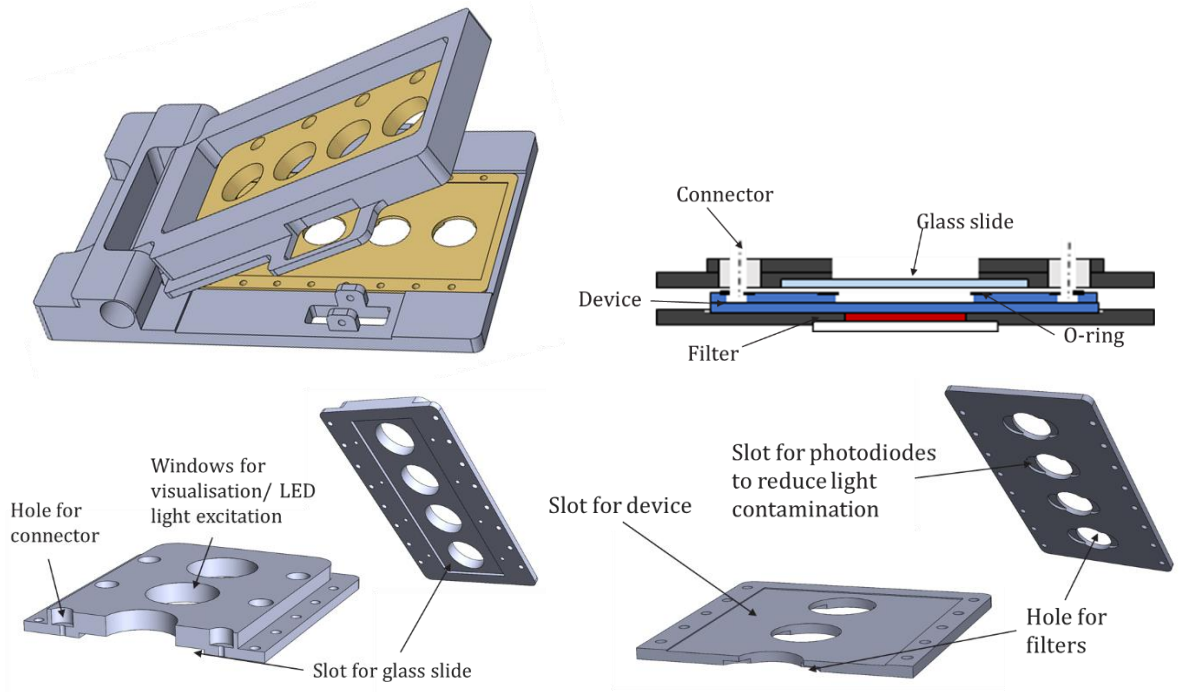

Figure 3.24: 3D model of the Micronit-inspired clamp with the device holders in place. On the top right, a cross-sectional view of the closed system. On the bottom, detail of the top (left) and bottom (right) device holders and their key features. (Device holder v2)

3.3.1 Fabrication and assembly

The new design (Device v3) consisted of multiple layers, designed using AutoCAD and fabricated from PMMA of different thicknesses (0.25, 1 and 1.5 mm, Goodfellow) by laser cutting (Epilog Laser), with the channels in the fluidic layer obtained by rastering. After the separate pieces were prepared, the assembly was as follows: first, the 1 mm substrate surface was exposed to 4 mL of pure chloroform (ACROS Organics™) in a glass Petri dish (ø10 mm) for 6 minutes held by metal pins 1 cm above the surface of the solvent. The treated surface was then brought in contact with the fluidic layer and the assembly was placed in a multipress (LPKF Multipress S) using a pre-press force of 80 N/cm^2 at 70°C for 5 minutes, and a press force of 160 N/cm^2 at 90°C for

20 minutes. Then, the O-ring layer was exposed to the same solvent treatment and joined with the previous assembly prior to placing the final device into the multipress and repeating the previous cycle.

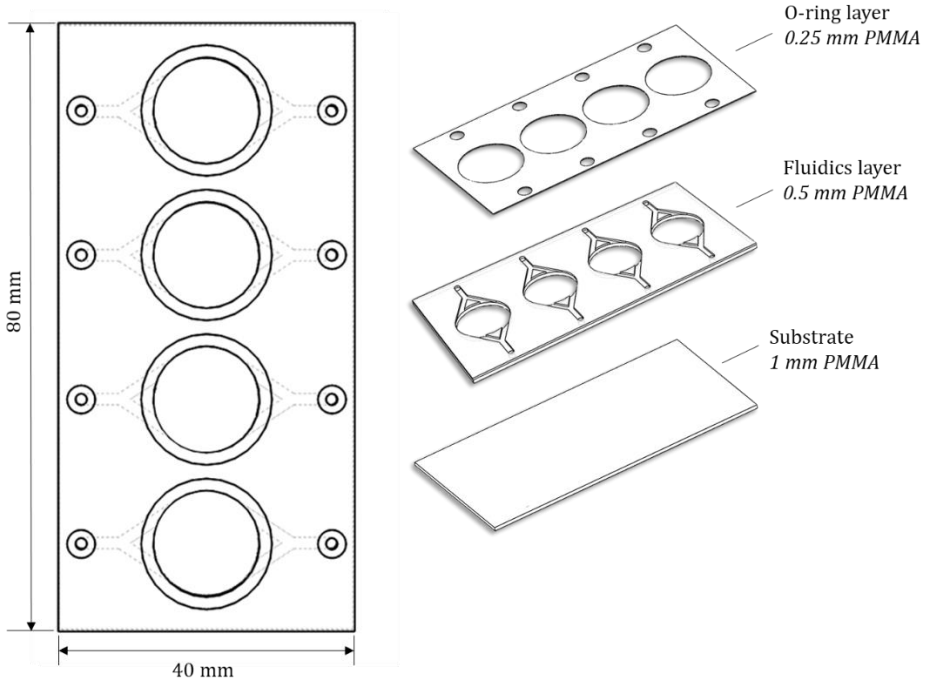

Figure 3.25: Exploded view and description of the layers comforming the device (Device v3).

3.3.2 Testing and evaluation

To test for leaks in the device, the device was filled with food dye. It was observed that treating the fluidic layer with chloroform caused cracks in the material leading to leaks. It was therefore decided to expose the other two layers only. To test for leaks within the complete setup, the system with the sealed device was immersed in soapy water and the chambers were pressurised. The pressure was increased to 2 bar or until bubbles appeared. If bubbles appeared, it indicated the presence of a leak, which meant that the chip had to be opened, realigned, and closed again. This was repeated until no leaks were observed. Due to the manual alignment, the number of times that this process was repeated until no leaks were observed was arbitrary and depended exclusively on the abilities of the handler. Additionally, to check for the hydraulic tightness over time, the outlets of the chambers were connected to a home-made manometer. The chambers were pressurised, and the pressure measured by the manometer for 24 h. These experiments showed no changes in pressure and therefore no leaks over extended periods (data not shown).

3.4 Real time, integrated electronic oxygen detector

To measure the intensity of the oxygen sensitive dyes used in the previous experiments, a confocal microscope was required. However, the purpose of this system is to culture live tissues, which requires for it to be inside an incubator at 37°C and 5% CO_2. In this situation, the entire setup would need to be taken out of the incubator and set it up on the microscope to measure the oxygen concentrations. This would disrupt the tissues, and it could lead to variations in the oxygen tensions during the mobilisation. It would also be cumbersome and time consuming, which means that it would not be possible to perform measurements often. Therefore, a new way to measure the dissolved oxygen was envisioned. An electronic oxygen detector was developed based on the work published by Shaegh *et al.*, 2016 [236]. In this system, the oxygen-sensitive dye PdTFPP was embedded in PDMS matrix, cut to the desired size, and manually placed on the substrate of the culture chambers (explained in detail in Section 3.4.1.1). The sensor was excited with a UV LED (400 nm wavelength) and a photodiode collected the light emitted. A long-pass filter was placed between the sensor and the photodiode to remove the unwanted wavelengths. To obtain a relative value, a second photodiode was connected in antiparallel direction to the previous one, but without a sensor between the light source and the filter, collecting the background light (Figure 3.26 (top)). In this way, each chamber was self-referenced and individually calibrated. Figure 3.26 (bottom), shows the electronic circuit transforming the signal collected into a voltage. The photodiodes converted the light into a current. The current generated by the second photodiode (background) was subtracted from that of the first (from the sensor), and the resulting signal was then converted into a voltage using a transimpedance amplifier. This voltage was then amplified with an operational amplifier, and the final signal was collected using an Arduino board. Each chamber has its own excitation LED and pair of photodiodes, and therefore, all the chambers can be measured separately or simultaneously, without the need to move the setup from the incubator. This means less disturbance to the tissues, more stable conditions, and the possibility of real-time measurements. The Arduino board controlled the LEDs, adjusting their intensity, the measuring time (time the LEDs are on), the measuring frequency, and collected the signals from the photodiode pairs of each chamber. The data was processed in Excel to convert the voltages into oxygen tensions using the Stern-Volmer equation (Eq. (3.1)) (Detailed explanation in Appendix 2.b).

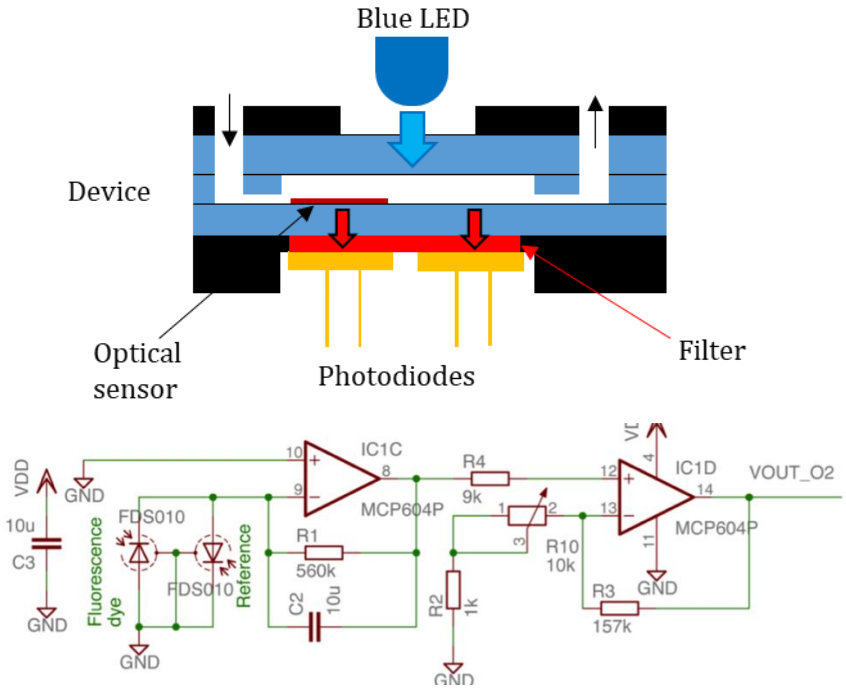

Figure 3.26: On top, cross-sectional view of the electronic oxygen sensor layout (elements not in scale). Below, schematic of the circuit for oxygen sensing.

3.4.1 Electronic components and fabrication

The PCB was designed to fit into the metal holder. The photodiodes fitted in the slots of the metal holders (Figure 3.24) to ensure correct alignment between the sensors, filters, and photodiodes, as well as to reduce the light contamination. A 3 mm thick black PMMA slab was incorporated between the PCB and the system to protect the PCB (the photodiode pins went through this slab as shown in Figure 3.27). The PCB was designed in DesignSpark PCB software (RS Components, UK) and fabricated by JLCPCB (JiaLiChuang Co., Ltd, Hong Kong). After all the components were soldered in place, the PCB was coated with acrylic resin (714-462, RS Components) to protect it from the humidity of the incubator. The light source consisted of four 1 W Ultraviolet LEDs with PCB (390-400 nm EPILED) (Future Eden, Ltd.) connected in series to a BuckPuck™ LED driver (3021-D-I-350, Digi-Key Electronics) (Figure 3.28). Heatsinks (750-0888, RS components) were glued onto the back of the PCBs where the LEDs were mounted using conductive adhesive foil. The LEDs were connected to the LED driver via ribbon cables (289-9896, RS components) and the LED driver and the PCB to the Arduino board. Ø12.5 mm, 1 mm-thick coloured glass long-pass filters (Schott RG610, 16-419, Edmund Optics) were mounted on the metal holders. Once the filters were in place, the device was sealed in the chip holder, and the assembly placed on top of the PCB, aligning the photodiodes with the bottom holder slots. The LED setup rested on top of the top holder.

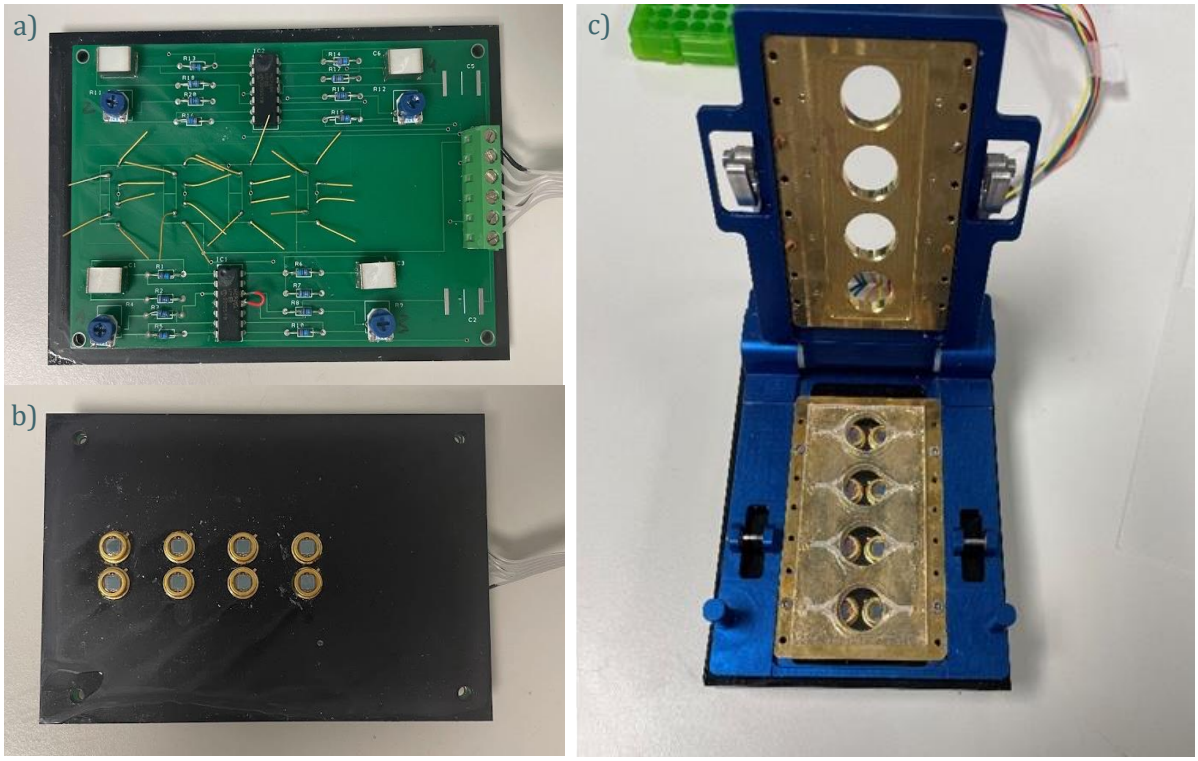

Figure 3.27: On the left, bottom and top view of the mounted PCB with the protective PMMA layer. On the right, open chip holder with a mounted device showing the alignment of the chambers with the photodiodes.

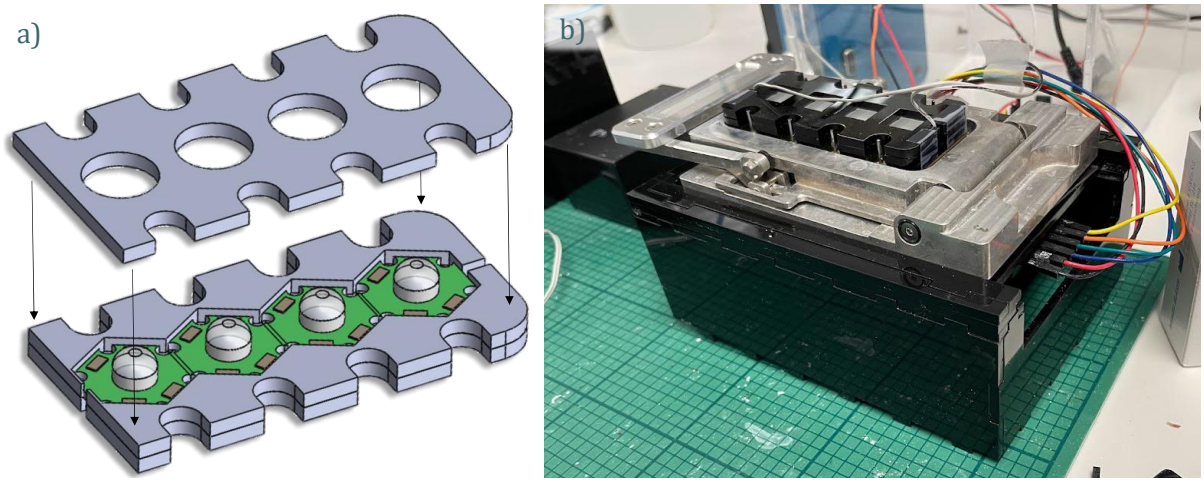

Figure 3.28: 3D model of the LED light source setup (a) and how they fit on the assembled system (b). A PMMA box was built to give extra protection to the electronics and to serve as a stand for the system.

3.4.1.1 Fabrication of the oxygen sensor

The fabrication protocol for the oxygen sensor was similar to the one explained in Section 3.1 and is shown in Figure 3.29. In brief, the oxygen-sensitive dye was dissolved in pure chloroform (1 mg/mL) and mixed with PDMS pre-polymer in a 1:1 ratio (1 mL of dye per 1 g of PDMS). The mixture was stirred magnetically to homogenise it and to allow for the solvent to evaporate. Once it was completely evaporated, the PDMS curing agent was added in a 1:10 ratio to the pre-

polymer. This was manually stirred and degassed in a desiccator until all the bubbles were removed (~20 min). The mixture was subsequently spin coated at 700 RPM for 60 s in a glass slide (75x50 mm^2) and placed in an oven at 60°C for curing. Once solidified, the sensors were cut with a biopsy punch (ø4 mm), peeled off gently and manually deposited on the required location on the substrate of the culture chambers to align with the photodiodes.

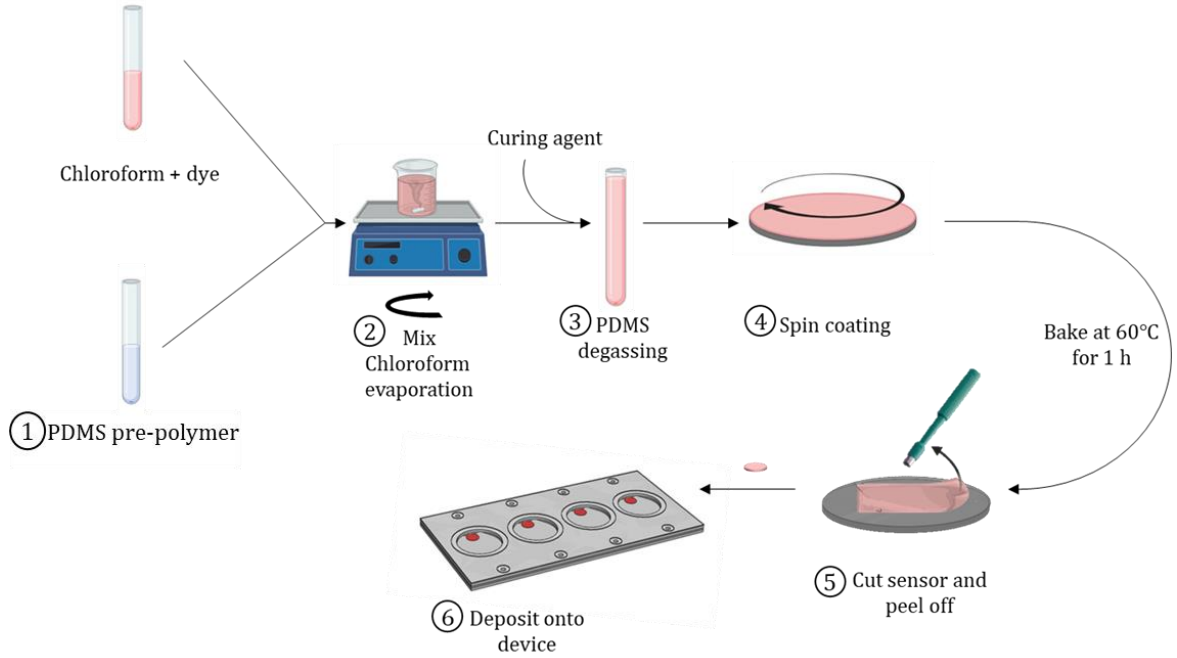

Figure 3.29: Diagram depicting the fabrication process of the oxygen sensors to incorporate into Device v3.

3.4.2 Test and evaluation

To calibrate the sensor and demonstrate linearity, the response of the oxygen sensor was compared against a commercial oxygen probe (proODO Optical Dissolved Oxygen Instrument, YSI). To do this, a small calibration platform was built (Figure 3.30, left). The platform consisted of an inlet and outlet and two windows. The first one for a simplified version of the electronic detector, and the second for the commercial probe. To perform the calibration, humidified nitrogen gas (N_2) was flushed through the device until both measurement methods were stable. At this point, the gas flow was reduced progressively to allow environmental oxygen to slowly diffuse into the setup, giving values across the entire range. Both methods had a time stamp so the measurements could be directly compared. In this way, the intensity measured by the electronic detector was correlated to the oxygen concentration measured by the commercial probe. Using the Stern-Volmer plots (Figure 3.30, right) the response was measured.

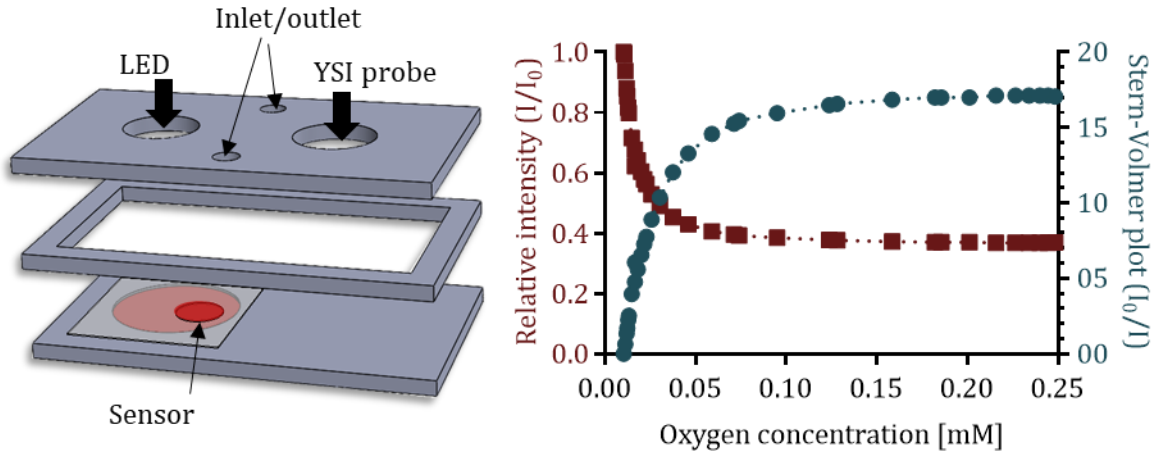

Figure 3.30: On the left, the bespoke calibration platform to correlate the measurements of the electronic oxygen detector developed for this work and the commercial oxygen sensing probe. On the right, the Stern-Volmer plots, showing the linearity of the signal and the wide range sensitivity.

PdTFPP did not show a linear response due to the saturation of the signal at higher oxygen concentrations (above 20% DO), and did not cover the range of interest for this project. Upon review in the literature, it became clear that PdTFPP is very sensitive and mainly used for detection of traces of oxygen [290], and it has been shown to have a low limit of detection [291]. Its platinum counterpart (PtTFPP), however, has been shown to have a linear response for the entire range of interest with a limit of detection two orders of magnitude larger than PdTFPP [291]. The same calibration experiment was carried out for this new dye, presented in Figure 3.31. With this dye, a linear response was obtained. It can be argued that the R^2 value is too low to be considered linear. Some published works have reported this non-linear behaviour have used two-site models [290,291], whereas others have reported good linearity and used the Stern-Volmer equation [292,293]. For the simplicity of the calculations, and because the lower R^2 value could also be due to errors in the measurement setup, a linear model was assumed for subsequent experiments.

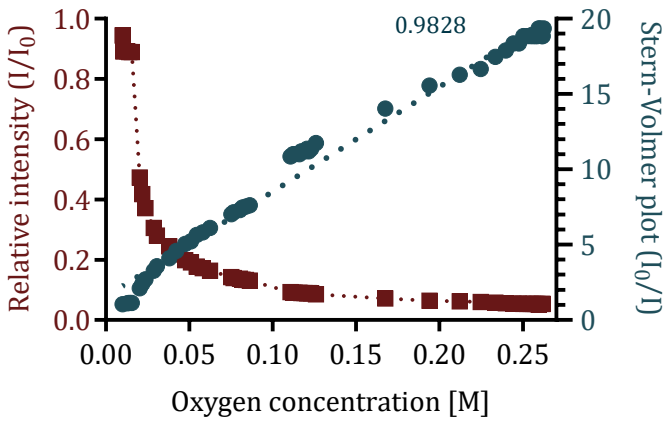

Figure 3.31: Stern-Volmer plot for the PtTFPP dye.

Electronic components heat up in the incubator, especially the high-power LEDs used as light sources. Therefore, it was decided to look into the effect of these in the temperature of the chambers where the tissues would be cultured. The assembled setup was placed in the incubator and a thermocouple was placed inside the culture chambers. The LEDs were switched on continuously for 10 minutes and the temperature in the chambers was measured every 10 s (Figure 3.32a). During the experiments with the tissues in the chambers, the LEDs would not be on constantly, so the temperature was also monitored for different measuring periods (Figure 3.32b). The LEDs were turned on for 40 s and off until the next measurement. It was observed that with a measuring frequency of 2 minutes, the temperature in the chambers did not have time to cool down to the original level, and the therefore the temperature slowly increased. This behaviour was not observed for a measuring frequency greater than 5 minutes. However, even at these lower frequencies, the temperature increased over 1°C. This increase was significantly lower when the time the LEDs were on was reduced. To avoid these fluctuations, and reduce the risk of disrupting the cultures, heat sinks were mounted on the back of the LEDs. These reduced the increase in the temperature to below 0.2°C (Figure 3.32c). It was decided to include the LEDs and use measure times shorter than 20 s, and measuring frequencies above 5 min.

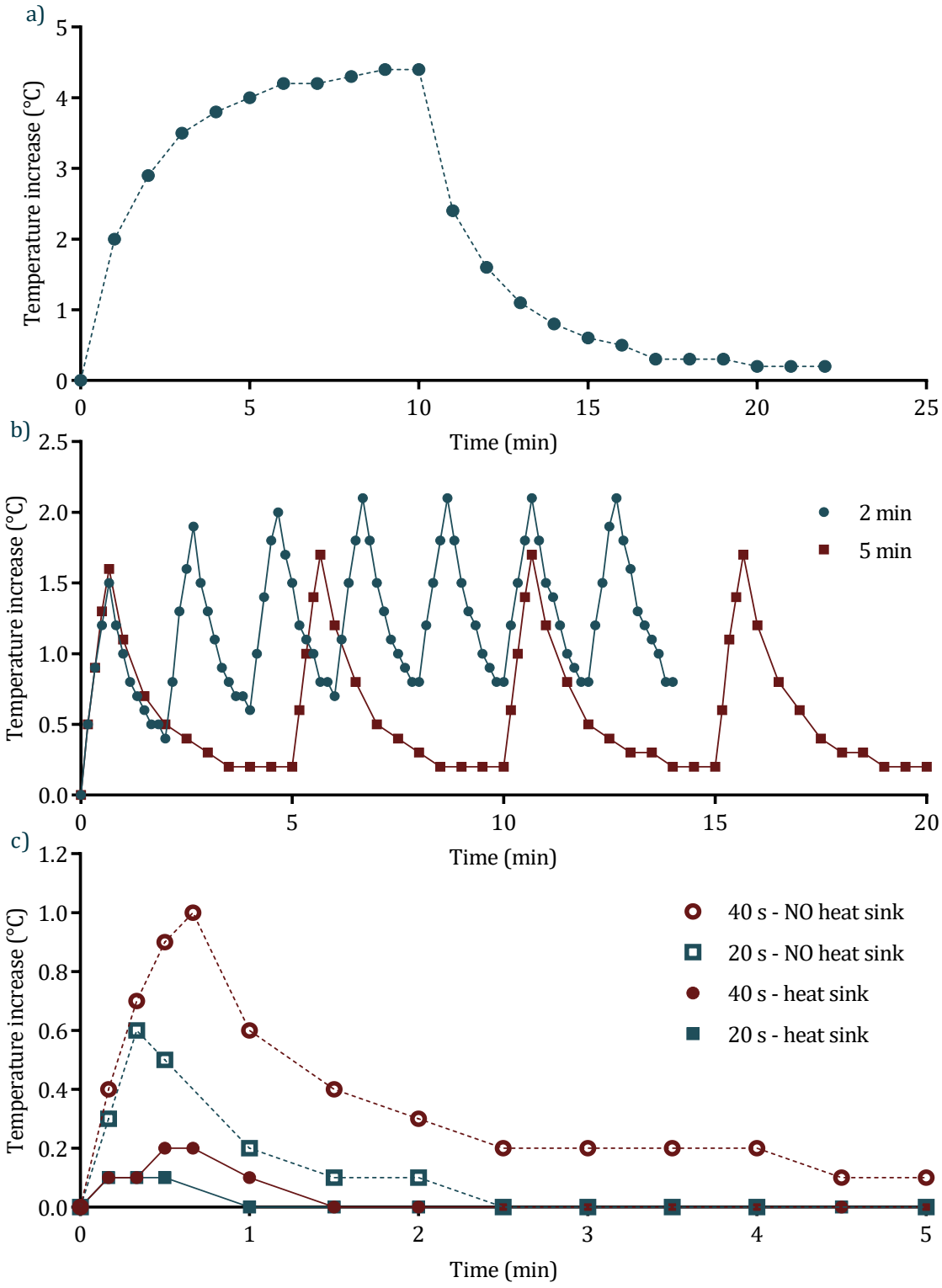

Figure 3.32: a) temperature increase when the LED light was on for 10 minutes continuously. B) temperature fluctuations upon cycles of turning on and off the LED at different frequencies. C) comparison between the temperature increases with and without the heat sinks. Each condition repeated in duplicates, 10 cycles each.

The system was also tested for stability. The complete setup, with the chambers containing a saturated solution of sodium sulphite (Na_2SO_3) to ensure a constant 0% DO concentration

was placed inside the incubator. The oxygen concentration was measured with the electronic detector for 24 h turning on the LEDs for 10s for each measurement at varying measuring frequencies (time between measurements). It was observed that the signal declined over time, due to photobleaching of the dye, a process that was accelerated by the higher temperature in the incubator (37°C). The photobleaching was reduced by reducing the measuring frequency. A stable signal with less than 2% variation was obtained for a measurement frequency of 15 minutes (Figure 3.33).

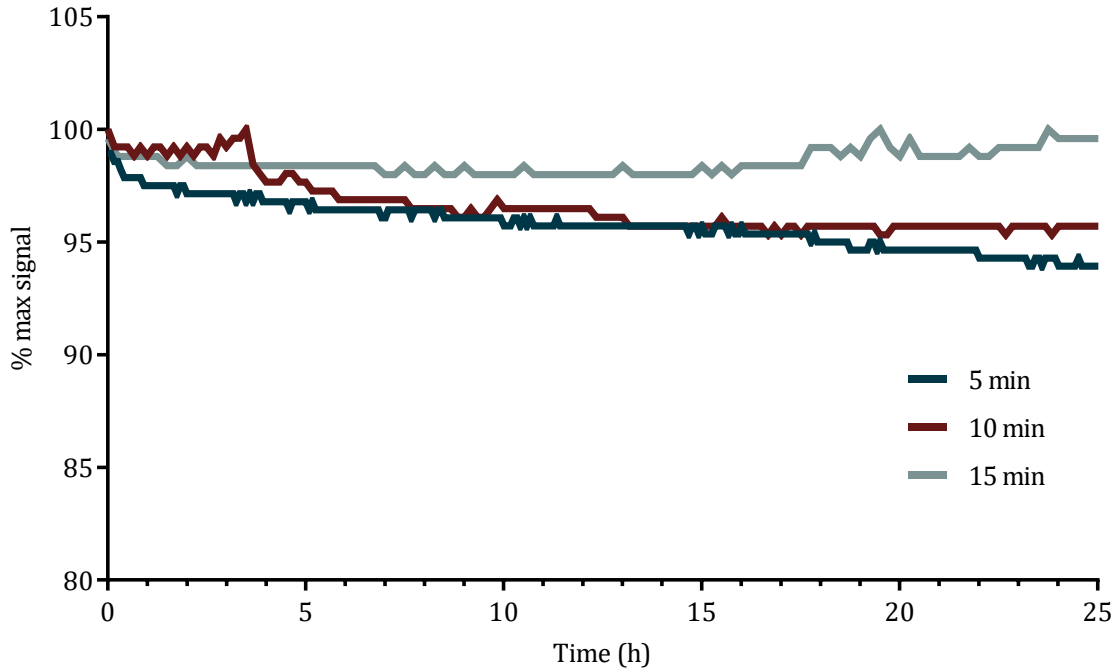

Figure 3.33: Signal stability over 24 h for various measuring frequencies. Higher frequencies led to more photobleaching and loss of signal.

3.5 Oxygen-gradient generator

The method originally sought to control the oxygen concentration using a chemical sink did not produce the expected results. Therefore, the concept was changed, as explained in Section 3.3. It was decided to use a separate module with a split and combine a network of microchannels to obtain a range of oxygen tensions, as shown in previous papers [294]. This design included long serpentine channels to increase the time the two streams were in contact to allow for complete mixing to take place. In this setup, the cell culture medium was equilibrated by bubbling it with either compressed air or pure nitrogen for over 1 h to obtain 100% and 0% dissolved oxygen respectively. These solutions were then directed through oxygen-impermeable tubing to the oxygen gradient generator, and the outlets connected to an array of devices (Device v2) holding the tissue samples (Figure 3.34). With this method, it was expected to obtain and maintain more stable oxygen levels, and also to improve the fabrication process, requiring fewer complex devices. The system would allow for the maintenance of multiple tissue slices at different oxygen tensions using only two inlets. However, as discussed above, the PDMS devices had high permeability to oxygen, and with the original chip holder design, required bolts to be screwed in making the setup difficult to assemble with a very large footprint (Figure 3.35). This was changed to the multichamber system presented in Section 3.3 (Device v3). This setup was much more compact, and the devices fabricated in PMMA were expected to stop oxygen from diffusing in, thus maintaining the oxygen concentration in the medium directed from the gradient generator (Figure 3.36).

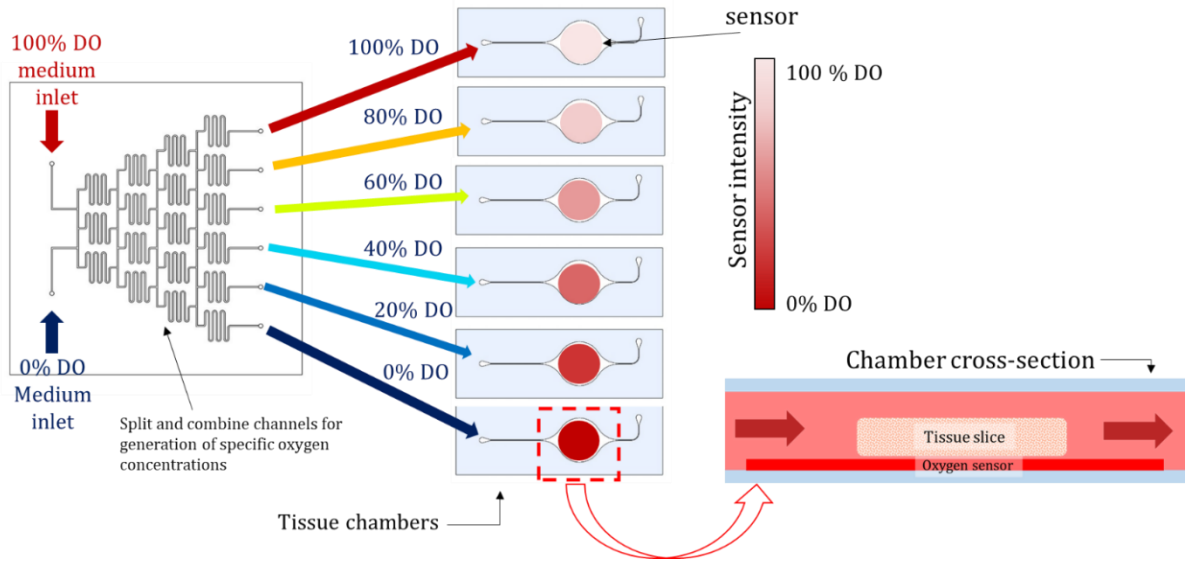

Figure 3.34: Schematic view of the oxygen gradient generator module connected to the tissue chambers (Device v2). On the left, cross-section detail of the tissue chamber with the oxygen sensor deposited on the glass substrate.

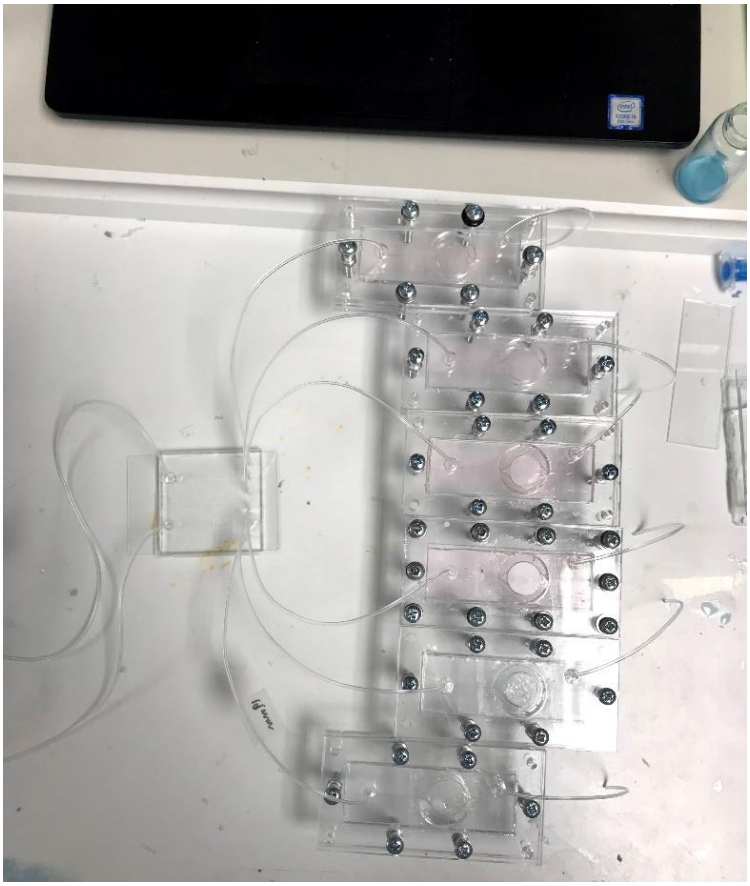

Figure 3.35:Picture of the set up in real life. The laptop on the top of the image can be use as scale to show the large footprint of the system.

Figure 3.36: New setup with the serial dilutor as the gradient generator and the multichamber device (Device v3) mounted on the chip holder and on the electronic oxygen detector.

3.5.1 Fabrication and assembly

The serial dilutor was designed in AutoCAD and made from PMMA. The channels were cut with the laser cut and bonded to a substrate and a top connector layer. However, the heat produced by the laser melted the plastic, producing uneven surfaces, which had a big impact due to the size of the features and the need for accuracy on the details to form the desired gradient.

In a second attempt, PDMS was used. However, PDMS is highly permeable to oxygen, which would defeat the aim of this device. To overcome this, the surfaces of the PDMS channels were coated with a glass-like, sol-gel solution, based on the work presented by Khan *et al.*, [294]. Silica coating results in highly stable hydrophilic surfaces, with increased wettability, resistance to solvents and decreased absorption of hydrophobic compounds. More relevant to this project, it also prevents the diffusion of gas molecules such as oxygen. In brief, tetraethoxysilane (TEOS, Sigma-Aldrich) and methyltryethoxysilane (MTES, Sigma-Aldrich) were used as precursors to silicon dioxide. The alkoxysilanes are pre-converted by adding acid to catalyse the condensation and hydrolysis reactions. The pre-converted sol mixture was prepared by mixing TEOS, MTES, ethanol and pH2 DI water adjusted with HCl in a 1:1:1:1 volumetric ratio. The surfaces were treated with oxygen plasma to generate hydroxyl groups and placed in close contact with a non-treated PMMA slide. The mixture was flushed immediately after and placed on a hotplate at 100°C for gelation. After 2 minutes, the non-reacted solution was flushed out with air and the devices were cooled down slowly to room temperature (1 h at 60°C, then 1 h at 40°C, then waited until room temperature was reached). The PDMS devices were then peeled from the temporary PMMA substrates and permanently bonded to the glass substrates. The formation of the coating was confirmed by mixing the sol-gel solution with fluorescent microspheres (1 µm diameter) at a 1:10 volumetric ratio before infusing it into the devices. The chemical resistance of the barrier was tested by looking at the swelling of the PDMS channels in contact with an organic solvent, in this case toluene. The toluene was flushed through a coated and uncoated device at 10 µl/min and images taken every second for 10 minutes to observe the evolution of the channel shape over time (Figure 3.37). Although the method seemed to reduce the swelling of the polymer, the coat on the surfaces showed cracks. As observed in Figure 3.38, the coating was not uniform across the entire network and oxygen leaks were still observed. Therefore, this plan was abandoned after several attempts (n=16).

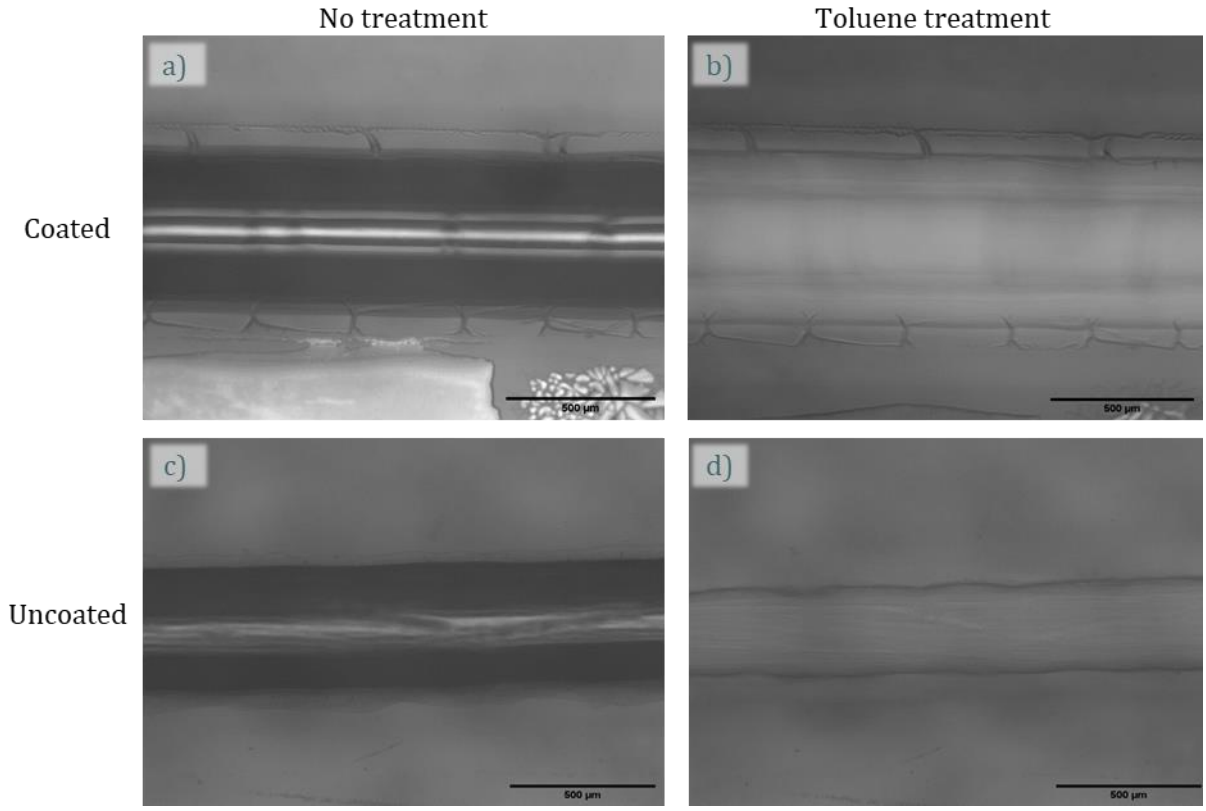

Figure 3.37: Channel widths before (a and c) and after (b and d) flushing toluene at 10 µL/min for 5 minutes in the presence of the sol-gel coating (a and b) and without it (c and d). It can be observed that the coated channel maintains its size while the non-coated channel shrinks due to the swelling caused by the absorption of toluene by the polymer. Scale bar represents 500 µm.

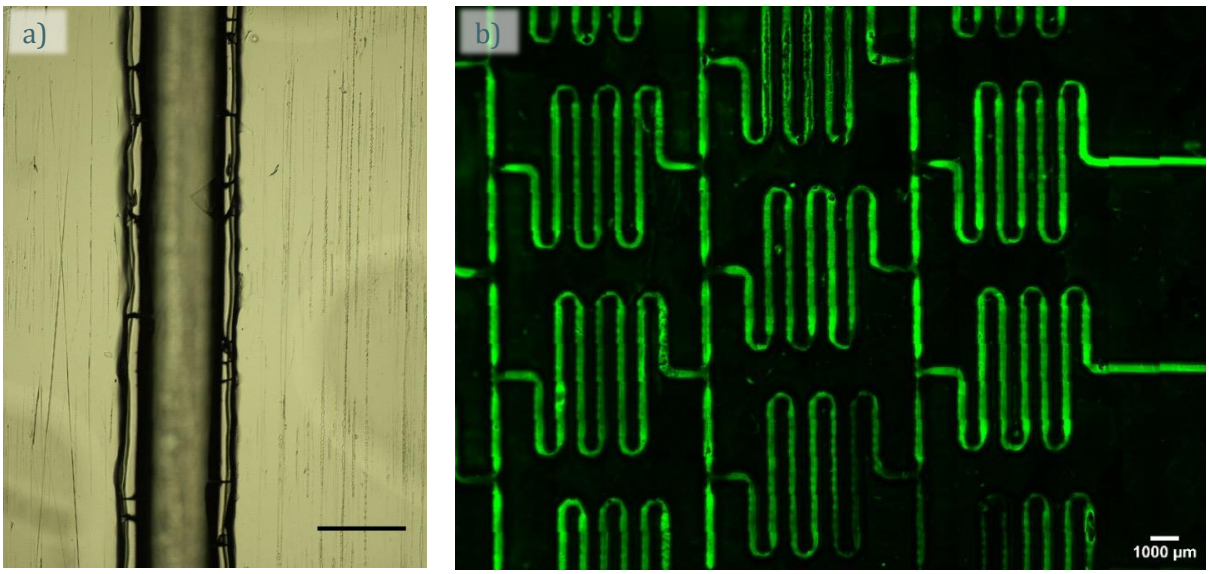

Figure 3.38: Channel coating formation. A) Brightfield image where the coat is visible on both walls of the channel. Scale bar represents 0.5 mm b) tile scan fluorescence image of the oxygen gradient generator device with the walls coated with the sol-gel solution mixed with the fluorescent microspheres. Scale bar represents 1 mm. Note the presence of cracks in a) and the uneven coating in the intersections in b).

Finally, it was decided to outsource the fabrication of this part due to its complexity and the need for high accuracy to ensure the pressure drop in all the branches was equal and the

gradient generator performed correctly. The 0.5 mm-high square channels were micromilled into 5 mm-thick clear PMMA slabs at the University's workshop. Prior to bonding of the milled microchannels, they were cleaned in a sonicator for 20 minutes. Then, the channels were exposed to chloroform vapour for 5 minutes to reduce the roughness of the surfaces to minimise the risk of bubble nucleation and/or trapping. After the surface was treated, the substrate (3 mm thick clear PMMA) and the microchannels were exposed to chloroform vapour for 7 and 2 minutes respectively, then brought into contact, and bonded in the Multipress at 70°C and 160 N/cm^2 for 30 minutes. The inlets and outlets consisted of ø1.6 mm holes milled with the rest of the features. To interface them with the system, ø1.5 mm biopsy punch needles were glued with epoxy resin (Araldite Syringe Epoxy Adhesive, RS Components).

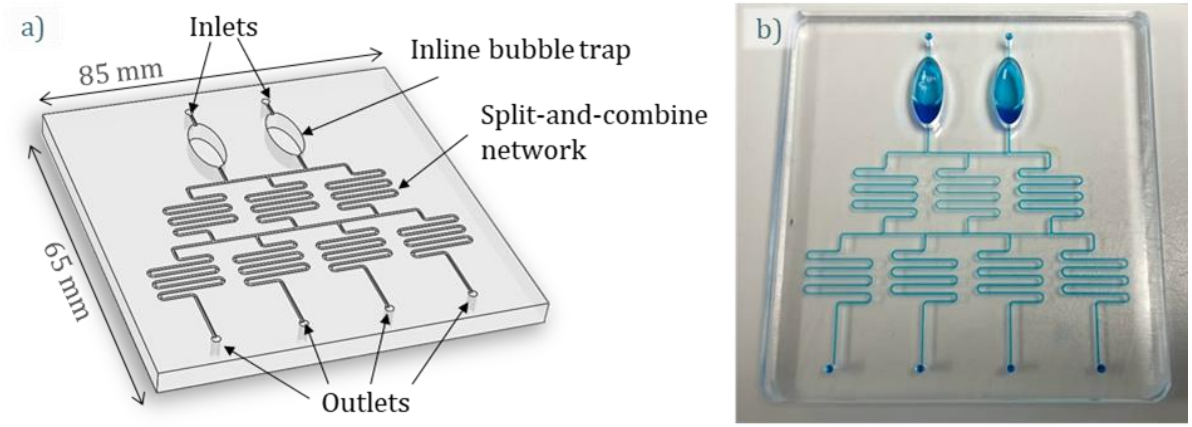

Figure 3.39: 3D model of the final gradient generator device and picture of the finished bonded version, filled with blue dye to check for leaks.

3.5.2 Test and evaluation

To test the ability of the gradient generator to produce multiple concentrations, two solutions (PBS and 0.1 mg/L fluorescein in DI water) were infused separately into the inlets, and the flow rate was controlled with pressure controllers (Flow EZ™, Fluigent) ranging from 2.5 to 50 µL/min. The outputs were collected and weighted to assess the equilibrium between the branches, and the fluorescence intensity of the outflow measured with a microplate reader to quantify the concentration at each outlet (Ex/Em = 460/515 nm). Given the large size of the channels, the pressure drop within the serial dilutor was very small, which meant that low pressures at the inlets lead to very high flow rates at the outlets, which affected the gradient generator efficiency. To increase the pressure drop, fluidic resistors were connected to each outlet. Additionally, this system was highly sensitive to the presence of bubbles within the channels as they could cause pressure imbalances and skew the gradient. To avoid bubbles nucleating within the channels, the surfaces were treated with chloroform vapour as explained above. Furthermore, inline bubble traps were included in the design. These traps consisted of a small chamber, with a height much larger than the channels. Bubbles coming in would rise due to their buoyancy whilst

the rest of the fluid would continue through the channel, therefore avoiding them from entering the microchannel network [295] (shown in Figure 3.39). The results showed no major pressure imbalances in the gradient generator and equally distributed flow rates at the outlets, which is key to ensure the formation of a predictable and reproducible gradient (Figure 3.40). The concentrations at the output are presented in Figure 3.41. The COMSOL simulation (black diamonds) is the ideal linear gradient that the system is trying to achieve. Experimentally, for flow rates above 20 µL/min the speed of the fluid was too fast, and mixing was not completed in the serpentine channels, leading to two outlets with a very high fluorescein concentration and two with a low one. With flow rates below 10 µL/min it was possible to obtain the gradient concentration really close to the ideal simulation. The data demonstrates the robustness and reliability of the method developed for producing an array of concentrations.

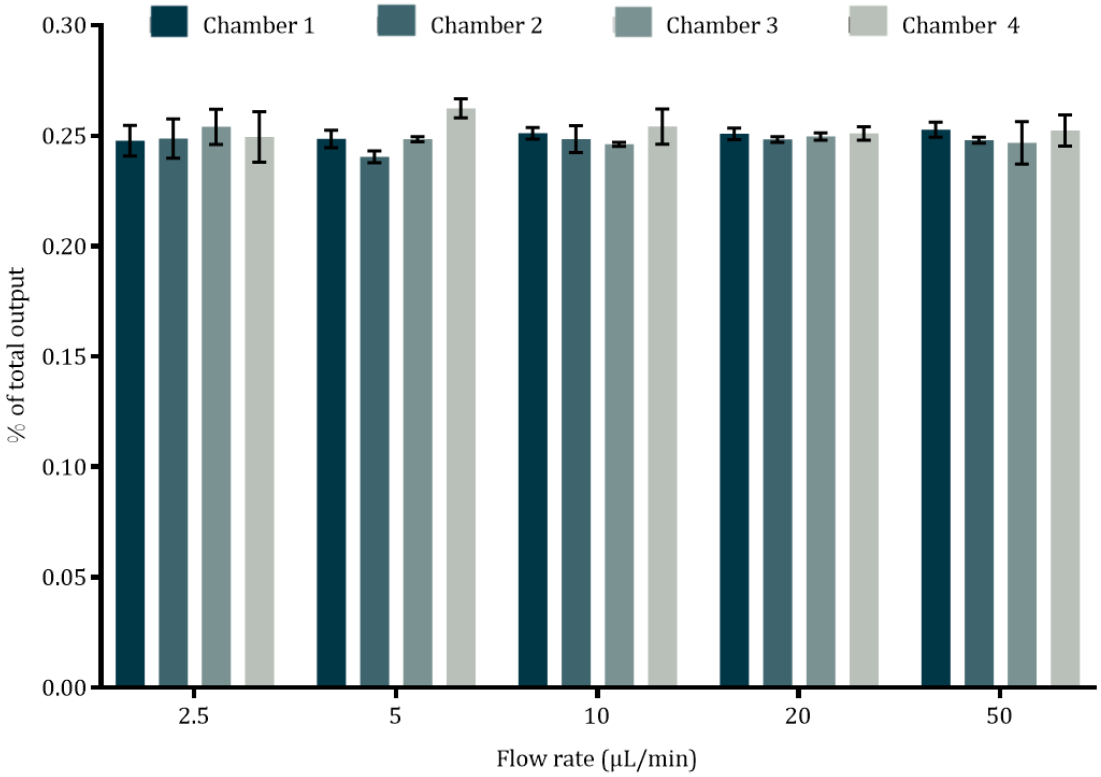

Figure 3.40: Outputs of each outlet of the gradient generator device in % of the total output (sum of the volume of the four outlets). Bars represent mean ± SD; n=3.

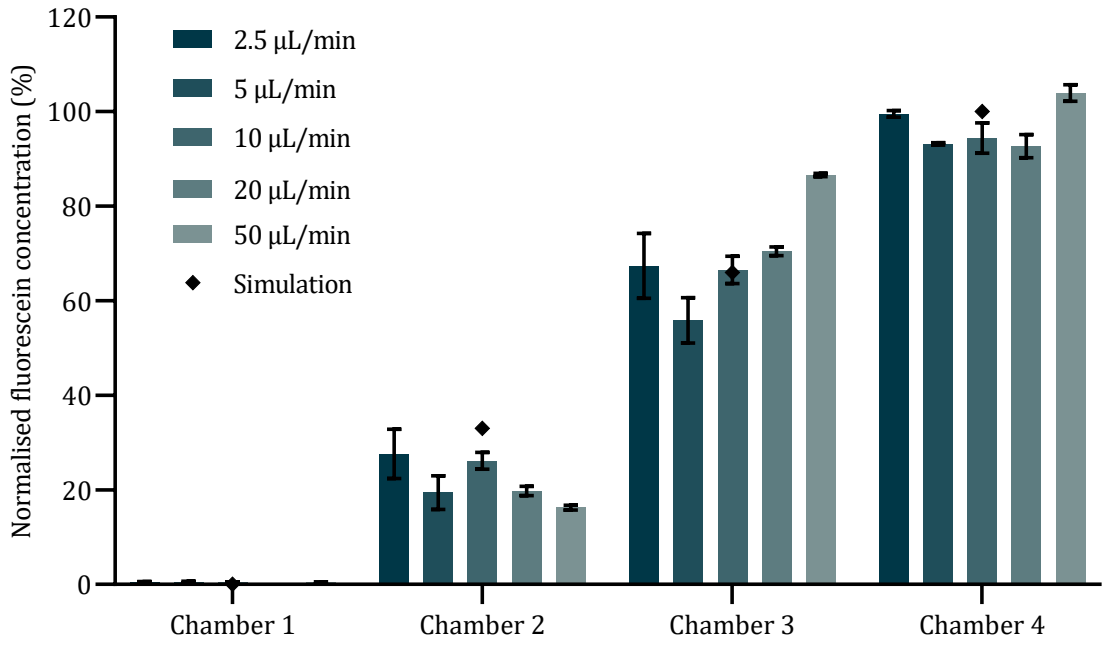

Figure 3.41: Concentration gradients at the outlets depending on the flow rate at the inlets. Bars represent mean ± SD; n=3.

Once all the parts were optimised separately, the system was brought together. Two PBS solutions were bubbled for over 1 h with pure nitrogen to obtain 0% DO solutions. These were then injected into the serial dilutor at 5 µL/min (corresponding to flow rates at each outlet of 2.5 µL/min) and the four outlets directed to the four culture chambers with the integrated sensors via glass capillaries. The sensors were calibrated prior to the start of the experiment with a saturated Na_2SO_3 solution to obtain the maximum signal. Measuring parameters were set to 10 s of excitation measured every 5 minutes. Once the experiment started, a significant reduction in the signal occurred. The signal approached its maximum (considered as 0% O_2) at very high flow rates, above 100 µL/min (Figure 3.42a). This indicated the presence of oxygen leaks within the setup. This was further corroborated by flushing the N_2-bubbled solution at a really high flow rate (150 µL/min) and then stopping the flow and monitoring the decay in the signal, indicating diffusion of oxygen into the chambers (Figure 3.42b). This was the case for all the devices tested (n=7+).

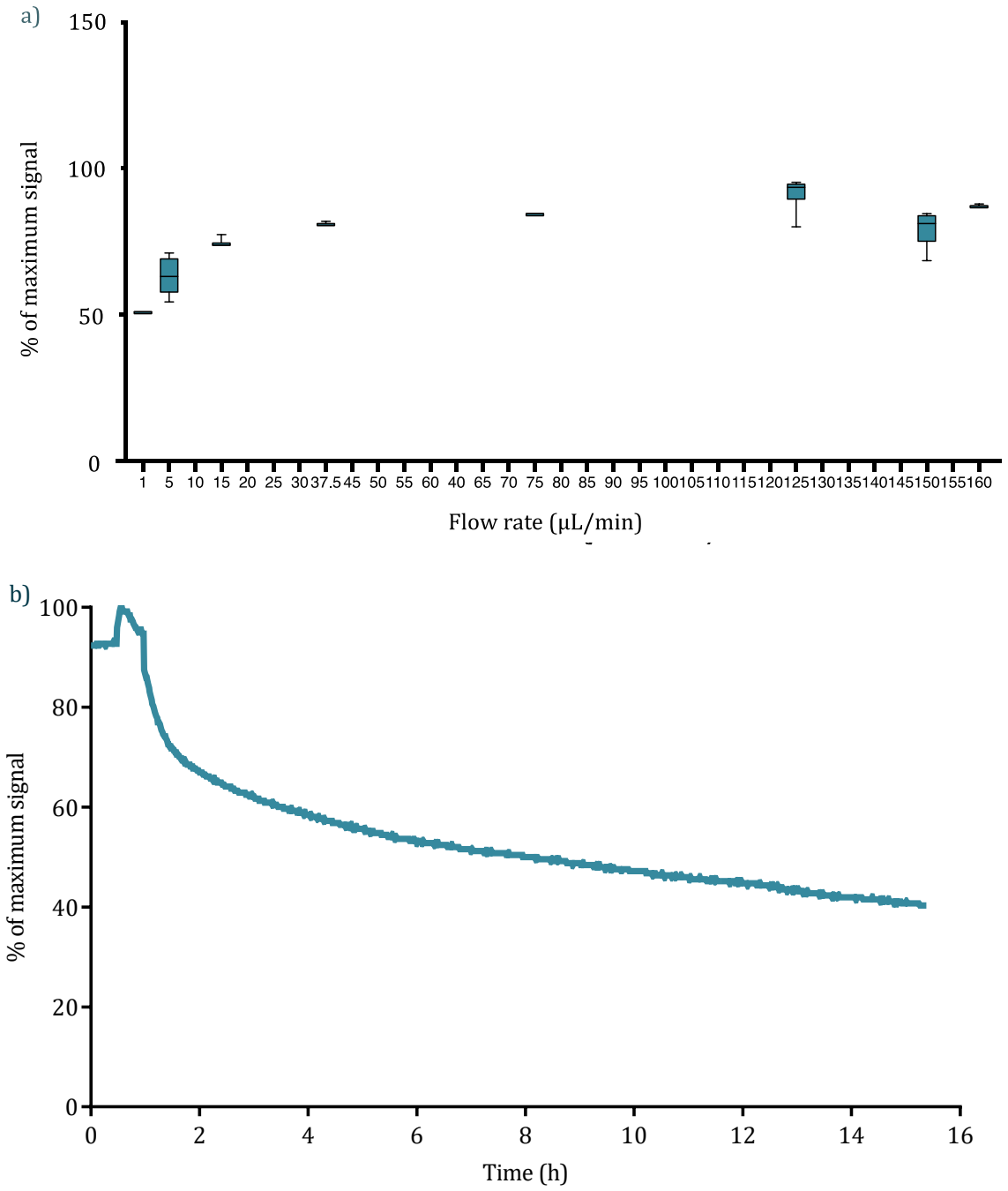

Figure 3.42: a) signal collected by the detector for multiple flow rates. Data represents box and whiskers 10-90 percentile, the lines represent the mean b) the oxygen tension decay after the flow stopped, indicating that oxygen is diffusing into the chamber .

3.6 Final device

Due to the inability of the previous attempts (with Device v3) to generate and maintain an oxygen gradient over extended periods of time during culture, a new method was developed, slightly modifying the previous system. Instead of obtaining the oxygen concentrations in a previous step and avoiding diffusion into the chambers, active oxygen removal was used again, but instead of using a chemical sink like in the Devices v1 and v2, a gas mixture with the desired oxygen concentration was flushed underneath the culture chamber to control the oxygen by equilibration of the gas concentrations between the two chambers. The desired gas concentrations were obtained using the gradient generator presented in Section 3.5. This required modifying the design of the chip and the chip holder.

In this new design (Device v4) depicted in Figure 3.43 and Figure 3.44, the culture chambers (in red) were similar to the previous multichamber design (Device v3), but a set of chambers were added underneath them (in blue), in which the gas mixtures coming from the serial dilutor was flowed, separated by an oxygen-permeable PDMS membrane (in grey). The fabrication process was more complex, but it allowed for faster equilibration of the oxygen in the chambers. The chip holders presented in Section 3.3 (Figure 3.24) were kept as they were but with 8 holes for the gas inlets and outlets at the end, close to the hinge. In this setup, the gradient generator is flushed with compressed air and pure nitrogen gas at the inlets, and the four outlets are directed into the inlets of the gas layer in the new setup. A COMSOL simulation was carried out to study the effect of the flow rates of the gas and the medium on the final oxygen concentration at the outlet of the culture chamber. Figure 3.45 shows a contour map of the oxygen tension at the outlet for combination of Péclet number for the media (*Pe(m)*) and the gas (*Pe(g)*). The results show that oxygen tension increased with increasing media flow, since the medium is convected downstream before it has time to equilibrate with the gases in the layer underneath. However, the gas flow rate had little influence on the oxygen tension over the range of interest, given that high flow rates can lead to high shear stresses on the tissues, and the working flow rate will be set around 1 μL/min, which equates to *Pe(m)* of 10, for which all the oxygen is removed for the whole range of gas flow rates.

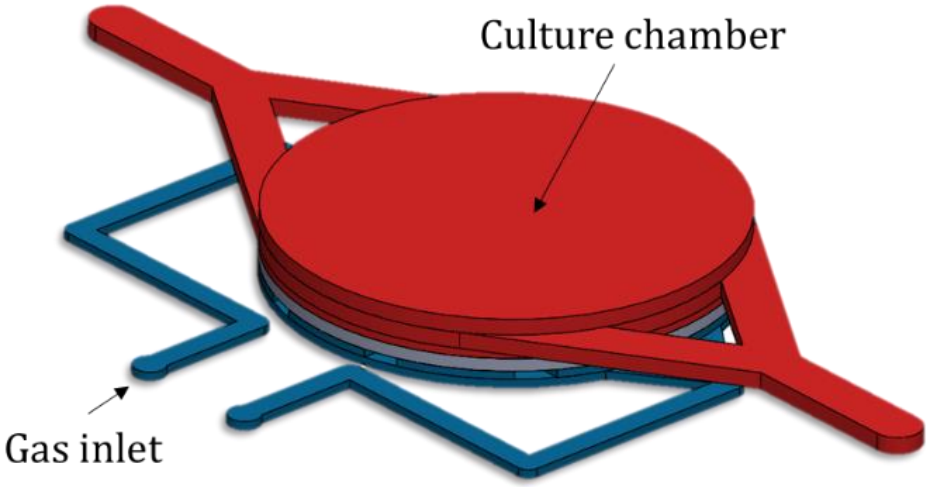

Figure 3.43: Model of the new design with the two layers separated by the PDMS membrane. The gas channel network (blue) allowed to distribute the gas without modifying the culture chamber (red) design or the chip holder.

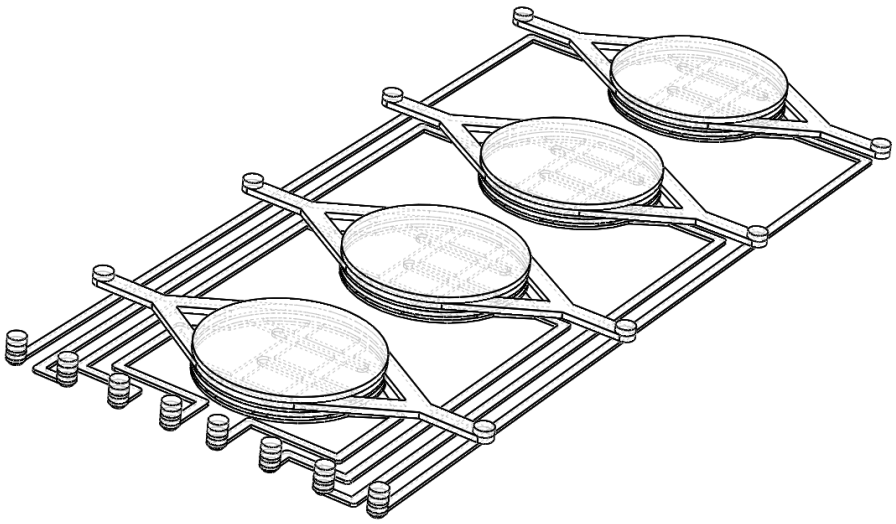

Figure 3.44: 3D rendition of the assembled new modified design (Device 4).

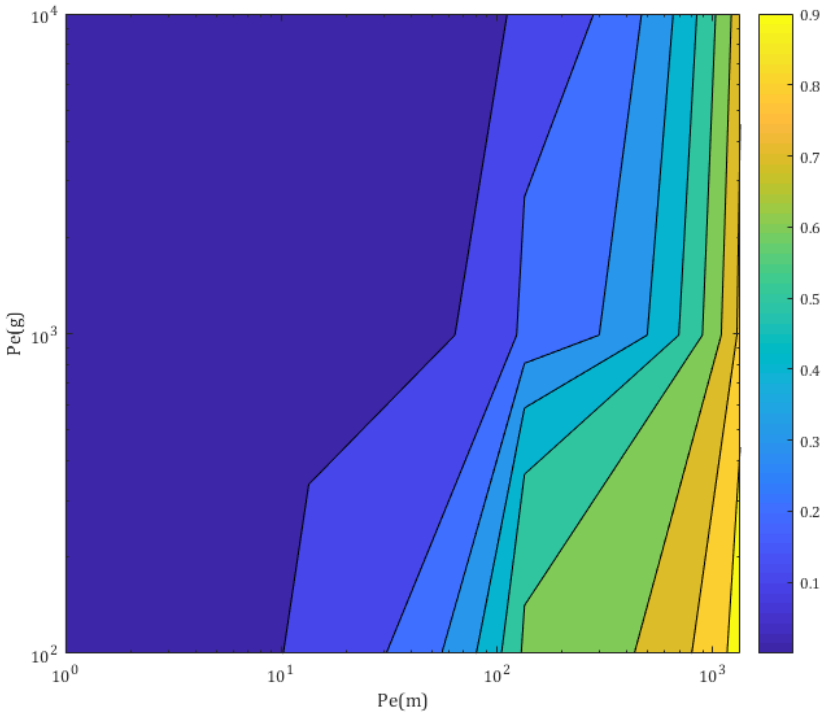

Figure 3.45: Result of the numerical simulation of oxygen tensions (normalised) supplying pure nitrogen gas at the gas inlet and equilibrated medium (oxygen saturated) in the culture chamber and combinations of the flow rates for each. When the flow rate of the medium was too high (high Pe(m)), the diffusion time was too short and oxygen was not removed from the medium. At higher gas flow rates (high Pe(g)) oxygen was removed more effectively from the medium. For lower medium flow rates, more desirable for the perfusion to the cells, all the gas flow rates evaluated were sufficient to completely remove the oxygen. Colour bar represents the normalised DO concentration.

The distribution of the oxygen around the chamber depending on the flow rate was also simulated to check for the presence of gradients within the chamber (Figure 3.46). The results plotted in Figure 3.46b and c showed that for flow rates of 1 µL/min and below (which are better to reduce shear stress on the cells) the oxygen concentration was uniform and constant for the entire chamber.

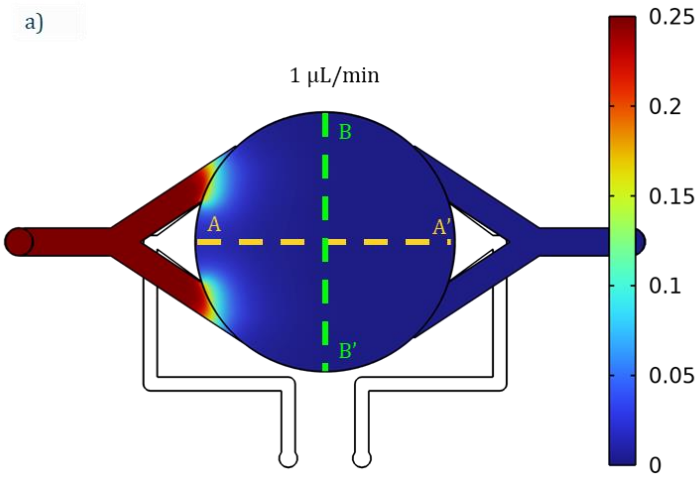

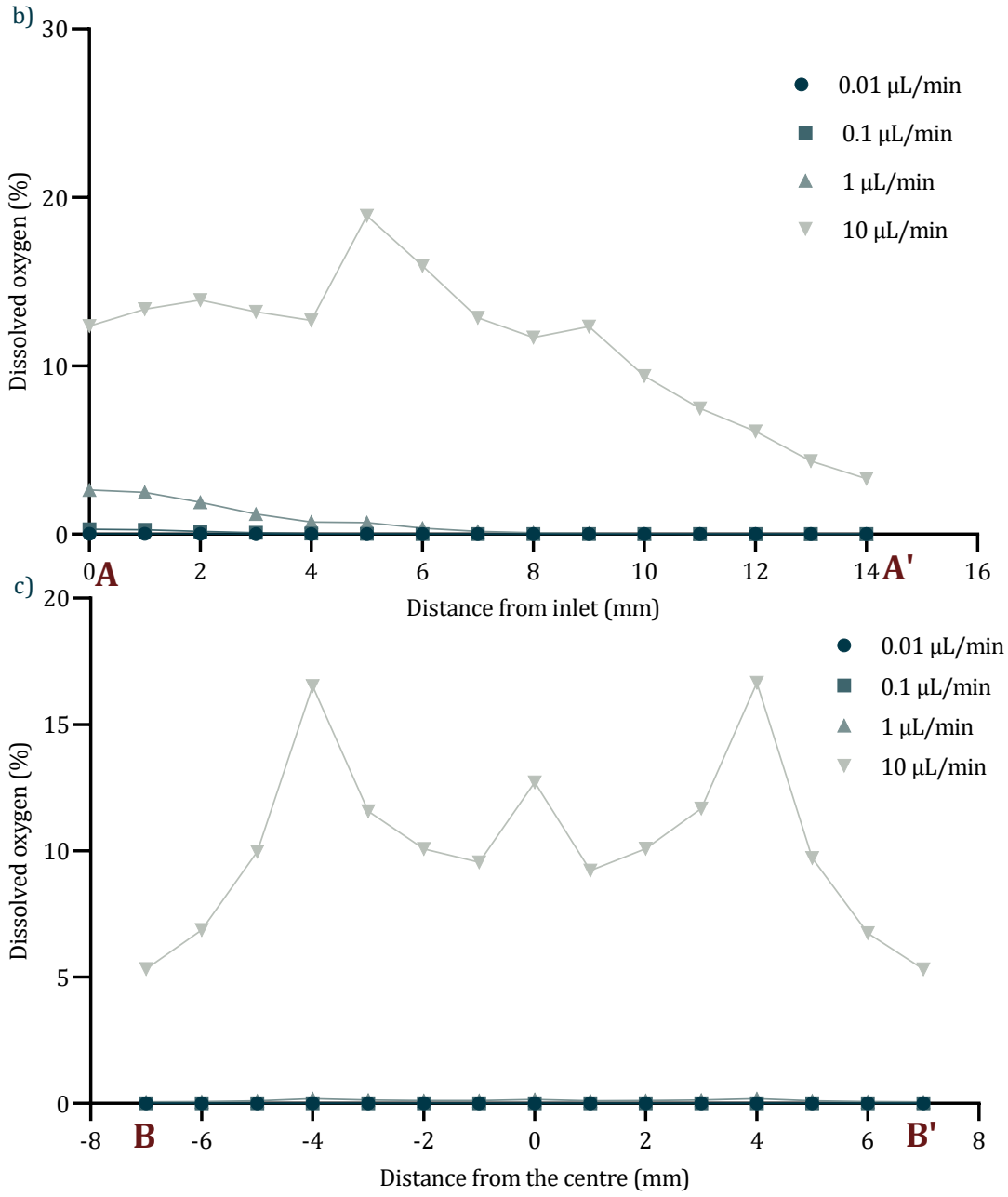

Figure 3.46: a) Simulations of the oxygen concentration distribution for increasing flow rates. B), measurements of the oxygen tensions along the direction of the flow (line A in yellow) and c), along the direction perpendicular to the flow (line B in green).

As mentioned above, the metal chip holders required a slight modification to incorporate the inlets and outlets for the gas mixtures (Device holder v3). Holes were drilled to the same holders that were fabricated for the previous design. Figure 3.47 shows the modifications made. 21G gauge needles (Agani™, Terumo®) were fitted and held in place with epoxy resin as interface to connect the gas lines.

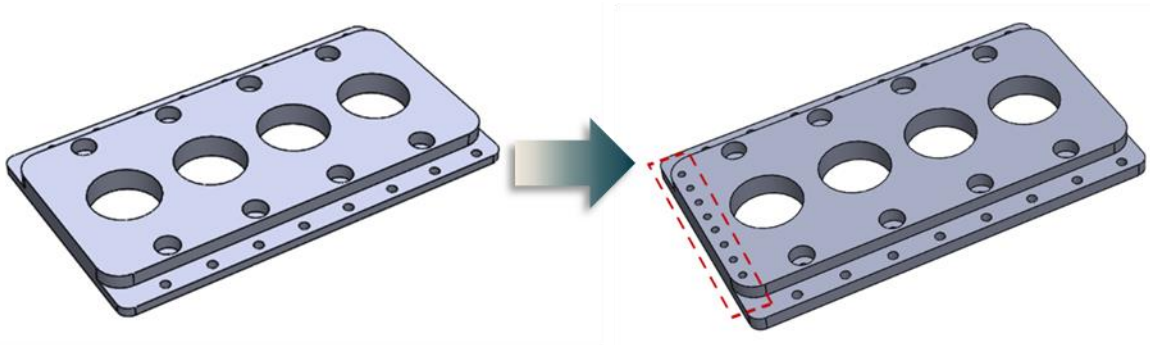

Figure 3.47: Modification in the chip holder. All the features remained from the previous design and eight holes acting as inlets and outlets for the gas mixtures were added.

Given that the serial dilutor would now be used to generate mixtures of gases instead of liquids, a set of simulations were carried out to test the ability of the design to generate the desired gradient as well as the flow rates necessary to achieve it. Unlike the case with liquids, the slow flow rates resulted in the generation of 4 equal oxygen concentrations at the outlets (darker bars in Figure 3.40). This is due to the much higher diffusivity of oxygen in air compared to water. Hence, flow rates above 50 µL/min were used to ensure that chamber 1 reached 0% DO (Figure 3.48). In our system, the calculated hydraulic resistance was 7.55×10^{-11} Pa·s/m^3. Using the equivalent of the Ohm's law, when the pressure at the controllers was set at 200 mbar, that would give a gas flow rate of 1.5 mL/min, well above the maximum simulated flow rate. In subsequent experiments, the pressure controllers were set above 200 mbar.

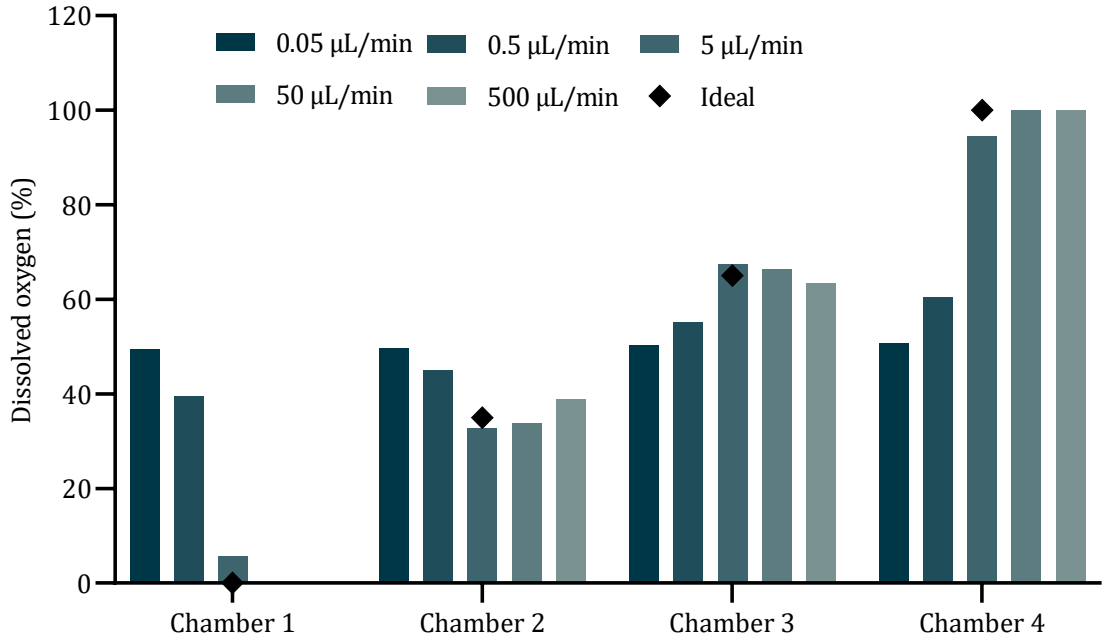

Figure 3.48: Simulated concentration gradients at the outlets depending on the flow rate at the inlets. The ideal situation was the linear gradient obtained in the simulation with a liquid at 5 µL/min.

3.6.1 Fabrication and assembly

The devices (device v4) were designed in AutoCAD and fabricated in PMMA, depicted in Figure 3.49). One of the layers was exposed to 5 mL of pure chloroform at 1 cm distance between the treated surface and the solvent surface for 5 minutes. The surface was then brought into contact with the corresponding untreated layer and bonded using a laminator at 40°C. This ensured complete bonding, removing air trapped between the layers and was much faster than the previous method using the Multipress. The oxygen sensors were prepared as explained in Section 3.4.1.1 and deposited on the gas layer substrate. Once all PMMA layers were assembled, the PDMS membrane was bonded to the gas layer assembly first and then to the culture chambers assembly by treating the tape and the PDMS membrane with oxygen plasma (Femto A Plasma Etcher, Diener Electronic GmbH) at 7.5 sccm for 30 s and 100W [296]. The treated surfaces were brought into contact and passed through the laminator. Before the final bond to the culture chamber assembly, the gas inlets and outlets were punched in the PDMS membrane.

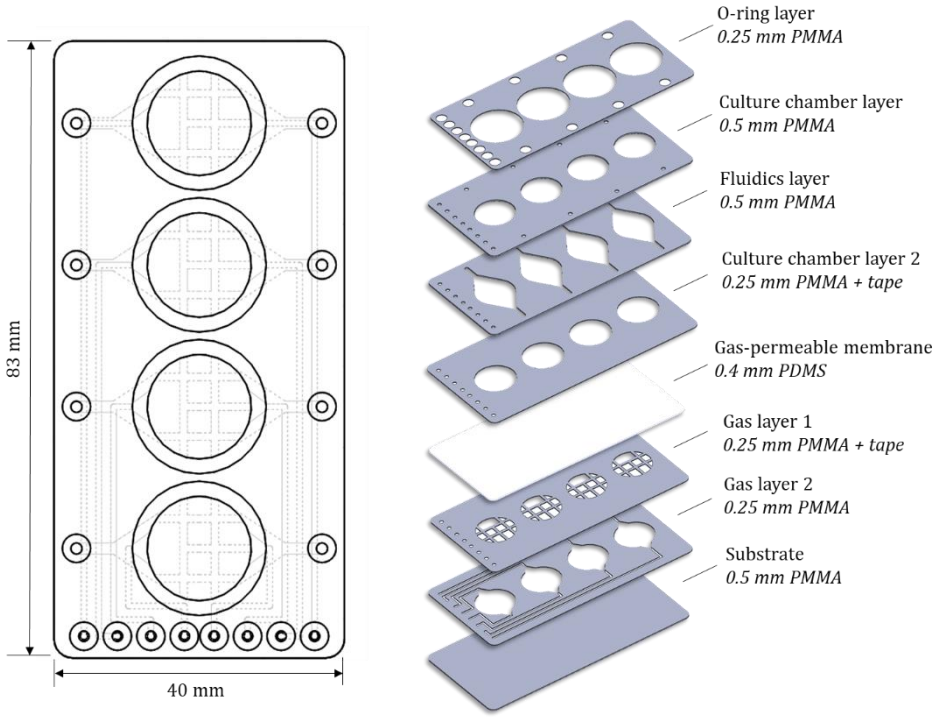

Figure 3.49: Exploded view and description of the layers comforming the device (device v4).

3.6.2 Test and evaluation

The device (Device v4) was tested for leaks and delamination to evaluate the quality of the bonds. Blue and yellow food dyes were infused in alternating gas channels to detect leaks between the channels. The device was mounted on the chip holder, the O-rings fitted in place and the clamp closed to seal the chambers. The hydraulic tightness of the chambers was tested by

pressurising the chambers immersed in water mixed with soap. All tests were successful, and no leaks were observed.

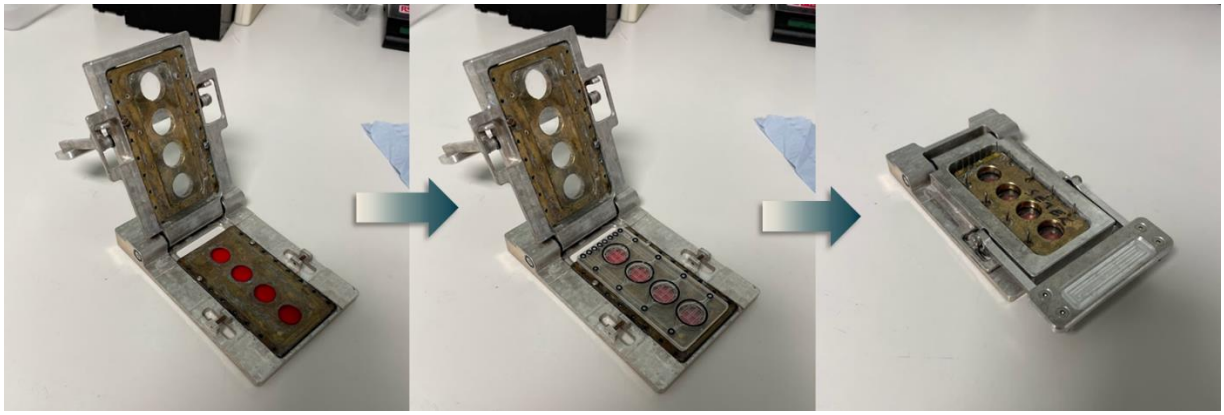

Figure 3.50: Setting up the system. First, the chip holders are clean and the filters place in the holes. Next, the device is aligned in the bottom holder and the O-rings places in their grooves. Finally, the chip holder is closed by the clamp, sealing the four chambers simultaneously.

The ability of the system to generate and maintain an oxygen gradient was also tested. Once the device was sealed and leak checks done, a line of compressed air and pure nitrogen gas were connected to the pressure controllers, and the outputs to the inlets of the gradient generator. The four outlets were connected to the gas inlets of the device and the oxygen concentrations were measured with the electronic oxygen detector (after its calibration). The pressure ratios between compressed air and nitrogen were varied to obtain different gradient shapes. The results are shown in Figure 3.51. Despite the system not following the ideal gradient simulated in COMSOL, 4 different and stable oxygen concentrations were achieved and maintained for over 15 hours (Figure 3.51b). The possibility to obtain different gradient shapes by varying the ratios of the pressures at the inlets gives additional opportunities for the study of oxygen in living tissues. Because of the small pressure drop in the system, fluidic resistors were added at the outlets of the gas layers. This helped stabilise the signal.

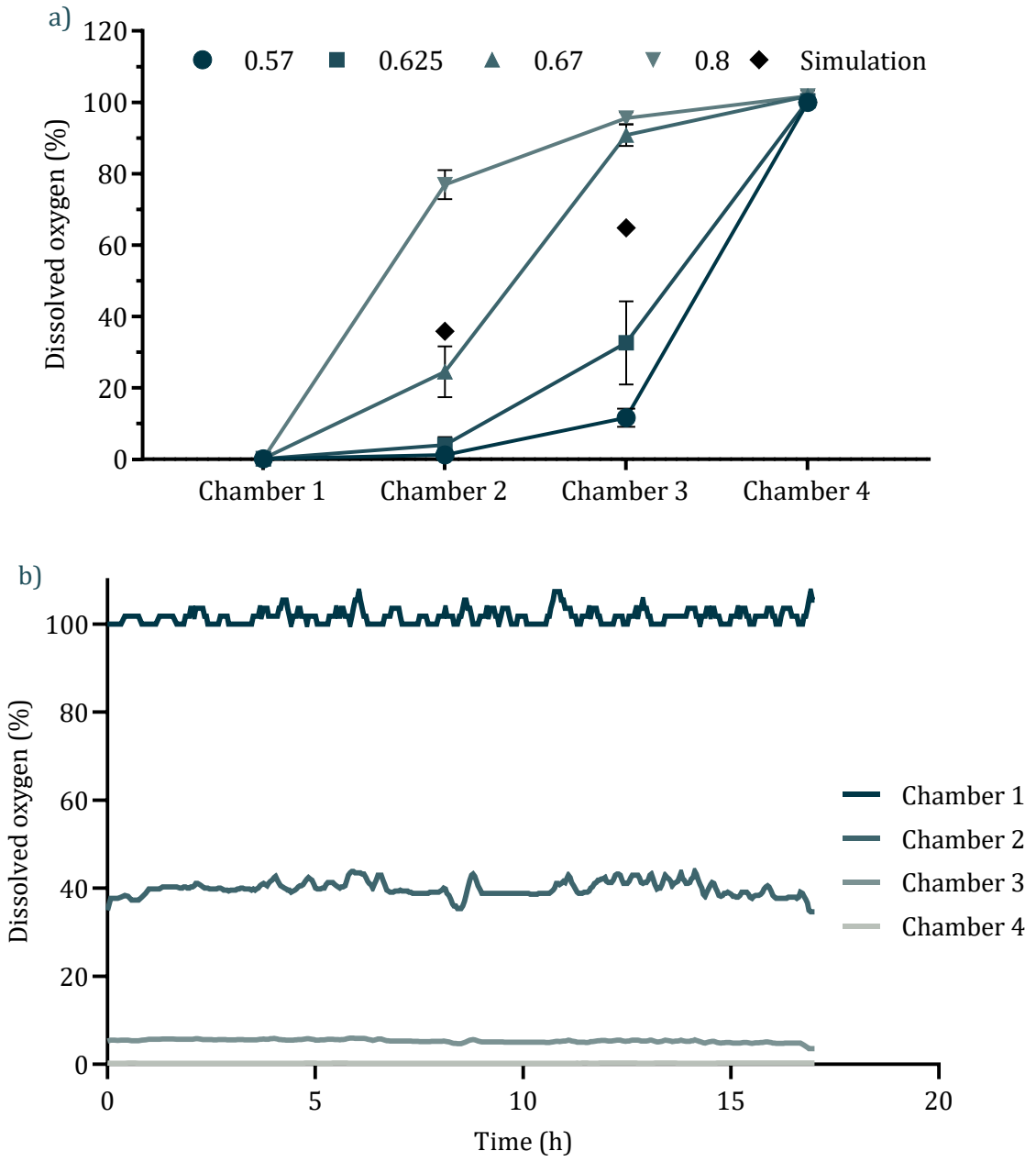

Figure 3.51: a) Oxygen gradients obtained with the complete setup depending on the ratio between the pressures of compressed air and pure nitrogen gas at the inlets. Data points represent mean ± SD, n=3. b) Established oxygen gradient across 4 chamber for over 15 hours using the 0.625 ratio.

3.7 Conclusions

In this chapter, a microfluidic platform for the control and monitoring of oxygen tensions was developed. Multiple methods for achieving the desired oxygen concentrations were attempted: chemical sink, pre-equilibrating the oxygen of the medium by bubbling with gas mixtures and, finally, equilibrating the chambers with gas mixtures flowing underneath.

To achieve this, multiple designs were tried. For each design, simulations were carried out to optimise the design parameters and different fabrication processes were developed in order to obtain an oxygen-impermeable device able to control the oxygen tensions within the culture chambers. The final device consisted of two sections, the bottom one for the flow of gas mixtures of specific oxygen concentrations and the top one, hosting 4 cell culture chambers. The devices were fabricated bonding several PMMA layers via solvent vapour exposure with an intermediate PDMS membrane separating both sections, to allow for oxygen equilibration. The PDMS membrane was bonded to the PMMA parts via pressure sensitive adhesive tape functionalised with oxygen plasma. The bottom section included features to provide structural rigidity to the PDMS membrane, on top of which cells would be cultured. A chip holder in a clamp fashion was also built to host the devices and seal them, producing uniform and reproducible pressures on the chambers.

To measure the oxygen in the chambers, an oxygen sensor was developed. Using a platinum porphyrin oxygen-sensitive dye embedded in a polymer matrix, whose fluorescence intensity in inversely related to the amount of oxygen present, an electronic detector was built. The detector captured the emission intensity of the sensor and transformed the signal into an oxygen tension using the Stern-Volmer equation. The detector was controlled by an Arduino board, and it was integrated with the device, so that the oxygen could be monitored in real time inside the incubator, reducing the disruption to the tissues cultured.

To obtain multiple oxygen tensions, an oxygen gradient generator was built. Using a network of microchannels in a split-and-combine fashion. Two streams of gases at known oxygen tensions were introduced at the inlets. The two streams mixed and separated sequentially until four different oxygen concentrations were obtained. These gas mixtures were then directly connected to the gas layer of the microfluidic device. In this way, each chamber of the device was equilibrated with the gas mixture flowing underneath, therefore subjecting each chamber to a different oxygen tension. The system was able to generate and monitor 4 different oxygen tensions stably.

Chapter 4. Cell experiments

4.1 Materials and methods

4.1.1 HeLa cell standard subculture

To establish HeLa cells from frozen stocks, the cryotubes containing the frozen cells were taken out of the nitrogen tank. In an MSC, using a 1 mL pipette, media pre-warmed at room temperature was taken and pipetted up and down on top of the frozen pellet within the cryovial. As cells began to defrost, the thawed supernatant was transferred into a 25 mL universal tube, and the process was repeated until all cells were thawed. The universal tubes were then centrifuged at 300 x g for 5 min at room temperature. Subsequently, the cell pellet was re-suspended in 13 mL of media and transferred to a T75cm^2 filter flask, and placed in an incubator at 37°C, 5% CO_2. After 24 hours, the cultures were checked for infection and the media was replaced with fresh complete HeLa media to remove non-adherent cells. The cultures were monitored daily, replacing the media every 2 days until they reached 70-80% confluence (percentage of the surface of the culture dish covered by the adherent cells) when they were considered ready for passaging (this part was performed by Anna Willis, PhD student in the Brooke Lab).

The cells were then rinsed with 10 mL HBSS, followed by exposure to 1 mL of trypsin/EDTA/HBSS solution (0.5%, #15400054, ThermoFisher) at 37°C for ~2.5 min. The trypsin/EDTA solution was neutralised with 10 mL of complete HeLa medium. The cell suspension was transferred into a conical tube (15 mL) and centrifuged at 300 x g for 5 min at room temperature to form a pellet. The supernatant was removed, the cell pellet disrupted, and the cells resuspended in 1 mL complete media and viable cells counted using a haemocytometer and the trypan blue exclusion method (Section 4.1.2). Finally, the cells were diluted to a predetermined density, and the cell suspension was added to each plate/flask as required for the experiments or for continuous culture.

4.1.2 Exclusion assay

The exclusion assay using Trypan Blue Solution (0.4%, #15250061, ThermoFisher) was used to count cells to determine the volumes required to prepare the cell suspensions for continuous culture or the experiments. It was also used as a method to determine viability of the cells during passaging and to calculate growth rates.

Once the cells were resuspended in 1 mL of complete media, a microtube was prepared with 40 µL of fresh complete media, 10 µL of the cell suspension and 50 µL of trypan blue. 10 µL of that solution were then transferred to a haemocytometer to perform cell counting (Figure 4.1). The cell density was calculated as:

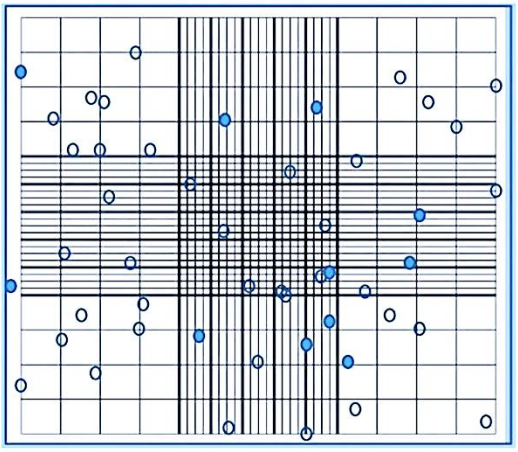

Figure 4.1: Depiction of a haemocytometer for live/dead cell counting. Empty circles represent live cells and filled circles represent dead cells.

$$Cell\ density\left[{}^{cells}/_{mL}\right] = \frac{Live\ cells\ counted\ [cells]}{number\ of\ squares\ \times\ volume\ of\ a\ square\ [mL]} \qquad \textit{Eq. (4.1)}$$

Where the volume of each square is 0.1 µL. With this number, the volume of the cell suspension needed to add to obtain the desired cell concentration could be calculated as:

$$Volume\ to\ add\ [mL] = \frac{Desired\ number\ of\ cells\ [cells]}{cell\ density\ [{}^{cells}/_{mL}]} \qquad \textit{Eq. (4.2)}$$

The viability was calculated as the number of live cells divided by the number of total cells counted in the haemocytometer, and the growth rate was calculated as:

$$Growth\ rate\left[{}^{div}/_{h}\right] = \frac{\log_2\left(\frac{Cell\ density\left[\frac{cells}{mL}\right] \times\ suspension\ volume\ [mL]}{number\ of\ cells\ seeded\ [cells]}\right)}{time\ [h]} \qquad \textit{Eq. (4.3)}$$

4.1.3 LDH assay

The LDH assay was performed using the CytoTox 96® Non-Radioactive Cytotoxicity Assay Kit (#G1780, Promega). Aliquots of the supernatants were collected at the desired timepoints from the samples and transferred into centrifuge tubes. If the aliquots were not going to be used immediately, they were frozen at -20°C. To perform the reference curve, the kit's lysis buffer was added to the positive control in a 1:10 ratio to the total volume to generate the maximum LDH release control. It was left to incubate for 45 minutes at 37°C before transferring the contents to a tube and centrifuged at 300 x *g* for 5 min. Subsequently, a 1 in 2 serial dilution was made in fresh serum-free media to obtain the reference curve. Once the serial dilution and the aliquoted

samples were ready, 25 µL of each condition was transferred in a flat bottom 96-well plate in duplicate. Then, 25 µL of the *CytoTox 96® Reagent* was added to each sample aliquot. The plate was covered with foil to protect it from the light and left to incubate at room temperature for 30 min. After that time, 25 µL of the *Stop* solution was added to each well. Finally, the absorbance was measured at 492 nm in a conventional microplate reader within an hour of adding the *Stop* solution. To calculate the results, the average of the background signal (culture media only) was subtracted from the average of the signal for each condition. Then the cytotoxicity was calculated as:

$$\%Cytotoxicity = \frac{Experimental\ LDH\ release}{Maximum\ LDH\ release} \qquad \textit{Eq. (4.4)}$$

4.1.4 Resazurin assay

To prepare the reagent stock, 1.1 mg of resazurin sodium salt (#199303, Sigma-Aldrich) was diluted in 10 mL of sterile PBS. The solution was then filtered using a 22 µm filter and aliquoted in centrifuge tubes and stored at -20°C. The reagent was added in a 1:10 ratio to the samples, so the final working concentration was 44 µM. The reagent was thawed and warmed to 37°C in a water bath before use. A working solution of 1:10 was prepared in serum-free complete media. The supernatant of the samples was removed and 500 µL of the working reagent solution was added to each well. The plate was shaken gently before covering it with foil to protect it from ambient light and incubated for 1 h at 37°C and 5% CO_2. After the incubation, the fluorescence intensity was measured in a microplate reader at Ex/Em = 560-10/590. All the experiments were performed with a standard curve to calculate the number of live cells present in each condition. Cells were suspended at the desired density and a 1 in 2 serial dilution was performed to obtain the intermediate cell densities. The cells in the standard curve were untreated and used as controls. The measured signal was normalised as:

$$Relative\ signal = \frac{measured\ signal - background}{background} \qquad \textit{Eq. (4.5)}$$

A model curve was interpolated and used to calculate the number of cells in each condition.

4.1.5 Cell culture on-chip

4.1.5.1 Cleaning and priming

After the system was assembled and the leak test performed to ensure hydraulic tightness, the system is sprayed with 70% Ethanol and placed inside a class II MSC. Each chamber was manually flushed with 2 mL of 1:50 bleach solution (Sainsbury's thin bleach, <5% Sodium Hypochlorite) and left for 10 minutes. After this, the chambers were manually rinsed with 4 mL of sterile dH_2O and left to soak for ~5 h. After the soaking time, 1 mL of collagen solution (30 ng/mL, Advanced BioMatrix, Cat No 5005-B) was flushed through, and the system was placed in the incubator at 37°C overnight. Afterwards, the excess of collagen was washed with 2 mL sterile PBS, and then with 2 mL of HBSS. To prime the chambers before introducing the cells, the chambers were rinsed with 1 mL of complete culture media.

4.1.5.2 Cell seeding

Once the device was cleaned and primed, the cells were subcultured following the protocol detailed above. After counting the cells and calculating the cell density, a cell suspension at 300,000 cells/mL was prepared. 1 mL of this suspension was transferred to a 1 mL syringe using a pipette and connected a chamber of the device. The suspension was slowly injected into the chamber to avoid disrupting the cells. This was repeated for each chamber. The outlets of the chambers were then blocked, and the cells were allowed to adhere to the substrate for 3 h. After the adherence time, the chambers were connected to 10 mL syringes containing 5 mL of complete culture media, mounted onto a 4-channel syringe pump (Fusion 400, Chemyx Inc.) and the flow was started at 1 µL/min. The entire setup was then placed inside an incubator at 37°C with 5% CO_2.

4.1.6 RNA extraction

To extract the RNA from the samples, the RNeasy Mini Kit (#74104, Qiagen N.V.) was used. First, the cells were lysed with the provided lysis buffer. This had to be done still under hypoxic conditions to avoid the hypoxic markers to degrade in the presence of oxygen. Therefore, the gas flow was maintained until the lysates were extracted from the chambers. After 24 h of hypoxic challenge, the flow of fresh media was stopped, and the system was taken out of the incubator and placed in the MSC. The chambers were washed with 2 mL sterile PBS and then emptied completely before flushing 400 µL of Lysis buffer. The buffer was left to act for ~5 min after which, with a pair of syringes connected at the inlets and outlets of each chamber, the buffer was rinsed from one to the other to ensure mixing and lysis of the cells from the substrate. The contents of

each chamber were removed completely into one of the syringes and transferred into an RNAse-free microtube. Once all the chambers were emptied, the gas flow was stopped, and the system removed from the MSC for cleaning before the next experiment.

After extracting the lysate of each chamber, the same volume was added of 70% ethanol, mixed thoroughly by pipetting, and the mixture was transferred into the spin columns provided by the kit. These were then centrifuged at 8000 x *g* for 30 seconds. The waste in the collection tubes was discarded and 700 µL of the RW1 buffer was added to wash the membranes. The columns were spun again at 8000 x *g* for 30 s, the waste removed and 500 µL of RPE buffer added. The columns were spun again for 30 s at 8000 x *g*, the waste discarded, and another 500 µL of RPF buffer was added again. This time, the columns were spun for 2 min at 8000 x *g* to completely dry the column membrane. The spin columns were then placed in new 1.5 mL collection tubes and 30 µL of RNAse-free water was added to detach the RNA from the columns into solution. The columns were centrifuged again for 1 min at 8000 x *g*. After this step, the spin column was disposed of, and the sample containing the extracted RNA was in the collection tube.

4.1.6.1 Quantification of RNA

Before running the PCR to measure the gene expression of the hypoxic factors, the RNA content of the samples was quantified, and the purity of the sample assessed using a NanoDrop 2000 spectrophotometer (Thermo Scientific™). Using UV/visible spectrophotometry, the spectrum of each nucleic acid present in the sample is examined. In this system, a 1 µL sample drop is place between two fibre optic cables, and held in place via surface tension. The nucleic acid sample concentration is based on the absorbance at 260 nm, corrected with a baseline normalisation at a 340 nm wavelength. The quantification is calculated using a modification of the Beer-Lambert equation:

$$c = \frac{A * \varepsilon}{b} \qquad \textit{Eq. (4.6)}$$

Where c is the nucleic acid concentration (ng/µL), A is the absorbance in AU, ε is the wavelength-dependent extinction coefficient (usually 40 ng·cm/µL) and b is the path length (cm). To assess the purity, the 260/280 ratio was used, with a value of ~2.0 as the generally accepted value for a "pure" sample.

4.1.7 Reverse Transcription quantitative Polymerase Chain Reaction

DNA is composed of two complementary strands that form a double helix. The two strands are composed of nucleotides (adenine (A), cytosine (C), guanine (G) and thymine (T)),

held together by hydrogen bonds. According to the base-pairing rules, nucleotide A only binds to T and C to G. This means that if you know the sequence of one strand, you always know how to replicate the other half. The polymerase chain reaction (PCR) is a biochemical process capable of amplifying a single DNA molecule, or a section of it, into millions of copies in a short period of time. It uses temperature cycling to initiate and end bursts of enzyme-catalysed DNA synthesis. Each cycle consists of three steps: (1) denaturation, (2) annealing, and (3) extension.

The starting DNA sample (template DNA) is heated to around 95°C to break the hydrogen bonds and separating the complementary DNA strands (denaturation). Then, the region of DNA to amplify (target sequence) is identified using short pieces of single-stranded synthetic DNA (primers). The primers match the target sequence on the separated DNA template strand and anneal (stick) to it when the reaction is cooled down (~55°C). The lower temperature allows for hydrogen bonds to form between the primers and the template. Next, the reaction is heated again to 72°C to extend (copy) these new double stranded where the primers and template have annealed. For this, an enzyme called DNA polymerase is used. DNA polymerases are enzymes that can read a strand of DNA and make a complementary copy following the base-pairing rules. The polymerase will find the end of the double stranded regions of DNA where the primers have bound, and will start moving along the DNA, base by base, adding the correct complementary DNA nucleotide. After one cycle of these three steps, the original target DNA has been duplicated. The cycle is then repeated several times (25-35 times), creating new identical copies of the target region of the DNA, exponentially amplifying the number of copies. This process is carried out in a programmable device called thermal cycler [297].

Quantitative reverse transcription PCR is used when the starting material is RNA. In this method, RNA is first transcribed into complementary DNA (cDNA) by reverse transcriptase. The cDNA is then used as the template for the PCR. RT-qPCR can be performed in a one- or two-step assay. In the first, the reverse transcription and PCR happen in the same tube and buffer. In the latter, the reverse transcription and PCR steps are performed in separate tubes, with different optimised buffers, reaction conditions, and priming strategies. Even though it is less sensitive, in this project the one-step method was selected as it reduces experimental variation, pipetting steps, and risk of contamination [298].

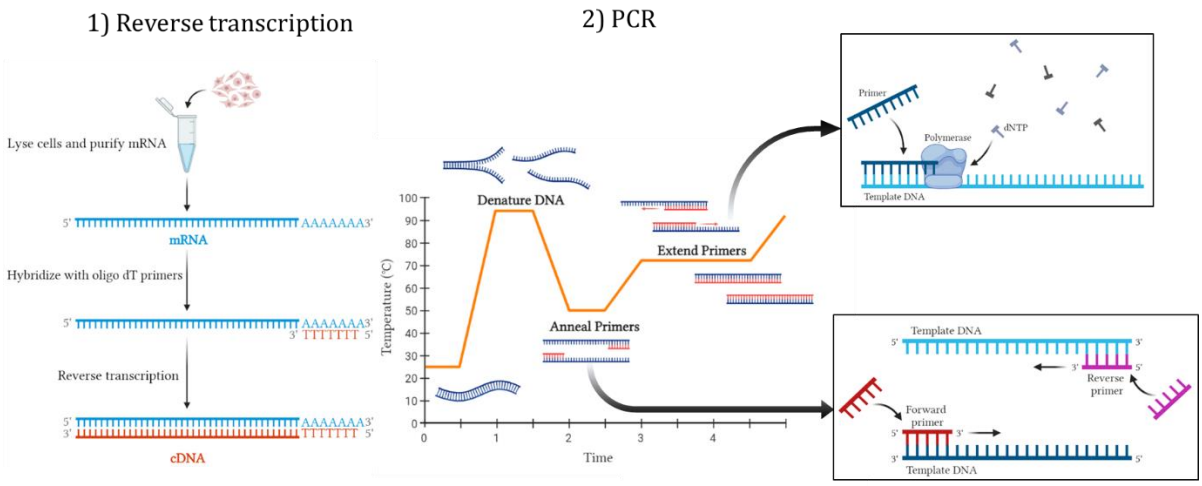

Figure 4.2: Steps for RT-qPCR. The sample RNA is extracted and isolated and converted into cDNA, which is then used as template for the PCR. The cycle is repeated several times until millions of copies of the target sequence are obtained. Created using Biorender.com

In RT-qPCR, the amplification of DNA is monitored by the detection and quantitation of a fluorescent reporter signal, which increases in direct proportion to the amount of PCR product in the reaction. To detect the PCR products in RT-qPCR, several methods have been developed (Taq-Man, LightCycler, LUX…). For this experiments, SYBR green is used. The SYBR Green I is a dye that emits light only when bound to double-stranded DNA (dsDNA). During the PCR, the target sequence is amplified, creating new copies of dsDNA. The dye binds to each one of these new copies, resulting in an increase in fluorescence intensity. It binds to all dsDNA, including non-specific reaction products, which means that a high signal could be due to the amplification of a region that is not the target. To visualise non-specific PCR products, a melting curve analysis can be performed, as different fragments will usually appear as separate distinct melting peaks. Fast loss of fluorescence can be observed at the denaturing (melting) temperature of a DNA fragment, which is unique to that fragment. The melting peak is obtained by plotting the negative first derivative of the fluorescence against temperature [299]. On the other hand, Taqman is a sequence-specific, dually fluorophore-labelled DNA oligonucleotide (one fluorophore is the quencher and the other the reporter). The quencher absorbs the signal from the reporter during amplification. During the extension phase, the DNA polymerase activity making the complimentary strand encounters the probe and breaks it apart, liberating the reporter and allowing it to fluoresce. Because the oligonucleotide only binds to a specific sequence, only when that sequence is replicated the fluorescent signal increases. This makes this method more accurate as it only detects amplification of the desired product, and it also allows to be multiplexed as multiple probes attaching to different regions and with different colours can be combined in the same experiment, reducing the sample usage. However, they require a thorough process for designing the oligonucleotide and they are much more costly than the SYBR Green counterpart [300].

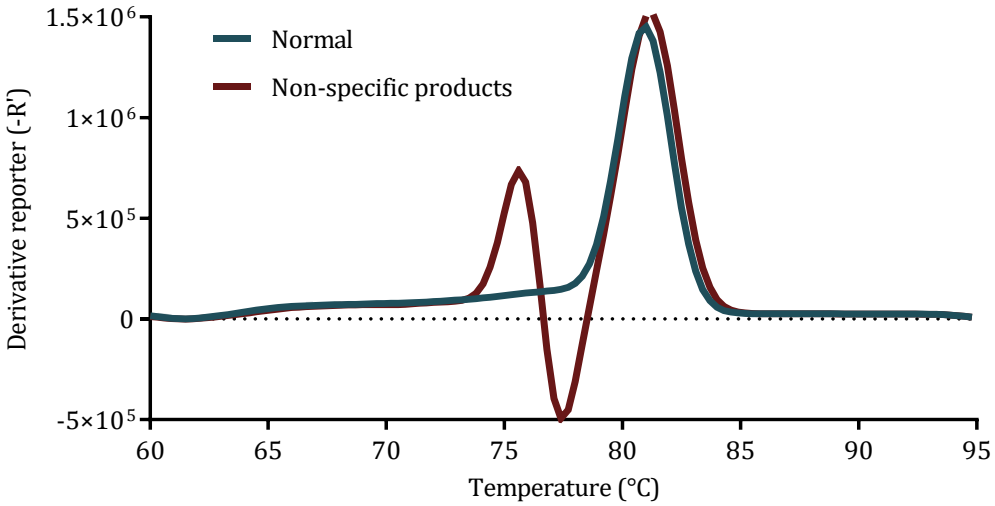

Figure 4.3: Comparison of melting curves with samples containing a single product (green) and a sample with products that are not the target (red).

RT-qPCR is able to monitor the progress of the PCR as it occurs. The data is collected after each cycle, rather than only at the end. In the initial cycles, there is little change in fluorescence signal. This defines the baseline. An increase in fluorescence above baseline indicates the detection of accumulated target. A fluorescence threshold is set above this baseline (around 10 times the baseline value). The parameter C_T is defined as the fractional cycle number at which the fluorescence passes the threshold. The higher the starting copy number of the target, the sooner a significant increase in fluorescence is observed. The efficiency of a PCR eventually drops as a result of either product inhibition, or because the concentration of one of the components becomes limiting. The reaction then enters a linear phase, indicating the end of the PCR. Traditionally, the threshold is set automatically within the exponential phase of the PCR. The ability to quantify the amplified DNA during the exponential phase of the PCR, when none of the components is limiting, results in an improved precision in the quantitation of the target sequences [301].

In this project, the RT-qPCR was performed using QuantiNova RT-PCR kit (#208152, Qiagen N.V.) was used, with SYBR Green as the detection dye and ROX as the reference dye. To prepare the samples for the PCR, two mixtures were prepared: Mix 1 contained the SYBR Green master mix, the ROX reference dye, the Reverse-transcriptase mix and the primer of the target gene. Mix 2 contained the RNA sample diluted in RNase-free water to 20 ng/µL (dilution factor calculated using the values obtain as explained in Section 4.1.6.1). Each target gene required a separate Mix 1, and each biological sample condition required a separate Mix 2. Both mixes were then added to a white v-bottom 96-well plate according to the plate plan. The plate was centrifuged for 20 s to ensure the samples were at the bottom of the wells and then placed in the real-

time cycler (StepOnePlus™ Instrument, Thermofisher). RT-qPCR was performed at 95°C for 2 min, followed by 40 cycles of denaturing at 95°C for 5 s and annealing/extending at 60°C for 10 s. Melting curves were performed to assess the specificity of the reaction (ensure there were no unexpected products), and the results were analysed using the comparative C_T method.

4.1.7.1 Comparative C_T method

Relative quantitation is used to analyse changes in gene expression in a given sample relative to another reference sample (calibrator). This method is most commonly used for quantifying mRNA levels by RT-qPCR and is adequate for most purposes to investigate physiological changes in gene expression levels. In relative quantification, the target gene in the test sample and calibrator is first normalised to the endogenous reference gene, and the normalised values are then compared with each other to obtain a fold difference. The normalised target gene expression in the calibrator is set to 1, and the normalised target gene expression in the test samples is expressed as some n-fold increase or decrease relative to the calibrator. The main advantage of this technique is that the use of than internal standard can minimise potential variations in sample preparation and handling and circumvents the needs for accurate quantification and loading of the starting material [301,302]. There are two relative quantitation methods: the standard curve method, and the comparative C_T method. In the first, the target quantity determined from the standard curve is divided by the target quantity of the calibrator. In the second, an arithmetic formula is used:

First, the cycle threshold value of the target gene is normalised to that of the reference gene, for both the test sample and the calibrator:

$$\Delta C_{T(test)} = C_{T(target,test)} - C_{T(reference,test)} \qquad \textit{Eq. (4.7)}$$

$$\Delta C_{T(calibrator)} = C_{T(target,calibrator)} - C_{T(reference,calibrator)} \qquad \textit{Eq. (4.8)}$$

Then, the ΔC_T of the test sample is normalised to that of the calibrator:

$$\Delta\Delta C_T = \Delta C_{T(test)} - \Delta C_{T(calibrator)} \qquad \textit{Eq. (4.9)}$$

Finally, the normalised expression ratio is calculated using the equation:

$$RQ = 2^{-\Delta\Delta C_t} \qquad \textit{Eq.(4.10)}$$

The comparative C_T method eliminates the need for a standard curve, increasing the throughput.

4.1.8 Statistical analysis

Normal distribution of the data was initially assessed with a Shapiro-Wilk normality test Statistical comparisons were carried out using a one-way ANOVA with Bonferroni correction with *p≤0.05, **p≤0.01, ***p≤0.001, or ****p≤0.0001. Alternatively, statistical comparisons were carried out using a two-tailed unpaired Student's t-test, correction with *p≤0.05, **p≤0.01, ***p≤0.005. Number of replicates for each condition are specified in the figure legends. Measurements are reported as mean ± standard deviation (SD) or standard error of the mean (SEM) as specified in each figure legend.

4.2 Viability assay

Cell health and metabolism are affected by changes in their microenvironment and the presence of physical and/or chemical agents. In order to determine cell responses upon stimuli, there is a need for reliable and reproducible cell viability and cytotoxicity assays. Viability levels and/or proliferation rates of cells are good indicators of cell health. A broad spectrum of cytotoxicity and cell viability assays is currently available. A common classification of assays is according to the measurement type of end points: dye exclusion, colorimetric, fluorometric or luminometric.

In dye exclusion assays, the proportion of viable cells in a cell population can be determined by staining exclusively viable or dead cells. The staining procedure is simple, rapid, and requires a small number of cells, but it is time consuming for large samples. Trypan blue has been extensively used for this purpose. This assay is used to determine the number of viable cells in a cell suspension and is based on the principle that live cells possess intact membranes that do not allow the dye to cross into the cytoplasm, whereas dead cells have permeable membranes which allows the dye to enter the cytoplasm and hence stain blue. Under visual inspection, viable cells have a clear cytoplasm, and dead cells have a blue cytoplasm (Figure 4.1). However, it presents some disadvantages. For example, it cannot distinguish between healthy cells and cells that are alive but losing cell functions, and the amount of information it provides about the condition of the samples is limited [303].

In colorimetric assays, the reagents undergo a colour change in response to the viability of the cells. One of the most common colorimetric assays used in cell biology is the LDH cytotoxicity assay. Quantification of LDH release is a well-established method for cell viability. It provides fast, robust, and reproducible insights into the potential toxicity of experimental compounds. LDH is a cytoplasmic enzyme found in nearly all living cells that catalyses the concomitant interconversions of pyruvate to L-lactate and NADH to NAD+ during glycolysis. It converts pyruvate, the final product of glycolysis, to lactate when oxygen is absent or in short supply. At high concentrations of lactate, the enzyme exhibits feedback inhibition, and the rate of conversion of pyruvate to lactate is decreased. In response to cellular damage, the plasma membrane is compromised, and LDH is released from the cytoplasm into the extracellular environment, so it is commonly used as a marker for injuries and tissue breakdown. Its stability in cell culture medium makes it a well-suited correlate for the presence of damage and toxicity in tissues and cells [304]. Due to the ability of microfluidic devices to have a continuous flow, the effluent can be collected periodically and analysed to assess the health of the tissue samples throughout the length of the experiments. This feature is especially useful when the samples are subjected to challenges, as it is possible to obtain a measurement of the temporal response. For this reason, this assay is particularly common in tissue-on-chip literature [99,119,201,282].

This assay measures the stable, cytosolic LDH enzyme quantitatively: the released LDH is measured with a coupled enzymatic reaction that results in the conversion of a tetrazolium salt into red coloured formazan by the catalyst diaphorase (Figure 4.4). The red formazan absorbs at 492 nm and can be measured quantitatively using a conventional microplate reader. This assay, however, presents some drawbacks, such as the inherent LDH activity of the serum present in the medium, which gives high background readings. This requires the assay to be performed in low or serum-free conditions, limiting the assay culture period, and reducing the scope of the assay as it can no longer allow determination of cell death caused under normal growth conditions [305].

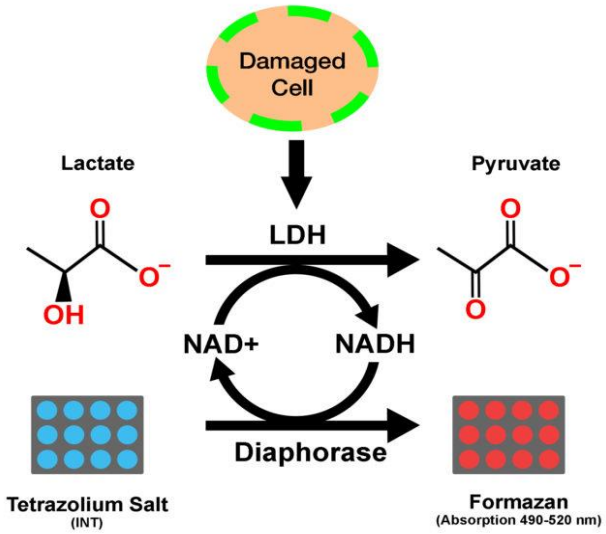

Figure 4.4: Schematic of the reaction converting the tetrazolium salt into formazan to measure the LDH release. From https://www.cephamls.com/ldh-cytotoxicity-assay-kit-colorimetric-2/

In this work, the ability of the LDH assay to monitor cell/tissue viability in the developed devices (presented in 3.3) was tested. HeLa cells were cultured in T25cm^2 flasks at 37°C and 5% CO_2 until the cells were confluent. Then, lysis buffer was added in a 1:10 ratio to the total volume to obtain the maximum LDH release. After 45 minutes of incubation time with the lysis buffer, an aliquot was transferred into a tube and centrifuged at 300 x g for 5 min to remove debris, before performing a 1 in 2 serial dilutions to obtain the reference curve. In the results presented in Figure 4.5, it can be observed that the absorption of the assay saturated at the higher concentrations of LDH release, and there were no clear differences in the cytotoxicity of the reference curve above 50% (calculations shown in Section 4.1.3). Furthermore, large variability in the optical densities measured were also observed for experiments with the same number of cells, which could indicate saturation of the assay, i.e., too many cells for the amount of reagent. This could lead to large calculation errors in the subsequent experiments; thus, it was decided to investigate other viability assays. This assay, however, could be used in the future, but taking into account that the

samples would need to be diluted in order to avoid saturation of the assay. It was also observed that the signal was reduced when the samples were frozen after collection for analysis on a different day (Figure 4.6). This feature would be particularly convenient to reduce the length of each experiment and optimise the number of assays run. However, as already observed previously by others [306,307], the LDH enzyme loss its activity after the samples were frozen and thawed.

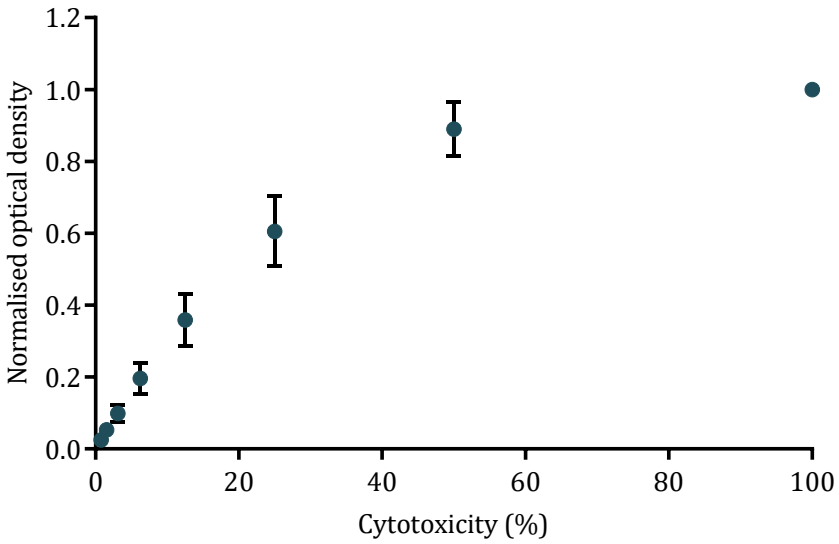

Figure 4.5: Cytotoxicity reference curve for the LDH assay. Data are mean ± SD, n=5.

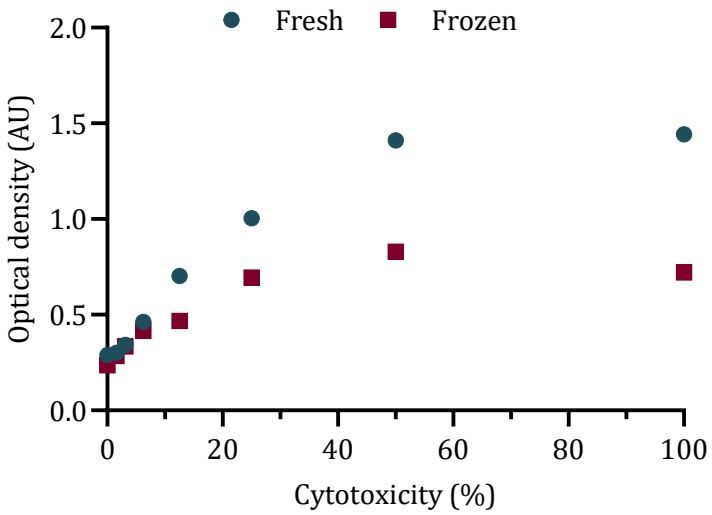

Figure 4.6: Comparison of reference curve for fresh and frozen samples. N=1.

Fluorometric assays are easy to perform and present some advantages over the previously explained assays, primarily, their higher sensitivity. The resazurin reduction assay is based on the conversion of the blue non-fluorescent dye resazurin into the pink resorufin by accepting an electron from the mitochondrial respiratory chain in live cells (Figure 4.7). Resazurin is a phenoxazine-3-one dye and a cell permeable redox indicator that can be used to monitor viable cell

numbers. It is a non-toxic and cell permeable compound. Viable cells convert continuously resazurin into resorufin, which is released from the cell and results in increased overall fluorescence of the cell culture medium. The quantity of resorufin produced is directly proportional to the aerobic respiration rate of the cells, which is generally correlated to the number of viable cells. The amount of resorufin can be measured with a conventional microplate reader (Ex/Em = 530-560/590 nm) by absorption or fluorescence, the latter being the most common due to the higher sensitivity of fluorescent measurements over absorption detection. The incubation period required to generate a sufficient fluorescent signal is usually between 1 and 24 hours, and it depends on the metabolic activity of the cells, the cell density, and other factors such as the culture medium type. This assay is relatively inexpensive and more sensitive than tetrazolium-based assays. It can also be multiplexed with other methods to gather more information.

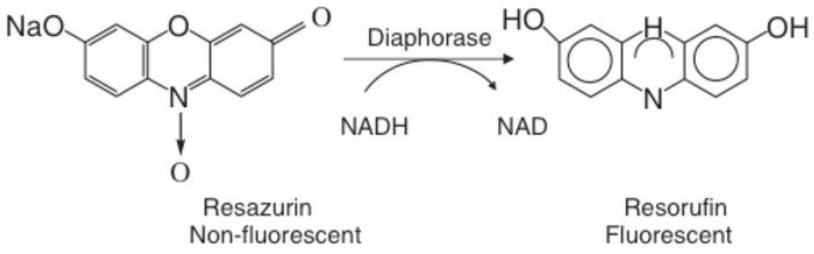

Figure 4.7: Reduction reaction of resazurin into resorufin due to the mitochondrial respiration of metabolically active cells.

As previously mentioned, resazurin is converted into resorufin as a result of cellular respiration. An in-house resazurin reagent was prepared instead of using a commercial one by diluting resazurin salt in sterile PBS (further details in Section 4.1.4). The optimal incubation times and ratio of resazurin reagent to total volume were initially investigated. For this, cells were seeded in conventional 24-well plates at 100,000 cells per well (~50,000 cells/cm^2) and cultured for 24 h in complete medium. The supernatant was then removed and replaced with serum-free medium for another 24 h. After that time, the resazurin reagent was added at different ratios (1:5, 1:10 and 1:20) to the wells, and the plate was placed inside a microplate reader with temperature control (Fluostar Optima, BMG Labtech). The intensity in each well was measured every hour for 7 h (Ex/Em = 560-10/590 nm). The results in Figure 4.8 show the evolution of the signal over time. The measured intensity increased with the incubation time until it saturated after around 4 h due to the depletion of the resazurin present in the well, as it was converted into resorufin. Longer incubation times were investigated but this led to errors in the viability measurements, especially at higher cell densities. The differences in the value of the maximum signal for each reagent ratio can also be observed in Figure 4.8c. As expected, there was a proportional relation between the resolution and the reagent ratio, as well as with the incubation time. After 4 h of incubation, the resazurin did not improve significantly due to the saturation of the signal. The

resolution was calculated by subtracting the background values (controls with no cells) to the measured signal and divided by the number of cells.

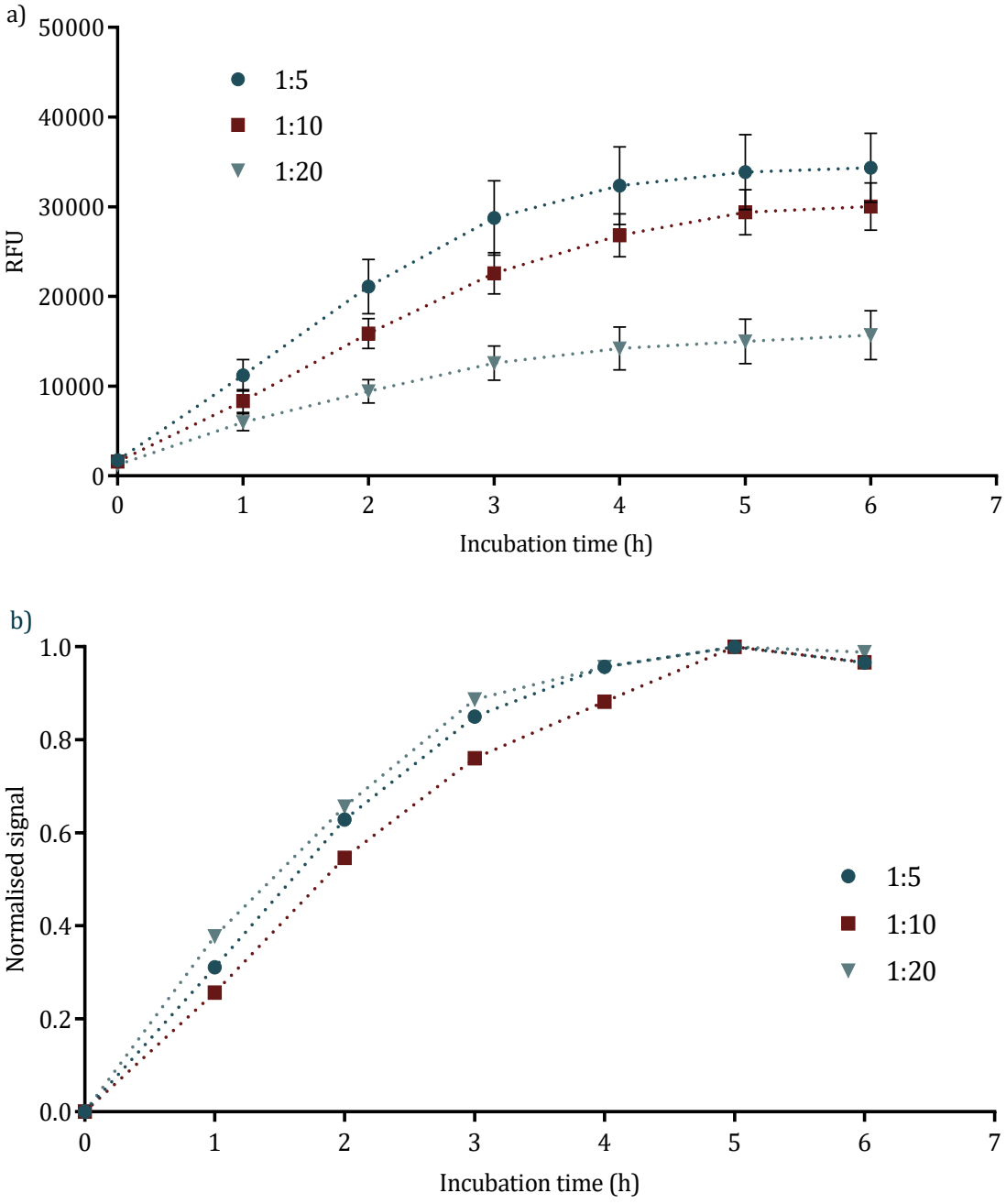

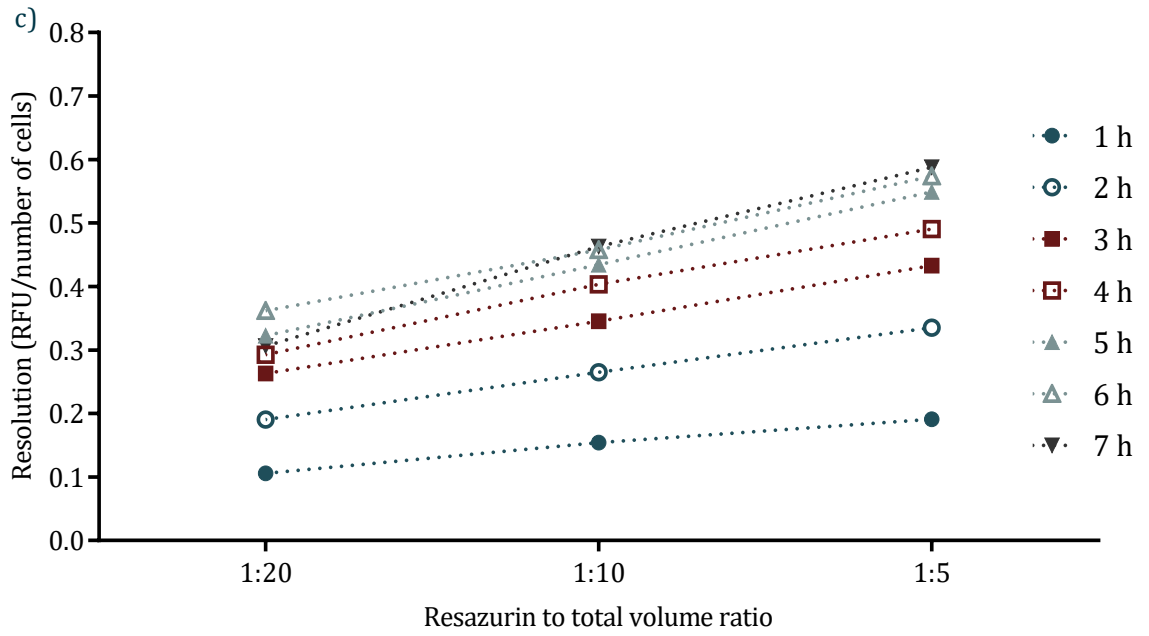

Figure 4.8: a) evolution of the fluorescence signal of the resazurin assay with incubation time. Data represents mean ± SD. b) normalised signal to compare the changes for the different ratios tested. c) the evolution of the resolution over time for the reagent ratios. Data represents mean; SD are not plotted for clearer visualisation of the results but variability is maintained as in the top graph. n=3

The optimal incubation times and reagent ratios over multiple cell densities were also studied. In this case, the cells were plated at multiple concentrations (1 in 2 serial dilutions to generate a standard curve) and incubated for 24 h at 37°C and 5% CO_2, after which the supernatant was removed and replaced with serum-free media. After a further 24 h of incubation, the resazurin reagent was added in different ratios (1:5, 1:10 and 1:20), placed in the microplate reader with controlled temperature, and measurements of the fluorescent signal were taken every hour for 6 h (Ex/Em = 560-10/590 nm). The results show a linear relationship between the signal collected and the number of cells on the wells for reagent ratios of 1:5 and 1:10, but not for a ratio of 1:20 (Figure 4.9a). This was due to the faster depletion of the resazurin present in the well for the higher cell densities. The linearity of the standard curve was analysed by performing a linear interpolation of the values and evaluating the goodness of the fit by calculating the R^2 value. The linearity was maintained for the first two ratios over the entire experimental time, but it noticeably worsened for the lowest ratio (Figure 4.9b). Given the good linearity even at the shortest incubation time (1h) and with a reagent ratio of 1:10, these parameters were established as the protocol from then on. In this manner, the assay time was reduced, and the reagent consumption was minimised.

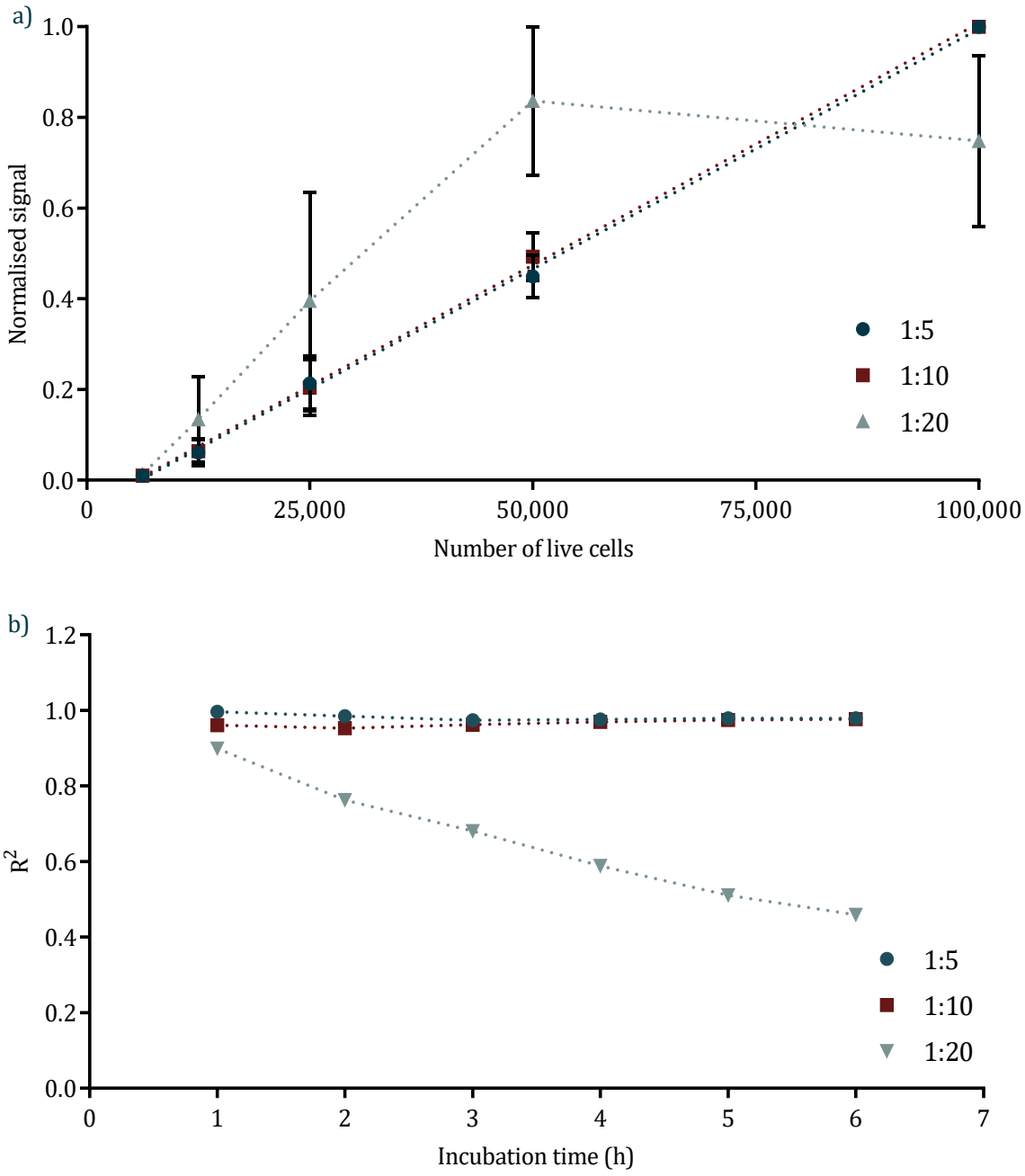

Figure 4.9: a) standard curves at multiple reagent ratios. Values plotted represent the mean ± SEM for n=3. The linearity is maintained as shown by the plot below (b) of the R^2 values. Data represents mean for n=3.

These results also show the linearity of the standard curve using the resazurin assay compared to the results from the LDH assay discussed previously (Figure 4.5). The differences between these two assays were further tested by challenging the cells with hydrogen peroxide (H_2O_2). Cells were plated at 40,000 cells/cm² in a 24-well plate and incubated for 24 h at 37°C and 5% CO_2. The media was switched to serum-free and the H_2O_2 was added in multiple concentrations (0.1 µM to 10 mM in 10-fold increases) and incubated for another 24 h. Subsequently, the effluents were collected for the LDH assay and the resazurin assay was added at a 1:10 ratio to the total volume and incubated for 1 h. The untreated control was lysed to obtain the maximum

LDH release for the reference curve. The results are plotted together in Figure 4.10. The resazurin assay showed a typical concentration response curve for H_2O_2 treatment, whereas the LDH assay showed misleading results with lower cytotoxicity at the highest H_2O_2 concentration tested. This was misrepresentative as all the cells were dead under the microscope and the LDH release should be maximum; however, as seen in Figure 4.5, the assay saturated at higher cytotoxicity levels, which could lead to large calculation errors and misleading results. Furthermore, LDH activity could have been affected by the presence of the hydrogen peroxide [308,309]. It was decided to use the resazurin assay as the preferred method to measure viability for this project.

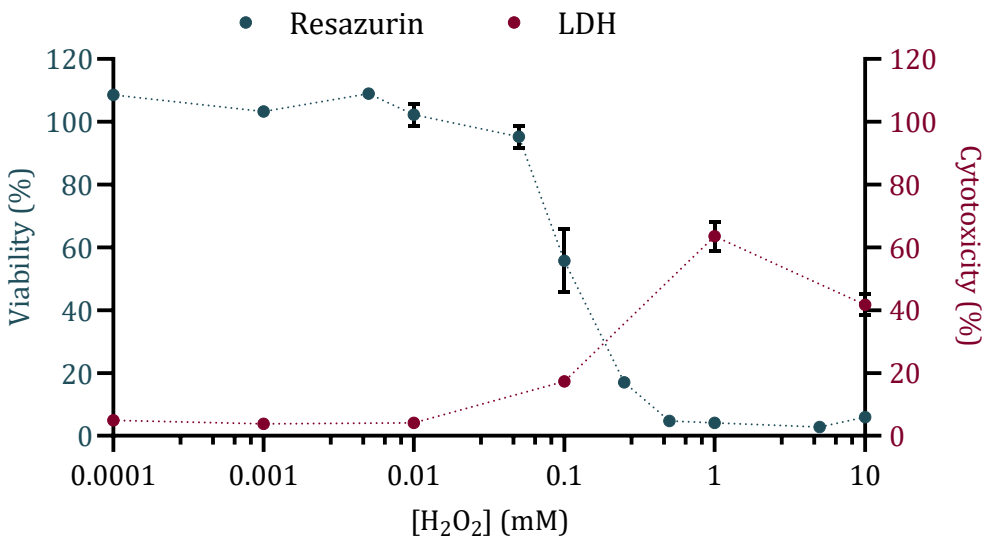

Figure 4.10: Response curves to increasing H_2O_2 concentrations using the resazurin and LDH viability assays to observe the differences in sensitivity between the assays. Data points represent mean ± SD, n=4 and 2 respectively.

In the experiments presented so far, the assay reagent was added in the wells and the plate containing the cells with the assay was placed in the microplate reader machine to perform the measurements. This would not be possible when the cells are cultured in the developed devices, as the device would not fit in the machine. To test if it was possible to adapt the viability assay to the devices, cells were plated and cultured in standard 24-well plates as explained above. After the resazurin reagent was added, instead of transferring the plates to the microplate reader, aliquots of supernatant were taken every hour. The culture plate was placed back in the incubator between measurements. These aliquots were then plated in a 384-well plate and the fluorescence intensity was measured in the same manner as in the previous experiment. The results showed a comparable response between both methods, with a noticeable reduction of the error with the new method (Figure 4.11). This could be due to the change from optically transparent well plates in the first case, to black well plates in the second, which increase the sensitivity of the measurements due to the reduction in light reflection and interference from adjacent wells. These results

showed that this viability assay could be used in the devices under continuous perfusion as the assay could be added into the chambers and the effluents could be collected and measured offline, while maintaining the samples in the incubator, and reducing the disruption.

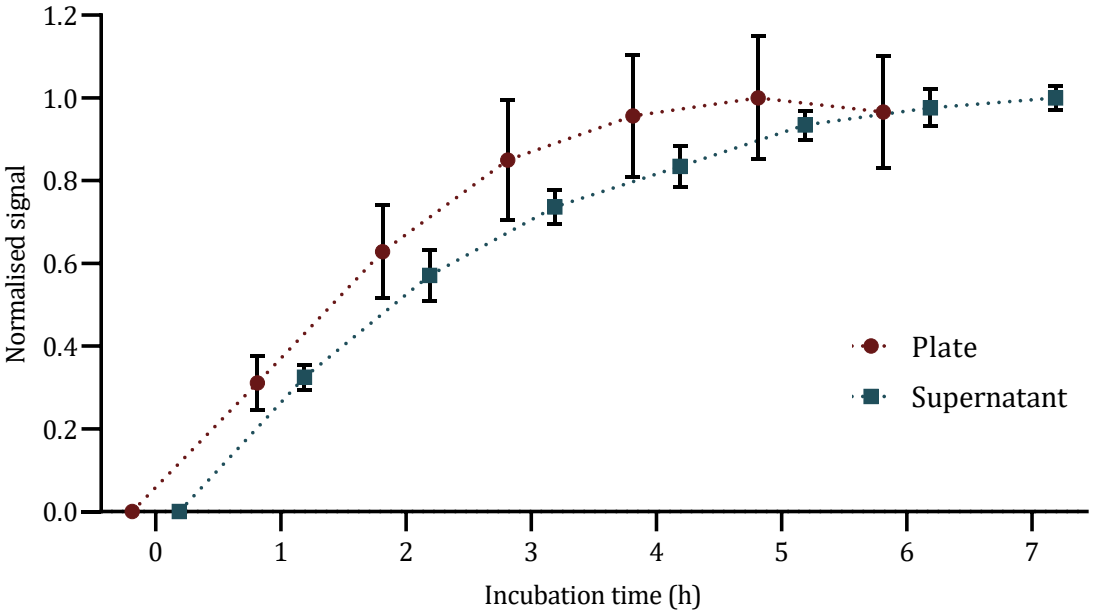

Figure 4.11: Comparison between the signals measured directly from the well plates containing the cells or taken from the aliquots of the supernatants. Data represents mean ± SEM, n=3.

4.3 Media optimisation

4.3.1 Choosing the media formulation

The cell culture environment is crucial for the survival of the tissues, and it can influence their health, viability, and responses to changes and challenges. The cell culture medium has the ability to manipulate the physicochemical and physiological environment in which the cells are cultured. Therefore, it is vital to choose the correct culture media. Standard culture media for continuous culture of OHIO HeLa cells is Dulbecco's Modified Eagle's Medium (DMEM– high glucose, #D5671, Sigma-Aldrich) as a base medium supplemented with 10% Foetal Bovine Serum (FBS, #F9665, Scientific Laboratory Supplies), 1% Penicillin/Streptomycin (5,000 U/mL of penicillin and 5000 µg/mL of streptomycin, #15070063, ThermoFisher) and 1% GlutaMax (#11574466, Fisher Scientific), and will be here referred to as complete DMEM (cDMEM). This medium requires of a gaseous environment of 5% CO_2 to equilibrate the pH. Biological processes are extremely sensitive to pH, as it modulates the activity of proton-dependent transporters present on cells and influences the interaction and functionality of lipids and proteins. Therefore, pH in the culture media must be balanced and stable. Most mammalian cell lines require a pH value of 7.4. Buffering systems are used to avoid significant pH changes of the culture media. The most common buffering system nowadays is the bicarbonate/CO_2, which mimics the main buffer system in organisms and minimises toxic side effects. The CO_2 dissolves in the medium, forming carbonic acid as it reacts with water, and then that carbonic acid establishes an equilibrium with the HCO_3^- ions contained in the medium, lowering the pH. Simultaneously, the additional HCO_3^- ions react with protons present in the medium, increasing the pH (Figure 1.16). In this system, it is required to keep the cultures in an artificial 5% CO_2 environment inside an incubator. However, the devices developed for this project weremade of a gas-impermeable material to avoid the diffusion of oxygen into the chambers (Section 3.3.1). This also means that the diffusion of CO_2 is limited, and therefore the pH equilibration mechanism is hindered. For this reason, other ways to maintain the desired pH were sought. Another common buffering system is the addition of 4-(2-hydroxyethyl)-1-piperazinetanesulphonic acid (HEPES) to the culture media. HEPES is a zwitterionic sulphonic acid, i.e., it contains an equal number of positively and negatively charged functional groups, so it can act as a base or an acid, reacting and neutralising any base or acid added to the medium, and keeping the pH stable. It is water soluble, has low cell membrane permeability, high chemical stability, and the concentration, temperature, and ionic composition of the medium in which it is added has minimal effect on its buffering capacity.

An alternative medium composition designed for use in closed containers or in equilibrium to the atmospheric air was chosen: Minimum Essential Medium (MEM) with Hank's salts

(#M5775, Sigma-Aldrich). To guarantee the maintenance of pH within the chambers, the optimal concentration of HEPES to add to the medium was first investigated. MEM culture media with increasing HEPES concentrations were plated without cells in conventional well plates and placed in an incubator at 37°C and atmospheric CO_2. After 24 h, the volume of the corresponding well was collected, and the pH was measured using a pH sensor (InLab Micro, Mettler Toledo). The results showed a high pH for the medium without HEPES, and a constant level for the wells with HEPES of around 8.6. This was due to the lack of CO_2 or buffer for equilibrating the pH (See Figure 1.16). The value at which each media composition stabilised depended on the concentration of HEPES, decreasing said value for higher HEPES concentrations. It has been reported that HEPES, when exposed to ambient light, produces hydrogen peroxide [310] which can lead to toxic effects on the cultures. Therefore, the chosen concentration was 15 mM as it was the lowest possible concentration able to maintain the pH between 7.4 and 7.6. The complete formulation for this medium consisted of MEM (with Hank's salts), 10% FBS, 1% Penicillin/Streptomycin, 1% L-glutamine (200 mM, #25030024, ThermoFisher), 1% Non-essential amino acids (NEAAs, 100X, #11140035, ThermoFisher) and 1.5% HEPES (1 M stock, #H0887, Sigma-Aldrich), which will be referred to as complete MEM (cMEM).

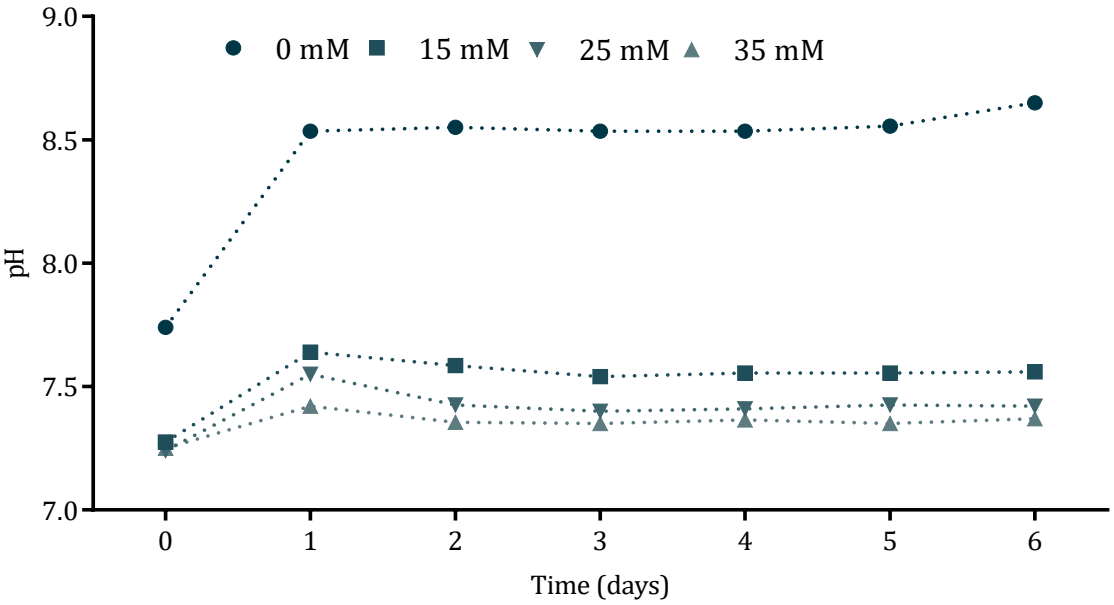

Figure 4.12: pH evolution over several days for different HEPES concentrations. Data represent mean; n=2.

HeLa cells were subcultured in parallel several times in both cDMEM and cMEM media in T25cm^2 flasks to observe the differences between them. As can be observed in the images of the cultures, the cells in cMEM had a much slower growth rate (Figure 4.13, left), with stellated shape and not forming adherences.

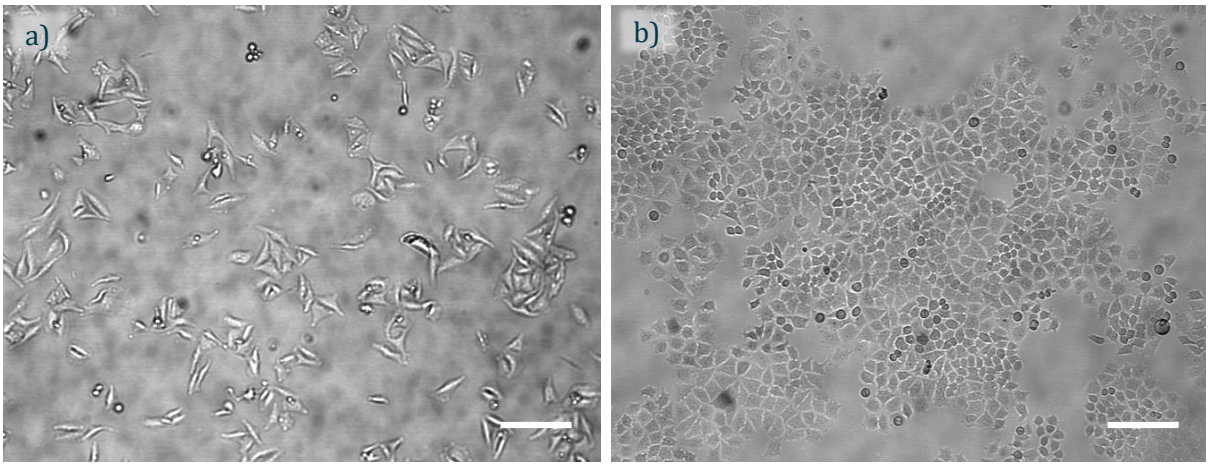

Figure 4.13: Microscope images of HeLa cells cultured in a) cMEM or b) cDMEM in T25cm² flasks. The same number of cells was seeded in each flask and the pictures were taken after the same culture time (3 days postseeding) for direct comparison. Differences in the shape and confluence can be observed. Images representative of 12 and 22 experiments respectively. Scale bars represent 100 µm.

Due to the poor viability and slow growth under the cMEM medium, a different media composition was studied. Leibovitz L-15 medium is a CO_2-independent medium formulated to facilitate the maintenance of cell cultures even in the absence of an incubator, and it was mainly used for transportation of cells and tissues. Its buffering capacity is mediated by phosphates and free-base amino acids instead of sodium bicarbonate. The metabolism is maintained by galactose due to the total lack of glucose present, and pyruvate is added to enable the cells to increase their endogenous CO_2 production, making it independent of exogenous CO_2. It is also formulated with modified Hank's salts with double the concentration of magnesium salts to promote cell growth. This media (#11570396, Fisher Scientific) was supplemented with 10% FBS, 1% Penicillin/Streptomycin, 1.5% HEPES (1 M) and 3% vitamins (MEM Vitamin Solution 100X, #11120037, ThermoFisher), referred to from here on as complete L-15 (cL-15). Vitamins were added to match as closely as possible the formulation of the cDMEM (comparison between media in Appendix 3). HeLa cells were subcultured several times in both cDMEM and cL-15 media in T25cm² flasks in parallel to observe the differences between them.

Figure 4.14 shows the differences in growth rates in the different media (as explained in Section 4.1.2). The growth rates for cMEM, cL-15 and cDMEM were 0.356, 0.5761 and 1.07 divisions per days respectively, which meant that the time the cells required to double the population was 2.81, 1.74 and 0.93 days respectively. The difference in viability after each passage was also noticeable, with much higher viabilities for cL-15 (87%) and cDMEM (90%) than cMEM (79%) media. It was decided to use cL-15 for the experiments on-chip from then on as the viability was high and, even if the growth rate was slower, the cells maintained their morphology and formed adherences.

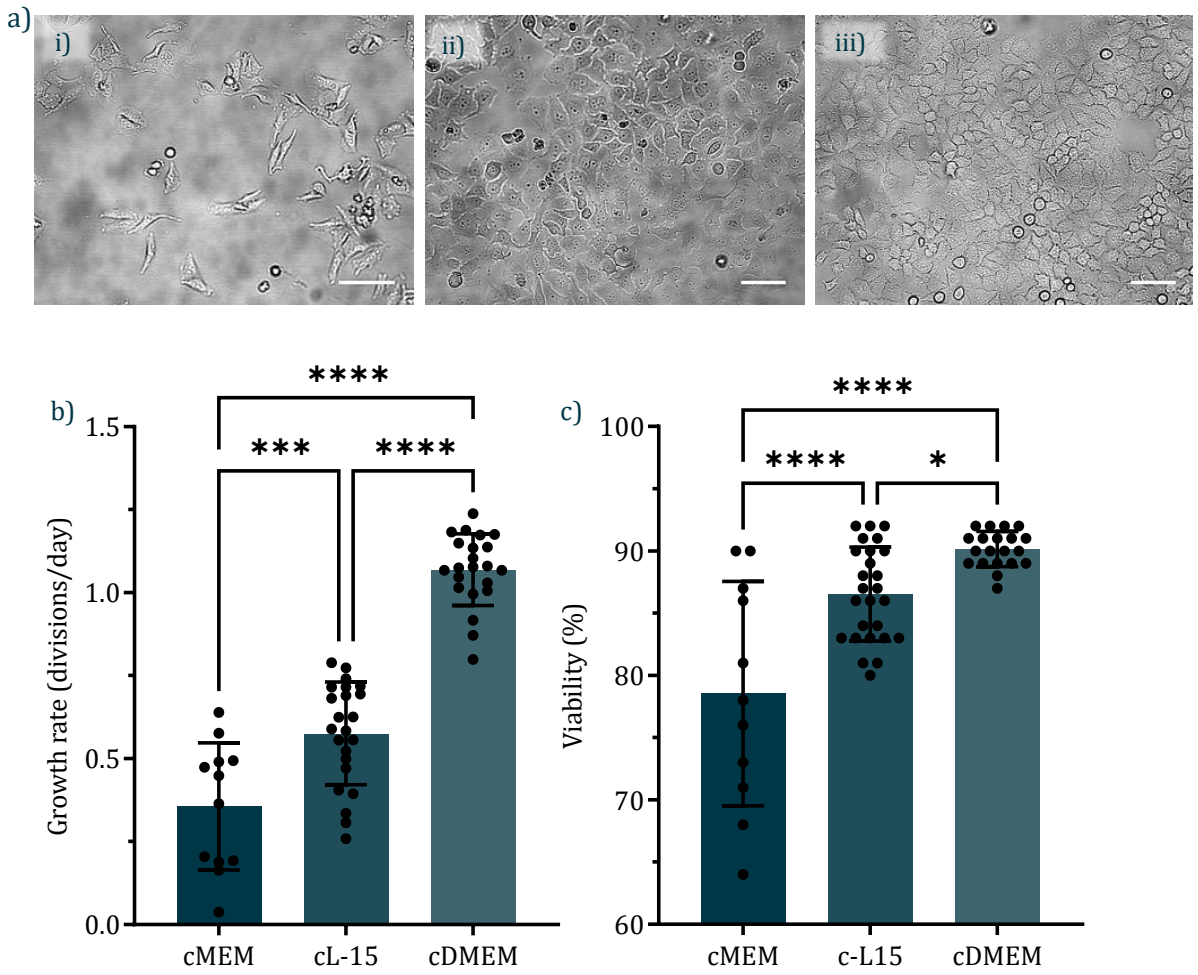

*Figure 4.14: a) Microscope images of the HeLa cells culturedin i) cMEM, ii) cL-15 or iii) cDMEM in T25cm² flasks. The same number of cells was seeded in each flask and the pictures were taken after the same culture time for direct comparison (3 days postseeding). Differences in the shape and confluence can be observed. Images representative of 12, 23 and 22 independent experiments for (i), (ii) and (iii) respectively. Scale bars represent 200 µm. Below, growth rates (b) and viability (c) for each culture media. Results represent mean ±SD. Experimental replicates are plotted individually as dots. From left to right, n=12, 23 and 22. Normal distribution of data was confirmed by a Shapiro-Wilk normality test and significance between groups was determined by a one-way ANOVA with Bonferroni correction were *p≤0.05, **p≤0.01, ***p≤0.001, or ****p≤0.0001.*

4.4 Material compatibility

Once the culture medium able to maintain the cells at a constant pH without the need of equilibration with an external gas was established, the compatibility of the cells with the materials used for the fabrication of the device was tested. As explained in Section 3.3, device v3 was fabricated in PMMA, and the chambers were sealed with a glass slide. The oxygen sensors were deposited on the substrates as explained in Section 3.4.1.1. The substrates of conventional well plates were modified by adding PMMA covers, collagen coatings and including the oxygen sensor, and combinations of these. The cells were seeded at 50,000 cells per well with 1 mL of fresh cDMEM for 24 h in the incubator at 37°C with 5% CO_2. Images of all the conditions were taken to visually analyse the changes in cell morphology as well as assessing the viability in each condition with the resazurin assay. Untreated wells (polypropylene plastic) were used as the controls for reference. The results are shown in Figure 4.15. Good cell attachment and coverage of the substrates can be observed in PMMA covered wells as well as in the collagen-coated PMMA wells (Figure 4.15b-c). However, few cells were adhered to the oxygen sensors (Figure 4.15d). This reduced cell number could be due to the toxicity of the oxygen-sensitive dye or to the hydrophobicity of the PDMS polymer in which the dye is embedded, that prevents cells from adhering. The overall viability of the wells with the oxygen sensor did not show significant differences with the untreated wells (Figure 4.16) because the oxygen sensor only covered a small portion of the substrate, mimicking the situation in the culture chambers (Figure 3.29). The high overall viability indicated that only the cells in contact with the sensor were affected, whilst the rest remained healthy (not shown in the images). This was slightly improved by coating the sensors with collagen (Figure 4.15f). This was further confirmed by the viability assay (Figure 4.16) which showed that, despite good adherence to the substrate, there were less viable cells present in the PMMA covered wells. Viability was calculated as the number of live cells measured with the resazurin assay as explained above compared to the number of live cells measured in the control. This could be due to a slower growth rate or a change in the cells behaviour due to the sudden change of the properties of the substrate. The addition of the sensors further reduced the number of viable cells in the well. In all conditions, the addition of collagen coating increased cell viability. Even if the number of live cells was lower, the good adherence of the cells to the PMMA substrates coated with collagen proved the compatibility of the chosen fabrication materials with the cell culture.

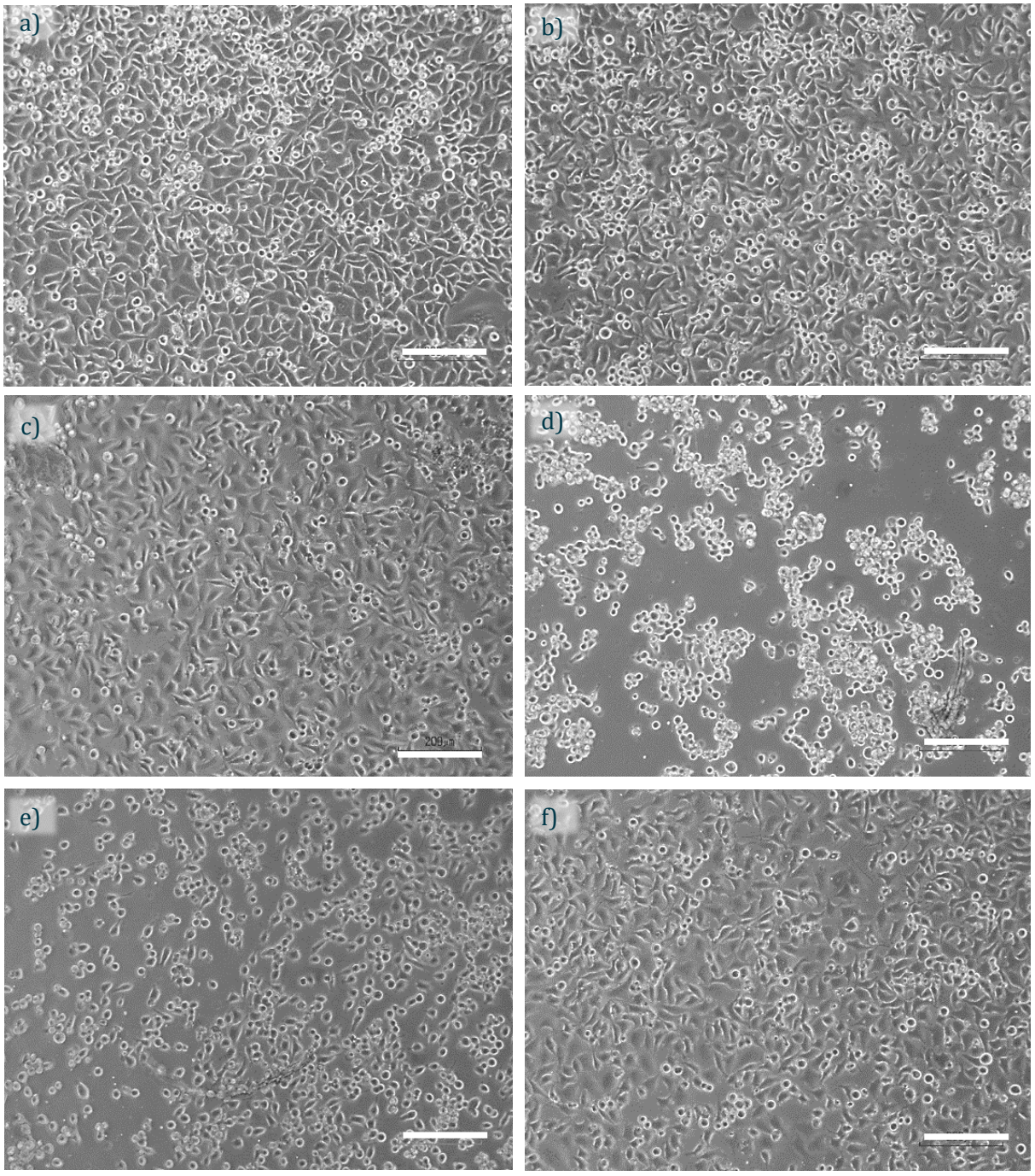

Figure 4.15: Microscope images of the HeLa cells cultured in conventional well plates with modified substrates a) untreated control, b) PMMA, c) PMMA coated with collagen, d) Oxygen sensor (only cells in contact with the sensor have been imaged here), e) PMMA + sensor and f) PMMA coated with collagen + sensor. Differences in the shape, adherence and confluence can be observed. Images representative of 3 experiments. Scale bars represent 200 µm.

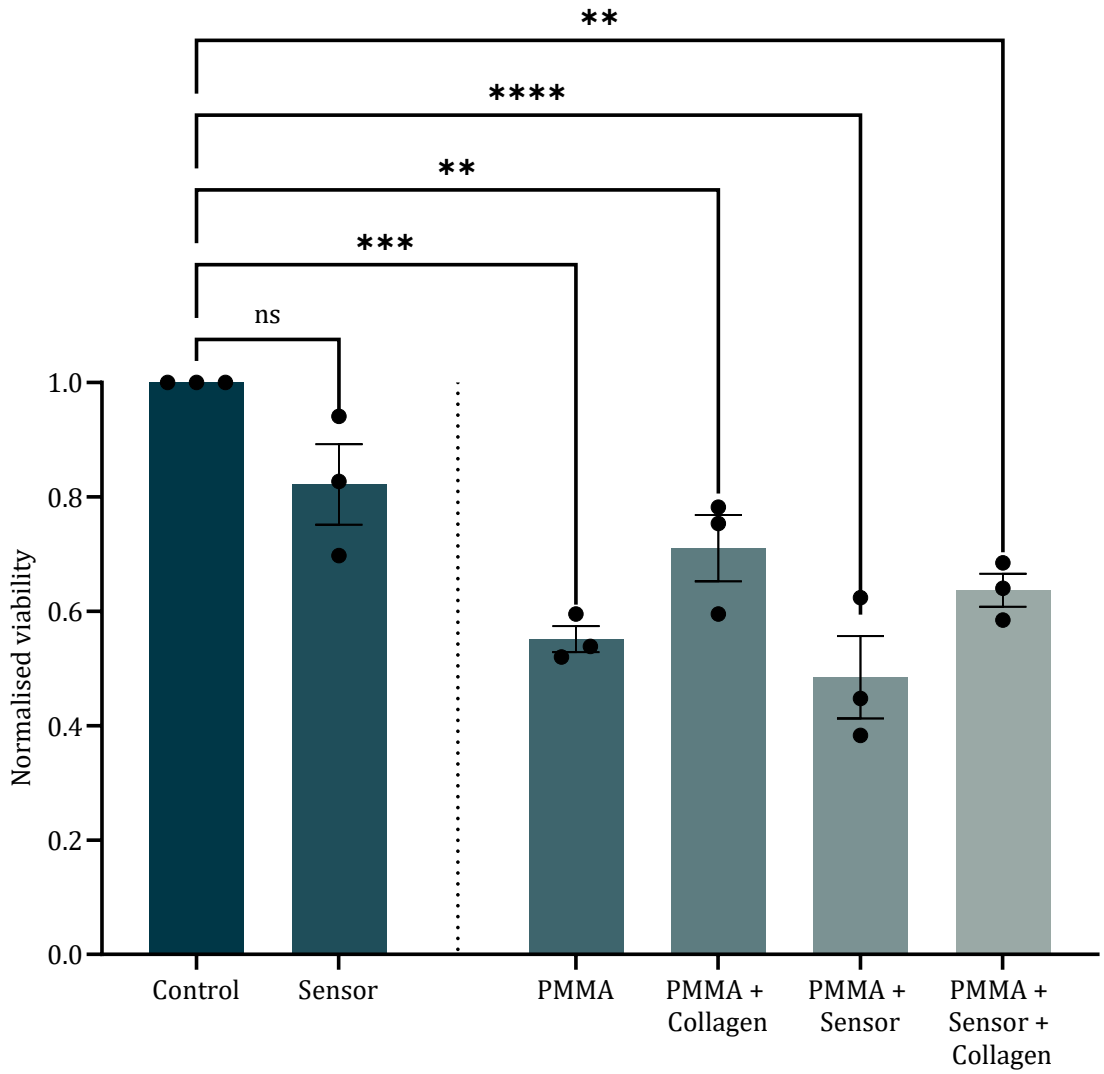

*Figure 4.16: Viability of the cells in each substrate condition normalised to the control (untreated substrate). Bars represent mean ± SEM. Experimental replicates are plotted individually as dots, n=3. Normal distribution of data was confirmed by a Shapiro-Wilk normality test and significance between groups was determined by a one-way ANOVA with Bonferroni correction were *p≤0.05, **p≤0.01, ***p≤0.001, or ****p≤0.0001.*

4.5 Cell culture on-chip

The ability to grow cells on the materials and with a CO_2-independent media was proven for our chosen cell line, and therefore the next step was to culture the cells on the developed devices and optimise the preparation and culture conditions. The first step was to develop a protocol for cleaning and disinfecting the devices. After the assembly of the chip on the chip holders with the O-rings, the hydraulic tightness was tested as previously described (Section 3.3.2) by immersing the closed system in soapy water and pressurising the chambers to observe leaks. The sealed system was then placed in a Microbiological Safety Cabinet (MSC) and the chambers were cleaned by flushing 1:50 bleach in water and incubated for 20 minutes, after which the chambers were rinsed with sterile deionised water (dH_2O) followed by Hanks Balanced Salt Solution (HBSS, #H9394, Sigma-Aldrich) and finally with cL-15 to prime the device before cell seeding. The cells were prepared in the same manner as for normal subculture (see Section 4.1.1) to a cell suspension of 100,000 cells/mL prior to loading them into 1 mL syringes and flushed them through the chambers of the device manually. Given that the volume of the chambers was around 300 µL, the final cell number in each chamber was around 30,000 cells, and an equivalent concentration was prepared and seeded in static well plates as controls. After leaving the cells to adhere for 30 minutes, the flow of fresh media was started at 5 µL/min. After 24 h of culture with continuous perfusion, the cells were imaged to assess their health. A picture of the cells in a standard static well plate was also taken as a control for comparison. In Figure 4.17a, it can be clearly observed that the cells inside the chambers were rounded in shape and not attached to the substrate and in some cases the compromised membranes could also be observed. Therefore, it was necessary to study the cleaning and seeding protocol to establish where the issues were.

First, the seeding method was assessed and results are shown in Figure 4.17b-d. Cell suspensions and devices prepared as previously described were seeded into static well plates by 1) normal pipetting (control); 2) using a syringe connected to a piece of PTFE tubing, to test if the cells were disturbed by the stress caused by the transfer into a syringe and the pushed through the tubing; and 3) flushing the cells through the device and collecting them, then plating them via pipetting, to test if the cleaning protocol affected cell viability. Cells in all the conditions were cultured for 24 h at 37°C and imaged after that time. The images (Figure 4.17b-d) showed that the cells displayed good morphology and attachment of the cells to the substrates (assessed visually), which proved that the cells were not affected by the tubing, and that the devices were sterile and did not introduce infections, and therefore, the seeding protocol did not affect the cells. However, differences in the cell densities were observed, which could be attributed to dead volumes or different material affinities of the seeding methods (tubing, syringes, PMMA), which could lead to a loss of cellular material in the seeding process. The images showed the presence

of debris in the wells with cells that were flushed through, so an additional cleaning step was added to sonicate the devices before mounting them on the holders to remove this debris. Although the compatibility of the cultures with the materials was already tested, cells were seeded in open devices (not mounted on the holders) by normal pipetting and left inside a petri dish for 24 h, to test that there were no issues with the final fabricated device either. Confluent and viable cells were observed after 24 h of culture, so any problems with the seeding method or the devices were discarded (Figure 4.17e).

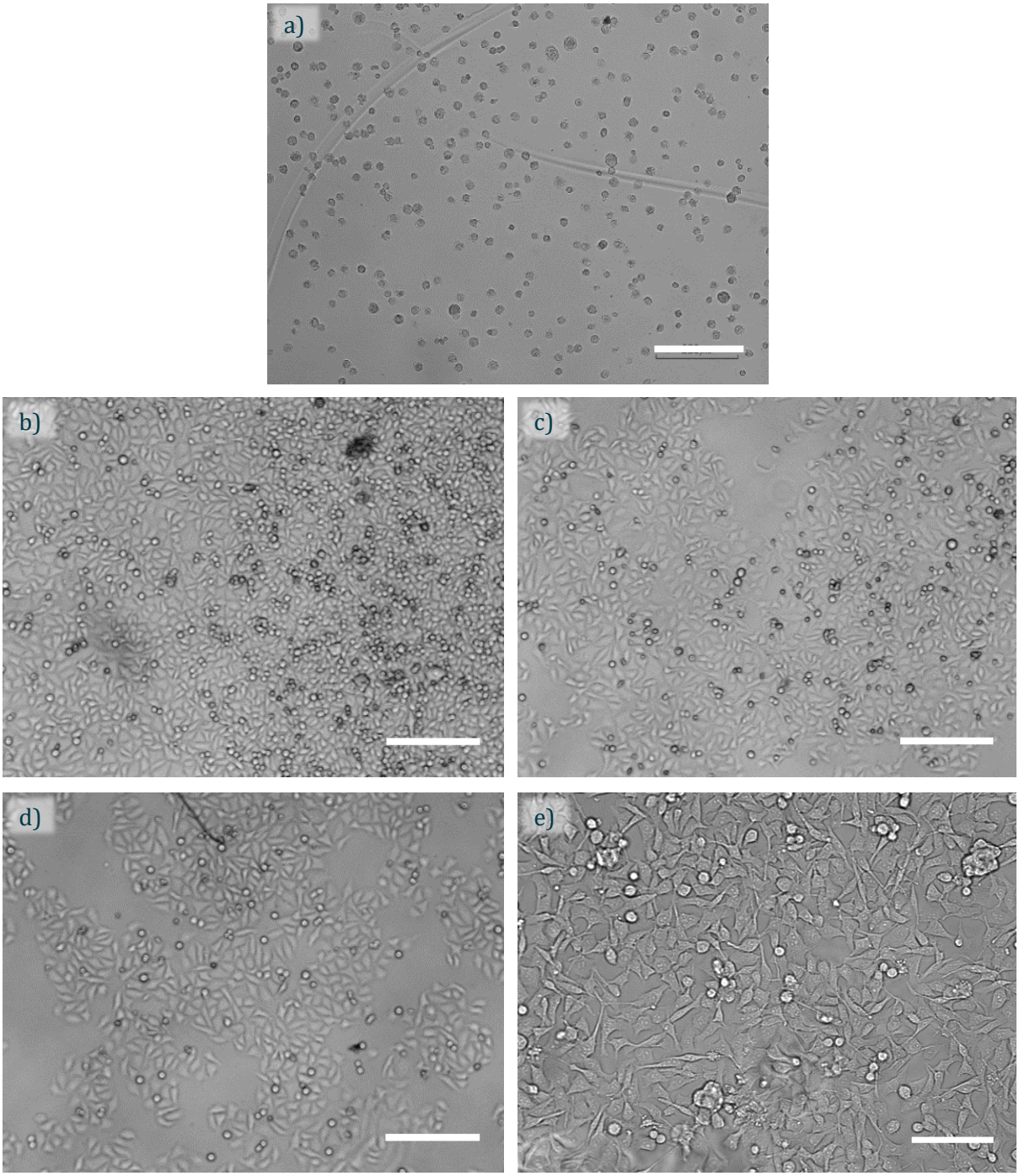

Figure 4.17: Microscope images of the HeLa cells cultured in conventional well plates with different seeding methods. a) Cells on the chip, b) traditional pipetting, c) cells transferred into a syringe and plated via a piece

of tubing, d) cells flushed through the device, collected then plated, and e) cells seeded in the unmounted chip via traditional pipetting. Images representative of 1 experiment. Scale bars represent 200 µm.

Next, the cell density at which the cells were seeded for subsequent experiments was optimised. Cell suspensions at 100,000, 120,000, 150,000 and 180,000 cells/mL were prepared, seeded into the devices and left to adhere for 30 min with no flow. This equated to around 30,000, 40,000, 50,000 and 60,000 cells per chamber respectively. The cells were cultured for 24 h at 37°C with continuous perfusion of fresh media at 5 µL/min. It was observed that, when the seeding density was increased, more live and attached cells could be seen in the devices (Figure 4.18). A cell density of 60,000 cells per chamber was selected and used from then on as it gave a good coverage of the substrates without reaching over confluence.

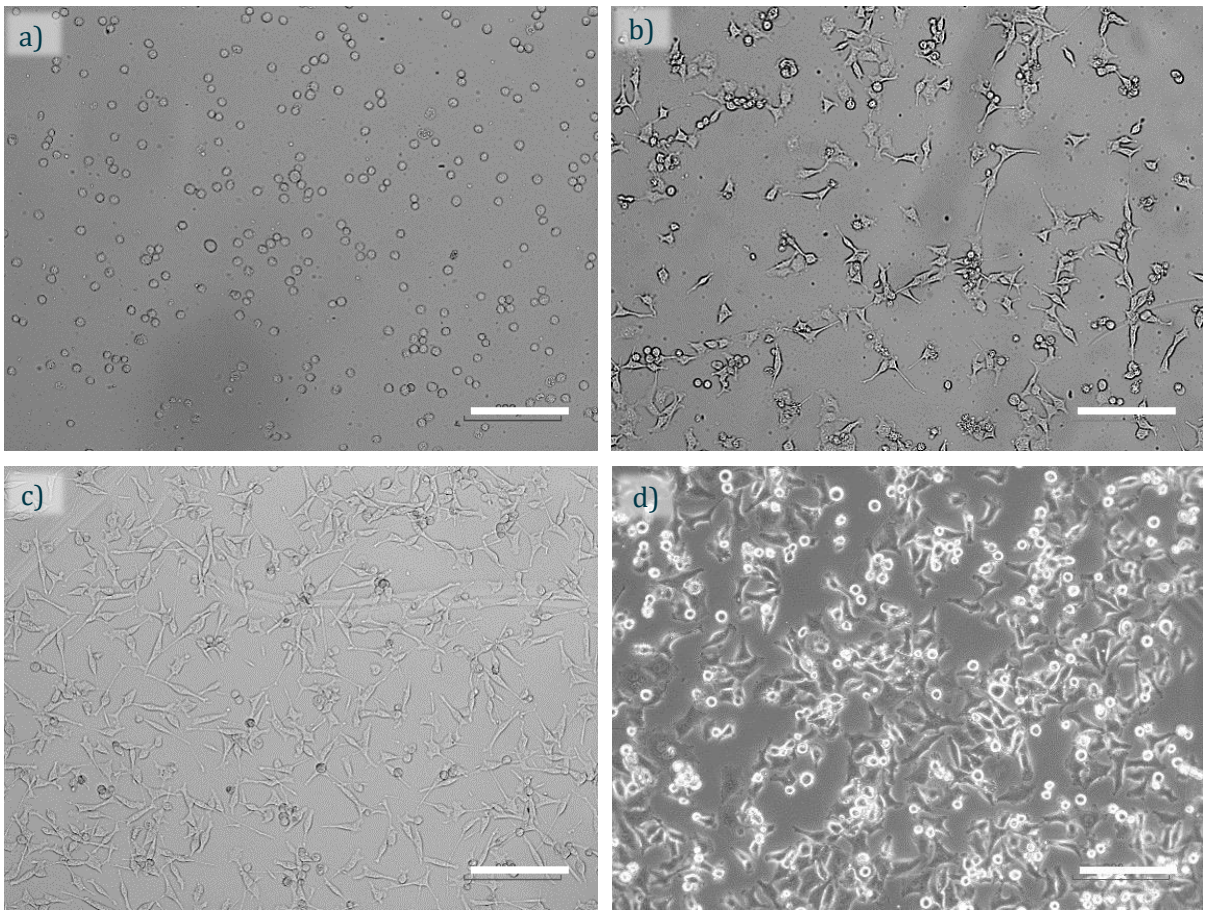

Figure 4.18: Microscope images of the HeLa cells cultured in the devices under continuous perfusion at multiple cell seeding densities a) 30,000, b) 40,000, c) 50,000 and d) 60,000 cells per chamber. Images representative of 4 experiments. Scale bars represent 200 µm.

The flow rate of the fresh media was also investigated to look into the effect of the shear stress induced by the flow on the cells. Cells were seeded at 60,000 cells per chamber and cultured for 24 h at 37°C under multiple flow rates (1, 2.5, 5 and 10 µL/min). All flow rates tested were able to maintain the cells viable for the length of the experiment, but, as it can be observed from the images in Figure 4.19, the chambers with higher flow rates had more rounded cells, which

implies not full attachment to the substrate. For subsequent experiments, the flow rate was established at 2.5 µL/min to minimise the effect of the shear stress but ensuring continuous replenishment of the media to avoid nutrient depletion.

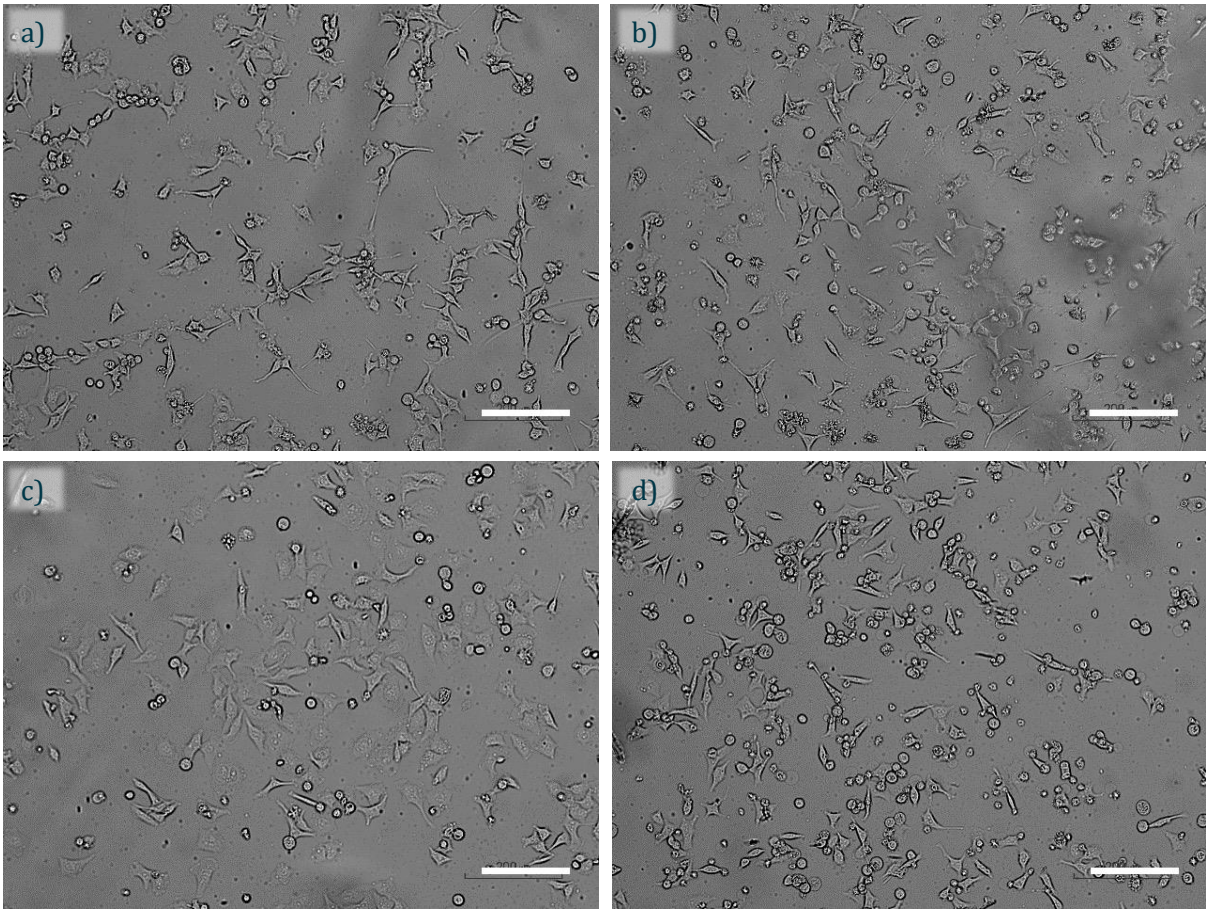

Figure 4.19: Microscope images of the HeLa cells cultured in the devices under continuous perfusion at multiple flow rates a) 1, b) 2.5, c) 5 and d) 10 µL/min. Images representative of 1 experiment. Scale bars represent 200 µm.

It is also worth noting that over the several repeats to obtain the previously presented information, it was observed that the speed of the seeding did also affect the number of cells that attached to the substrate (Figure 4.20). When the cell suspension was flushed in a slow and controlled manner and pausing after every 100 µL (instead of rapidly flushing the suspension through) more cells were present and fully attached to the substrate. This detail was also added to the protocol.

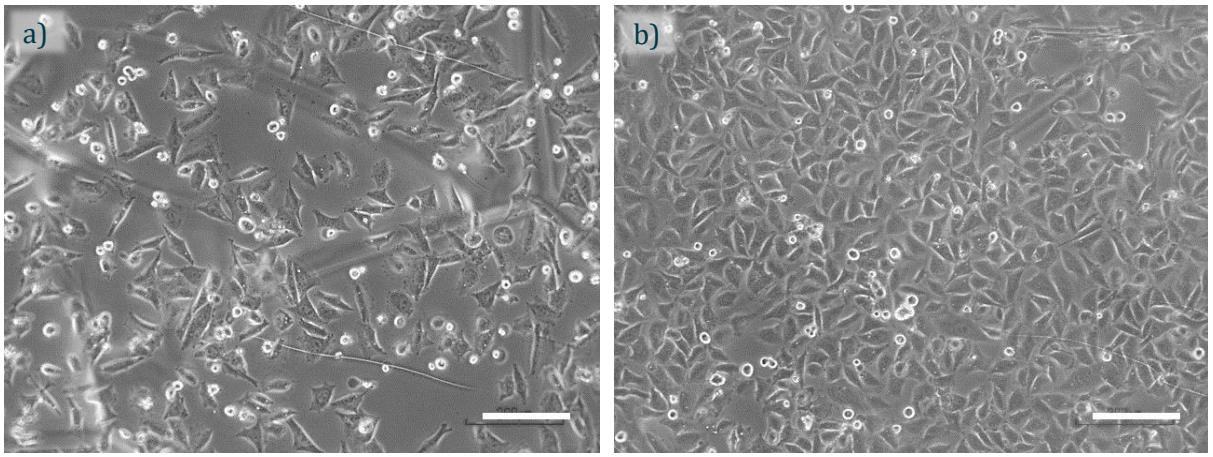

Figure 4.20: Microscope images of the HeLa cells cultured in the devices under continuous perfusion with different cell seeding speeds a) fast seeding (approx 6 mL/min) and b) slow seeding (approx 0.6 mL/min). Images representative of 2 experiments. Scale bars represent 200 µm.

4.5.1 Viability assay on-chip

Once the protocol for cleaning the device and seeding the cells was successful, the viability assay was adapted to the system. At the desired time point to perform the viability assay, the system was removed from the incubator and placed inside an MSC. The flow of fresh media was stopped, and the chambers were rinsed manually with serum-free media before flushing 1 mL of the resazurin solution prepared in a 1:10 ratio (final concentration 44 µM) from the outlets, to avoid introducing bubbles. The fresh media syringes were reconnected to the inlets again and the system was placed back inside the incubator with no flow. After 1 h of incubation, the flow was started at 3 µL/min and the effluent was collected every 30 min. Aliquots of the effluents at the multiple collection time points were transferred to a black, flat-bottom 384-well plate. The measurements were taken by a microplate reader with Ex/Em = 560-10/590 nm. The results are shown in Figure 4.21. After the initial 30 minutes, the effluent had no signal, as it was flushing out the unreacted reagent that was left in the outlet tubing during the loading of the assay. After that point, the signal increased with time until the total volume expelled was 300 µL (which is the approximate volume of the chambers). Then, it started decreasing again due to the mixing of the reagent with the fresh media. Thus, the final protocol for measuring viability on chip was established as follows: rinse the chambers with serum-free media, add the 1:10 resazurin solution, incubate for 1 h at 37°C and then start flow at 3 µL/min. Collect the effluent for 30 min, 1 h after the flow was started, plate the aliquots, and measure the fluorescence intensity in a conventional microplate reader.

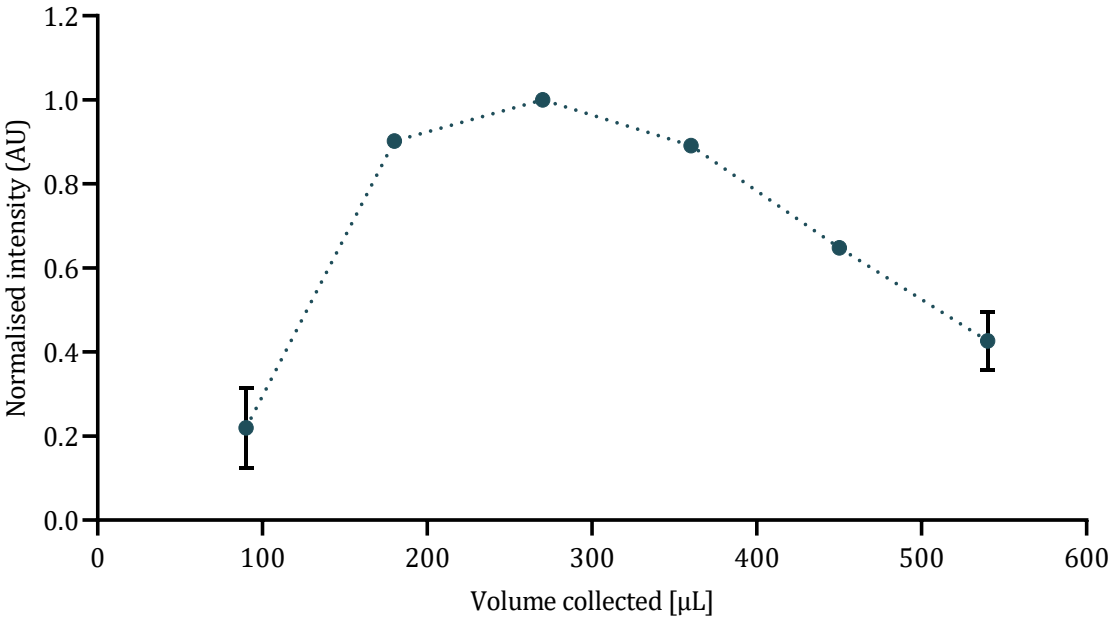

Figure 4.21: Evolution of the signal of the collected effluents. Data represent mean ± SD; n=2.

It was noticed that the measured values from the effluents were higher than the static controls despite being seeded at the same densities (Figure 4.22). This could be due to the smaller volume of the chambers compared to a conventional 24-well plate, which would result in a higher concentration of the products of the reaction. This increase in sensitivity has already been observed by others and it is one of the advantages of the microfluidic technology, as the reaction rates are maintained constant, but the products are more concentrated than in standard cultures due the reduced sample volumes in the chips [110].

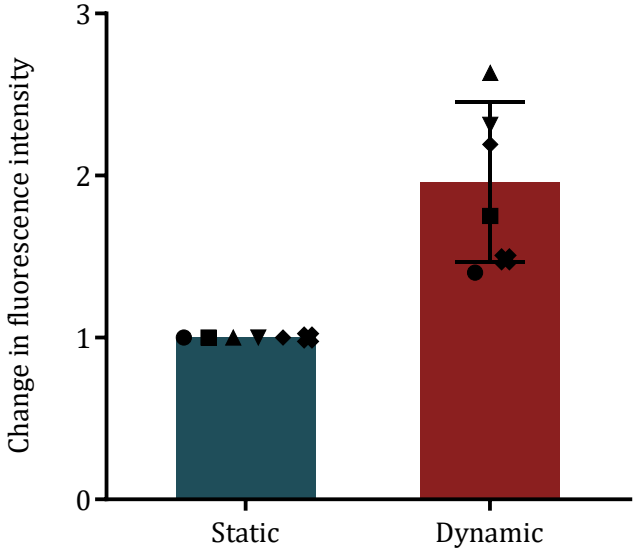

Figure 4.22: Differences in the fluorescence intensities measured between the static controls and the samples in the devices. Each experiment was normalised to the value of the static control for interexperimental comparison. Each experiment is represented with a difference shape. Bars represent mean ± SD. Each pair of symbols represents an experiment. n=5.

To study the consistency and reproducibility of the assay, several repeats of the complete experiment culturing cells in the device for 48 h were carried out. The complete protocol for culturing cells on the chip was established as follows: after fabrication, the devices were sonicated in DI water for 10 minutes and dried with a nitrogen gas gun. Then, the device was placed on the chip holders with the mounted O-rings and the clamp was closed to seal the chambers. A leak test was carried out by immersing the assembled system in soapy water and pressurising the chambers. Subsequently, the system was placed in a MSC to maintain sterility and the chambers were disinfected with diluted bleach (1:50) for 20 min. Then, the chambers were rinsed with sterile dH_2O and HBSS to remove the bleach and finally with cL-15 to prime them. The system was placed inside the incubator at 37°C while the cells suspensions were prepared. HeLa cells were suspended at 200,000 cells/mL, transferred to a 1 mL syringe, and flushed through the devices. 10 mL syringes with fresh media were mounted onto syringe pumps and connected via PTFE tubing to the chambers. The setup was placed in the incubator for 30 min before starting the flow at 2.5 µL/min. Standard curves were prepared and plated in 24-well plates and used as controls to measure the viability and calculate the number of live cells present in the chambers. After the desired culture time, the flow was stopped, and the chambers were rinsed with serum-free media before flushing 1 mL of resazurin solution (1:10 ratio). The syringes with fresh media were reconnected to the inlets and the system was placed back in the incubator. The assay was left to incubate for 1 h before starting the flow at 3 µL/min. The effluent collected within the first 60 min was discarded, and the effluent collected for 30 min after that was collected and aliquoted into wells of a black 384-well plate. The fluorescence intensity was measured in a microplate reader at Ex/Em = 560-10/590 nm. The results are shown in Figure 4.23. The average calculated number of cells in each chamber was higher than the static controls, as they were seeded at 60,000 cells per chamber but, as discussed before, this number could be misleading due to the higher concentration of resazurin product in the effluents. It is worth noting the high variability between experiments, which could be attributed to differences in the number of cells initially seeded, potentially related to the seeding method; or to differences in the effluent collection time point, as the syringes are mounted manually in the syringe pump, and flow might not start simultaneously in all the chambers. There was also high variability between experiments in terms of the number of chambers per device with viable cells (Figure 4.23 top right corner). The source of this variability was not completely understood as the protocol was the same for all the chambers and set of experiments. The potential cause for the death of cells in certain chambers and not the adjacent ones could be due to the introduction of contamination in the tubing and connectors or during handling.

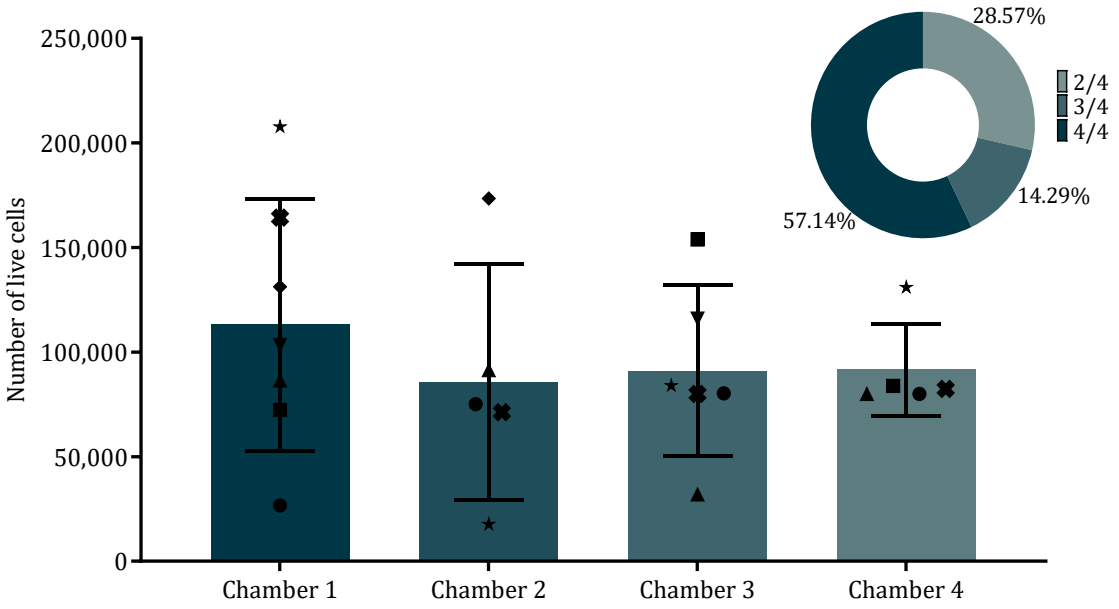

Figure 4.23: Number of live cells in each chamber. Bars represent mean ± SEM. Experimental replicates are plotted individually as dots. From left to right, n=7, 5, 6 and 5 respectively. Chambers without live cells were excluded from the calculation. On the top right corner, success rate of the experiments. Each area represents how many chambers were alive per experiment, n=7.

4.6 Final design

After the optimisation of the culture of cells on chip, the system was unable to maintain an oxygen gradient across the chambers (as explained in Section 3.5.2). Therefore, the chamber design was modified, which resulted in a change of the substrate material in which the cells were going to be cultured on, from PMMA to PDMS. PDMS is a material widely used in microfluidics and organ-on-chip research and it is known for its biocompatibility. However, it is a hydrophobic material and thus cells do not adhere correctly to it. PDMS is also known for absorbing small molecules. The cleaning protocol established previously used bleach to disinfect the chambers. Even though PDMS has good resistance to it, bleach diffuses into the bulk of the polymer, and is released afterwards when in the presence of other liquids, which would effectively mean exposing the cells to bleach. Therefore, the cleaning protocol had to be revised. Conventional 24-well plate wells were coated with PDMS and allowed to cure for 1 h at 60 °C. Subsequently, the wells were subjected to different cleaning protocols: 1) exposed to 1:50 bleach for 10 minutes, then rinse with sterile water; 2) exposed to 1:50 bleach for 10 minutes, then soak in sterile water overnight; 3) exposed to 70% ethanol, then rinse with sterile water; and 4) exposed to UV light for 30 minutes, then rinse with sterile water. After all the wells were treated with the different cleaning conditions, cells were seeded at 50,000 cells per well and incubated in cDMEM at 37°C and 5% CO_2 for 24 h. Then, the conditions were imaged to observe differences in cell morphology, and viability was calculated as the number of live cells measured with the resazurin assay as explained above compared to the number of live cells measured in the control. The results (Figure 4.24) showed poor viability for every cleaning protocol except for the second one (soaking in water overnight). This could be due to the fact that soaking overnight allowed for the bleach absorbed into the bulk of the PDMS to diffuse out, whereas with a quick rinse, the bleach stayed in the polymer and leached out during cell culture when the medium was introduced. Ethanol and UV treatment did not show any improvements compared to the bleach. Due to the lack of compatibility of ethanol with PMMA and the additional complexity of the UV method, bleach followed by an overnight soak was selected as the cleaning protocol for subsequent experiments.

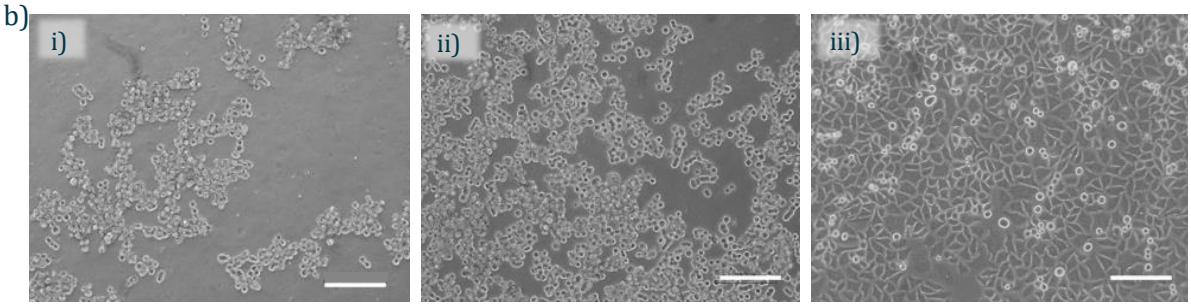

Figure 4.24: a) Number of live cells on PDMS-coated wells depending on the cleaning protocol compared to the untreated control (no PDMS coating). n=1. b) microscope image of cells on PDMS cleaning with bleach (i), ethanol (ii) or uncoated for control (iii). Scale bar represents 200 µm.

Despite the improvement in cell viability when soaking the PDMS overnight, the viability was still significantly lower than in the uncoated controls. Other researchers have coated PDMS devices with collagen and/or fibronectin to increase cell adherence [83,85,228]. Thus, the effect of adding a collagen coat to the PDMS-modified well plates was investigated. After coating the wells with PDMS as previously explained, the wells were cleaned in the same conditions and then 0.5 mL of Type I Collagen was added and incubated for 1 h at 37°C. After the incubation time, the excess collagen was removed, and the wells were rinsed with sterile PBS before cell seeding at 60,000 cells per chamber. After 24 h of culture in cDMEM, the conditions were imaged, and the viability measured with the resazurin assay. The viability measurements indicated an improvement in the viability in all the conditions (Figure 4.25). However, the microscope images showed differences in the shape and adherence of the cells to the substrate and to each other (Figure 4.26). The cells on the PDMS substrate were not viable and appeared floating (Figure 4.26c), but their adherence was improved when the PDMS was coated with collagen (Figure 4.26d).

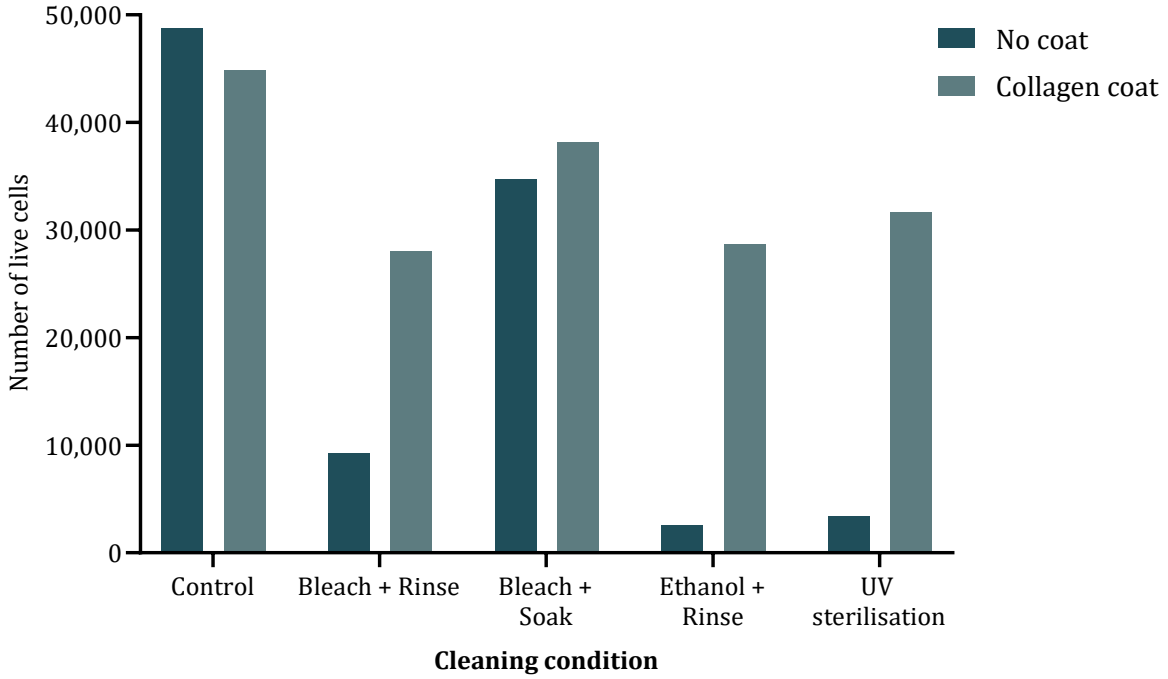

Figure 4.25: Cell viability dependent of the cleaning method. Darker bars represent uncoated wells and lighter bars represent collagen coated wells.

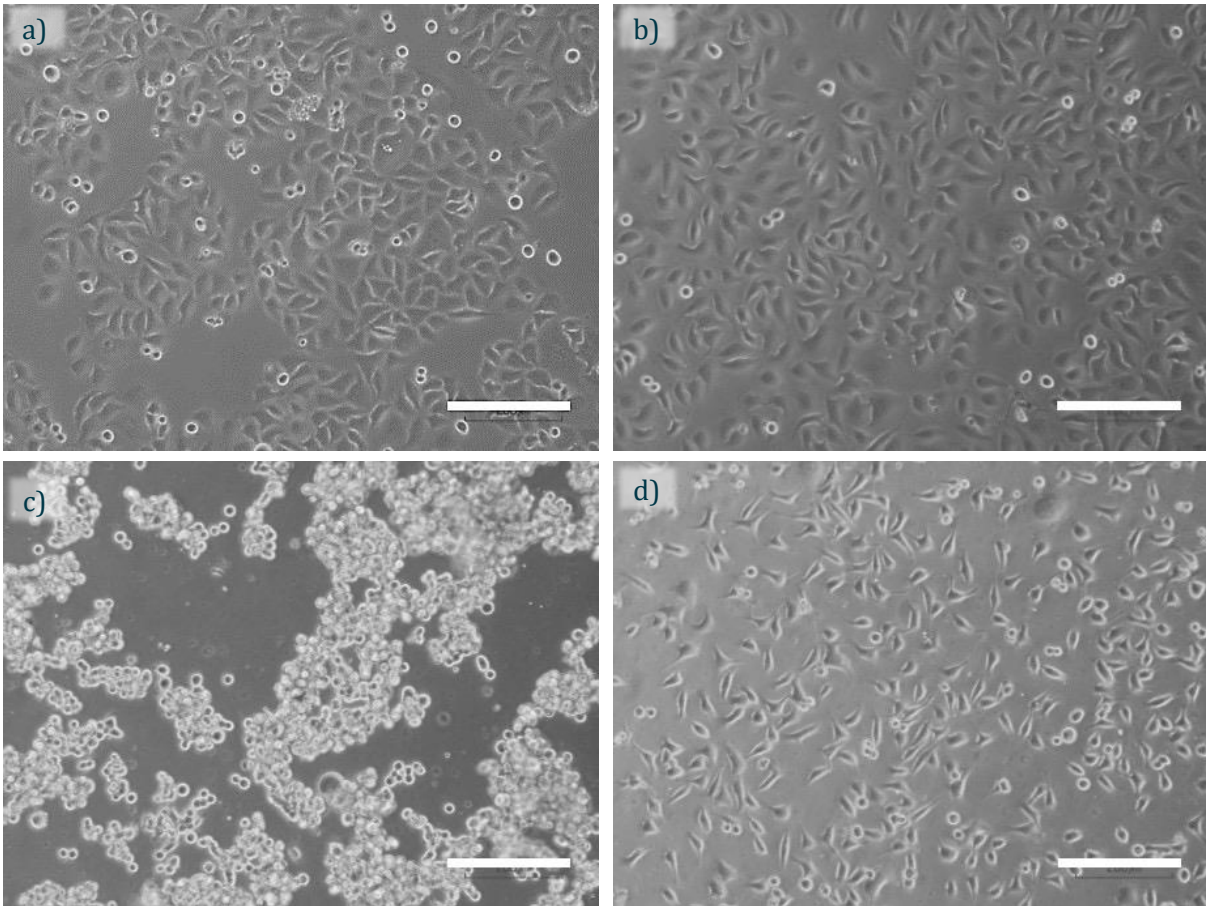

Figure 4.26: Microscope images of the HeLa cells cultured in the modified well plate substrates. a) untreated control (no PDMS), b) collagen coating (no PDMS), c) PDMS and d) PDMS + collagen. Images representative of 1 experiment. Scale bars represent 200 µm.

Given the promising results with the addition of the collagen coat, it was decided to optimise the collagen coating procedure, as PDMS and the proteins in collagen establish weak bonds and they can degrade when exposed to shear stresses [311]. The incubation time was increased to test this hypothesis. Wells were coated with PDMS and cleaned with 1:50 bleach and soaked in sterile water overnight. Then, 0.5 mL of collagen were added and left to incubate for 1, 2, 4 or 24 h, after which the excess was removed and washed with sterile PBS. The cells were plated and incubated for 24 h in cDMEM. Images were taken and viability measured with resazurin assay. The results showed an increase in viability with increasing incubation times with the 24 h coating procedure showing the same number of cells as the static control (Figure 4.27, above). The images of the cultures showed that cells on the wells with an incubation time of 24 h (Figure 4.27, below, d) presented the same morphology and confluence as the static controls in uncoated wells (Figure 4.26a). Therefore, the culture on chip protocol was modified as follows: after sealing the system and checking for leaks, the chambers were disinfected with 1:50 bleach for 10 min. Then, sterile water was flushed to rinse out the bleach and was left to soak for >5 h. Subsequently, the collagen

solution was flushed through, the inlets and outlets blocked, and the system placed in the incubator at 37°C overnight. Next, the excess of collagen was rinsed out by flushing sterile PBS, followed by HBSS and complete media to prime the chambers before adding the cells.

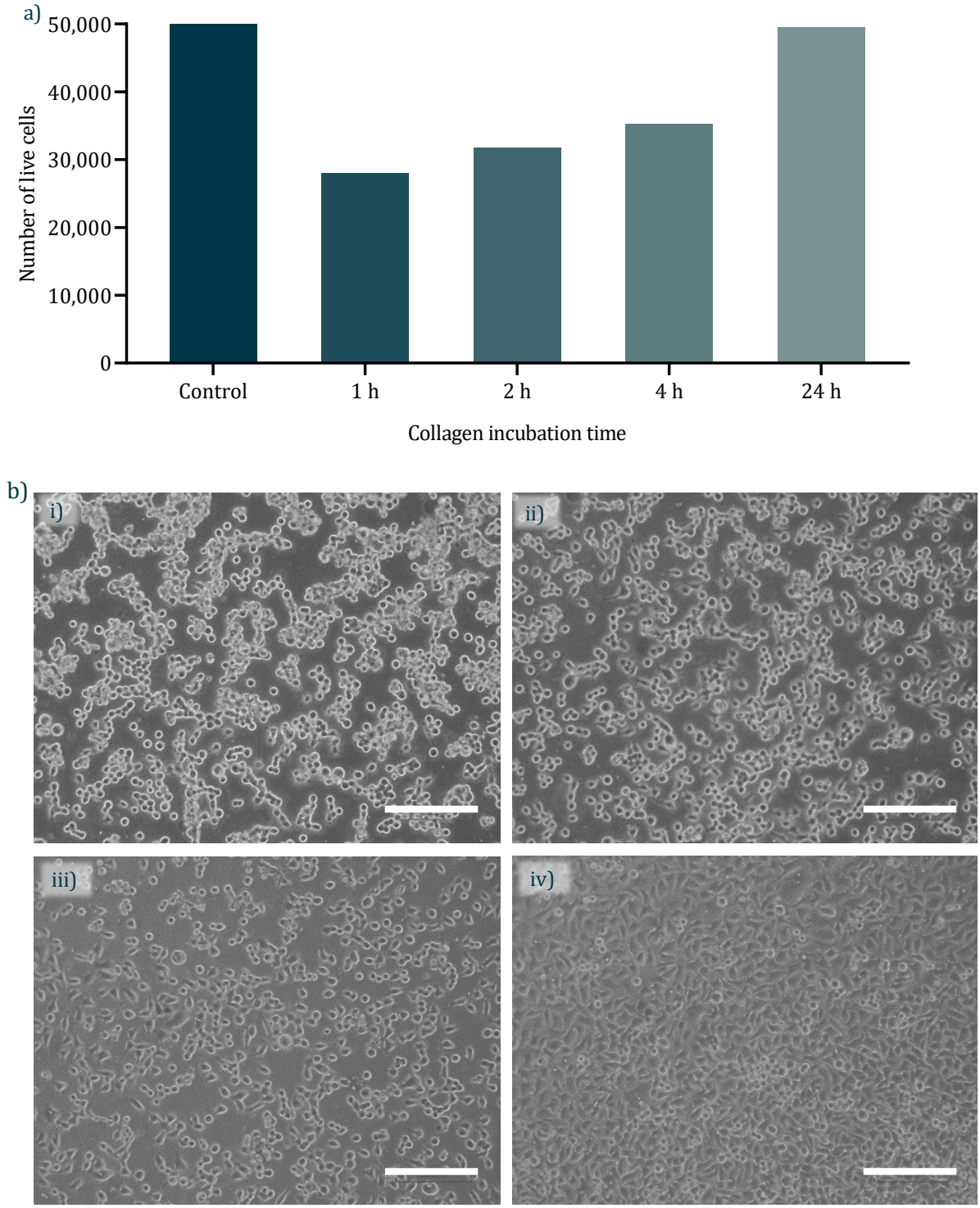

Figure 4.27: a) number of live cells on PDMS + collagen coated wells depending on the incubation time compared to the untreated control (no coating, static culture). N=1. b) Microscope images of the HeLa cells cultured in the PDMS-coated well plates with different collagen incubation times. i) 1, ii) 2, iii) 4 and iv) 24 h. Images representative of 1 experiment. Scale bars represent 200 µm.

However, when the cells were seeded in the devices following this new protocol, poor viability and adherence was still observed (Figure 4.28, left). Given that the cells were cultured on stiff substrates and the PDMS membrane (acting as the substrate in the devices) was not completely rigid and warped in some places due to the pressure in the chambers when the device was sealed, it was hypothesised that the rigidity of the substrate could play an important role in the adherence of the cells. To test this, a modified version of the device was fabricated in which the gas layers were substituted for a PMMA slab without features (Figure 4.28, centre). The PDMS membrane was then bonded to this stiff substrate and the rest of the device was fabricated and assembled as normal. The experiment was repeated, and this time the cells showed good adherence and coverage of the substrate (Figure 4.28, centre), and even the cells reached high confluence after 48 h of culture under continuous perfusion. Although it proved the hypothesis and improved the viability of the cells in the device, the gas impermeable PMMA would not allow for gas diffusion between the gas and culture chambers. Therefore, a way to increase the stiffness of the membrane but still allowing the equilibration of gases was sought. The gas layer design was modified to add a mesh to support the membrane (Figure 4.28, right). A COMSOL simulation confirmed that the gas diffusion was not affected by the new structure (Figure 4.29). When the cells were seeded in this new design, good cell attachment was observed in the entire chamber, although the cells still had a preference for the regions where the membrane was in contact with the rigid mesh. Using the well plates coated with PDMS and collagen as control to check for complete adherence, the adherence time (time between the cells are seeded and the flow of fresh media starts) was increased to 3 h from then on.

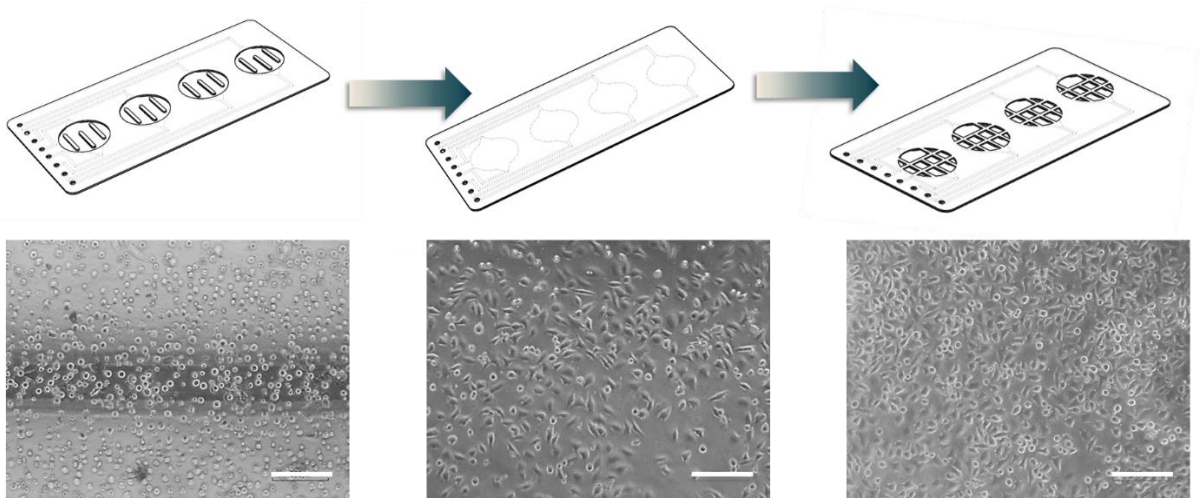

Figure 4.28: Evolution of the design to improve the cell adherence to the PDMS substrate. On the left, small pillars prevented the membrane from collapsing the chamber but did not provide rigidity to it. In the centre, the modified device with a PMMA slab without features to provide the cells with a stiff substrate. On the right, the final design with the mesh to support the membrane while allowing the gas exchange between the chambers. On the bottom, microscope images of HeLa cells cultured in the device version depicted on top of them. Images representative of 3 experiments. Scale bars represent 200 µm.

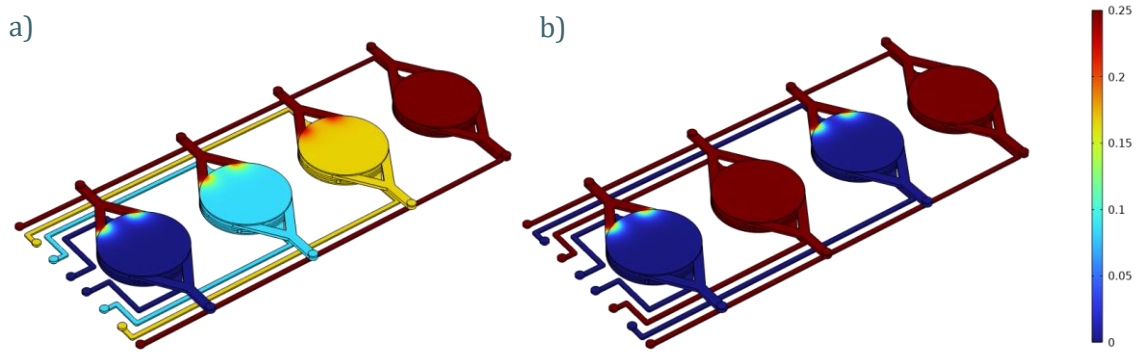

Figure 4.29: COMSOL simulation of the oxygen removal in the culture chambers. The culture media entering the chambers at atmospheric oxygen levels is rapidly equilibrated to the oxygen concentration of the gas mixture flowing underneath. a) gradient of oxygen concentrations, b) binary oxygen concentrations on alternating chambers to show no interference of the oxygen concentration of adjacent chambers.

4.7 Hypoxia experiments

To prove the ability of the developed system to culture tissues under multiple oxygen tensions, the effect of oxygen in the cells was studied by looking into the gene expression changes of hypoxia-related markers.

Cells have a number of mechanisms to adapt to changes in their environment. As explained in more details in Section 1.5, HIF play an essential role in the adaptation to hypoxia. It transcriptionally regulates the expression of a large number of genes involved in angiogenesis, glycolysis, invasion and metastasis. One of the best characterised targets of *HIF-1* is the carbonic anhydrase IX (*CA9*). *CA9* is a transmembrane protein, with its active side on the extracellular domain. It can function as a pro-migratory factor, as a signalling molecule transducing signals to pathways between the intra and extracellular environments, and as a survival factor protecting cells from hypoxia and acidosis by regulating pH through the catalysation of the reversible conversion of CO_2 to bicarbonate and a proton [312]. Hypoxia triggers a shift towards the glycolytic metabolism, which produces lactic acid, decreasing the intracellular pH [312]. *CA9* contributes to the neutralisation of the elevated intracellular proton concentration caused by the hypoxia-induced glycolysis, resulting in the acidification of the extracellular enviroment, which is associated with increased invasion and metastasis and can affect negatively treatments by modulating the uptake of drugs [313]. Therefore, the dynamic upregulation of *CA9* is triggered by HIF-1 as one of the mechanisms supporting cellular adaptation to hypoxia [314].

Another primary target regulated by HIF is vascular endothelial growth factor (*VEGF*). *VEGF* is considered to be an important regulator of both physiological and pathological angiogenesis [315]. Hypoxia affects endothelial cellular physiology in a number of ways, including transcriptionally regulated expression of vasoactive substances and matrix proteins involved in modulating vascular tone or remodelling the vasculature and the surrounding tissue [316]. The expression of *VEGF* is dramatically induced by hypoxic conditions in several types of tumour cells as well as fibroblasts and smooth muscle cells, and is a key mediator of hypoxia-induced angiogenesis [317]. Given the high relevance of these two genes in the hypoxic response, they were selected as the target genes to study the response of the cells to the oxygen tensions in the developed devices. β-actin (*ACTB*) was selected as the housekeeping gene (HKG), as it is a cytoskeleton component, very important in cell morphology maintenance and is very commonly use as a reference gene [318].

As a proof of concept, once the culture of the cells in the devices was optimised, the cells were subjected to either normoxia or hypoxia in the device by flushing compressed air (100% DO) or nitrogen gas (0% DO) in the gas layers. CO_2 was not taken into account in these

experiments due to the equipment limitations for mixing gases. After the device was cleaned and primed, the oxygen sensors were calibrated. Then, the cells were seeded as explained previously. After 24 h of culture under continuous flow of fresh media without flow of gases (normoxic conditions), the syringes were changed with fresh complete media and the flow was continued for another 24 h. When the new syringes were mounted, the gas flow was started (Figure 4.30). The oxygen detector was turned on and measurements were taken every 10 minutes for the 24 h of the challenge (Figure 4.31).

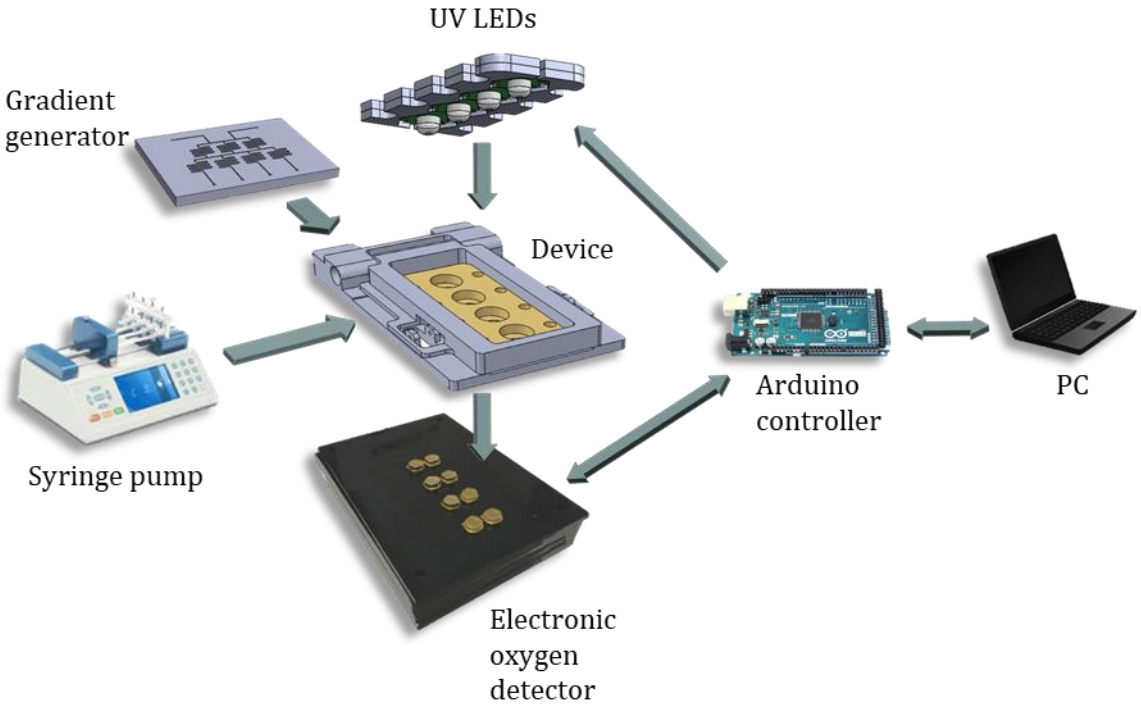

Figure 4.30: Schematic of the complete system. The fabricated devices are mounted in the clamp chip holder and placed on top of the electronic detector. The LED setup rests on top, each LED aligned with each chamber. Once the devices are cleaned, primed and seeded, the syringe pump provides continuous perfusion of fresh media to the culture chambers. The gradient generator is connected to two lines of gases with known oxygen concentration, and the four outlets are connected to the device's gas layer inlets. The Arduino board controls and collects the signals from the LEDs and the detector, and sends it to the PC, where they are processed.

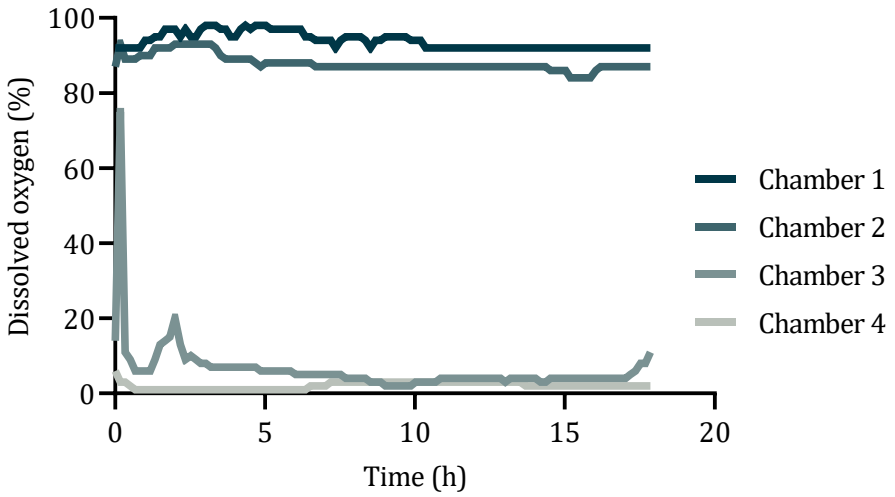

Figure 4.31: Measured oxygen tensions in each chamber during the experiment. Chambers 1 and 2 were flushed with compressed air and chambers 3 and 4 with pure nitrogen gas. Measurements taken every 15 min.

Subsequently, the cells in the chambers were lysed while maintaining the flow of gases, and the RNA was extracted (Section 4.1.6) and its concentration measured (Section 4.1.6.1). Samples with an RNA content over 20 ng/µL were used. The purity of the samples was checked by looking at the 260/280 ratio. The changes in gene expression of *CA9* and *VEGF* were evaluated by performing a reverse-transcriptase quantitative polymerase chain reaction (RT-qPCR) (Section 4.1.7) and analysed using the comparative C_T (threshold cycle) method (Section 4.1.7.1). When the C_T values of *CA9* of several experiments were normalised to the C_T values of *ACTB*, a tendency to a decrease in the C_T values for *CA9* in the hypoxic condition could be observed, indicating a higher expression of the gene as expected (Figure 4.32, a). However, the results had high variability and no statistically significant conclusions could be drawn from them. This could be due to the high variability in gene expression obtained from the chosen HKG. Indeed, when *ACTB* was stable, a steep increase in the *CA9* and *VEGF* expression could be observed (Figure 4.32, b). More time would be required to optimise the experiment and obtain more consistent results. Improvements in the cell culture on chip protocol, the RNA extraction from the chambers, or in the

fabrication of the device are needed. Another possible way to improve this experiment could involve the selection of a more relevant HKG. Other works have reported preferable genes for HeLa cell line normalisation over *ACTB*, such as *HPRT1*, *RPS18*, *HSPC3* or *SDHA* [319].

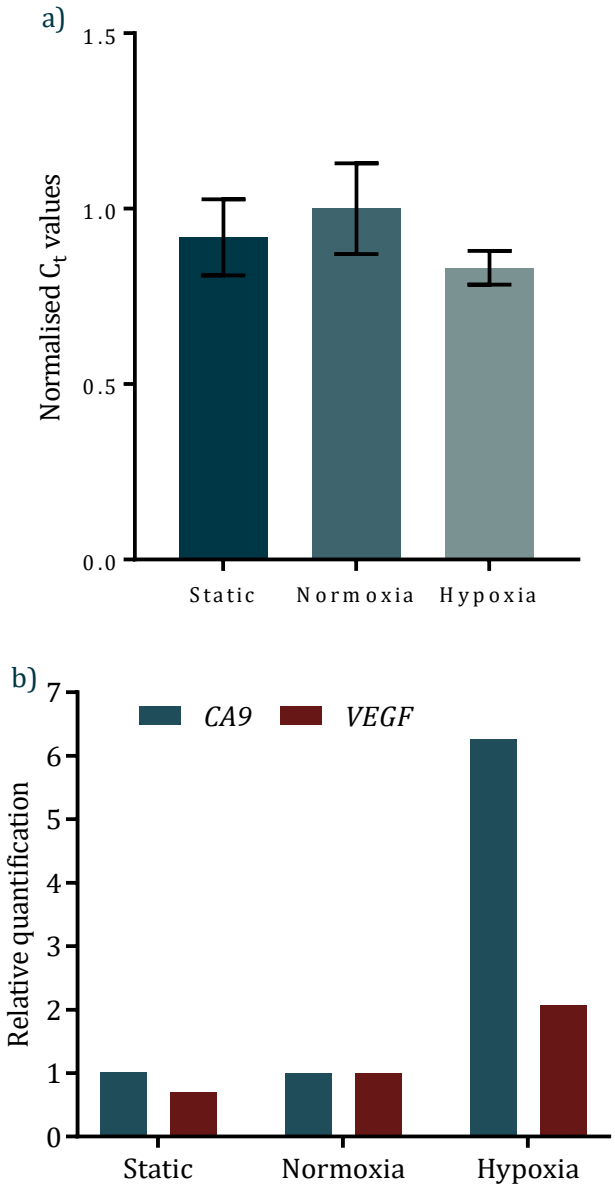

Figure 4.32: a) C_T values for CA9 normalised to the C_T values of ACTB to show the high variability between the experiments. Data represent mean ± SD; from left to right, n=6, 6 and 3, respectively. b) Gene expressions changes under different conditions. n=1.

To prove the hypothesis that the main source of error was the chosen HKG, two new HKGs were tested, *TOP1* and *YWHAZ*. These experiments were performed at the Brooke Lab, who kindly provided the primers. However, these primers used Taqman technology instead of SYBR Green. A direct comparison of the C_T values obtained for the three HKGs can be seen in Figure 4.33. The coefficient of variation is calculated to measure the level of dispersion of the C_T values obtained. For the three HKGs tested, the coefficients of variation were 0.12, 0.036 and 0.032 for *ACTB*, *TOP1*

and *YWHAZ* respectively, indicating a 4-fold reduction of the variability between housekeeping genes and PCR methods. It was therefore decided to use *YWHAZ* with Taqman technology as the HKG for the subsequent experiments.

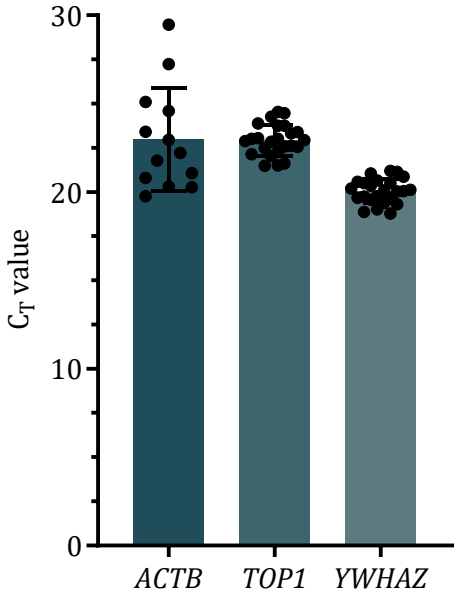

Figure 4.33: C_T values measured for housekeeping genes ACTB, TOP1, and YWHAZ. Data represents mean ± SD. Experimental replicates are plotted indivdually as dots. N=13, 24 and 24 respectively.

With this new housekeeping gene, the PCRs were repeated with the samples from the previous experiments. The new results are shown in Figure 4.34. A 12.3-fold and 2.73-fold increase in the expression of *CA9* and *VEGF* respectively can be observed between the normoxia and hypoxia conditions. Nevertheless, a big variability can still be observed between experiments (points on each graph). This could be due to other variabilities inherent to the system, such as the amount of starting material. It has been already discussed how there was high variability in the number of cells in each chamber and experiment. This could be seen when the nucleic acid concentration was measured before carrying out the PCRs. A coefficient of variation of 0.41 and 0.43 can be seen between the samples subjected to normoxia and hypoxia, respectively, across 5 different experiments. Even the static controls used as reference had a coefficient of variation of 0.17. Errors during pipetting and manual handling, as well as while performing the RNA extraction could be the reason for this.

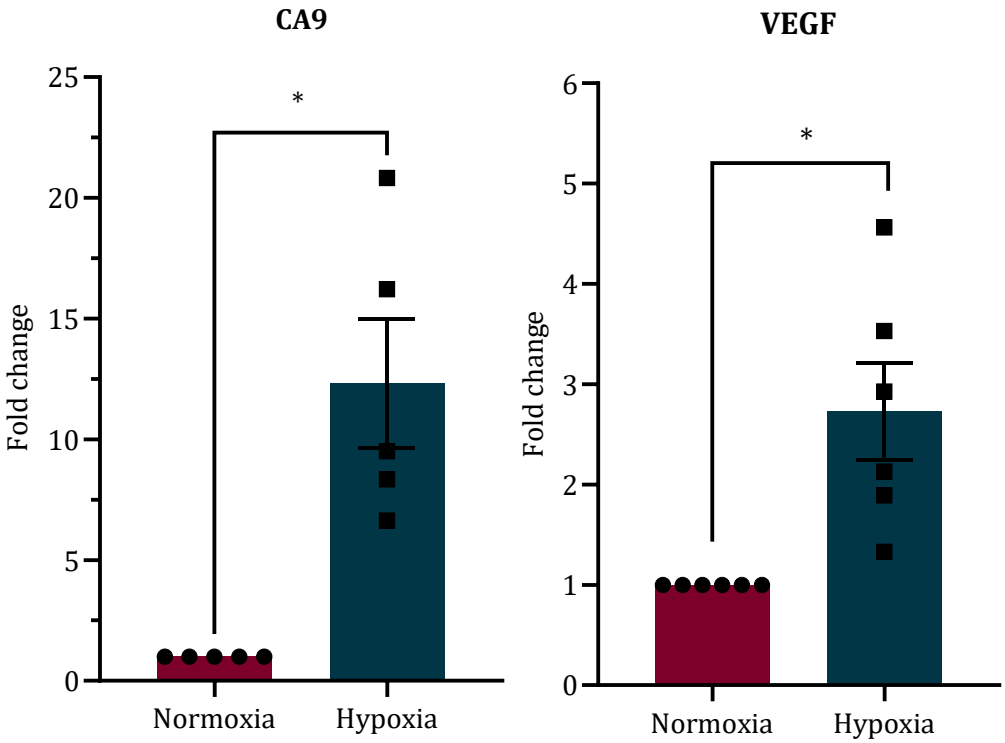

*Figure 4.34: Fold change in the expresion of hypoxia-related genes. Bars represent fold change ± SEM, experimental replicates are plotted individually as dots, n=6. Normal distribution of data was confirmed by a Shapiro-Wilk normality test and significance between groups was determined by a paired T test where *p≤0.05.*

Finally, an experiment to obtain the responses of the cells subjected to an oxygen gradient was carried out. The results are shown in Figure 4.35. It can be observed that there was an inverse relationship between the *CA9* expression and the oxygen concentration. The results also suggest that there is an oxygen concentration threshold below which *CA9* expression starts to change, i.e., hypoxic response is triggered. This relationship was not so clear for *VEGF*. The chamber with the lowest oxygen concentration had a gene expression change similar to the one observed in previous experiments, but the rest of the chambers with higher oxygen concentrations did not show a clear relationship between oxygen and gene expression change. This could be because *VEGF* is a non-specific indicator of stress on the cells and, as we have discussed previously, the cells are subjected to several stresses during the culture in the chambers due to the continuous perfusion, the lack of rigidity of the substrate and the material of the substrate.

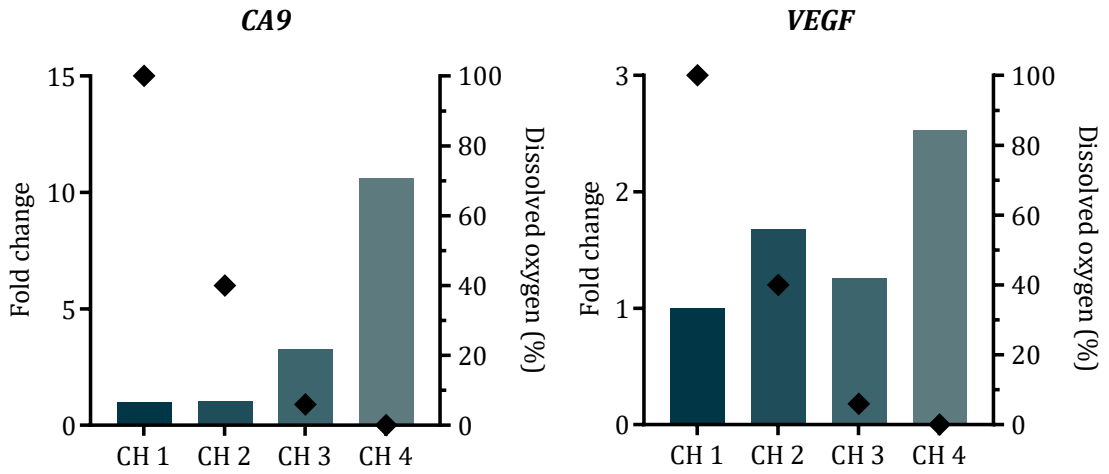

Figure 4.35: Fold change of hypoxia-related genes expression in response to an oxygen gradient across the chambers. The oxygen tension in each chamber is depicted as a black diamond. The bars represent the fold change. N=1.

4.8 Conclusions

After developing a system able to generate, maintain and monitor four different oxygen tensions, in this chapter, the ability of the system to culture cells, and to subject them to those oxygen concentrations as well as the study of their effect on the tissues were tested.

First, multiple methods to assess and monitor the viability and health of the cells were optimised. The resazurin assay presented several advantages such as its higher sensitivity, cost efficiency, ease of use and the potential to be readily adapted to the culture on chip for in line analysis. Secondly, the optimum culture media for the culture of cells in the devices was investigated. The gas-impermeability of the materials used for the fabrication of the device with the aim to avoid oxygen diffusion allowed for a tighter control of the gaseous environment. However, it also limited the diffusion of CO_2, which meant that the cell culture media was not able to equilibrate its pH, which could drastically affect the cells. CO_2-independent media were studied, using HEPES as the buffering system. Analysing the effect of the media studied on cell viability, morphology, and growth rate, it was decided to use a culture media based on Leibovitz supplemented with FBS, antibiotics, vitamins and HEPES.

Thirdly, the compatibility of the materials with which the tissues were going to be in contact with was investigated. Culturing cells in conventional well plates with modified substrates revealed good adherence and health of the cells in PMMA and collagen-coated PMMA, indicating the suitability of the developed devices for cell culture. In the next step, the protocol to culture the cells in the devices was studied. Seeding method, seeding speed, cell density and perfusion flow rate were examined to determine the optimal conditions. The viability assay was also adapted for measuring the health of the samples in the chambers. This protocol had to be modified due to changes in the design of the device. These changes entailed a different substrate on which the cells were going to attach. Given the hydrophobicity of the PDMS, methods to improve adherence were sought. The cleaning method was improved and modified to avoid bleach diffusing into the bulk of the polymer, which could impact the viability of the cells, and the coating with collagen was optimised to improve the cell adherence. Finally, due to the lack of rigidity of the membrane, which also contributed negatively to the adherence of cells, the design was slightly modified to incorporate a mesh that supported the membrane whilst allowing for the diffusion of gases between the chambers.

Lastly, once the cell culture protocol was established, the potential for this system to subject tissues to multiple oxygen concentrations was validated by exposing the cells to either normoxic (100% DO) or hypoxic (0% DO) environments for 24 h and determining the changes in the gene expression of the hypoxia-induced markers *CA9* and *VEGF*. The results showed a high

variability in the HKG, which therefore resulted in high variability in the calculated gene expressions of the hypoxic factors. It was decided to change to Taqman technology for the PCR and, after studying different HKG possibilities, *YWHAZ* was selected for subsequent experiments. A clear upregulation trend was observed for those markers when the hypoxic challenge was applied, as well as a response proportional to the oxygen concentration when a gradient was applied, showing the ability of the system to culture tissues, subject them to oxygen tension changes and monitor the cell response.

Chapter 5. Discussion

In this project, we developed a novel platform for the culture of cells under controlled gaseous microenvironments. There is extensive research on the effect of oxygen on tissues, and yet the effects of the concentration of oxygen or its spatial and temporal distribution *in vivo* are not fully understood. Microfluidic technology provides a very interesting tool for the tight control of the oxygen microenvironment during cell culture providing new methods for the generation and manipulation of oxygen concentrations and gradients, as well as for measuring and monitoring them. The majority of these platforms aim to study the effect of oxygen in cells culture in microchambers [320–323]. In this project, we aim to develop a platform that allows for study of those effects on more complex samples, such as tissue slices. The main difference, and challenge, compared to the published works to date is the size of our culture chambers, which makes the system more susceptible to unwanted oxygen diffusion, with longer equilibration times, and requiring a more complex control and monitoring, as well as several fabrication challenges. Our aim was to replicate the size of a conventional 24-well plate well (~16 mm in diameter), which is rather large compared to most microchambers that are typically less than 1 mm in width [320,324]. The biggest culture chamber used for these purposes published to the best of our knowledge is the one presented by Rexius-Hall *et al*., with a culture surface area of 55x25 mm. However, in this device, the culture chamber was an open well with no continuous perfusion, which could be considered more as an upgraded well plate system rather than a microfluidic device. Another additional challenge for the design of our system was the intent of creating a platform able to host several tissues with accessibility, which will allow for their manipulation during experimental preparation, for the assessment of their evolution during the experiment, and for the removal of the samples at the end of the experiments for subsequent processing and analysis using conventional methods. All this had to be integrated with a method to generate, control, and monitor multiple oxygen concentrations.

The two most common methods for controlling the oxygen concentration within microfluidic devices are oxygen removal via a chemical sink, using scavenging reagents such as pyrogallol [320,321,324,325] or sodium sulphite [326–328], and equilibration with a gas mixture of known oxygen concentration [277,329,330]. Due to the need for expensive equipment to generate accurate gas mixtures, in this project it was decided to adopt the chemical sink method. In this design, the cell culture medium would be equilibrated to the desired oxygen concentration before reaching the cells (Devices v1.1, v1.2 and v1.3). Similar to the work presented by Barmaki *et al*., different geometries for the optimisation of oxygen removal were tested (Figure 3.12). In our simulations, there were little differences in the oxygen removal efficiency between geometries. This differs from the results presented by Barmaki *et al*., where a higher efficiency in the "chamber" method was observed compared to the serpentine [327]. The main difference between the one presented in this work and their serpentine designs is that ours has more meanders and

covers the entire surface of which the oxygen is going to be removed. This leads to longer residence times of the scavenging reaction, and therefore to more oxygen diffusion. This proposal, however, was discarded due to the inability of establishing a reliable fabrication method to produce reproducible devices. Another reason for looking for a new design was the result of the simulation calculating the time required to completely change the oxygen concentration within the culture chamber. The long equilibration time (around 3 h) led to the next design iteration that sought to increase the oxygen scavenging efficiency by increasing the gas interchange area. This design (Device v2) was inspired by the work presented by Peng *et al*., in which the cell culture chamber lies on top of an oxygen scavenging chamber, with an array of micropillars to structurally hold the gas-permeable membrane [321]. The pyrogallol concentration used for oxygen scavenging varies widely across the literature, and depends on the size of the channels, the aim of the experiment, and the accuracy needed. Li *et al*., required a tight control of the oxygen removal rate in order to obtain specific oxygen concentration in an array of microchambers, and therefore used pyrogallol concentrations varying from 0 to 700 μg/mL [325], whereas Chang *et al*., aimed for a strong and fast removal and chose a concentration of 200 mg/mL [322]. The same situation takes place when selecting the flow rate of the reaction. In this case, not only the reaction flow rate is relevant, but also the ratio to the medium flow rate. In the work previously mentioned by Li *et al*., they optimised the flow rates of the culture medium for each pyrogallol concentration, ranging from 1 to 50 μL/min, at a constant reaction flow rate of 5 μl/min to obtain the desired oxygen concentrations. In the same way, Skolimowski *et al*., adjusted the medium flow rate to obtain different gradient shapes in their microchambers to study the effect on bacterial biofilms [326]. In general, more efficient oxygen removal happens when the reaction flow rate is faster than the medium flow rate. We also looked at this effect in our system (Figure 3.16) and we established that a uniform oxygen concentration across the entire chamber was obtained with a medium flow rate below 5 μL/min, matching with the observations and simulations by Skolimowski. We opted for a pyrogallol concentration in the higher end of the range observed in the literature (100 mg/mL) given that our chambers were large and therefore required a highly efficient oxygen removal. Moreover, a reaction flow rate of 5 μL/min was used, faster than the medium flow rate but minimising the amount of reagent consumed. Our results showed a reduction of the oxygen content in the culture chamber down to ~6% DO, requiring 5 h to reach this level. This is much longer than the equilibration time calculated in the simulation (~15 min) and also much longer than the times reported in the literature (for example, Chen *et al*., used the same pyrogallol concentration and obtained an equilibration time of 30 min [320]), which could be due to unwanted oxygen diffusion through the device's material. Given the difficulties observed to obtain and maintain a single oxygen concentration, and that the desired minimum level was not reached, it was decided to change the oxygen removal method. If it were to work, the obtention

of several oxygen concentrations in parallel would have required optimisation of the pyrogallol concentrations as well as the flow rates, as mentioned above. The complexity of this method along with the poor reliability of our system lead to a change in the oxygen removal approach. In order to simplify the system and the fabrication, it was decided to pre-equilibrate the medium by bubbling with gas mixtures of known oxygen concentrations before perfusing the culture chambers. This method has been used before [331,332]. However, this requires special attention to the materials and connectors used, as the diffusion of oxygen into the fluid between the reservoirs and the culture chamber can alter the oxygen content and therefore result in misleading outcomes.

Most microfluidic devices are fabricated in PDMS due to its many advantages, for example, ease of fabrication, high resolution in the microscale, as well as its good biocompatibility, optical properties, and gas permeability. This last property is of particular interest for cell culture applications, as it ensures good oxygenation of the samples. Even for the works presented in this report that aim to accurately manipulate oxygen concentrations, the go-to material is PDMS [322,325,329]. This increases the difficulty to control the concentration as the diffusion through the bulk of the material is very significant, gradients appear, and even interaction between adjacent chambers with different oxygen concentration happens [328]. It also means that the scavenging method has to be more efficient to compensate for this oxygen inflow. Researchers have worked around this by increasing the thickness of the material [329], adding a layer of a material with lower diffusion rate, such as polycarbonate [322,329] or coating the PDMS walls with gas-impermeable materials such as parylene-C [333,334] or sol-gel solutions [332]. There are also reports of other bulk materials with lower diffusivity used such as COC [335], NOA81 [336], or PMMA [337]. In this project we have attempted fabrication with PDMS and PMMA due to their availability and ease of manufacture. PDMS was initially used due to the need for an intermediate gas-permeable membrane in the system in order to allow the scavenging reaction to remove the oxygen in the medium via diffusion while protecting said medium from the toxic scavenging reagents. Bonding PDMS to PDMS is a very well-known process and yields really good results. However, it had to be abandoned due to the large diffusion into the culture chambers. We hypothesised that the larger size of our chambers was the main reason for not being able to obtain the same results as other published works, as the system would be more sensitive to external diffusion due to the larger diffusion area available for gas interchange. In the next iteration (Device v3) where the oxygen in the medium was pre-equilibrated before infusing it in the device, the use of PDMS would have been an even bigger issue, as there would be no active oxygen removal. It was therefore decided to use PMMA instead. There are several existing PMMA to PMMA bonding methods, using thermal or solvent bonding or a combination of both [338,339]. In microfluidic applications, some researchers have also used double-sided adhesive for this purpose [337]. In this project, the PMMA layers were bonded together using the solvent vapour method

previously developed in our lab. This fabrication method proved to be repeatable and yielded good results, with the devices able to hold up to 2 bars of pressure without leaks or delamination. Despite this, when the devices were flushed with DI water pre-equilibrated with pure nitrogen to obtain a 0% DO, the oxygen concentration measured in the devices did not match. A low oxygen concentration within the culture chambers was only obtained at very high flow rates (>100 μL/min). This flow rate would incur in high shear stress levels on the cells or tissues and therefore it would not be usable for biological experiments. Additionally, when the flow was stopped after flushing the chamber with the pre-equilibrated solution, the oxygen concentration immediately started to increase, evidencing the diffusion of oxygen into the system, even though all the materials involved in the system were selected because of their low gas permeability. For this reason, the active oxygen removal approach was revisited. In this case, instead of using a chemical sink like in the previous attempt, it was decided to use equilibration with flowing gas mixtures (Device v4), similar to others [277,329,330,340].

To achieve this, the device was redesigned to include the chambers where gas mixtures would flow to equilibrate each culture chamber. To avoid diffusion between chambers, it was decided to use PMMA as the bulk material. However, an oxygen-permeable membrane was required to allow the transport of oxygen. There have been several works published describing techniques to bond PDMS and PMMA, involving the modification of the chemistry of the surfaces with sulphuric acid, APTES, GPTES and other reagents [341]. However, these are complex and time consuming. A novel method for bonding these two materials in a fast and efficient manner was presented by Hassanpour, *et al*., which involves the combination of plasma treatment with a pressure sensitive adhesive tape [342]. This method produced very good results, with no leaks detected during operation for all the devices fabricated, with a fabrication time of around 2 h[339].

As previously mentioned, to obtain gas mixtures with the desired oxygen concentration, bulky and expensive instruments such as gas flow meters, regulators and sensors are required, similar to the ones used by Prof Eddington's group [275,277,330], which were not available in our facilities. To overcome this, a microfluidic gradient generator was designed. In this device, two gases with known oxygen concentrations were flushed in directly from the cylinders, and the gases were mixed in a split-and-combine microchannel network. This resulted in four different oxygen concentrations at the outlets, which were then directed to the previously described device, where they would equilibrate the culture chambers. As shown by Jeon *et al*., the shape of the fluorescein gradient at the outlets can be adjusted by tuning the concentrations and flow rates at the inlet channels, obtaining linear or curved gradients with different sharpness [343]. Similarly, the shape of the gradient could be modified by adjusting the flow rates of each gas at the inlets,

and also adjusting the pressure drop at each outlet via fluidic resistors as shown in Figure 3.51. This split-and-combine technique, also known as Christmas tree, has been previously used as an efficient way to obtain multiple concentrations from just two inputs, and it can easily be scaled up [322,332,344]. Microfluidic technology offers means to obtain a wide range of gradients with possibility of modulating the shape of those gradients depending on their application. For example, some reports use the gas permeability of the material to generate the gradient, by scavenging oxygen from one of the sides of the culture chamber [322,324], by controlling the oxygen concentration at each side of the culture chamber [320,329,330] or by controlling the oxygen scavenging rate in each culture chamber [325]. In our case, we used the split-and-combine technique into separate chambers as this leads to a better control of the output concentrations. Additionally, our use of oxygen impermeable materials led to less oxygen diffusion and interaction between adjacent chambers [328]. Each one of these published devices produces a different gradient shape in a different range of oxygen concentrations and with different oxygen measurement methods, which makes them difficult to correlate and directly compare.

As discussed in previous sections, optical methods for the measurement of oxygen are less invasive and highly sensitive. Amongst the large number of oxygen-sensitive dyes available, ruthenium-based and metalloporphyrins are the most commonly used [345]. Tris(2,2'-bipyridyl) dichlororuthenium (II) hexahydrate was chosen for the initial tests as it is easily dissolved in water and therefore could be used to mimic the medium to test the oxygen removal efficiency. A concentration of 5 mg/mL resulted in better signal (Figure 3.4), so it was selected for our subsequent experiments, which correlates with other concentrations used in other works [320]. However, this dye is cytotoxic and cannot be used during culture, which limits its use for real-time monitoring of oxygen levels during culture [333]. Indeed, most papers that use ruthenium-based dyes only perform the tests and calibration of their systems with the dye previous to cell seeding, and then switch to the corresponding medium before seeding the devices, and assume that the oxygen concentration does not change - which can be misleading given that cells consume oxygen during respiration [321,324,325]. To overcome this issue, some researchers have tried to cover the dye with a polymer matrix [337], and there are even some embedded sensors commercially available (PreSense, for example). Using commercial products, although convenient, have the drawback that they are more difficult to integrate with custom-made systems such as the one presented here. Thus, we attempted to embed the ruthenium-dye in our lab into a PDMS matrix. This proved to be difficult, as the dye is not readily dissolved in the polymer and formed clusters (Figure 3.5), similar to the observations made by Bedlek *et al*. They observed a spatially heterogeneous response with poor response which they concluded was due to the polarity of the ruthenium-based dye molecule, rendering it less soluble. They also tried to embed a metalloporphyrin (PtTFPP) in PDMS and they obtained a much more uniform and highly responsive sensor

with a 50-fold increase in the K_{SV} value [346]. Based on this, we also compared the ruthenium-based indicator with a metalloporphyrin, PdTFPP. In the same manner, we obtained a sensor with a uniform response and much higher sensitivity. However, we only observed a 10-fold increase in the K_{SV}. This could be due to the difference in the thickness of the sensors, as Bedlek *et al*., used a spray to obtain a 5 µm-thick film whereas our spin coating method produced films between 100 and 200 µm-thick, which could have higher intensity of the ruthenium dye from clusters across the thickness of the sensor. We observed, however, that the response of this dye was not linear as expected, saturating at values above 20% DO, which did not cover the range of interest for this project, and therefore it was decided to switch to PtTFPP. PtTFPP embedded in PDMS as the matrix has been widely used previously [293,340,347,348]. It is interesting to note that there does not seem to be a consensus on the units for the K_{SV}, or the conditions to calibrate the sensors in order to obtain this constant. For example, Bedlek *et al*., and Thomas *et al*., used the same dye in the same matrix but they obtained K_{SV} values of 0.06 and 584 atm-1 respectively. This makes it difficult for other researchers to directly compare the results. It is also interesting to note that this optical method seems quite variable and highly dependent on the experimental conditions and instrumentation used for measurement. In our experiments, the PtTFPP sensor embedded in the PDMS matrix calibrated using a spectrophotometer gave a K_{SV} value of 482.6 mM^{-1}, whereas using the electronic detector, this value was of 73.5 mM^{-1} (despite the fabrication method being the same). This is also observable across the literature: Thomas *et al*., measured a standard deviation of 71 atm^{-1} between their repeats, which equates to 12% of the K_{SV} value [293]. Additionally, Chang *et al*., noted discrepancies of up to 2% DO between their triplicates [322], Li *et al*., had differences of 1% DO within the same chamber that was meant to be uniform [325], Wang et al., were only able to reach 3.5% O_2 as the lowest achievable concentration [328] whereas Barmaki *et al*., measured below 0% concentrations compared to their own calibration [327,349]. These observations can be attributed to differences in the manual preparation of the sensors, variability of the measurement tool, the microfluidic devices, or environmental conditions. It is therefore difficult to understand the limits of detection and the resolution of these methods, as a 1% variation in the oxygen tension could influence the response of the cells but the measurement methods have variabilities larger than that value. Indeed, Ghafoory *et al*., claimed that reducing the oxygen tension from 17.5% to 15.9% was enough to increase the mRNA expression of HIF1A and induce its translocation from the cytoplasm to the nucleus in hepatocytes [349], whereas Rexius *et al*., only observed activation of HIF1-alpha for oxygen tensions below 2.5% in endothelial cells [277]. We tried to overcome this issue by self-referencing our sensors and performing calibration for each sensor before the experiments started, adapting the K_{SV} for each experiment.

We set to develop a method for continuous monitoring of the developed oxygen sensors integrated in our system such that manual handling and variability were minimised. Based on the

work by Shaegh *et al*., [337] we envisioned an electronic oxygen detector in which each sensor is self-referenced, and the measurements are automatised, removing the need for complicated set-ups on microscope stages, or changing the location of the system to perform the measurements. Our results matched with those presented by them and previous published work with a similar measurement method by Vollmer *et al*., as we also observed a quick response to changes in oxygen concentration and a linear correlation between the signal and the oxygen concentration, as established by the Stern-Volmer equation [331], which is also similar to that observed by others using this dye [293,347]. Similarly, we had a stable signal for over 24 h with a slight decline over time. We observed that this decline was related to photobleaching effect, as a reduction in the measuring frequency directly correlated with the decline. There could be other effects as explained by Koren *et al*., that are particularly relevant in sensors where the dye molecule is able to freely migrate within the matrix, as the dye molecules can move over time leading to aggregation [290]. This aggregation can result in a self-quenching phenomenon that reduces the dye sensitivity, as observed by Zhao *et al*., [348]. To overcome this, Koren *et al*., developed a method to covalently link the indicator dye to the polymer, but this was a complex process, time consuming and required significant effort for preparing functionalised indicators and couplings, while Zhao *et al*., switch the PDMS matrix with PTFE, which, again, led to a complex process involving a thermal polymerisation that required nitrogen protection. Furthermore, the diffusion of the dye in the matrix is thermodynamically favoured, that is, the dye molecules have a higher migration rate at higher temperatures, which again could be critical for our system since it would be placed in an incubator at 37ºC. For this reason, we monitored the effect of the LEDs on the temperature of the culture chambers (Figure 3.32). This can also be crucial during cell culture as cells can have negative responses to changes in the temperature of the environment. We observed that reducing the measuring frequency, as well as the measuring time, reduced the temperature increases. These rises were further reduced by adding heat sinks at the back of the LEDs. In all, our results showed good stability for the experimental time and therefore decided on the easier and more straight forward sensor fabrication method using PtTFPP embedded in PDMS (Figure 3.29). An advantage of our system compared to the one presented in Shaegh *et al*., is that our measurement system is integrated in the culture chambers, compared to the off-chip in-line system presented by them, which gives us more accurate readings of the gaseous microenvironment. In this way, we eliminate the possibility of misleading readings caused by the diffusion of oxygen through the materials into the samples between the bioreactor and the sensing platform. Similar to our results mentioned above, when testing the sensor with pre-equilibrated solutions, they also had to use a high flow rate (200 µl/min) which could indicate that their measurements were accurate. However, they do not mention the effect on the cells caused by the shear stress due to the high flow

rates. Besides the reduction of variability due to manual handling, another advantage of our platform compared to others presented in the literature is the self-referencing of each sensor to reduce misleading results due to background signals. In most of the related papers found, they used fluorescent microscopes in which the absolute fluorescence of the oxygen-sensitive dye is measured [293,320,325,328]. This does take into account potential effects of background signals, or photobleaching effects, or variability between sensors. Some works have presented self-referenced sensors by combining two or more dyes, one oxygen-sensitive and the other oxygen-insensitive, to measure the colorimetric ratio [350–353] but this requires more complex fabrication methods. In the case of Tian *et al*., the secondary dye also acted as a pH sensor, which could be of interest to obtain more information of the culture conditions during the experiment [353].

Once we were able to prove that we could obtain a platform in which an array of oxygen concentrations could be delivered to multiple culture chambers, with a stable and reliable optical oxygen sensor and an automatised system to collect the signals with minimal interference, the system had to be optimised for culturing cells. This step showed its biocompatibility and its ability to challenge the samples and collect the responses, whether that meant visually, or by integrating on-chip assays, before using it for other more complex samples. In parallel with the development of the platform, we carried out the first steps for making the devices suitable for cell culture. This work started with Device v3, which was entirely fabricated in PMMA and did not have a gas-permeable membrane. The device consisted of four culture chambers with the size of 24-well plate wells, each one with an inlet and an outlet that allowed for continuous perfusion. A pillar in a triangular shape was included in the design to serve as structural support for the top layer (avoiding its collapse when the system was closed), and for a more uniform distribution of the flow speed across the culture chamber.

In first place, we looked for a method to measure viability so we could assess the state of the cultures (keeping in mind that this method would have to be adapted later on for on-chip analysis). A great deal of papers reviewed in this report use LDH assays as their preferred way to measure viability, as under continuous perfusion conditions, the effluents can be easily collected for off-chip analysis [147,354]. Our preliminary results (culturing cells in conventional well-plates) using this assay showed a reference curve with small variation above 50% cytotoxicity, as well as a large variability. This could be due to the operator's ability, the assay reagents, or the measurement instruments. Giving that the optical density signal did not saturate, it can be hypothesised that the assay saturated, not the instrument, and therefore either the starting number of cells should be reduced, or the samples collected should be diluted before running the assay. Another source of variability of this assay was the instability of the enzyme upon storage. In order to reduce the number of assays run, we froze the samples after collection at -20°C, but this led to

a large decrease of the signal collected, indicating a lower LDH activity. Indeed, Starnes *et al.*, reported a 42% decline of LDH activity for samples stored 24 h at room temperature, which further decrease to 98% after 48 h. When the samples were stored at -80°C or -20°C, a 40% and 79% loss was observed [307,355]. It has been also reported that even the freezing rate affects the enzyme activity, as fast freezing results in activity loss, structural changes and aggregation [306] . Additionally, this method requires a positive control where the entire well is lysed to obtain the reference curve, which would mean that one of the chambers of our system would have to be used for this purpose, reducing the number of oxygen concentrations that can be tested simultaneously in a single experiment. Thus, a simpler viability assay was sought. We selected a widely used fluorometric assay based on the reduction of non-fluorescent resazurin into fluorescent resorufin caused by the mitochondrial respiration [356]. This assay gives an idea of the number of live cells present in the culture. Once the reagent is prepared, it only has to be introduced into the culture chambers, leave it for a few minutes/hours to react with the substrate and measure the fluorescence intensity. At first, following the manufacturer's protocol, the measurement was performed by placing the well plate on the microplate reader. In order to assess if this could be integrated in the chip (which cannot be placed in the microplate reader), we collected aliquots of the effluent after the incubation time and plated them in a separate well-plate, which was then measured in the microplate reader. This method has previously been used in traditional cultures [357–359], with good linearity and fast results, able to detect as little as 1000 cells in 1 h of incubation [357], as well as for organ-on-chip devices [321,360]. As shown in our results Figure 4.11, the aliquoting method yielded results similar to the ones obtained following the manufacturer's protocol, with much lower variability, potentially due to the difference in the well-plates used (cells were cultured in transparent well-plates whereas aliquots were plated in black ones, reducing the interference of the signal of adjacent wells). We therefore assessed that this method would be suitable to use in our devices.

Prior to seeding the cells in the devices, we optimised certain culture parameters on conventional static well plates to ensure these were not affecting the cells and could mislead our experiments. Due to the properties of PMMA, the chambers were impermeable to gases, avoiding interchange with the incubator, and therefore no possibility to equilibrate the pH with CO2. We set out to find a culture medium that could maintain the pH without CO2 influx, which we attempted with MEM adding HEPES and with Leibovitz culture media. Multiple passages of HeLa cells cultured in these different conditions showed that MEM was not suitable for our chosen cell type due to the continuous decline in viability and the low growth rate compared to the cells cultured in DMEM (used as control). On the other hand, the cells cultured in Leibovitz, although with a slower growth rate, maintained a good viability over several passages, and therefore, was our chosen medium for experiments from this point on.

We also checked the biocompatibility of the materials used in our system by measuring the viability and adherence of the cells to those materials in modified conventional well plates. We deposited PMMA cut outs with and without collagen coating on the bottom of the well plates, and we also looked at the adherence on the sensors by depositing them on the bottom of the plates, with or without the PMMA cut outs, to assess the effect of each material, and their joint effect on the cell viability. Analysing the images, the cells showed good morphology on the PMMA substrates, but quite bad adherence on the sensor, which has also been reported by Thomas *et al.*, 2009. This could be due to the bad adherence of the cells to the hydrophobic PDMS or to the PtTFPP dye leaching out and damaging the cells. To overcome this, they added a PTFE layer to stop the migration of the molecules and another layer of PDMS coated with fibronectin to promote adhesion. In our chambers, the oxygen sensor only occupied a small section of the surface, and the cells not in direct contact with the sensor were not affected; however, this will become an issue in later versions of the device and will have to be revisited.

With these learnings, we moved onto seeding the cells into the devices to check if they were able to sustain cell viability and proliferation compared to static conventional well plates. After harvesting the cells, they were resuspended in fresh medium at the desired concentration and then seeded into the culture chambers. In most conventional cultures and microfluidic devices, this is done via pipetting, to reduce the impact on the cells. For ease of operation, we compared seeding the cells via traditional pipetting with a syringe transfer. In this method, the resuspended cells are transferred into a syringe and then seeded into the chambers by connecting the syringe to the inlets with PTFE tubing. Despite the many additional steps and the potential stress caused by the flow of the cells through the tubing, the cells looked unaffected, proving the validity of our protocol. We then studied the seeding density, as it can impact cell viability and survival to flow [361,362]. This value does not seem to be detailed in the methods of the papers studied, as each system is optimised for the specific experimental requirements. We observed that in our system, higher seeding densities led to better survival of the cells on the chip. Finally, we looked into the optimal flow rate for the perfusion of the chambers. We did not observe significant differences in the range observed, however, less attached cells were detected at the highest flow rate, an indication of cells lifting off the substrate or dying because of excessive shear stress. The range of flow rates used in literature varies depending on the application, but in general range between 1 and 10 µL/min (30µL/h [363], 1 µL/min [322], 2 µL/min [328], 10 µL/min [320,364]). We chose 2.5 µL/min for the subsequent experiments to avoid nutrient depletion while ensuring low shear stress and lifting of the cells. This value was reduced to 1 µL/min when the chip design changed to avoid gradients in the chamber (as observed in the simulations in Figure 3.46). It was important to reduce the shear stress in our system given that it has previously

been reported that the presence of shear stress significantly alters the proteomic response of pulmonary endothelial cells to hypoxia [365].

Thus far, we could only assess the adherence and viability visually, as a viability assay on-chip could only be optimised once there were live cells seeded in the chambers. Once we had a reliable protocol, the assay previously developed was adjusted for the chips. It proved to be easy and straight-forward. Similarly, to the results observed by Stucki *et al*., with this same assay, the samples cultured dynamically showed a higher number of live cells compared to static cultures. We did observe a high variability between experiments. This could be due to discrepancies in the seeding concentrations, as they are prepared and seeded manually. This has been observed by others [322,332]. To overcome it, they quantified the initial number of cells in each experiment before starting the challenge in order to obtain the baseline and normalise their results, which could be implemented in our system given the non-toxicity of the resazurin dye.

As previously explained, the devices used up until this point had to be discarded due to their inability to produce an oxygen gradient. The new devices were more complex and integrated a gas permeable PDMS membrane in between the PMMA layers (Device v4). Thus, the substrate on which the cells were cultured changed, which meant changes in the surface chemistry and stiffness. It also meant that the sterilisation protocol had to be reviewed. Most microfluidic devices based on PDMS use ethanol to clean the channels before introducing the cells [327,366]. This was not possible in our system due to the incompatibility of PMMA with solvents. Two other methods for chip sterilisation were tried: rinse with bleach, and UV sterilisation. Due to the high porosity of the PDMS, bleach is readily absorbed and is later diffused out, damaging the cells. On the other hand, UV treatment could affect the properties of the PDMS [367]. It was observed that treatment with bleach followed by a long soak in DI water reduced the bleach absorbed in the membrane. Nevertheless, the number of live cells in the treated chamber compared to the control was still low, which can be attributed to the hydrophobicity of the PDMS. To create a more engaging environment for the cells we coated our membranes with collagen type I, an extracellular matrix protein, which improved the cell adherence, specially at longer incubation times. However, collagen is not the most commonly used extracellular matrix protein. Usually, fibronectin leads to better adhesion in HeLa cells, although the concentration and incubation times vary widely across the literature [368,369]. Yet, we lacked access to this reagent. Others have used more complicated processes to increase cell attachment, such as treating the PDMS with poly-L-lysine to provide a bioactive surface [335] or treating with oxygen plasma and polyvinylpyrrolidone [364].

Another factor of our device that can impact negatively cell survival and adherence is the stiffness of the membrane. Indeed, Li *et al*., 2016 observed that cells aggregated together and exhibited poor adhesion when they added less curing agent to the PDMS prepolymer, which leads

to a softer polymer. When they increased the stiffness, more cells anchored on the surface, suggesting that the stiffness of the membrane was related to cell adhesion and proliferation. In the same manner, we observed that cells tended to aggregate on regions sustained by the pillars underneath our membrane - the pillars were added to avoid the soft membrane from collapsing and blocking the chamber underneath. Thus, we made a series of changes to the bottom layer to provide more rigidity to the membrane while still allowing for gases to diffuse through. The rest of the parameters of the culture on-chip established with the previous design were maintained, as they were not affected.

With a consistent fabrication of the devices, a reliable method to generate and monitor oxygen concentrations, and an optimised on-chip culture protocol, the functionality of the system was tested by subjecting HeLa cells cultured in the chambers to different oxygen conditions. To do this, the system was first evaluated by subjecting the cells to either 100% or 0% oxygen levels, and hypoxia-related factors (*CA9* and *VEGF*) were studied. Our initial results showed a high variability in the expression of these genes, which can be attributed to the instability of the housekeeping gene that was selected (*ACTB*). *ACTB* is a cytoskeleton component whose main function is related to cell morphology maintenance. In our system, the cells were subjected to multiple mechanical stresses, mainly the stiffness of the substrate and the shear stress caused by the continuous perfusion. This is a source of variability for this reference gene [370], therefore confounding the measurements of the changes of the hypoxia-related genes. To test this hypothesis, *ACTB* was directly compared to *TOP1* and *YWHAZ*. The levels of dispersion of the C_T values were assessed calculating the coefficient of variation, and showed a 4-fold reduction of the variability of both *TOP1* and *YWHAZ* compared to *ACTB*. This was further proved when in later experiments, using *TOP1* and *YWHAZ* as housekeeping genes, much more consistent results with a 12-fold and 3-fold increase in the expressions of *CA9* and *VEGF* respectively were obtained. It is worth mentioning that this reduction in variability of the HKG could also be attributed to the higher specificity of the Taqman technology compared to SYBR Green. A final experiment subjecting the cells to a gradient of oxygen tensions indicated the potential of the system to provide specific gaseous microenvironments and to observe the differences in the cell response across the chambers. Although the upregulation trend was very clear, even with these housekeeping genes there was still a high variability between experiments. This could be due to the varying starting material, as mentioned above, since not all the chambers had the same initial number of cells. The upregulation of these factors is in accordance with the observations made by others [371–375], and evidences the ability of our system to subject the samples to different oxygen tensions and to collect those samples for analysis using conventional methods. We were not able to integrate both viability and gene expression measurements, but we could assess visually the

condition of the cells after the exposure to hypoxia. Similar to Sun *et al*., we did not observe significant morphological differences between the cells under hypoxic and normoxic conditions, showing the limited effect of hypoxia on cancer cells [324]. However, this could be also due to the fact that dead cells are lifted off the substrate and carried out of the culture chambers by the flow, as noted by Wang *et al*., [328]. Indeed, Barmaki *et al*., observed that 2.3-fold fewer cells remained adhered under hypoxic conditions compared to the control [327]. As discussed above, poor adherence could also be related to the mechanical stresses on the cells and could be further accentuated by the hypoxic environment. Interestingly, Wulftange *et al*., observed that cancer cells had lower growth rates under 3% O_2 concentrations compared to 21% O_2, but when the cells were subjected to a gradient between 0 and 3% O_2, they had similar growth rates to the normoxic condition, suggesting that geometric delivery of oxygen could be an important factor [376].

Overall, in this work we have presented a microfluidic device for the culture of live tissues under controlled gaseous microenvironments, with the ability to monitor the effects and responses of the samples to changes in the microenvironmental parameters. This platform offers high versatility in the type of samples that can be used, from immortalised cells to whole tissue samples, and can be integrated with multiple sensors, as well as with different assays.

Chapter 6. Conclusions and future work

This thesis has presented the development and optimisation of a microfluidic device able to generate and monitor an oxygen gradient across multiple chambers in which cells can be cultured. This system allows for the study of the cell response to specific oxygen tensions. It addresses challenges currently facing the biomedical, clinical, and pharmaceutical research fields: it has the potential to become a tool to study the effect of microenvironmental factors in the survival of tissues *ex vivo*, and to improve the viability of the samples and increase their lifespan while maintaining a high level of physiological accuracy in their responses.

The platform consists of a microfluidic device fabricated in biocompatible materials (PMMA, PDMS and glass) with two layers separated by a gas permeable membrane. The top one consists of four chambers for culturing cells or tissues under continuous perfusion without recirculation, to allow for waste removal and provide nutrients, as well as for downstream analysis if desired. The bottom layer contains a network of channels and chambers that allow for the flow of gases underneath the culture chambers, thus allowing for gas diffusion and equilibration between the layers through the membrane, providing control over the gaseous microenvironment in which the samples are cultured.

An integrated oxygen sensing system was also developed to monitor the oxygen concentrations in the culture chambers. An oxygen-sensitive dye embedded in a gas permeable polymer was deposited on the substrates of the chambers and acted as the optical oxygen sensor. The fluorescent emission was captured by photodiodes, and after processing the signal, the oxygen concentration in the culture chambers was determined. In this manner, a measurement of the microenvironmental conditions in which the samples are being cultured is provided. With these integrated sensors, the ability of the system to generate an oxygen gradient was proven. The desired oxygen concentrations were obtained by flowing mixtures of atmospheric air and nitrogen gas at different ratios through the serial dilutor.

A protocol to culture cells within the device was optimised. Steps for cleaning, sterilising, priming, and seeding cells were refined to allow for the cells to be cultured and maintain their viability for at least 48 h. A fluorometric viability assay based on the reduction of resazurin was adapted to assess the viability of the samples on chip. Even though there was some variability between the chambers in terms of the number of cells and their viability, this system provided a means for the study of the cellular response to hypoxic environments. An upregulation of the hypoxic markers *CA9* and *VEGF* was observed, and even the system showed potential to study the responses of these markers when subjecting the cells to an oxygen gradient across the chambers, indicating the ability of the system for subjecting tissues to a hypoxic challenge and for monitoring their responses.

Oxygen is a key parameter that is often overlooked in traditional cell cultures. Cells consume oxygen continuously, but the oxygen tension in the pericellular environment is usually assumed as constant and sufficient. Microfluidic technology allows for the tight control of the oxygen microenvironment without the need of bulky instruments or hypoxic chambers. Most devices controlling the oxygen microenvironment within microfluidic chambers do so with cell lines grown as a monolayer [144,224,225]. Due to timing issues, this project used cell lines but can be considered a stepping-stone towards the long-term culture of whole tissue samples, such as MDT or PCTS, in the quest for improved *in vitro* models. Therefore, the chambers had to be much larger compared to other published works, providing good accessibility to the samples. This increased the difficulty of controlling the microenvironment and the many challenges that had to be overcome have been described in this thesis. Some research papers that describe the control of oxygen tension in whole tissue slices within microfluidic devices are focused on the effect of oxygen changes during acute events (e.g., neuronal function during hypoxic insults [141]), but they do not focus on the effects on the long-term survival, neither do they study how oxygen affects their lifespan. Richardson *et al.*, 2020 cultured mouse colon explants for 72 h in low and ambient dissolved oxygen and observed that the tissues were viable in both conditions, but the bacterial presence was enhanced at the lower oxygen level since most bacteria in the colon are anaerobic, proving the importance of mimicking the physiological environment to obtain accurate models and responses [118]. However, they obtained low oxygen tensions by adding an oxygen scavenging salt (Na_2SO_3) and so, they had limited control over the oxygen levels provided to the tissues. Microfluidic technology also allows for the integration of sensors to monitor microenvironmental parameters. Including them in the culture systems provides more information of the culture conditions, which allows for the study of the effect of each parameter, or combination of, on the samples and their responses. Optimising the conditions of *in vitro* models to mimic the physiological environment would increase the prediction power of those models, which would have a vital impact on research and medicine. This project aimed to bring the capabilities of previously published works together by providing a platform for the culture of cells and tissue samples with the ability to control and monitor the gaseous microenvironment.

Additionally, a major drawback of *ex vivo* models is the low throughput, compared to cell monolayer cultures. The system has four chambers, each with a different oxygen concentration to test an array of conditions simultaneously, which would be particularly useful for *ex vivo* studies where the sample availability is limited, or for testing in a clinical setting, to test simultaneously the samples of a single patient. The presented platform has potential to be scaled up in terms of the number of chambers and the number of devices, as they have the same footprint as a conventional well-plate, and also in terms of the number of oxygen concentrations that can

be achieved. Possibilities to automate it can also increase the output as less human interaction would be required to run several platforms in parallel.

The system focussed on proof of concept, and although the results obtained were encouraging, more experiments are required to build confidence in the platform and fully prove its reliability, robustness, and functionality. If more time was available, the first step would be to prove the ability of the system to measure the responses to the hypoxic challenge with good reproducibility. In order to do that, other HKGs should be tested. Due to the high variability of the selected HKG, it was not possible to obtain conclusive and consistent results. To elucidate the origin of this variability, the aforementioned experiments should be repeated with other HKGs such as those proposed in Section 4.7. Switching to a more sensitive RNA isolation kit would also help reduce that variability, especially in the chambers with hypoxic conditions, where the viability and the amount of RNA extracted tends to be lower. Some commercial kits are specially designed for samples with limited starting material, like in our case. These kits purify higher amounts of RNA with more efficient gDNA (guide DNA) removal, improving the quality of the samples.

Once the protocol for this experiment is optimised and consistent results obtained, the next step would be to subject the samples to oxygen gradients generated by the serial dilutor. This would allow the challenge of the cells to intermediate oxygen concentrations, not only 0 or 100%, and thus obtain an oxygen-dependent response. It would also give information on the threshold oxygen tension at which the cells trigger the hypoxic response, which would allow for refinement of the oxygen gradient. It would also be important to include methods to regulate the CO_2 levels, neglected in this work.

Furthermore, additional viability measurements could be included to provide more information on the condition of the cells. The data obtained from the gene expression changes could be complemented with the viability assay developed in this project. Other hypoxia-related genes could be examined such as *LOXL2* [377], *EGFR* [378] or heat shock proteins [379]. Other potential assays could include direct measurements of HIF activity, for example, looking at the translocation of HIF to the nucleus by immunofluorescence assay, or phosphorylation of HIF by western blots and ELISA. However, it should be taken into account that HIF degrades very fast in the presence of oxygen and therefore direct measurements are complicated and potentially misleading. Indirect measurements of HIF could include the use of HIF reporter assays, although these require infection of the cells with lentivirus or the use of modified cell lines, which require highly specific skills and laboratory infrastructures. The final test to validate the platform would be to perform

these experiments using other cell types more sensitive to hypoxia such as endothelial or epithelial cells, or even primary cells to prove the ability of the system to maintain a wide variety of tissue types.

Once the system has been proven to be functional and reliable, further improvements could be explored to expand the capabilities of the platform. This further work is outlined below:

1) Device design:

The devices are fabricated in PMMA by bonding multiple layers using chloroform vapour. The layers are manually aligned, which leads to misalignments. Reducing the number of steps in the fabrication procedure, as well as the need for manual alignment would improve the outcome and reduce the variability between the devices. This could be potentially achieved by using micro-milled devices. Additionally, the assembled device is mounted onto the chip holders and manually aligned with the inlets and outlets. Modifications to the chip holders could be made to include a slot in which the device can fit fitted and locked, in a Lego-like fashion, to increase the user-friendliness of the platform. Other future prospects could include methods to multiplex this concept to increase the throughput.

2) Oxygen gradient control:

The oxygen gradient generator consists of a network of microfluidic channels in a split-and-combine design to mix gases and generate four different oxygen concentrations at the outputs. This design could be modified to obtain different gradient profiles, and/or upgraded to increase the number of concentrations generated. One of the challenges faced in this project was the lack of accurate control of the gases, because only pressure controllers were available. Mass flow controllers give a much higher level of control over the flow and would allow accurate gas mixtures to be injected in the gradient generator inlets to fine tune concentrations at the outlets. Automation of the oxygen gradient generation and monitoring system would also be an interesting pursuit and would further increase the user-friendliness of the system.

3) Tissue models:

Cells adapt to the environment. In this project, the immortalised cell line used has been adapting over several decades to the standard culture conditions: 5% CO_2, 20% O_2, stiff substrate and no flow. Therefore, changes in those parameters, such a culture in the devices, even if they are physiologically more accurate, would trigger responses. It would be interesting to explore other tissues such primary cells after direct extraction from patients, or with a low passage, so they still preserve their phenotypes, and whole tissue samples, such as PCTS. This would require further

exploration of the optimal culture conditions (perfusion flow rate, thickness of the sample, viability assays, culture medium…) and include other tests to check on the functionality, for example, treating PCLS with methacholine to provoke airway constriction [380].

Bibliography

[1] Cavero, I., Guillon, J. M., and Holzgrefe, H. H., 2019, "Human Organotypic Bioconstructs from Organ-on-Chip Devices for Human-Predictive Biological Insights on Drug Candidates," Expert Opin Drug Saf, **18**(8), pp. 651–677.

[2] Shamir, E. R., and Ewald, A. J., 2014, "Three-Dimensional Organotypic Culture: Experimental Models of Mammalian Biology and Disease," Nat Rev Mol Cell Biol, **15**(10), pp. 647–664.

[3] Herrmann, K., 2019, "Beyond the 3Rs: Expanding the Use of Human-Relevant Replacement Methods in Biomedical Research," ALTEX, **36**(3), pp. 343–352.

[4] Benam, K. H., Dauth, S., Hassell, B., Herland, A., Jain, A., Jang, K.-J., Karalis, K., Kim, H. J., MacQueen, L., Mahmoodian, R., Musah, S., Torisawa, Y., van der Meer, A. D., Villenave, R., Yadid, M., Parker, K. K., and Ingber, D. E., 2015, "Engineered In Vitro Disease Models," Annual Review of Pathology: Mechanisms of Disease, **10**(1), pp. 195–262.

[5] Roser, M., Ortiz-Ospina, E., and Ritchie, H., 2013, "Life Expectancy," OurWorldInData.org [Online]. Available: https://ourworldindata.org/life-expectancy#how-did-life-expectancy-change-over-time.

[6] Kola, I., and Landis, J., 2004, "Can the Pharmaceutical Industry Reduce Attrition Rates?," Nat Rev Drug Discov, **3**(8), pp. 711–716.

[7] European Federation of Pharmaceutical Industries and Associations, 2019, *The Pharmaceutical Industry in Figures*.

[8] Hay, M., Thomas, D. W., Craighead, J. L., Economides, C., and Rosenthal, J., 2014, "Clinical Development Success Rates for Investigational Drugs," Nat Biotechnol, **32**(1), pp. 40–51.

[9] Wong, C. H., Siah, K. W., and Lo, A. W., 2019, "Estimation of Clinical Trial Success Rates and Related Parameters," Biostatistics, **20**(2), pp. 273–286.

[10] FDA, 2018, "The Drug Development Process" [Online]. Available: https://www.fda.gov/patients/drug-development-process/step-1-discovery-and-development. [Accessed: 03-Sep-2023].

[11] Friedman, L. M., Furberg, C. D., and DeMets, D. L., 2010, "Introduction to Clinical Trials," *Fundamentals of Clinical Trials*, Springer New York, New York, NY, pp. 1–18.

[12] Arrowsmith, J., and Miller, P., 2013, "Phase II and Phase III Attrition Rates 2011–2012," Nat Rev Drug Discov, **12**(8), pp. 569–569.

[13] Paul, S. M., Mytelka, D. S., Dunwiddie, C. T., Persinger, C. C., Munos, B. H., Lindborg, S. R., and Schacht, A. L., 2010, "How to Improve RD Productivity: The Pharmaceutical Industry's Grand Challenge," Nat Rev Drug Discov, **9**(3), pp. 203–214.

[14] Personalized Medicine Coalition, 2017, *The Personalized Medicine Report. Opportunity, Challenges, and the Future*.

[15] Sciences, A. of M., 2015, *Stratified, Personalised or P4 Medicine: A New Direction for Placing the Patient at the Centre of Healthcare and Health Education*, Southampton, UK.

[16] Personalized Medicine Coalition, 2014, *The Case for Personalized Medicine 4th Edition*, Washington DC.

[17] Academy of Medical Sciences, 2015, *Stratified, Personalised or P4 Medicine: A New Direction for Placing the Patient at the Centre of Healthcare and Health Education*, Southampton, UK.

[18] Personalized Medicine Coalition, 2017, *The Personalized Medicine Report. Opportunity, Challenges, and the Future*.

[19] van den Berg, A., Mummery, C. L., Passier, R., and van der Meer, A. D., 2019, "Personalised Organs-on-Chips: Functional Testing for Precision Medicine," Lab Chip, **19**(2), pp. 198–205.

[20] Li, M., de Graaf, I. A. M., and Groothuis, G. M. M., 2016, "Precision-Cut Intestinal Slices: Alternative Model for Drug Transport, Metabolism, and Toxicology Research," Expert Opin Drug Metab Toxicol, **12**(2), pp. 175–190.

[21] Rous, P., and Jones, F. S., 1916, "A Method for Obtaining Suspensions of Living Cells from the Fixed Tissues, and for the Plating out of Individual Cells," Proceedings of the Society for Experimental Biology and Medicine, **13**(4), p. 73.

[22] Kaur, G., and Dufour, J. M., 2012, "Cell Lines," Spermatogenesis, **2**(1), pp. 1–5.

[23] Macdonald, C., 1990, "Development of New Cell Lines for Animal Cell Biotechnology," Crit Rev Biotechnol, **10**(2), pp. 155–178.

[24] Kapałczyńska, M., Kolenda, T., Przybyła, W., Zajączkowska, M., Teresiak, A., Filas, V., Ibbs, M., Bliźniak, R., Łuczewski, Ł., and Lamperska, K., 2018, "2D and 3D Cell Cultures – a Comparison of Different Types of Cancer Cell Cultures," Archives of Medical Science, **14**(4), pp. 910–919.

[25] Watson, D. E., Hunziker, R., and Wikswo, J. P., 2017, "Fitting Tissue Chips and Microphysiological Systems into the Grand Scheme of Medicine, Biology, Pharmacology, and Toxicology.," Exp Biol Med (Maywood), **242**(16), pp. 1559–1572.

[26] Antoni, D., Burckel, H., Josset, E., and Noel, G., 2015, "Three-Dimensional Cell Culture: A Breakthrough in Vivo," Int J Mol Sci, **16**(12), pp. 5517–5527.

[27] Astashkina, A., Mann, B., and Grainger, D. W., 2012, "A Critical Evaluation of in Vitro Cell Culture Models for High-Throughput Drug Screening and Toxicity," Pharmacol Ther, **134**(1), pp. 82–106.

[28] Ryan, J. A., 2003, "Introduction to Animal Cell Culture," pp. 1–8.

[29] Maqsood, M. I., Matin, M. M., Bahrami, A. R., and Ghasroldasht, M. M., 2013, "Immortality of Cell Lines: Challenges and Advantages of Establishment," Cell Biol Int, **37**(10), pp. 1038–1045.

[30] Hirsch, C., and Schildknecht, S., 2019, "In Vitro Research Reproducibility: Keeping up High Standards," Front Pharmacol, **10**.

[31] Popescu, N. C., DiPaolo, J. A., and Amsbaugh, S. C., 1987, "Integration Sites of Human Papillomavirus 18 DNA Sequences on HeLa Cell Chromosomes," Cytogenet Genome Res, **44**(1), pp. 58–62.

[32] Hoppe-Seyler, F., and Butz, K., 1993, *Repression of Endogenous P53 Transactivation Function in HeLa Cervical Carcinoma Cells by Human Papillomavirus Type 16 E6, Human Mdm-2, and Mutant P53*.

[33] Takahashi, K., and Yamanaka, S., 2006, "Induction of Pluripotent Stem Cells from Mouse Embryonic and Adult Fibroblast Cultures by Defined Factors," Cell, **126**(4), pp. 663–676.

[34] Takahashi, K., Tanabe, K., Ohnuki, M., Narita, M., Ichisaka, T., Tomoda, K., and Yamanaka, S., 2007, "Induction of Pluripotent Stem Cells from Adult Human Fibroblasts by Defined Factors," Cell, **131**(5), pp. 861–872.

[35] Tobita, K., Liu, L. J., Janczewski, A. M., Tinney, J. P., Nonemaker, J. M., Augustine, S., Stolz, D. B., Shroff, S. G., and Keller, B. B., 2006, "Engineered Early Embryonic Cardiac Tissue Retains Proliferative and Contractile Properties of Developing Embryonic Myocardium," American Journal of Physiology-Heart and Circulatory Physiology, **291**(4), pp. H1829–H1837.

[36] Bokhari, M., Carnachan, R. J., Cameron, N. R., and Przyborski, S. A., 2007, "Culture of HepG2 Liver Cells on Three Dimensional Polystyrene Scaffolds Enhances Cell Structure and Function during Toxicological Challenge," J Anat, **211**(4), pp. 567–576.

[37] Severn, C. E., Eissa, A. M., Langford, C. R., Parker, A., Walker, M., Dobbe, J. G. G., Streekstra, G. J., Cameron, N. R., and Toye, A. M., 2019, "Ex Vivo Culture of Adult CD34+ Stem Cells Using Functional Highly Porous Polymer Scaffolds to Establish Biomimicry of the Bone Marrow Niche," Biomaterials, **225**(September), p. 119533.

[38] Sung, J. H., Yu, J., Luo, D., Shuler, M. L., and March, J. C., 2011, "Microscale 3-D Hydrogel Scaffold for Biomimetic Gastrointestinal (GI) Tract Model," Lab Chip, **11**(3), pp. 389–392.

[39] Lin, R. Z., and Chang, H. Y., 2008, "Recent Advances in Three-Dimensional Multicellular Spheroid Culture for Biomedical Research," Biotechnol J, **3**(9–10), pp. 1172–1184.

[40] Spence, J. R., Mayhew, C. N., Rankin, S. A., Kuhar, M. F., Vallance, J. E., Tolle, K., Hoskins, E. E., Kalinichenko, V. V., Wells, S. I., Zorn, A. M., Shroyer, N. F., and Wells, J. M., 2011, "Directed Differentiation of Human Pluripotent Stem Cells into Intestinal Tissue in Vitro," Nature, **470**(7332), pp. 105–110.

[41] Lancaster, M. A., Renner, M., Martin, C. A., Wenzel, D., Bicknell, L. S., Hurles, M. E., Homfray, T., Penninger, J. M., Jackson, A. P., and Knoblich, J. A., 2013, "Cerebral Organoids Model Human Brain Development and Microcephaly," Nature, **501**(7467), pp. 373–379.

[42] Sakib, S., Uchida, A., Valenzuela-Leon, P., Yu, Y., Valli-Pulaski, H., Orwig, K., Ungrin, M., and Dobrinski, I., 2019, "Formation of Organotypic Testicular Organoids in Microwell Culture," Biol Reprod, **100**(6), pp. 1648–1660.

[43] Huch, M., Gehart, H., Van Boxtel, R., Hamer, K., Blokzijl, F., Verstegen, M. M. A., Ellis, E., Van Wenum, M., Fuchs, S. A., De Ligt, J., Van De Wetering, M., Sasaki, N., Boers, S. J., Kemperman, H., De Jonge, J., Ijzermans, J. N. M., Nieuwenhuis, E. E. S., Hoekstra, R., Strom, S., Vries, R. R. G., Van Der Laan, L. J. W., Cuppen, E., and Clevers, H., 2015, "Long-Term Culture of Genome-Stable Bipotent Stem Cells from Adult Human Liver," Cell, **160**(1–2), pp. 299–312.

[44] Nath, S., and Devi, G. R., 2016, "Three-Dimensional Culture Systems in Cancer Research: Focus on Tumor Spheroid Model," Pharmacol Ther, **163**, pp. 94–108.

[45] Lee, J. W., Krasnodembskaya, A., McKenna, D. H., Song, Y., Abbott, J., and Matthay, M. A., 2013, "Therapeutic Effects of Human Mesenchymal Stem Cells in Ex Vivo Human Lungs Injured with Live Bacteria," Am J Respir Crit Care Med, **187**(7), pp. 751–760.

[46] O'Neill, J. D., Anfang, R., Anandappa, A., Costa, J., Javidfar, J., Wobma, H. M., Singh, G., Freytes, D. O., Bacchetta, M. D., Sonett, J. R., and Vunjak-Novakovic, G., 2013, "Decellularization of Human and Porcine Lung Tissues for Pulmonary Tissue Engineering," Annals of Thoracic Surgery, **96**(3), pp. 1046–1056.

[47] Schwab, A., Meeuwsen, A., Ehlicke, F., Hansmann, J., Mulder, L., Smits, A., Walles, H., and Kock, L., 2017, "Ex Vivo Culture Platform for Assessment of Cartilage Repair Treatment Strategies," ALTEX, **34**(2), pp. 267–277.

[48] de Graaf, I. A. M., de Kanter, R., de Jager, M. H., Camacho, R., Langenkamp, E., van de Kerkhof, E. G., and Groothuis, G. M. M., 2006, "Empirical validation of a rat in vitro organ slice model as a tool for in vivo clearance prediction", Drug Metabolism and Disposition, **34**(4), pp. 591–599.

[49] de Graaf, I. A. M., Olinga, P., De Jager, M. H., Merema, M. T., De Kanter, R., Van De Kerkhof, E. G., and Groothuis, G. M. M., 2010, "Preparation and Incubation of Precision-Cut Liver and Intestinal Slices for Application in Drug Metabolism and Toxicity Studies," Nat Protoc, **5**(9), pp. 1540–1551.

[50] Siwczak, F., Hiller, C., Pfannkuche, H., and Schneider, M. R., 2023, "Culture of Vibrating Microtome Tissue Slices as a 3D Model in Biomedical Research," J Biol Eng, **17**(1).

[51] Granitzny, A., Knebel, J., Schaudien, D., Braun, A., Steinberg, P., Dasenbrock, C., and Hansen, T., 2017, "Maintenance of High Quality Rat Precision Cut Liver Slices during Culture to Study Hepatotoxic Responses: Acetaminophen as a Model Compound," Toxicology in Vitro, **42**(May), pp. 200–213.

[52] Wu, X., Roberto, J. B., Knupp, A., Kenerson, H. L., Truong, C. D., Yuen, S. Y., Brempelis, K. J., Tuefferd, M., Chen, A., Horton, H., Yeung, R. S., and Crispe, I. N., 2018, "Precision-Cut Human Liver Slice Cultures as an Immunological Platform," J Immunol Methods, **455**(February), pp. 71–79.

[53] Schwerdtfeger, L. A., Ryan, E. P., and Tobet, S. A., 2016, "An Organotypic Slice Model for Ex Vivo Study of Neural, Immune, and Microbial Interactions of Mouse Intestine," Am J Physiol Gastrointest Liver Physiol, **310**(4), pp. G240–G248.

[54] Temann, A., Golovina, T., Neuhaus, V., Thompson, C., Chichester, J. A., Braun, A., and Yusibov, V., 2017, "Evaluation of Inflammatory and Immune Responses in Long-Term Cultured Human Precision-Cut Lung Slices," Hum Vaccin Immunother, **13**(2), pp. 351–358.

[55] Starokozhko, V., Abza, G. B., Maessen, H. C., Merema, M. T., Kuper, F., and Groothuis, G. M. M., 2015, "Viability, Function and Morphological Integrity of Precision-Cut Liver Slices during Prolonged Incubation: Effects of Culture Medium," Toxicology in Vitro, **30**(1), pp. 288–299.

[56] Neuhaus, V., Schaudien, D., Golovina, T., Temann, U. A., Thompson, C., Lippmann, T., Bersch, C., Pfennig, O., Jonigk, D., Braubach, P., Fieguth, H. G., Warnecke, G., Yusibov, V., Sewald, K.,

and Braun, A., 2017, “Assessment of Long-Term Cultivated Human Precision-Cut Lung Slices as an Ex Vivo System for Evaluation of Chronic Cytotoxicity and Functionality,” Journal of Occupational Medicine and Toxicology, **12**(1), pp. 1–8.

[57] Duff, K., Noble, W., Gaynor, K., and Matsuoka, Y., 2002, “Organotypic Slice Cultures from Transgenic Mice as Disease Model Systems,” Journal of Molecular Neuroscience, **19**(3), pp. 317–320.

[58] Croft, C. L., Cruz, P. E., Ryu, D. H., Ceballos-Diaz, C., Strang, K. H., Woody, B. M., Lin, W. L., Deture, M., Rodríguez-Lebrón, E., Dickson, D. W., Chakrabarty, P., Levites, Y., Giasson, B. I., and Golde, T. E., 2019, “RAAV-Based Brain Slice Culture Models of Alzheimer’s and Parkinson’s Disease Inclusion Pathologies,” Journal of Experimental Medicine, **216**(3), pp. 539–555.

[59] Martin, I., Wendt, D., and Heberer, M., 2004, “The Role of Bioreactors in Tissue Engineering,” Trends Biotechnol, **22**(2), pp. 80–86.

[60] Blume, C., and Davies, D. E., 2013, “In Vitro and Ex Vivo Models of Human Asthma,” European Journal of Pharmaceutics and Biopharmaceutics, **84**(2), pp. 394–400.

[61] Karra, N., Swindle, E. J., and Morgan, H., 2019, “Drug Delivery for Traditional and Emerging Airway Models,” Organs-on-a-Chip, **1**(December 2019), p. 100002.

[62] Chang, M. G., Zhang, Y., Chang, C. Y., Xu, L., Emokpae, R., Tung, L., Marbán, E., and Abraham, M. R., 2009, “Spiral Waves and Reentry Dynamics in an In Vitro Model of the Healed Infarct Border Zone,” Circ Res, **105**(11), pp. 1062–1071.

[63] Beauchamp, P., Desplantez, T., McCain, M. L., Li, W., Asimaki, A., Rigoli, G., Parker, K. K., Saffitz, J. E., and Kleber, A. G., 2012, “Electrical Coupling and Propagation in Engineered Ventricular Myocardium with Heterogeneous Expression of Connexin43,” Circ Res, **110**(11), pp. 1445–1453.

[64] March, S., Ng, S., Velmurugan, S., Galstian, A., Shan, J., Logan, D. J., Carpenter, A. E., Thomas, D., Sim, B. K. L., Mota, M. M., Hoffman, S. L., and Bhatia, S. N., 2013, “A Microscale Human Liver Platform That Supports the Hepatic Stages of Plasmodium Falciparum and Vivax,” Cell Host Microbe, **14**(1), pp. 104–115.

[65] Sun, L., Wang, X., and Kaplan, D. L., 2011, “A 3D Cartilage – Inflammatory Cell Culture System for the Modeling of Human Osteoarthritis,” Biomaterials, **32**(24), pp. 5581–5589.

[66] De Lange, W. J., Hegge, L. F., Grimes, A. C., Tong, C. W., Brost, T. M., Moss, R. L., and Ralphe, J. C., 2011, “Neonatal Mouse-Derived Engineered Cardiac Tissue: A Novel Model System for Studying Genetic Heart Disease,” Circ Res, **109**(1), pp. 8–16.

[67] Parker, J., Sarlang, S., Thavagnanam, S., Williamson, G., O'Donoghue, D., Villenave, R., Power, U., Shields, M., Heaney, L., and Skibinski, G., 2010, "A 3-D Well-Differentiated Model of Pediatric Bronchial Epithelium Demonstrates Unstimulated Morphological Differences Between Asthmatic and Nonasthmatic Cells," Pediatr Res, **67**(1), pp. 17–22.

[68] Comer, D. M., Kidney, J. C., Ennis, M., and Elborn, J. S., 2013, "Airway Epithelial Cell Apoptosis and Inflammation in COPD, Smokers and Nonsmokers," European Respiratory Journal, **41**(5), pp. 1058–1067.

[69] Fang, H.-W., Fang, S.-B., Chiang Chiau, J.-S., Yeung, C.-Y., Chan, W.-T., Jiang, C.-B., Cheng, M.-L., and Lee, H.-C., 2010, "Inhibitory Effects of Lactobacillus Casei Subsp. Rhamnosus on Salmonella Lipopolysaccharide-Induced Inflammation and Epithelial Barrier Dysfunction in a Co-Culture Model Using Caco-2/Peripheral Blood Mononuclear Cells," J Med Microbiol, **59**(5), pp. 573–579.

[70] Chamcheu, J. C., Pal, H. C., Siddiqui, I. A., Adhami, V. M., Ayehunie, S., Boylan, B. T., Noubissi, F. K., Khan, N., Syed, D. N., Elmets, C. A., Wood, G. S., Afaq, F., and Mukhtar, H., 2015, "Prodifferentiation, Anti-Inflammatory and Antiproliferative Effects of Delphinidin, a Dietary Anthocyanidin, in a Full-Thickness Three-Dimensional Reconstituted Human Skin Model of Psoriasis," Skin Pharmacol Physiol, **28**(4), pp. 177–188.

[71] Miller, C., George, S., and Niklason, L., 2010, "Developing a Tissue-Engineered Model of the Human Bronchiole," J Tissue Eng Regen Med, **4**(8), pp. 619–627.

[72] Rashid, S. T., Corbineau, S., Hannan, N., Marciniak, S. J., Miranda, E., Alexander, G., Huang-Doran, I., Griffin, J., Ahrlund-Richter, L., Skepper, J., Semple, R., Weber, A., Lomas, D. A., and Vallier, L., 2010, "Modeling Inherited Metabolic Disorders of the Liver Using Human Induced Pluripotent Stem Cells," Journal of Clinical Investigation, **120**(9), pp. 3127–3136.

[73] Itzhaki, I., Maizels, L., Huber, I., Zwi-Dantsis, L., Caspi, O., Winterstern, A., Feldman, O., Gepstein, A., Arbel, G., Hammerman, H., Boulos, M., and Gepstein, L., 2011, "Modelling the Long QT Syndrome with Induced Pluripotent Stem Cells," Nature, **471**(7337), pp. 225–229.

[74] Sun, N., Yazawa, M., Liu, J., Han, L., Sanchez-Freire, V., Abilez, O. J., Navarrete, E. G., Hu, S., Wang, L., Lee, A., Pavlovic, A., Lin, S., Chen, R., Hajjar, R. J., Snyder, M. P., Dolmetsch, R. E., Butte, M. J., Ashley, E. A., Longaker, M. T., Robbins, R. C., and Wu, J. C., 2012, "Patient-Specific Induced Pluripotent Stem Cells as a Model for Familial Dilated Cardiomyopathy," Sci Transl Med, **4**(130).

[75] Whitesides, G. M., 2006, "The Origins and the Future of Microfluidics," Nature, **442**(7101), pp. 368–373.

[76] Doutel, E., Galindo-Rosales, F. J., and Campo-Deaño, L., 2021, "Hemodynamics Challenges for the Navigation of Medical Microbots for the Treatment of CVDs," Materials, **14**(23).

[77] Zhang, J., Yan, S., Yuan, D., Alici, G., Nguyen, N. T., Ebrahimi Warkiani, M., and Li, W., 2016, "Fundamentals and Applications of Inertial Microfluidics: A Review," Lab Chip, **16**(1), pp. 10–34.

[78] Webster, A., Greenman, J., and Haswell, S. J., 2011, "Development of Microfluidic Devices for Biomedical and Clinical Application," Journal of Chemical Technology and Biotechnology, **86**(1), pp. 10–17.

[79] Blutt, S. E., Broughman, J. R., Zou, W., Zeng, X. L., Karandikar, U. C., In, J., Zachos, N. C., Kovbasnjuk, O., Donowitz, M., and Estes, M. K., 2017, "Gastrointestinal Microphysiological Systems," Exp Biol Med, **242**(16), pp. 1633–1642.

[80] Wang, Y. I., Oleaga, C., Long, C. J., Esch, M. B., McAleer, C. W., Miller, P. G., Hickman, J. J., and Shuler, M. L., 2017, "Self-Contained, Low-Cost Body-on-a-Chip Systems for Drug Development," Exp Biol Med, **242**(17), pp. 1701–1713.

[81] Ewart, L., Fabre, K., Chakilam, A., Dragan, Y., Duignan, D. B., Eswaraka, J., Gan, J., Guzzie-Peck, P., Otieno, M., Jeong, C. G., Keller, D. A., de Morais, S. M., Phillips, J. A., Proctor, W., Sura, R., Van Vleet, T., Watson, D., Will, Y., Tagle, D., and Berridge, B., 2017, "Navigating Tissue Chips from Development to Dissemination: A Pharmaceutical Industry Perspective," Exp Biol Med, **242**(16), pp. 1579–1585.

[82] Bhatia, S. N., and Ingber, D. E., 2014, "Microfluidic Organs-on-Chips.," Nat Biotechnol, **32**(8), pp. 760–72.

[83] Huh, D., Matthews, B. D., Mammoto, A., Montoya-Zavala, M., Hsin, H. Y., and Ingber, D. E., 2010, "Reconstituting Organ-Level Lung Functions on a Chip," Science (1979), **328**(5986), pp. 1662–1668.

[84] Stucki, J. D., Hobi, N., Galimov, A., Stucki, A. O., Schneider-Daum, N., Lehr, C. M., Huwer, H., Frick, M., Funke-Chambour, M., Geiser, T., and Guenat, O. T., 2018, "Medium Throughput Breathing Human Primary Cell Alveolus-on-Chip Model," Sci Rep, **8**(1), pp. 1–13.

[85] Kim, H. J., Huh, D., Hamilton, G., and Ingber, D. E., 2012, "Human Gut-on-a-Chip Inhabited by Microbial Flora That Experiences Intestinal Peristalsis-like Motions and Flow," Lab Chip, **12**(12), p. 2165.

[86] Jang, K. J., Mehr, A. P., Hamilton, G. A., McPartlin, L. A., Chung, S., Suh, K. Y., and Ingber, D. E., 2013, "Human Kidney Proximal Tubule-on-a-Chip for Drug Transport and Nephrotoxicity Assessment," Integrative Biology (United Kingdom), **5**(9), pp. 1119–1129.

[87] Lee, P. J., Hung, P. J., and Lee, L. P., 2007, "An Artificial Liver Sinusoid with a Microfluidic Endothelial-like Barrier for Primary Hepatocyte Culture," Biotechnol Bioeng, **97**(5), pp. 1340–1346.

[88] Booth, R., and Kim, H., 2012, "Characterization of a Microfluidic in Vitro Model of the Blood-Brain Barrier (MBBB)," Lab Chip, **12**(10), pp. 1784–1792.

[89] Kimura, H., Sakai, Y., and Fujii, T., 2018, "Organ/Body-on-a-Chip Based on Microfluidic Technology for Drug Discovery.," Drug Metab Pharmacokinet, **33**(1), pp. 43–48.

[90] Cavero, I., Guillon, J. M., and Holzgrefe, H. H., 2019, "Human Organotypic Bioconstructs from Organ-on-Chip Devices for Human-Predictive Biological Insights on Drug Candidates," Expert Opin Drug Saf, **18**(8), pp. 651–677.

[91] Wu, Q., Liu, J., Wang, X., Feng, L., Wu, J., Zhu, X., Wen, W., and Gong, X., 2020, "Organ-on-a-Chip: Recent Breakthroughs and Future Prospects," Biomed Eng Online, **19**(1), pp. 1–19.

[92] Maschmeyer, I., Lorenz, A. K., Schimek, K., Hasenberg, T., Ramme, A. P., Hübner, J., Lindner, M., Drewell, C., Bauer, S., Thomas, A., Sambo, N. S., Sonntag, F., Lauster, R., and Marx, U., 2015, "A Four-Organ-Chip for Interconnected Long-Term Co-Culture of Human Intestine, Liver, Skin and Kidney Equivalents," Lab Chip, **15**(12), pp. 2688–2699.

[93] Xiao, S., Coppeta, J. R., Rogers, H. B., Isenberg, B. C., Zhu, J., Olalekan, S. A., McKinnon, K. E., Dokic, D., Rashedi, A. S., Haisenleder, D. J., Malpani, S. S., Arnold-Murray, C. A., Chen, K., Jiang, M., Bai, L., Nguyen, C. T., Zhang, J., Laronda, M. M., Hope, T. J., Maniar, K. P., Pavone, M. E., Avram, M. J., Sefton, E. C., Getsios, S., Burdette, J. E., Kim, J. J., Borenstein, J. T., and Woodruff, T. K., 2017, "A Microfluidic Culture Model of the Human Reproductive Tract and 28-Day Menstrual Cycle," Nat Commun, **8**(1), p. 14584.

[94] Edington, C. D., Chen, W. L. K., Geishecker, E., Kassis, T., Soenksen, L. R., Bhushan, B. M., Freake, D., Kirschner, J., Maass, C., Tsamandouras, N., Valdez, J., Cook, C. D., Parent, T., Snyder, S., Yu, J., Suter, E., Shockley, M., Velazquez, J., Velazquez, J. J., Stockdale, L., Papps, J. P., Lee, I., Vann, N., Gamboa, M., Labarge, M. E., Zhong, Z., Wang, X., Boyer, L. A., Lauffenburger, D. A., Carrier, R. L., Communal, C., Tannenbaum, S. R., Stokes, C. L., Hughes, D. J., Rohatgi, G., Trumper, D. L., Cirit, M., and Griffith, L. G., 2018, "Interconnected Microphysiological Systems for Quantitative Biology and Pharmacology Studies," Sci Rep, **8**(1), pp. 1–18.

[95] Wikswo, J. P., Samson, P. C., Block, F. E., Reiserer, R. S., Parker, K. K., McLean, J. A., McCawley, L. J., Markov, D. A., Levener, D., Ingber, D. E., Hamilton, G. A., Goss, J. A., Cunningham, R.,

Cliffel, D. E., McKenzie, J. R., Bahinski, A., and Hinojosa, C. D., 2017, "Integrated Human Organ-on-Chip Microphysiological Systems. US20150004077A1 United States Patent Application."

[96] Marx, U., Andersson, T. B., Bahinski, A., Beilmann, M., Beken, S., Cassee, F. R., Cirit, M., Daneshian, M., Fitzpatrick, S., Frey, O., Gaertner, C., Giese, C., Griffith, L., Hartung, T., Heringa, M. B., Hoeng, J., de Jong, W. H., Kojima, H., Kuehnl, J., Leist, M., Luch, A., Maschmeyer, I., Sakharov, D., Sips, A. J. A. M., Steger-Hartmann, T., Tagle, D. A., Tonevitsky, A., Tralau, T., Tsyb, S., van de Stolpe, A., Vandebriel, R., Vulto, P., Wang, J., Wiest, J., Rodenburg, M., and Roth, A., 2016, "Biology-Inspired Microphysiological System Approaches to Solve the Prediction Dilemma of Substance Testing.," ALTEX, **33**(3), pp. 272–321.

[97] Mastrangeli, M., Millet, S., Mummery, C., Loskill, P., Braeken, D., Eberle, W., Cipriano, M., Fernandez, L., Graef, M., Gidrol, X., Picollet-D'Hahan, N., van Meer, B., Ochoa, I., Schutte, M., and Van den Eijnden-van Raaij, J., 2019, "Organ-on-Chip in Development. ORCHID Final Report," **36**(4), pp. 650–668.

[98] Webster, A., Dyer, C. E., Haswell, S. J., and Greenman, J., 2010, "A Microfluidic Device for Tissue Biopsy Culture and Interrogation," Analytical Methods, **2**(8), p. 1005.

[99] Fisher, R. L., Shaughnessy, R. P., Jenkins, P. M., Austin, M. L., Roth, G. L., Gandolfi, A. J., and Brendel, K., 1995, "Dynamic Organ Culture Is Superior to Multiwell Plate Culture for Maintaining Precision-Cut Tissue Slices: Optimization of Tissue Slice Culture, Part 1," Toxicology Methods, **5**(2), pp. 99–113.

[100] Schumacher, K., Khong, Y.-M., Chang, S., Ni, J., Sun, W., and Yu, H., 2007, "Perfusion Culture Improves the Maintenance of Cultured Liver Tissue Slices," Tissue Eng, **13**(1), pp. 197–205.

[101] Schumacher, K., Khong, Y.-M., Chang, S., Ni, J., Sun, W., and Yu, H., 2007, "Perfusion Culture Improves the Maintenance of Cultured Liver Tissue Slices," Tissue Eng, **13**(1), pp. 197–205.

[102] McLean, I. C., Schwerdtfeger, L. A., Tobet, S. A., and Henry, C. S., 2018, "Powering Ex Vivo Tissue Models in Microfluidic Systems.," Lab Chip, **18**(10), pp. 1399–1410.

[103] Li, C.-L., and McIlwain, H., 1957, "Maintenance of Resting Membrane Potentials in Slices of Mammalian Cerebral Cortex and Other Tissues in Vitro," J Physiol, **139**(2), pp. 178–190.

[104] Haas, H. L., Schaerer, B., and Vosmansky, M., 1979, "A Simple Perfusion Chamber for the Study of Nervous Tissue Slices in Vitro," J Neurosci Methods, **1**(4), pp. 323–325.

[105] Passeraub, P. A., Almeida, A. C., and Thakor, N. V., 2003, "Design, Microfabrication and Analysis of a Microfluidic Chamber for the Perfusion of Brain Tissue Slices," Biomed Microdevices, **5**(2), pp. 147–155.

[106] Blake, A. J., Pearce, T. M., Rao, N. S., Johnson, S. M., and Williams, J. C., 2007, "Multilayer PDMS Microfluidic Chamber for Controlling Brain Slice Microenvironment," Lab Chip, **7**(7), pp. 842–849.

[107] Hattersley, S. M., Dyer, C. E., Greenman, J., and Haswell, S. J., 2008, "Development of a Microfluidic Device for the Maintenance and Interrogation of Viable Tissue Biopsies," Lab Chip, **8**(11), p. 1842.

[108] Bakmand, T., Troels-Smith, A. R., Dimaki, M., Nissen, J. D., Andersen, K. B., Sasso, L., Waagepetersen, H. S., Gramsbergen, J. B., and Svendsen, W. E., 2015, "Fluidic System for Long-Term in Vitro Culturing and Monitoring of Organotypic Brain Slices," Biomed Microdevices, **17**(4), pp. 1–7.

[109] Queval, A., Ghattamaneni, N. R., Perrault, C. M., Gill, R., Mirzaei, M., McKinney, R. A., and Juncker, D., 2010, "Chamber and Microfluidic Probe for Microperfusion of Organotypic Brain Slices," Lab Chip, **10**(3), pp. 326–334.

[110] van Midwoud, P. M., Groothuis, G. M. M., Merema, M. T., and Verpoorte, E., 2010, "Microfluidic Biochip for the Perifusion of Precision-Cut Rat Liver Slices for Metabolism and Toxicology Studies," Biotechnol Bioeng, **105**(1), pp. 184–194.

[111] van Midwoud, P. M., Merema, M. T., Verweij, N., Groothuis, G. M. M., and Verpoorte, E., 2011, "Hydrogel Embedding of Precision-Cut Liver Slices in a Microfluidic Device Improves Drug Metabolic Activity," Biotechnol Bioeng, **108**(6), pp. 1404–1412.

[112] Choi, Y., McClain, M. A., LaPlaca, M. C., Frazier, A. B., and Allen, M. G., 2007, "Three Dimensional MEMS Microfluidic Perfusion System for Thick Brain Slice Cultures," Biomed Microdevices, **9**(1), pp. 7–13.

[113] Khong, Y. M., Zhang, J., Zhou, S., Cheung, C., Doberstein, K., Samper, V., and Yu, H., 2007, "Novel Intra-Tissue Perfusion System for Culturing Thick Liver Tissue," Tissue Eng, **13**(9), pp. 2345–2356.

[114] Rambani, K., Vukasinovic, J., Glezer, A., and Potter, S. M., 2009, "Culturing Thick Brain Slices: An Interstitial 3D Microperfusion System for Enhanced Viability," J Neurosci Methods, **180**(2), pp. 243–254.

[115] Cheah, L. T., Fritsch, I., Haswell, S. J., and Greenman, J., 2012, "Evaluation of Heart Tissue Viability under Redox-Magnetohydrodynamics Conditions: Toward Fine-Tuning Flow in Biological Microfluidics Applications," Biotechnol Bioeng, **109**(7), pp. 1827–1834.

[116] Huang, Y., Williams, J. C., and Johnson, S. M., 2012, "Brain Slice on a Chip: Opportunities and Challenges of Applying Microfluidic Technology to Intact Tissues," Lab Chip, **12**(12).

[117] Dawson, A., Dyer, C., Macfie, J., Davies, J., Karsai, L., Greenman, J., and Jacobsen, M., 2016, "A Microfluidic Chip Based Model for the Study of Full Thickness Human Intestinal Tissue Using Dual Flow," Biomicrofluidics, **10**(6), p. 064101.

[118] Richardson, A., Schwerdtfeger, L. A., Eaton, D., Mclean, I., Henry, C. S., and Tobet, S. A., 2020, "A Microfluidic Organotypic Device for Culture of Mammalian Intestines Ex Vivo," Analytical Methods, **12**(3), pp. 297–303.

[119] Eslami Amirabadi, H., Donkers, J. M., Wierenga, E., Ingenhut, B., Pieters, L., Stevens, L., Donkers, T., Westerhout, J., Masereeuw, R., Bobeldijk-Pastorova, I., Nooijen, I., and van de Steeg, E., 2022, "Intestinal Explant Barrier Chip: Long-Term Intestinal Absorption Screening in a Novel Microphysiological System Using Tissue Explants," Lab Chip, **22**(2), pp. 326–342.

[120] Baydoun, Treizeibré, Follet, Vanneste, Creusy, Dercourt, Delaire, Mouray, Viscogliosi, Certad, and Senez, 2020, "An Interphase Microfluidic Culture System for the Study of Ex Vivo Intestinal Tissue," Micromachines (Basel), **11**(2), p. 150.

[121] Ota, N., Kanda, G. N., Moriguchi, H., Aishan, Y., Shen, Y., Yamada, R. G., Ueda, H. R., and Tanaka, Y., 2019, "A Microfluidic Platform Based on Robust Gas and Liquid Exchange for Long-Term Culturing of Explanted Tissues," Analytical Sciences, **35**(10), pp. 1141–1147.

[122] Chakrabarty, S., Quiros-Solano, W. F., Kuijten, M. M. P., Haspels, B., Mallya, S., Lo, C. S. Y., Othman, A., Silvestri, C., Van De Stolpe, A., Gaio, N., Odijk, H., Van De Ven, M., De Ridder, C. M. A., Van Weerden, W. M., Jonkers, J., Dekker, R., Taneja, N., Kanaar, R., and Van Gent, D. C., 2022, "A Microfluidic Cancer-on-Chip Platform Predicts Drug Response Using Organotypic Tumor Slice Culture," Cancer Res, **82**(3), pp. 510–520.

[123] Yissachar, N., Zhou, Y., Ung, L., Lai, N. Y., Mohan, J. F., Ehrlicher, A., Weitz, D. A., Kasper, D. L., Chiu, I. M., Mathis, D., and Benoist, C., 2017, "An Intestinal Organ Culture System Uncovers a Role for the Nervous System in Microbe-Immune Crosstalk," Cell, **168**(6), pp. 1135-1148.e12.

[124] Buskila, Y., Breen, P. P., Tapson, J., van Schaik, A., Barton, M., and Morley, J. W., 2015, "Extending the Viability of Acute Brain Slices," Sci Rep, **4**(1), p. 5309.

[125] Dondzillo, A., Quinn, K. D., Cruickshank-Quinn, C. I., Reisdorph, N., Lei, T. C., and Klug, A., 2015, "A Recording Chamber for Small Volume Slice Electrophysiology," J Neurophysiol, **114**(3), pp. 2053–2064.

[126] Liu, J., Pan, L., Cheng, X., and Berdichevsky, Y., 2016, "Perfused Drop Microfluidic Device for Brain Slice Culture-Based Drug Discovery," Biomed Microdevices, **18**(3), p. 46.

[127] Ahrar, S., Nguyen, T. V., Shi, Y., Ikrar, T., Xu, X., and Hui, E. E., 2013, "Optical Stimulation and Imaging of Functional Brain Circuitry in a Segmented Laminar Flow Chamber," Lab Chip, **13**(4), pp. 536–541.

[128] Thomas, M. G., Covington, J. A., and Wall, M. J., 2013, "A Chamber for the Perfusion of in Vitro Tissue with Multiple Solutions," J Neurophysiol, **110**(1), pp. 269–277.

[129] Blake, A. J., Rodgers, F. C., Bassuener, A., Hippensteel, J. A., Pearce, T. M., Pearce, T. R., Zarnowska, E. D., Pearce, R. A., and Williams, J. C., 2010, "A Microfluidic Brain Slice Perfusion Chamber for Multisite Recording Using Penetrating Electrodes," J Neurosci Methods, **189**(1), pp. 5–13.

[130] Tokuoka, Y., Kondo, K., Nakaigawa, N., and Ishida, T., 2021, "Development of a Microfluidic Device to Form a Long Chemical Gradient in a Tissue from Both Ends with an Analysis of Its Appearance and Content," Micromachines (Basel), **12**(12).

[131] Mohammed, J. S., Caicedo, H. H., Fall, C. P., and Eddington, D. T., 2008, "Microfluidic Add-on for Standard Electrophysiology Chambers," Lab Chip, **8**(7), p. 1048.

[132] Caicedo, H. H., Hernandez, M., Fall, C. P., and Eddington, D. T., 2010, "Multiphysics Simulation of a Microfluidic Perfusion Chamber for Brain Slice Physiology," Biomed Microdevices, **12**(5), pp. 761–767.

[133] Ross, A. E., Belanger, M. C., Woodroof, J. F., and Pompano, R. R., 2017, "Spatially Resolved Microfluidic Stimulation of Lymphoid Tissue Ex Vivo," Analyst, **142**(4), pp. 649–659.

[134] Tang, Y. T., Kim, J., López-Valdés, H. E., Brennan, K. C., and Ju, Y. S., 2011, "Development and Characterization of a Microfluidic Chamber Incorporating Fluid Ports with Active Suction for Localized Chemical Stimulation of Brain Slices," Lab Chip, **11**(13), pp. 2247–2254.

[135] Dodson, K. H., Echevarria, F. D., Li, D., Sappington, R. M., and Edd, J. F., 2015, "Retina-on-a-Chip: A Microfluidic Platform for Point Access Signaling Studies," Biomed Microdevices, **17**(6), pp. 1–10.

[136] Catterton, M. A., Ball, A. G., and Pompano, R. R., 2021, "Rapid Fabrication by Digital Light Processing 3d Printing of a Slipchip with Movable Ports for Local Delivery to Ex Vivo Organ Cultures," Micromachines (Basel), **12**(8).

[137] Chang, T. C., Mikheev, A. M., Huynh, W., Monnat, R. J., Rostomily, R. C., and Folch, A., 2014, "Parallel Microfluidic Chemosensitivity Testing on Individual Slice Cultures," Lab Chip, **14**(23), pp. 4540–4551.

[138] Rodriguez, A. D., Horowitz, L. F., Castro, K., Kenerson, H., Bhattacharjee, N., Gandhe, G., Raman, A., Monnat, R. J., Yeung, R., Rostomily, R. C., and Folch, A., 2020, "A Microfluidic Platform for Functional Testing of Cancer Drugs on Intact Tumor Slices," Lab Chip.

[139] Horowitz, L. F., Rodriguez, A. D., Dereli-Korkut, Z., Lin, R., Castro, K., Mikheev, A. M., Monnat, R. J., Folch, A., and Rostomily, R. C., 2020, "Multiplexed Drug Testing of Tumor Slices Using a Microfluidic Platform," NPJ Precis Oncol, **4**(1).

[140] van Midwoud, P. M., Merema, M. T., Verpoorte, E., and Groothuis, G. M. M., 2010, "A Microfluidic Approach for in Vitro Assessment of Interorgan Interactions in Drug Metabolism Using Intestinal and Liver Slices," Lab Chip, **10**(20), p. 2778.

[141] Mauleon, G., Fall, C. P., and Eddington, D. T., 2012, "Precise Spatial and Temporal Control of Oxygen within In Vitro Brain Slices via Microfluidic Gas Channels," PLoS One, **7**(8), p. e43309.

[142] Carreau, A., Hafny-Rahbi, B. El, Matejuk, A., Grillon, C., and Kieda, C., 2011, "Why Is the Partial Oxygen Pressure of Human Tissues a Crucial Parameter? Small Molecules and Hypoxia," J Cell Mol Med, **15**(6), pp. 1239–1253.

[143] Jagannathan, L., Cuddapah, S., and Costa, M., 2016, "Oxidative Stress Under Ambient and Physiological Oxygen Tension in Tissue Culture," Curr Pharmacol Rep, **2**(2), pp. 64–72.

[144] Rexius-Hall, M. L., Rehman, J., and Eddington, D. T., 2017, "A Microfluidic Oxygen Gradient Demonstrates Differential Activation of the Hypoxia-Regulated Transcription Factors HIF-1α and HIF-2α," Integrative Biology (United Kingdom), **9**(9), pp. 742–750.

[145] Peng, C.-C., Liao, W.-H., Chen, Y.-H., Wu, C.-Y., and Tung, Y.-C., 2013, "A Microfluidic Cell Culture Array with Various Oxygen Tensions," Lab Chip, **13**(16), p. 3239.

[146] Chiang, H.-J., Yeh, S.-L., Peng, C.-C., Liao, W.-H., and Tung, Y.-C., 2017, "Polydimethylsiloxane-Polycarbonate Microfluidic Devices for Cell Migration Studies Under Perpendicular Chemical and Oxygen Gradients," Journal of Visualized Experiments, (120), pp. 1–8.

[147] Christensen, M. G., Cawthorne, C., Dyer, C. E., Greenman, J., and Pamme, N., 2021, "Investigating Oxygen Transport Efficiencies in Precision-Cut Liver Slice-Based Organ-on-a-Chip Devices," Microfluid Nanofluidics, **25**(4), p. 35.

[148] Cheah, L. T., Fritsch, I., Haswell, S. J., and Greenman, J., 2012, "Evaluation of Heart Tissue Viability under Redox-Magnetohydrodynamics Conditions: Toward Fine-Tuning Flow in Biological Microfluidics Applications," Biotechnol Bioeng, **109**(7), pp. 1827–1834.

[149] Cheah, R., Srivastava, R., Stafford, N. D., Beavis, A. W., Green, V. L., and Greenman, J., 2017, "Measuring the Response of Human Head and Neck Squamous Cell Carcinoma to Irradiation in a Microfluidic Model Allowing Customized Therapy," Int J Oncol, **51**(4), pp. 1227–1238.

[150] Carr, S. D., Green, V. L., Stafford, N. D., and Greenman, J., 2014, "Analysis of Radiation-Induced Cell Death in Head and Neck Squamous Cell Carcinoma and Rat Liver Maintained in Microfluidic Devices," Otolaryngology - Head and Neck Surgery (United States), **150**(1), pp. 73–80.

[151] Sylvester, D., M. Hattersley, S., D. Stafford, N., J. Haswell, S., and Greenman, J., 2013, "Development of Microfluidic-Based Analytical Methodology for Studying the Effects of Chemotherapy Agents on Cancer Tissue," Curr Anal Chem, **9**(1), pp. 2–8.

[152] Hattersley, S. M., Sylvester, D. C., Dyer, C. E., Stafford, N. D., Haswell, S. J., and Greenman, J., 2012, "A Microfluidic System for Testing the Responses of Head and Neck Squamous Cell Carcinoma Tissue Biopsies to Treatment with Chemotherapy Drugs," Ann Biomed Eng, **40**(6), pp. 1277–1288.

[153] Astolfi, M., Péant, B., Lateef, M. A., Rousset, N., Kendall-Dupont, J., Carmona, E., Monet, F., Saad, F., Provencher, D., Mes-Masson, A. M., and Gervais, T., 2016, "Micro-Dissected Tumor Tissues on Chip: An Ex Vivo Method for Drug Testing and Personalized Therapy," Lab Chip, **16**(2), pp. 312–325.

[154] Holton, A. B., Sinatra, F. L., Kreahling, J., Conway, A. J., Landis, D. A., and Altiok, S., 2017, "Microfluidic Biopsy Trapping Device for the Real-Time Monitoring of Tumor Microenvironment," PLoS One, **12**(1), pp. 1–21.

[155] Mulholland, T., McAllister, M., Patek, S., Flint, D., Underwood, M., Sim, A., Edwards, J., and Zagnoni, M., 2018, "Drug Screening of Biopsy-Derived Spheroids Using a Self-Generated Microfluidic Concentration Gradient," Sci Rep, **8**(1), pp. 1–12.

[156] Bower, R., Green, V. L., Kuvshinova, E., Kuvshinov, D., Karsai, L., Crank, S. T., Stafford, N. D., and Greenman, J., 2017, "Maintenance of Head and Neck Tumor On-Chip: Gateway to Personalized Treatment?," Future Sci OA, **3**(2), p. FSO174.

[157] Xiao, S., Coppeta, J. R., Rogers, H. B., Isenberg, B. C., Zhu, J., Olalekan, S. A., McKinnon, K. E., Dokic, D., Rashedi, A. S., Haisenleder, D. J., Malpani, S. S., Arnold-Murray, C. A., Chen, K., Jiang, M., Bai, L., Nguyen, C. T., Zhang, J., Laronda, M. M., Hope, T. J., Maniar, K. P., Pavone, M. E., Avram, M. J., Sefton, E. C., Getsios, S., Burdette, J. E., Kim, J. J., Borenstein, J. T., and Woodruff, T. K., 2017, "A Microfluidic Culture Model of the Human Reproductive Tract and 28-Day Menstrual Cycle," Nat Commun, **8**(1), p. 14584.

[158] Bakmand, T., Troels-Smith, A. R., Dimaki, M., Nissen, J. D., Andersen, K. B., Sasso, L., Waagepetersen, H. S., Gramsbergen, J. B., and Svendsen, W. E., 2015, "Fluidic System for Long-Term in Vitro Culturing and Monitoring of Organotypic Brain Slices," Biomed Microdevices, **17**(4), pp. 1–7.

[159] Liu, J., Pan, L., Cheng, X., and Berdichevsky, Y., 2016, "Perfused Drop Microfluidic Device for Brain Slice Culture-Based Drug Discovery," Biomed Microdevices, **18**(3), p. 46.

[160] Berdichevsky, Y., Sabolek, H., Levine, J. B., Staley, K. J., and Yarmush, M. L., 2009, "Microfluidics and Multielectrode Array-Compatible Organotypic Slice Culture Method," J Neurosci Methods, **178**(1), pp. 59–64.

[161] Ross, A. E., Belanger, M. C., Woodroof, J. F., and Pompano, R. R., 2017, "Spatially Resolved Microfluidic Stimulation of Lymphoid Tissue Ex Vivo," Analyst, **142**(4), pp. 649–659.

[162] Shim, S., Belanger, M. C., Harris, A. R., Munson, J. M., and Pompano, R. R., 2019, "Two-Way Communication between Ex Vivo Tissues on a Microfluidic Chip: Application to Tumor–Lymph Node Interaction," Lab Chip, **19**(6), pp. 1013–1026.

[163] Chakrabarty, S., Quiros-Solano, W. F., Kuijten, M. M. P., Haspels, B., Mallya, S., Lo, C. S. Y., Othman, A., Silvestri, C., van de Stolpe, A., Gaio, N., Odijk, H., van de Ven, M., de Ridder, C. M. A., van Weerden, W. M., Jonkers, J., Dekker, R., Taneja, N., Kanaar, R., and van Gent, D. C., 2022, "A Microfluidic Cancer-on-Chip Platform Predicts Drug Response Using Organotypic Tumor Slice Culture," Cancer Res, **82**(3), pp. 510–520.

[164] Kennedy, R., Kuvshinov, D., Sdrolia, A., Kuvshinova, E., Hilton, K., Crank, S., Beavis, A. W., Green, V. L., and Greenman, J., 2019, "A Patient Tumour-on-a-Chip System for Personalised Investigation of Radiotherapy Based Treatment Regimens," Sci Rep, **9**(1), pp. 1–10.

[165] Riley, A., Green, V. L., Cheah, R., McKenzie, G., Karsai, L., England, J., and Greenman, J., 2019, "A Novel Microfluidic Device Capable of Maintaining Functional Thyroid Carcinoma Specimens Ex Vivo Provides a New Drug Screening Platform," BMC Cancer, **19**(1), p. 259.

[166] Zambon, A., Zoso, A., Gagliano, O., Magrofuoco, E., Fadini, G. P., Avogaro, A., Foletto, M., Quake, S., and Elvassore, N., 2015, "High Temporal Resolution Detection of Patient-Specific Glucose Uptake from Human Ex Vivo Adipose Tissue On-Chip," Anal Chem, **87**(13), pp. 6535–6543.

[167] Baydoun, Treizeibré, Follet, Vanneste, Creusy, Dercourt, Delaire, Mouray, Viscogliosi, Certad, and Senez, 2020, "An Interphase Microfluidic Culture System for the Study of Ex Vivo Intestinal Tissue," Micromachines (Basel), **11**(2), p. 150.

[168] Ota, N., Kanda, G. N., Moriguchi, H., Aishan, Y., Shen, Y., Yamada, R. G., Ueda, H. R., and Tanaka, Y., 2019, "A Microfluidic Platform Based on Robust Gas and Liquid Exchange for Long-Term Culturing of Explanted Tissues," Analytical Sciences, **35**(10), pp. 1141–1147.

[169] Passeraub, P. A., Almeida, A. C., and Thakor, N. V., 2003, "Design, Microfabrication and Analysis of a Microfluidic Chamber for the Perfusion of Brain Tissue Slices," Biomed Microdevices, **5**(2), pp. 147–155.

[170] Chang, T. C., Mikheev, A. M., Huynh, W., Monnat, R. J., Rostomily, R. C., and Folch, A., 2014, "Parallel Microfluidic Chemosensitivity Testing on Individual Slice Cultures," Lab Chip, **14**(23), pp. 4540–4551.

[171] Eslami Amirabadi, H., Donkers, J. M., Wierenga, E., Ingenhut, B., Pieters, L., Stevens, L., Donkers, T., Westerhout, J., Masereeuw, R., Bobeldijk-Pastorova, I., Nooijen, I., and van de Steeg, E., 2022, "Intestinal Explant Barrier Chip: Long-Term Intestinal Absorption Screening in a Novel Microphysiological System Using Tissue Explants," Lab Chip, **22**(2), pp. 326–342.

[172] Dawson, A., Dyer, C., Macfie, J., Davies, J., Karsai, L., Greenman, J., and Jacobsen, M., 2016, "A Microfluidic Chip Based Model for the Study of Full Thickness Human Intestinal Tissue Using Dual Flow," Biomicrofluidics, **10**(6), p. 064101.

[173] Yissachar, N., Zhou, Y., Ung, L., Lai, N. Y., Mohan, J. F., Ehrlicher, A., Weitz, D. A., Kasper, D. L., Chiu, I. M., Mathis, D., and Benoist, C., 2017, "An Intestinal Organ Culture System Uncovers a Role for the Nervous System in Microbe-Immune Crosstalk," Cell, **168**(6), pp. 1135-1148.e12.

[174] Richardson, A., Schwerdtfeger, L. A., Eaton, D., Mclean, I., Henry, C. S., and Tobet, S. A., 2020, "A Microfluidic Organotypic Device for Culture of Mammalian Intestines Ex Vivo," Analytical Methods, **12**(3), pp. 297–303.

[175] Günther, A., Yasotharan, S., Vagaon, A., Lochovsky, C., Pinto, S., Yang, J., Lau, C., Voigtlaender-Bolz, J., and Bolz, S.-S., 2010, "A Microfluidic Platform for Probing Small Artery Structure and Function," Lab Chip, **10**(18), p. 2341.

[176] Yasotharan, S., Pinto, S., Sled, J. G., Bolz, S. S., and Günther, A., 2015, "Artery-on-a-Chip Platform for Automated, Multimodal Assessment of Cerebral Blood Vessel Structure and Function," Lab Chip, **15**(12), pp. 2660–2669.

[177] Blake, A. J., Pearce, T. M., Rao, N. S., Johnson, S. M., and Williams, J. C., 2007, "Multilayer PDMS Microfluidic Chamber for Controlling Brain Slice Microenvironment," Lab Chip, **7**(7), pp. 842–849.

[178] Blake, A. J., Rodgers, F. C., Bassuener, A., Hippensteel, J. A., Pearce, T. M., Pearce, T. R., Zarnowska, E. D., Pearce, R. A., and Williams, J. C., 2010, "A Microfluidic Brain Slice Perfusion Chamber for Multisite Recording Using Penetrating Electrodes," J Neurosci Methods, **189**(1), pp. 5–13.

[179] Shaikh Mohammed, J., Caicedo, H. H., Fall, C. P., and Eddington, D. T., 2007, "Brain Slice Stimulation Using a Microfluidic Network and Standard Perfusion Chamber," Journal of Visualized Experiments, (8), pp. 5–7.

[180] Mohammed, J. S., Caicedo, H. H., Fall, C. P., and Eddington, D. T., 2008, "Microfluidic Add-on for Standard Electrophysiology Chambers," Lab Chip, **8**(7), p. 1048.

[181] Choi, Y., McClain, M. A., LaPlaca, M. C., Frazier, A. B., and Allen, M. G., 2007, "Three Dimensional MEMS Microfluidic Perfusion System for Thick Brain Slice Cultures," Biomed Microdevices, **9**(1), pp. 7–13.

[182] Rambani, K., Vukasinovic, J., Glezer, A., and Potter, S. M., 2009, "Culturing Thick Brain Slices: An Interstitial 3D Microperfusion System for Enhanced Viability," J Neurosci Methods, **180**(2), pp. 243–254.

[183] Killian, N. J., Vernekar, V. N., Potter, S. M., and Vukasinovic, J., 2016, "A Device for Long-Term Perfusion, Imaging, and Electrical Interfacing of Brain Tissue In Vitro," Front Neurosci, **10**(MAR), pp. 1–14.

[184] Khong, Y. M., Zhang, J., Zhou, S., Cheung, C., Doberstein, K., Samper, V., and Yu, H., 2007, "Novel Intra-Tissue Perfusion System for Culturing Thick Liver Tissue," Tissue Eng, **13**(9), pp. 2345–2356.

[185] van Midwoud, P. M., Verpoorte, E., and Groothuis, G. M. M., 2011, "Microfluidic Devices for in Vitro Studies on Liver Drug Metabolism and Toxicity," Integrative Biology, **3**(5), p. 509.

[186] van Midwoud, P. M., Groothuis, G. M. M., Merema, M. T., and Verpoorte, E., 2010, "Microfluidic Biochip for the Perifusion of Precision-Cut Rat Liver Slices for Metabolism and Toxicology Studies," Biotechnol Bioeng, **105**(1), pp. 184–194.

[187] van Midwoud, P. M., Merema, M. T., Verpoorte, E., and Groothuis, G. M. M., 2010, "A Microfluidic Approach for in Vitro Assessment of Interorgan Interactions in Drug Metabolism Using Intestinal and Liver Slices," Lab Chip, **10**(20), p. 2778.

[188] van Midwoud, P. M., Merema, M. T., Verweij, N., Groothuis, G. M. M., and Verpoorte, E., 2011, "Hydrogel Embedding of Precision-Cut Liver Slices in a Microfluidic Device Improves Drug Metabolic Activity," Biotechnol Bioeng, **108**(6), pp. 1404–1412.

[189] van Midwoud, P. M., Janssen, J., Merema, M. T., de Graaf, I. A. M., Groothuis, G. M. M., and Verpoorte, E., 2011, "On-Line HPLC Analysis System for Metabolism and Inhibition Studies in Precision-Cut Liver Slices," Anal Chem, **83**(1), pp. 84–91.

[190] Berdichevsky, Y., Sabolek, H., Levine, J. B., Staley, K. J., and Yarmush, M. L., 2009, "Microfluidics and Multielectrode Array-Compatible Organotypic Slice Culture Method," J Neurosci Methods, **178**(1), pp. 59–64.

[191] Killian, N. J., Vernekar, V. N., Potter, S. M., and Vukasinovic, J., 2016, "A Device for Long-Term Perfusion, Imaging, and Electrical Interfacing of Brain Tissue In Vitro," Front Neurosci, **10**(MAR), pp. 1–14.

[192] Heuschkel, M. O., Fejtl, M., Raggenbass, M., Bertrand, D., and Renaud, P., 2002, "A Three-Dimensional Multi-Electrode Array for Multi-Site Stimulation and Recording in Acute Brain Slices," J Neurosci Methods, **114**(2), pp. 135–148.

[193] Rajaraman, S., Choi, S.-O., Shafer, R. H., Ross, J. D., Vukasinovic, J., Choi, Y., DeWeerth, S. P., Glezer, A., and Allen, M. G., 2007, "Microfabrication Technologies for a Coupled Three-Dimensional Microelectrode, Microfluidic Array," Journal of Micromechanics and Microengineering, **17**(1), pp. 163–171.

[194] Scott, A., Weir, K., Easton, C., Huynh, W., Moody, W. J., and Folch, A., 2013, "A Microfluidic Microelectrode Array for Simultaneous Electrophysiology, Chemical Stimulation, and Imaging of Brain Slices," Lab Chip, **13**(4), pp. 527–535.

[195] Hattersley, S. M., Greenman, J., and Haswell, S. J., 2011, "Study of Ethanol Induced Toxicity in Liver Explants Using Microfluidic Devices," Biomed Microdevices, **13**(6), pp. 1005–1014.

[196] Hattersley, S. M., Sylvester, D. C., Dyer, C. E., Stafford, N. D., Haswell, S. J., and Greenman, J., 2012, "A Microfluidic System for Testing the Responses of Head and Neck Squamous Cell

Carcinoma Tissue Biopsies to Treatment with Chemotherapy Drugs," Ann Biomed Eng, **40**(6), pp. 1277–1288.

[197] Carr, S. D., Green, V. L., Stafford, N. D., and Greenman, J., 2014, "Analysis of Radiation-Induced Cell Death in Head and Neck Squamous Cell Carcinoma and Rat Liver Maintained in Microfluidic Devices," Otolaryngology - Head and Neck Surgery (United States), **150**(1), pp. 73–80.

[198] Cheah, R., Srivastava, R., Stafford, N. D., Beavis, A. W., Green, V. L., and Greenman, J., 2017, "Measuring the Response of Human Head and Neck Squamous Cell Carcinoma to Irradiation in a Microfluidic Model Allowing Customized Therapy," Int J Oncol, **51**(4), pp. 1227–1238.

[199] Cheah, L.-T., Dou, Y.-H., Seymour, A.-M. L., Dyer, C. E., Haswell, S. J., Wadhawan, J. D., and Greenman, J., 2010, "Microfluidic Perfusion System for Maintaining Viable Heart Tissue with Real-Time Electrochemical Monitoring of Reactive Oxygen Species," Lab Chip, **10**(20), p. 2720.

[200] Kennedy, R., Kuvshinov, D., Sdrolia, A., Kuvshinova, E., Hilton, K., Crank, S., Beavis, A. W., Green, V. L., and Greenman, J., 2019, "A Patient Tumour-on-a-Chip System for Personalised Investigation of Radiotherapy Based Treatment Regimens," Sci Rep, **9**(1), pp. 1–10.

[201] Riley, A., Green, V. L., Cheah, R., McKenzie, G., Karsai, L., England, J., and Greenman, J., 2019, "A Novel Microfluidic Device Capable of Maintaining Functional Thyroid Carcinoma Specimens Ex Vivo Provides a New Drug Screening Platform," BMC Cancer, **19**(1), p. 259.

[202] Olubajo, F., Achawal, S., and Greenman, J., 2020, "Development of a Microfluidic Culture Paradigm for Ex Vivo Maintenance of Human Glioblastoma Tissue: A New Glioblastoma Model?," Transl Oncol, **13**(1), pp. 1–10.

[203] Günther, A., Yasotharan, S., Vagaon, A., Lochovsky, C., Pinto, S., Yang, J., Lau, C., Voigtlaender-Bolz, J., and Bolz, S.-S., 2010, "A Microfluidic Platform for Probing Small Artery Structure and Function," Lab Chip, **10**(18), p. 2341.

[204] Yasotharan, S., Pinto, S., Sled, J. G., Bolz, S. S., and Günther, A., 2015, "Artery-on-a-Chip Platform for Automated, Multimodal Assessment of Cerebral Blood Vessel Structure and Function," Lab Chip, **15**(12), pp. 2660–2669.

[205] Astolfi, M., Péant, B., Lateef, M. A., Rousset, N., Kendall-Dupont, J., Carmona, E., Monet, F., Saad, F., Provencher, D., Mes-Masson, A. M., and Gervais, T., 2016, "Micro-Dissected Tumor Tissues on Chip: An Ex Vivo Method for Drug Testing and Personalized Therapy," Lab Chip, **16**(2), pp. 312–325.

[206] Holton, A. B., Sinatra, F. L., Kreahling, J., Conway, A. J., Landis, D. A., and Altiok, S., 2017, "Microfluidic Biopsy Trapping Device for the Real-Time Monitoring of Tumor Microenvironment," PLoS One, **12**(1), pp. 1–21.

[207] Mulholland, T., McAllister, M., Patek, S., Flint, D., Underwood, M., Sim, A., Edwards, J., and Zagnoni, M., 2018, "Drug Screening of Biopsy-Derived Spheroids Using a Self-Generated Microfluidic Concentration Gradient," Sci Rep, **8**(1), pp. 1–12.

[208] Horowitz, L. F., Rodriguez, A. D., Au-Yeung, A., Bishop, K. W., Barner, L. A., Mishra, G., Raman, A., Delgado, P., Liu, J. T. C., Gujral, T. S., Mehrabi, M., Yang, M., Pierce, R. H., and Folch, A., 2021, "Microdissected 'Cuboids' for Microfluidic Drug Testing of Intact Tissues," Lab Chip, **21**(1), pp. 122–142.

[209] Scott, A., Weir, K., Easton, C., Huynh, W., Moody, W. J., and Folch, A., 2013, "A Microfluidic Microelectrode Array for Simultaneous Electrophysiology, Chemical Stimulation, and Imaging of Brain Slices," Lab Chip, **13**(4), pp. 527–535.

[210] Ahrar, S., Nguyen, T. V., Shi, Y., Ikrar, T., Xu, X., and Hui, E. E., 2013, "Optical Stimulation and Imaging of Functional Brain Circuitry in a Segmented Laminar Flow Chamber," Lab Chip, **13**(4), pp. 536–541.

[211] Tang, Y. T., Kim, J., López-Valdés, H. E., Brennan, K. C., and Ju, Y. S., 2011, "Development and Characterization of a Microfluidic Chamber Incorporating Fluid Ports with Active Suction for Localized Chemical Stimulation of Brain Slices," Lab Chip, **11**(13), pp. 2247–2254.

[212] Mauleon, G., Fall, C. P., and Eddington, D. T., 2012, "Precise Spatial and Temporal Control of Oxygen within In Vitro Brain Slices via Microfluidic Gas Channels," PLoS One, **7**(8), p. e43309.

[213] Heuschkel, M. O., Fejtl, M., Raggenbass, M., Bertrand, D., and Renaud, P., 2002, "A Three-Dimensional Multi-Electrode Array for Multi-Site Stimulation and Recording in Acute Brain Slices," J Neurosci Methods, **114**(2), pp. 135–148.

[214] Hattersley, S. M., Greenman, J., and Haswell, S. J., 2011, "Study of Ethanol Induced Toxicity in Liver Explants Using Microfluidic Devices," Biomed Microdevices, **13**(6), pp. 1005–1014.

[215] Hattersley, S. M., Dyer, C. E., Greenman, J., and Haswell, S. J., 2008, "Development of a Microfluidic Device for the Maintenance and Interrogation of Viable Tissue Biopsies," Lab Chip, **8**(11), p. 1842.

[216] Cheah, L.-T., Dou, Y.-H., Seymour, A.-M. L., Dyer, C. E., Haswell, S. J., Wadhawan, J. D., and Greenman, J., 2010, "Microfluidic Perfusion System for Maintaining Viable Heart Tissue

with Real-Time Electrochemical Monitoring of Reactive Oxygen Species," Lab Chip, **10**(20), p. 2720.

[217] Cyr, K. J., Avaldi, O. M., and Wikswo, J. P., 2017, "Circadian Hormone Control in a Human-on-a-Chip: In Vitro Biology's Ignored Component?," Exp Biol Med, **242**(17), pp. 1714–1731.

[218] Low, L. A., and Tagle, D. A., 2017, "Tissue Chips – Innovative Tools for Drug Development and Disease Modeling," Lab Chip, **17**(18), pp. 3026–3036.

[219] LeDuc, P. R., Messner, W. C., and Wikswo, J. P., 2011, "How Do Control-Based Approaches Enter into Biology?," Annu Rev Biomed Eng, **13**(1), pp. 369–396.

[220] Webster, A., Greenman, J., and Haswell, S. J., 2011, "Development of Microfluidic Devices for Biomedical and Clinical Application," Journal of Chemical Technology and Biotechnology, **86**(1), pp. 10–17.

[221] Brennan, M. D., Rexius-Hall, M. L., Elgass, L. J., and Eddington, D. T., 2014, "Oxygen Control with Microfluidics," Lab Chip, **14**(22), pp. 4305–4318.

[222] Funamoto, K., Zervantonakis, I. K., Liu, Y., Ochs, C. J., Kim, C., and Kamm, R. D., 2012, "A Novel Microfluidic Platform for High-Resolution Imaging of a Three-Dimensional Cell Culture under a Controlled Hypoxic Environment," Lab Chip, **12**(22), pp. 4855–4863.

[223] Chen, Y.-A., King, A. D., Shih, H.-C., Peng, C.-C., Wu, C.-Y., Liao, W.-H., and Tung, Y.-C., 2011, "Generation of Oxygen Gradients in Microfluidic Devices for Cell Culture Using Spatially Confined Chemical Reactions," Lab Chip, **11**(21), p. 3626.

[224] Li, Y., Li, L., Liu, Z., Ding, M., Luo, G., and Liang, Q., 2016, "A Microfluidic Chip of Multiple-Channel Array with Various Oxygen Tensions for Drug Screening," Microfluid Nanofluidics, **20**(7), p. 97.

[225] Sun, W., Chen, Y., Wang, Y., Luo, P., Zhang, M., Zhang, H., and Hu, P., 2018, "Interaction Study of Cancer Cells and Fibroblasts on a Spatially Confined Oxygen Gradient Microfluidic Chip to Investigate the Tumor Microenvironment," Analyst.

[226] Wang, X., and Wolfbeis, O. S., 2014, "Optical Methods for Sensing and Imaging Oxygen: Materials, Spectroscopies and Applications," Chem. Soc. Rev., **43**(10), pp. 3666–3761.

[227] Mehta, G., Mehta, K., Sud, D., Song, J. W., Bersano-Begey, T., Futai, N., Heo, Y. S., Mycek, M.-A., Linderman, J. J., and Takayama, S., 2007, "Quantitative Measurement and Control of Oxygen Levels in Microfluidic Poly(Dimethylsiloxane) Bioreactors during Cell Culture," Biomed Microdevices, **9**(2), pp. 123–134.

[228] Thomas, P. C., Halter, M., Tona, A., Raghavan, S. R., Plant, A. L., and Forry, S. P., 2009, "A Noninvasive Thin Film Sensor for Monitoring Oxygen Tension during in Vitro Cell Culture," Anal Chem, **81**(22), pp. 9239–9246.

[229] Ges, I. A., Ivanov, B. L., Schaffer, D. K., Lima, E. A., Werdich, A. A., and Baudenbacher, F. J., 2005, "Thin-Film IrOx PH Microelectrode for Microfluidic-Based Microsystems," Biosens Bioelectron, **21**(2), pp. 248–256.

[230] Wu, C. C., Lin, W. C., and Fu, S. Y., 2011, "The Open Container-Used Microfluidic Chip Using IrOx Ultramicroelectrodes for the in Situ Measurement of Extracellular Acidification," Biosens Bioelectron, **26**(10), pp. 4191–4197.

[231] Zhan, W., Seong, G. H., and Crooks, R. M., 2002, "Hydrogel-Based Microreactors as a Functional Component of Microfluidic Systems," Anal Chem, **74**(18), pp. 4647–4652.

[232] Zou, X., Pan, T., Chen, L., Tian, Y., and Zhang, W., 2017, "Luminescence Materials for PH and Oxygen Sensing in Microbial Cells – Structures, Optical Properties, and Biological Applications," Crit Rev Biotechnol, **37**(6), pp. 723–738.

[233] Welch, D., and Christen, J. B., 2014, "Real-Time Feedback Control of PH within Microfluidics Using Integrated Sensing and Actuation," Lab Chip, **14**(6), pp. 1191–1197.

[234] Wu, S., Wu, S., Yi, Z., Zeng, F., Wu, W., Qiao, Y., Zhao, X., Cheng, X., and Tian, Y., 2018, "Hydrogel-Based Fluorescent Dual PH and Oxygen Sensors Loaded in 96-Well Plates for High-Throughput Cell Metabolism Studies," Sensors, **18**(2), p. 564.

[235] Tian, Y., Shumway, B. R., Cody Youngbull, A., Li, Y., Jen, A. K.-Y., Johnson, R. H., and Meldrum, D. R., 2010, "Dually Fluorescent Sensing of PH and Dissolved Oxygen Using a Membrane Made from Polymerizable Sensing Monomers," Sens Actuators B Chem, **147**(2), pp. 714–722.

[236] Shaegh, S. A. M., De Ferrari, F., Zhang, Y. S., Nabavinia, M., Mohammad, N. B., Ryan, J., Pourmand, A., Laukaitis, E., Sadeghian, R. B., Nadhman, A., Shin, S. R., Nezhad, A. S., Khademhosseini, A., and Dokmeci, M. R., 2016, "A Microfluidic Optical Platform for Real-Time Monitoring of PH and Oxygen in Microfluidic Bioreactors and Organ-on-Chip Devices," Biomicrofluidics, **10**(4), pp. 1–14.

[237] De Mello, A. J., Habgood, M., Lancaster, N. L., Welton, T., and Wootton, R. C. R., 2004, "Precise Temperature Control in Microfluidic Devices Using Joule Heating of Ionic Liquids," Lab Chip, **4**(5), pp. 417–419.

[238] Velve Casquillas, G., Fu, C., Le Berre, M., Cramer, J., Meance, S., Plecis, A., Baigl, D., Greffet, J. J., Chen, Y., Piel, M., and Tran, P. T., 2011, "Fast Microfluidic Temperature Control for High Resolution Live Cell Imaging," Lab Chip, **11**(3), pp. 484–489.

[239] Mao, H., Yang, T., and Cremer, P. S., 2002, "A Microfluidic Device with a Linear Temperature Gradient for Parallel and Combinatorial Measurements," J Am Chem Soc, **124**(16), pp. 4432–4435.

[240] Guijt, R. M., Dodge, A., Van Dedem, G. W. K., De Rooij, N. F., and Verpoorte, E., 2003, "Chemical and Physical Processes for Integrated Temperature Control in Microfluidic Devices," Lab Chip, **3**(1), pp. 1–4.

[241] Ross, D., Gaitan, M., and Locascio, L. E., 2001, "Temperature Measurement in Microfluidic Systems Using a Temperature-Dependent Fluorescent Dye," Anal Chem, **73**(17), pp. 4117–4123.

[242] Wong, D., Yesiloz, G., Boybay, M. S., and Ren, C. L., 2016, "Microwave Temperature Measurement in Microfluidic Devices," Lab Chip, **16**(12), pp. 2192–2197.

[243] Borisov, S. M., Seifner, R., and Klimant, I., 2011, "A Novel Planar Optical Sensor for Simultaneous Monitoring of Oxygen, Carbon Dioxide, PH and Temperature," Anal Bioanal Chem, **400**(8), pp. 2463–2474.

[244] Weltin, A., Slotwinski, K., Kieninger, J., Moser, I., Jobst, G., Wego, M., Ehret, R., and Urban, G. A., 2014, "Cell Culture Monitoring for Drug Screening and Cancer Research: A Transparent, Microfluidic, Multi-Sensor Microsystem," Lab Chip, **14**(1), pp. 138–146.

[245] Bavli, D., Prill, S., Ezra, E., Levy, G., Cohen, M., Vinken, M., Vanfleteren, J., Jaeger, M., and Nahmias, Y., 2016, "Real-Time Monitoring of Metabolic Function in Liver-on-Chip Microdevices Tracks the Dynamics of Mitochondrial Dysfunction," Proceedings of the National Academy of Sciences, **113**(16), pp. E2231–E2240.

[246] Schöning, M. J., and Poghossian, A., 2002, "Recent Advances in Biologically Sensitive Field-Effect Transistors (BioFETs)," Analyst, **127**(9), pp. 1137–1151.

[247] Hafeman, D., Parce, J., and McConnell, H., 1988, "Light-Addressable Potentiometric Sensor for Biochemical Systems," Science (1979), **240**(4856), pp. 1182–1185.

[248] Eklund, S. E., Snider, R. M., Wikswo, J., Baudenbacher, F., Prokop, A., and Cliffel, D. E., 2006, "Multianalyte Microphysiometry as a Tool in Metabolomics and Systems Biology," Journal of Electroanalytical Chemistry, **587**(2), pp. 333–339.

[249] Wagner, T., Vornholt, W., Werner, C. F., Yoshinobu, T., Miyamoto, K. ichiro, Keusgen, M., and Schöning, M. J., 2016, "Light-Addressable Potentiometric Sensor (LAPS) Combined with Magnetic Beads for Pharmaceutical Screening," Physics in Medicine, **1**, pp. 2–7.

[250] Steiner, M. S., Duerkop, A., and Wolfbeis, O. S., 2011, "Optical Methods for Sensing Glucose," Chem Soc Rev, **40**(9), pp. 4805–4839.

[251] Carter, K. P., Young, A. M., and Palmer, A. E., 2014, "Fluorescent Sensors for Measuring Metal Ions in Living Systems," Chem Rev, **114**(8), pp. 4564–4601.

[252] Keenan, T. M., and Folch, A., 2008, "Biomolecular Gradients in Cell Culture Systems," Lab Chip, **8**(1), pp. 34–57.

[253] Chang, C.-W., Cheng, Y.-J., Tu, M., Chen, Y.-H., Peng, C.-C., Liao, W.-H., and Tung, Y.-C., 2014, "A Polydimethylsiloxane–Polycarbonate Hybrid Microfluidic Device Capable of Generating Perpendicular Chemical and Oxygen Gradients for Cell Culture Studies," Lab Chip, **14**(19), pp. 3762–3772.

[254] Dou, J., Mao, S., Li, H., and Lin, J. M., 2019, "Combination Stiffness Gradient with Chemical Stimulation Directs Glioma Cell Migration on a Microfluidic Chip," Anal Chem.

[255] LeDuc, P. R., Messner, W. C., and Wikswo, J. P., 2011, "How Do Control-Based Approaches Enter into Biology?," Annu Rev Biomed Eng, **13**(1), pp. 369–396.

[256] Rumaner, Horowitz, Ovadya, and Folch, A., 2019, "Thread as a Low-Cost Material for Microfluidic Assays on Intact Tumor Slices," Micromachines (Basel), **10**(7), p. 481.

[257] Lohasz, C., Frey, O., Bonanini, F., Renggli, K., and Hierlemann, A., 2019, "Tubing-Free Microfluidic Microtissue Culture System Featuring Gradual, in Vivo-like Substance Exposure Profiles," Front Bioeng Biotechnol, **7**(APR).

[258] Wikswo, J. P., Markov, D. A., Samson, P. C., Block, F. E., Schaffer, D. K., and Reiserer, R. S., 2018, "Interconnections of Multiple Perfused Engineered Tissue Constructs and Microbioreactors, Multi-Microformulators and Applications of the Same. US20170081625A1 United States Patent Application."

[259] Lee, R. E. C., Qasaimeh, M. A., Xia, X., Juncker, D., and Gaudet, S., 2016, "NF-KB Signalling and Cell Fate Decisions in Response to a Short Pulse of Tumour Necrosis Factor," Sci Rep, **6**(December), pp. 1–12.

[260] Song, J., Ryu, H., Chung, M., Kim, Y., Blum, Y., Lee, S. sik, Pertz, O., and Jeon, N. L., 2018, "Microfluidic Platform for Single Cell Analysis under Dynamic Spatial and Temporal Stimulation," Biosens Bioelectron, **104**(December 2017), pp. 58–64.

[261] Liu, Y., Gill, E., and Shery Huang, Y. Y., 2017, "Microfluidic On-Chip Biomimicry for 3D Cell Culture: A Fit-for-Purpose Investigation from the End User Standpoint," Future Sci OA, **3**(2), p. FSO173.

[262] Maoz, B. M., Herland, A., Henry, O. Y. F., Leineweber, W. D., Yadid, M., Doyle, J., Mannix, R., Kujala, V. J., FitzGerald, E. A., Parker, K. K., and Ingber, D. E., 2017, "Organs-on-Chips with Combined Multi-Electrode Array and Transepithelial Electrical Resistance Measurement Capabilities," Lab Chip, **17**(13), pp. 2294–2302.

[263] Giampetruzzi, L., Barca, A., Casino, F., Capone, S., Verri, T., Siciliano, P., and Francioso, L., 2018, "Multi-Sensors Integration in a Human Gut-On-Chip Platform," Proc West Mark Ed Assoc Conf, **2**(13), p. 1022.

[264] Zhang, Y. S., Aleman, J., Shin, S. R., Kilic, T., Kim, D., Mousavi Shaegh, S. A., Massa, S., Riahi, R., Chae, S., Hu, N., Avci, H., Zhang, W., Silvestri, A., Sanati Nezhad, A., Manbohi, A., De Ferrari, F., Polini, A., Calzone, G., Shaikh, N., Alerasool, P., Budina, E., Kang, J., Bhise, N., Ribas, J., Pourmand, A., Skardal, A., Shupe, T., Bishop, C. E., Dokmeci, M. R., Atala, A., and Khademhosseini, A., 2017, "Multisensor-Integrated Organs-on-Chips Platform for Automated and Continual in Situ Monitoring of Organoid Behaviors," Proceedings of the National Academy of Sciences, **114**(12), pp. E2293–E2302.

[265] Schumacher, S., Nestler, J., Otto, T., Wegener, M., Ehrentreich-Förster, E., Michel, D., Wunderlich, K., Palzer, S., Sohn, K., Weber, A., Burgard, M., Grzesiak, A., Teichert, A., Brandenburg, A., Koger, B., Albers, J., Nebling, E., and Bier, F. F., 2012, "Highly-Integrated Lab-on-Chip System for Point-of-Care Multiparameter Analysis," Lab Chip, **12**(3), pp. 464–473.

[266] Enders, J. R., Marasco, C. C., Kole, A., Nguyen, B., Sevugarajan, S., Seale, K. T., Wikswo, J. P., and McLean, J. A., 2010, "Towards Monitoring Real-Time Cellular Response Using an Integrated Microfluidics-Matrix Assisted Laser Desorption Ionisation/Nanoelectrospray Ionisation-Ion Mobility-Mass Spectrometry Platform," IET Syst Biol, **4**(6), pp. 416–427.

[267] Wikswo, J. P., Block, F. E., Cliffel, D. E., Goodwin, C. R., Marasco, C. C., Markov, D. A., McLean, D. L., McLean, J. A., McKenzie, J. R., Reiserer, R. S., Samson, P. C., Schaffer, D. K., Seale, K. T., and Sherrod, S. D., 2013, "Engineering Challenges for Instrumenting and Controlling Integrated Organ-on-Chip Systems," IEEE Trans Biomed Eng, **60**(3), pp. 682–690.

[268] Semenza, G. L., 2012, "Hypoxia-Inducible Factors in Physiology and Medicine," Cell, **148**(3), pp. 399–408.

[269] Popel, A. S., 1989, "Theory of Oxygen Transport to Tissue.," Crit Rev Biomed Eng, **17**(3), pp. 257–321.

[270] Hall, J. E., 2017, *Guyton and Hall: Textbook of Medical Physiology*, Elsevier, Philadelphia.

[271] Carreau, A., Hafny-Rahbi, B. El, Matejuk, A., Grillon, C., and Kieda, C., 2011, "Why Is the Partial Oxygen Pressure of Human Tissues a Crucial Parameter? Small Molecules and Hypoxia," J Cell Mol Med, **15**(6), pp. 1239–1253.

[272] Muz, B., de la Puente, P., Azab, F., and Azab, A. K., 2015, "The Role of Hypoxia in Cancer Progression, Angiogenesis, Metastasis, and Resistance to Therapy," Hypoxia, p. 83.

[273] PACKER, L., and FUEHR, K., 1977, "Low Oxygen Concentration Extends the Lifespan of Cultured Human Diploid Cells," Nature, **267**(5610), pp. 423–425.

[274] Pavlacky, J., and Polak, J., 2020, "Technical Feasibility and Physiological Relevance of Hypoxic Cell Culture Models," Front Endocrinol (Lausanne), **11**(February), pp. 1–15.

[275] Oppegard, S. C., Nam, K. H., Carr, J. R., Skaalure, S. C., and Eddington, D. T., 2009, "Modulating Temporal and Spatial Oxygenation over Adherent Cellular Cultures," PLoS One, **4**(9).

[276] Namiki, A., Brogi, E., Kearney, M., Kim, E. A., Wu, T., Couffinhal, T., Varticovski, L., and Isner, J. M., 1995, "Hypoxia Induces Vascular Endothelial Growth Factor in Cultured Human Endothelial Cells," Journal of Biological Chemistry, **270**(52), pp. 31189–31195.

[277] Rexius-Hall, M. L., Rehman, J., and Eddington, D. T., 2017, "A Microfluidic Oxygen Gradient Demonstrates Differential Activation of the Hypoxia-Regulated Transcription Factors HIF-1α and HIF-2α," Integrative Biology (United Kingdom), **9**(9), pp. 742–750.

[278] Reist, M., Marshall, K. A., Jenner, P., and Halliwell, B., 1998, "Toxic Effects of Sulphite in Combination with Peroxynitrite on Neuronal Cells," J Neurochem, **71**(6), pp. 2431–2438.

[279] Amini, H., Lee, W., and Di Carlo, D., 2014, "Inertial Microfluidic Physics," Lab Chip, **14**(15), pp. 2739–2761.

[280] Rexius-Hall, M. L., Mauleon, G., Malik, A. B., Rehman, J., and Eddington, D. T., 2014, "Microfluidic Platform Generates Oxygen Landscapes for Localized Hypoxic Activation," Lab Chip, **14**(24), pp. 4688–4695.

[281] Grist, S. M., Nasseri, S. S., Laplatine, L., Schmok, J. C., Yao, D., Hua, J., Chrostowski, L., and Cheung, K. C., 2019, "Long-Term Monitoring in a Microfluidic System to Study Tumour Spheroid Response to Chronic and Cycling Hypoxia," Sci Rep, **9**(1), p. 17782.

[282] Jalili-Firoozinezhad, S., Gazzaniga, F. S., Calamari, E. L., Camacho, D. M., Fadel, C. W., Bein, A., Swenor, B., Nestor, B., Cronce, M. J., Tovaglieri, A., Levy, O., Gregory, K. E., Breault, D. T., Cabral, J. M. S., Kasper, D. L., Novak, R., and Ingber, D. E., 2019, "A Complex Human Gut

Microbiome Cultured in an Anaerobic Intestine-on-a-Chip.," Nat Biomed Eng, **3**(7), pp. 520–531.

[283] Wu, Q., Liu, J., Wang, X., Feng, L., Wu, J., Zhu, X., Wen, W., and Gong, X., 2020, "Organ-on-a-Chip: Recent Breakthroughs and Future Prospects," Biomed Eng Online, **19**(1), pp. 1–19.

[284] Martin, H., Sarsat, J. P., Lerche-Langrand, C., Housset, C., Balladur, P., Toutain, H., and Albaladejo, V., 2002, "Morphological and Biochemical Integrity of Human Liver Slices in Long-Term Culture: Effects of Oxygen Tension," Cell Biol Toxicol, **18**(2), pp. 73–85.

[285] Gaikwad, K. K., Singh, S., and Lee, Y. S., 2017, "A New Pyrogallol Coated Oxygen Scavenging Film and Their Effect on Oxidative Stability of Soybean Oil under Different Storage Conditions," Food Sci Biotechnol, **26**(6), pp. 1535–1543.

[286] Ramasarma, T., Rao, A. V. S., Devi, M. M., Omkumar, R. V., Bhagyashree, K. S., and Bhat, S. V., 2014, "New Insights of Superoxide Dismutase Inhibition of Pyrogallol Autoxidation," Mol Cell Biochem, **400**(1–2), pp. 277–285.

[287] Taubert, D., Breitenbach, T., Lazar, A., Censarek, P., Harlfinger, S., Berkels, R., Klaus, W., and Roesen, R., 2003, "Reaction Rate Constants of Superoxide Scavenging by Plant Antioxidants," Free Radic Biol Med, **35**(12), pp. 1599–1607.

[288] Poulsen, L., and Ogilby, P. R., 2000, "Oxygen Diffusion in Glassy Polymer Films: Effects of Other Gases and Changes in Pressure," Journal of Physical Chemistry A, **104**(12), pp. 2573–2580.

[289] Ogilvie, I. R. G., Sieben, c V. J., Floquet, C. F. A., Zmijan, R., Mowlem, M. C., and Morgan, H., 2010, "SOLVENT PROCESSING OF PMMA AND COC CHIPS FOR BONDING DEVICES WITH OPTICAL QUALITY SURFACES," *14th International Conference on Miniaturized Systems for Chemistry and Life Sciences*, pp. 1244–1246.

[290] Koren, K., Borisov, S. M., and Klimant, I., 2012, "Stable Optical Oxygen Sensing Materials Based on Click-Coupling of Fluorinated Platinum(II) and Palladium(II) Porphyrins - A Convenient Way to Eliminate Dye Migration and Leaching," Sens Actuators B Chem, **169**(May 2015), pp. 173–181.

[291] Borisov, S. M., Lehner, P., and Klimant, I., 2011, "Novel Optical Trace Oxygen Sensors Based on Platinum(II) and Palladium(II) Complexes with 5,10,15,20-Meso-Tetrakis-(2,3,4,5,6-Pentafluorphenyl)-Porphyrin Covalently Immobilized on Silica-Gel Particles," Anal Chim Acta, **690**(1), pp. 108–115.

[292] Presley, K., Shahhosseini, M., Shi, D., Castro, C., and Lannutti, J., 2019, "Analysis of Long-Term Optical Performance of Phosphorescent Oxygen Sensing Polymeric Nanofibers," Polym Test, **80**(September), p. 106127.

[293] Thomas, P. C., Halter, M., Tona, A., Raghavan, S. R., Plant, A. L., and Forry, S. P., 2009, "A Noninvasive Thin Film Sensor for Monitoring Oxygen Tension during in Vitro Cell Culture," Anal Chem, **81**(22), pp. 9239–9246.

[294] Khan, D. H., Roberts, S. A., Cressman, J. R., and Agrawal, N., 2017, "Rapid Generation and Detection of Biomimetic Oxygen Concentration Gradients in Vitro," Sci Rep, **7**(1), pp. 1–11.

[295] Park, D. H., Jeon, H. J., Kim, M. J., Nguyen, X. D., Morten, K., and Go, J. S., 2017, "3D Microfluidic Perfuison Cell Culture System with Linear Concentration Gradient and Air Bubble Trapping," *2017 19th International Conference on Solid-State Sensors, Actuators and Microsystems (TRANSDUCERS)*, IEEE, pp. 281–284.

[296] Hassanpour-Tamrin, S., Sanati-Nezhad, A., and Sen, A., 2021, "A Simple and Low-Cost Approach for Irreversible Bonding of Polymethylmethacrylate and Polydimethylsiloxane at Room Temperature for High-Pressure Hybrid Microfluidics," Sci Rep, **11**(1), pp. 1–12.

[297] Green, M. R., and Sambrook, J., 2019, "Polymerase Chain Reaction," Cold Spring Harb Protoc, **2019**(6), p. pdb.top095109.

[298] ThermoFisher Scientific, "Basic Principles of RT-QPCR" [Online]. Available: https://www.thermofisher.com/uk/en/home/brands/thermo-scientific/molecular-biology/molecular-biology-learning-center/molecular-biology-resource-library/spotlight-articles/basic-principles-rt-qpcr.html.

[299] Lekanne Deprez, R. H., Fijnvandraat, A. C., Ruijter, J. M., and Moorman, A. F. M., 2002, "Sensitivity and Accuracy of Quantitative Real-Time Polymerase Chain Reaction Using SYBR Green I Depends on CDNA Synthesis Conditions," Anal Biochem, **307**(1), pp. 63–69.

[300] Tajadini, M., Panjehpour, M., and Javanmard, S., 2014, "Comparison of SYBR Green and TaqMan Methods in Quantitative Real-Time Polymerase Chain Reaction Analysis of Four Adenosine Receptor Subtypes," Adv Biomed Res, **3**(1), p. 85.

[301] Green, M. R., and Sambrook, J., 2018, "Analysis and Normalization of Real-Time Polymerase Chain Reaction (PCR) Experimental Data," Cold Spring Harb Protoc, **2018**(10), p. pdb.top095000.

[302] Livak, K. J., 1997, "ABI P RISM 7700 Sequence Detection System. User Bulletin No. 2," PE Applied Biosystems, **1997** [Online]. Available: http://docs.appliedbiosystems.com/pebiodocs/04303859.pdf.

[303] Aslantürk, Ö. S., 2018, "In Vitro Cytotoxicity and Cell Viability Assays: Principles, Advantages, and Disadvantages," *Genotoxicity - A Predictable Risk to Our Actual World*, InTech, p. 13.

[304] Kaja, S., Payne, A. J., Naumchuk, Y., and Koulen, P., 2017, "Quantification of Lactate Dehydrogenase for Cell Viability Testing Using Cell Lines and Primary Cultured Astrocytes," Curr Protoc Toxicol, **72**(1), pp. 139–148.

[305] Aslantürk, Ö. S., 2018, "In Vitro Cytotoxicity and Cell Viability Assays: Principles, Advantages, and Disadvantages," *Genotoxicity - A Predictable Risk to Our Actual World*, InTech, p. 13.

[306] Park, H., Park, J. Y., Park, K. M., and Chang, P. S., 2021, "Effects of Freezing Rate on Structural Changes in L-Lactate Dehydrogenase during the Freezing Process," Sci Rep, **11**(1).

[307] Starnes, J. W., 2008, "Effect of Storage Conditions on Lactate Dehydrogenase Released from Perfused Hearts," Int J Cardiol, **127**(1), pp. 114–116.

[308] Darnet, S., Thomas, D., and Legoy, M.-D., 1993, *Use of Enzymatic Oxygen Scavengers to Prevent Lactate Dehydrogenase Inactivation by Oxygen Radicals*.

[309] Kendig, D. M., and Tarloff, J. B., 2007, "Inactivation of Lactate Dehydrogenase by Several Chemicals: Implications for in Vitro Toxicology Studies," Toxicology in Vitro, **21**(1), pp. 125–132.

[310] Zigler, J. S., Lepe-Zuniga, J. L., Vistica, B., and Gery, I., 1985, "Analysis of the Cytotoxic Effects of Light-Exposed Hepes-Containing Culture Medium," In Vitro Cellular & Developmental Biology, **21**(5), pp. 282–287.

[311] Dabaghi, M., Shahriari, S., Saraei, N., Da, K., Chandiramohan, A., Selvaganapathy, P. R., and Hirota, J. A., 2021, "Article Surface Modification of Pdms-Based Microfluidic Devices with Collagen Using Polydopamine as a Spacer to Enhance Primary Human Bronchial Epithelial Cell Adhesion," Micromachines (Basel), **12**(2), pp. 1–11.

[312] Sedlakova, O., Svastova, E., Takacova, M., Kopacek, J., Pastorek, J., and Pastorekova, S., 2014, "Carbonic Anhydrase IX, a Hypoxia-Induced Catalytic Component of the PH Regulating Machinery in Tumors," Front Physiol, **4 JAN**(January), pp. 1–14.

[313] van den Beucken, T., Koritzinsky, M., Niessen, H., Dubois, L., Savelkouls, K., Mujcic, H., Jutten, B., Kopacek, J., Pastorekova, S., van der Kogel, A. J., Lambin, P., Voncken, W., Rouschop, K. M. A., and Wouters, B. G., 2009, "Hypoxia-Induced Expression of Carbonic Anhydrase 9 Is Dependent on the Unfolded Protein Response," Journal of Biological Chemistry, **284**(36), pp. 24204–24212.

[314] Juhász, P., Hasulyó, D., Bedekovics, J., Beke, L., Kacsala, N., Török, M., and Méhes, G., 2023, "Carbonic Anhydrase IX (CAIX) Expressing Hypoxic Micro-Environment Hampers CD8+ Immune Cell Infiltrate in Breast Carcinoma," Applied Immunohistochemistry and Molecular Morphology, **31**(1), pp. 26–32.

[315] Namiki, A., Brogi, E., Kearney, M., Kim, E. A., Wu, T., Couffinhal, T., Varticovski, L., and Isner, J. M., 1995, "Hypoxia Induces Vascular Endothelial Growth Factor in Cultured Human Endothelial Cells," Journal of Biological Chemistry, **270**(52), pp. 31189–31195.

[316] Faller, D. V., 1999, "Endothelial Cell Responses to Hypoxic Stress," Clin Exp Pharmacol Physiol, **26**(1), pp. 74–84.

[317] Liu, Y., Cox, S. R., Morita, T., and Kourembanas, S., 1995, "Hypoxia Regulates Vascular Endothelial Growth Factor Gene Expression in Endothelial Cells: Identification of a 5' Enhancer," Circ Res, **77**(3), pp. 638–643.

[318] da Conceição Braga, L., Gonçalves, B. Ô. P., Coelho, P. L., da Silva Filho, A. L., and Silva, L. M., 2022, "Identification of Best Housekeeping Genes for the Normalization of RT-QPCR in Human Cell Lines," Acta Histochem, **124**(1).

[319] Krainova, N. A., Khaustova, N. A., Makeeva, D. S., Fedotov, N. N., Gudim, E. A., Ryabenko, E. A., Shkurnikov, M. U., Galatenko, V. V., Sakharov, D. A., and Maltseva, D. V., 2013, "Evaluation of Potential Reference Genes for QRT-PCR Data Normalization in HeLa Cells," Appl Biochem Microbiol, **49**(9), pp. 743–749.

[320] Chen, Y.-A., King, A. D., Shih, H.-C., Peng, C.-C., Wu, C.-Y., Liao, W.-H., and Tung, Y.-C., 2011, "Generation of Oxygen Gradients in Microfluidic Devices for Cell Culture Using Spatially Confined Chemical Reactions," Lab Chip, **11**(21), p. 3626.

[321] Peng, C.-C., Liao, W.-H., Chen, Y.-H., Wu, C.-Y., and Tung, Y.-C., 2013, "A Microfluidic Cell Culture Array with Various Oxygen Tensions," Lab Chip, **13**(16), p. 3239.

[322] Chang, C.-W., Cheng, Y.-J., Tu, M., Chen, Y.-H., Peng, C.-C., Liao, W.-H., and Tung, Y.-C., 2014, "A Polydimethylsiloxane–Polycarbonate Hybrid Microfluidic Device Capable of Generating Perpendicular Chemical and Oxygen Gradients for Cell Culture Studies," Lab Chip, **14**(19), pp. 3762–3772.

[323] Chiang, H.-J., Yeh, S.-L., Peng, C.-C., Liao, W.-H., and Tung, Y.-C., 2017, "Polydimethylsiloxane-Polycarbonate Microfluidic Devices for Cell Migration Studies Under Perpendicular Chemical and Oxygen Gradients," Journal of Visualized Experiments, (120), pp. 1–8.

[324] Sun, W., Chen, Y., Wang, Y., Luo, P., Zhang, M., Zhang, H., and Hu, P., 2018, "Interaction Study of Cancer Cells and Fibroblasts on a Spatially Confined Oxygen Gradient Microfluidic Chip to Investigate the Tumor Microenvironment," Analyst.

[325] Li, Y., Li, L., Liu, Z., Ding, M., Luo, G., and Liang, Q., 2016, "A Microfluidic Chip of Multiple-Channel Array with Various Oxygen Tensions for Drug Screening," Microfluid Nanofluidics, **20**(7), p. 97.

[326] Skolimowski, M., Nielsen, M. W., Emnéus, J., Molin, S., Taboryski, R., Sternberg, C., Dufva, M., and Geschke, O., 2010, "Microfluidic Dissolved Oxygen Gradient Generator Biochip as a Useful Tool in Bacterial Biofilm Studies," Lab Chip, **10**(16), p. 2162.

[327] Barmaki, S., Jokinen, V., Obermaier, D., Blokhina, D., Korhonen, M., Ras, R. H. A., Vuola, J., Franssila, S., and Kankuri, E., 2018, "A Microfluidic Oxygen Sink to Create a Targeted Cellular Hypoxic Microenvironment under Ambient Atmospheric Conditions," Acta Biomater, **73**, pp. 167–179.

[328] Wang, L., Liu, W., Wang, Y., Wang, J. C., Tu, Q., Liu, R., and Wang, J., 2013, "Construction of Oxygen and Chemical Concentration Gradients in a Single Microfluidic Device for Studying Tumor Cell-Drug Interactions in a Dynamic Hypoxia Microenvironment," Lab Chip, **13**(4), pp. 695–705.

[329] Funamoto, K., Zervantonakis, I. K., Liu, Y., Ochs, C. J., Kim, C., and Kamm, R. D., 2012, "A Novel Microfluidic Platform for High-Resolution Imaging of a Three-Dimensional Cell Culture under a Controlled Hypoxic Environment," Lab Chip, **12**(22), pp. 4855–4863.

[330] Rexius-Hall, M. L., Mauleon, G., Malik, A. B., Rehman, J., and Eddington, D. T., 2014, "Microfluidic Platform Generates Oxygen Landscapes for Localized Hypoxic Activation," Lab Chip, **14**(24), pp. 4688–4695.

[331] Vollmer, A. P., Probstein, R. F., Gilbert, R., and Thorsen, T., 2005, "Development of an Integrated Microfluidic Platform for Dynamic Oxygen Sensing and Delivery in a Flowing Medium," Lab Chip, **5**(10), pp. 1059–1066.

[332] Khan, D. H., Roberts, S. A., Cressman, J. R., and Agrawal, N., 2017, "Rapid Generation and Detection of Biomimetic Oxygen Concentration Gradients in Vitro," Sci Rep, **7**(1), pp. 1–11.

[333] Mehta, G., Mehta, K., Sud, D., Song, J. W., Bersano-Begey, T., Futai, N., Heo, Y. S., Mycek, M.-A., Linderman, J. J., and Takayama, S., 2007, "Quantitative Measurement and Control of Oxygen Levels in Microfluidic Poly(Dimethylsiloxane) Bioreactors during Cell Culture," Biomed Microdevices, **9**(2), pp. 123–134.

[334] Lei, Y. H., Liu, Y. P., Wang, W., Wu, W. G., and Li, Z. H., 2011, "Fabrication and Characterization of Parylene C-Caulked PDMS for Low-Permeable Microfluidics," *2011 IEEE 24th International Conference on Micro Electro Mechanical Systems*, IEEE, pp. 1123–1126.

[335] Ochs, C. J., Kasuya, J., Pavesi, A., and Kamm, R. D., 2014, "Oxygen Levels in Thermoplastic Microfluidic Devices during Cell Culture," Lab Chip, **14**(3), pp. 459–462.

[336] Gao, Y., Stybayeva, G., and Revzin, A., 2019, "Fabrication of Composite Microfluidic Devices for Local Control of Oxygen Tension in Cell Cultures," Lab Chip, **19**(2), pp. 306–315.

[337] Shaegh, S. A. M., De Ferrari, F., Zhang, Y. S., Nabavinia, M., Mohammad, N. B., Ryan, J., Pourmand, A., Laukaitis, E., Sadeghian, R. B., Nadhman, A., Shin, S. R., Nezhad, A. S., Khademhosseini, A., and Dokmeci, M. R., 2016, "A Microfluidic Optical Platform for Real-Time Monitoring of PH and Oxygen in Microfluidic Bioreactors and Organ-on-Chip Devices," Biomicrofluidics, **10**(4), pp. 1–14.

[338] Bamshad, A., Nikfarjam, A., and Khaleghi, H., 2016, "A New Simple and Fast Thermally-Solvent Assisted Method to Bond PMMA–PMMA in Micro-Fluidics Devices," Journal of Micromechanics and Microengineering, **26**(6), p. 065017.

[339] Vlachopoulou, M. E., Tserepi, A., Pavli, P., Argitis, P., Sanopoulou, M., and Misiakos, K., 2009, "A Low Temperature Surface Modification Assisted Method for Bonding Plastic Substrates," Journal of Micromechanics and Microengineering, **19**(1).

[340] Boyce, M. W., Kenney, R. M., Truong, A. S., and Lockett, M. R., 2016, "Quantifying Oxygen in Paper-Based Cell Cultures with Luminescent Thin Film Sensors," Anal Bioanal Chem, **408**(11), pp. 2985–2992.

[341] Tang, L., and Lee, N. Y., 2010, "A Facile Route for Irreversible Bonding of Plastic-PDMS Hybrid Microdevices at Room Temperature," Lab Chip, **10**(10), pp. 1274–1280.

[342] Hassanpour-Tamrin, S., Sanati-Nezhad, A., and Sen, A., 2021, "A Simple and Low-Cost Approach for Irreversible Bonding of Polymethylmethacrylate and Polydimethylsiloxane at Room Temperature for High-Pressure Hybrid Microfluidics," Sci Rep, **11**(1), pp. 1–12.

[343] Jeon, N. L., Dertinger, S. K. W., Chiu, D. T., Choi, I. S., Stroock, A. D., and Whitesides, G. M., 2000, "Generation of Solution and Surface Gradients Using Microfluidic Systems," Langmuir, **16**(22), pp. 8311–8316.

[344] Dertinger, S. K. W., Chiu, D. T., Jeon, N. L., and Whitesides, G. M., 2001, "Generation of Gradients Having Complex Shapes Using Microfluidic Networks," Anal Chem, **73**(6), pp. 1240–1246.

[345] Wang, X., and Wolfbeis, O. S., 2014, "Optical Methods for Sensing and Imaging Oxygen: Materials, Spectroscopies and Applications," Chem. Soc. Rev., **43**(10), pp. 3666–3761.

[346] Bedlek-Anslow, J. M., Hubner, J. P., Carroll, B. F., and Schanze, K. S., 2000, "Micro-Heterogeneous Oxygen Response in Luminescence Sensor Films," Langmuir, **16**(24), pp. 9137–9141.

[347] Mao, Y., Gao, Y., Wu, S., Wu, S., Shi, J., Zhou, B., and Tian, Y., 2017, "Highly Enhanced Sensitivity of Optical Oxygen Sensors Using Microstructured PtTFPP/PDMS-Pillar Arrays Sensing Layer," Sens Actuators B Chem, **251**, pp. 495–502.

[348] Zhao, Y., Liu, L., Luo, T., Hong, L., Peng, X., Austin, R. H., and Qu, J., 2018, "A Platinum-Porphine/Poly(Perfluoroether) Film Oxygen Tension Sensor for Noninvasive Local Monitoring of Cellular Oxygen Metabolism Using Phosphorescence Lifetime Imaging," Sens Actuators B Chem, **269**, pp. 88–95.

[349] Ghafoory, S., Stengl, C., Kopany, S., Mayadag, M., Mechtel, N., Murphy, B., Schattschneider, S., Wilhelmi, N., and Wölfl, S., 2022, "Oxygen Gradient Induced in Microfluidic Chips Can Be Used as a Model for Liver Zonation," Cells, **11**(23).

[350] Wang, X., Meier, R. J., Link, M., and Wolfbeis, O. S., 2010, "Photographing Oxygen Distribution," Angewandte Chemie International Edition, **49**(29), pp. 4907–4909.

[351] Wang, X., Gorris, H. H., Stolwijk, J. A., Meier, R. J., Groegel, D. B. M., Wegener, J., and Wolfbeis, O. S., 2011, "Self-Referenced RGB Colour Imaging of Intracellular Oxygen," Chem Sci, **2**(5), p. 901.

[352] Ungerböck, B., Mistlberger, G., Charwat, V., Ertl, P., and Mayr, T., 2010, "Oxygen Imaging in Microfluidic Devices with Optical Sensors Applying Color Cameras," Procedia Eng, **5**, pp. 456–459.

[353] Tian, Y., Shumway, B. R., Cody Youngbull, A., Li, Y., Jen, A. K.-Y., Johnson, R. H., and Meldrum, D. R., 2010, "Dually Fluorescent Sensing of PH and Dissolved Oxygen Using a Membrane Made from Polymerizable Sensing Monomers," Sens Actuators B Chem, **147**(2), pp. 714–722.

[354] Vernetti, L. A., Senutovitch, N., Boltz, R., DeBiasio, R., Ying Shun, T., Gough, A., and Taylor, D. L., 2016, "A Human Liver Microphysiology Platform for Investigating Physiology, Drug Safety, and Disease Models," Exp Biol Med, **241**(1), pp. 101–114.

[355] Matteucci, E., Gregori, G., Pellegrini, L., Navalesi, R., and Giampietro, O., 1991, "Effects of Storage Time and Temperature on Urinary Enzymes," Clin Chem, **37**(8), pp. 1436–1441.

[356] Aslantürk, Ö. S., 2018, "In Vitro Cytotoxicity and Cell Viability Assays: Principles, Advantages, and Disadvantages," *Genotoxicity - A Predictable Risk to Our Actual World*, InTech, p. 13.

[357] Xu, M., McCanna, D. J., and Sivak, J. G., 2015, "Use of the Viability Reagent PrestoBlue in Comparison with AlamarBlue and MTT to Assess the Viability of Human Corneal Epithelial Cells," J Pharmacol Toxicol Methods, **71**, pp. 1–7.

[358] Dominijanni, A. J., Devarasetty, M., Forsythe, S. D., Votanopoulos, K. I., and Soker, S., 2021, "Cell Viability Assays in Three-Dimensional Hydrogels: A Comparative Study of Accuracy," Tissue Eng Part C Methods, **27**(7), pp. 401–410.

[359] Ren, X., Tapias, L. F., Jank, B. J., Mathisen, D. J., Lanuti, M., and Ott, H. C., 2015, "Ex Vivo Non-Invasive Assessment of Cell Viability and Proliferation in Bio-Engineered Whole Organ Constructs," Biomaterials, **52**, pp. 103–112.

[360] Stucki, J. D., Hobi, N., Galimov, A., Stucki, A. O., Schneider-Daum, N., Lehr, C. M., Huwer, H., Frick, M., Funke-Chambour, M., Geiser, T., and Guenat, O. T., 2018, "Medium Throughput Breathing Human Primary Cell Alveolus-on-Chip Model," Sci Rep, **8**(1), pp. 1–13.

[361] Kühn, K., Hashimoto, S., and Lotz, M., 1999, "Cell Density Modulates Apoptosis in Human Articular Chondrocytes," J Cell Physiol, **180**(3), pp. 439–447.

[362] Van Liedekerke, P., Neitsch, J., Johann, T., Alessandri, K., Nassoy, P., and Drasdo, D., 2019, "Quantitative Agent-Based Modeling Reveals Mechanical Stress Response of Growing Tumor Spheroids Is Predictable over Various Growth Conditions and Cell Lines," PLoS Comput Biol, **15**(3).

[363] Fernandes, J., Karra, N., Bowring, J., Reale, R., James, J., Blume, C., Pell, T. J., Rowan, W. C., Davies, D. E., Swindle, E. J., and Morgan, H., 2022, "Real-Time Monitoring of Epithelial Barrier Function by Impedance Spectroscopy in a Microfluidic Platform," Lab Chip.

[364] Orcheston-Findlay, L., Hashemi, A., Garrill, A., and Nock, V., 2018, "A Microfluidic Gradient Generator to Simulate the Oxygen Microenvironment in Cancer Cell Culture," Microelectron Eng, **195**, pp. 107–113.

[365] Kostyunina, D. S., Rowan, S. C., Pakhomov, N. V., Dillon, E., Rochfort, K. D., Cummins, P. M., O'Rourke, M. J., and McLoughlin, P., 2023, "Shear Stress Markedly Alters the Proteomic Response to Hypoxia in Human Pulmonary Endothelial Cells," Am J Respir Cell Mol Biol, **68**(5), pp. 551–565.

[366] Kim, H. J., Huh, D., Hamilton, G., and Ingber, D. E., 2012, "Human Gut-on-a-Chip Inhabited by Microbial Flora That Experiences Intestinal Peristalsis-like Motions and Flow," Lab Chip, **12**(12), p. 2165.

[367] Fu, Y. J., Qui, H. Z., Liao, K. S., Lue, S. J., Hu, C. C., Lee, K. R., and Lai, J. Y., 2010, "Effect of UV-Ozone Treatment on Poly(Dimethylsiloxane) Membranes: Surface Characterization and Gas Separation Performance," Langmuir, **26**(6), pp. 4392–4399.

[368] Bouafsoun, A., Othmane, A., Kerkeni, A., Jaffrézic, N., and Ponsonnet, L., 2006, "Evaluation of Endothelial Cell Adherence onto Collagen and Fibronectin: A Comparison between Jet Impingement and Flow Chamber Techniques," *Materials Science and Engineering C*, pp. 260–266.

[369] Schor, S. L., and Court, J., 1979, *DIFFERENT MECHANISMS IN THE ATTACHMENT OF CELLS TO NATIVE AND DENATURED COLLAGEN*.

[370] Choi, C. K., and Helmke, B. P., 2008, "Short-Term Shear Stress Induces Rapid Actin Dynamics in Living Endothelial Cells.," Mol Cell Biomech, **5**(4), pp. 247–258.

[371] Juhász, P., Hasulyó, D., Bedekovics, J., Beke, L., Kacsala, N., Török, M., and Méhes, G., 2023, "Carbonic Anhydrase IX (CAIX) Expressing Hypoxic Micro-Environment Hampers CD8+ Immune Cell Infiltrate in Breast Carcinoma," Applied Immunohistochemistry and Molecular Morphology, **31**(1), pp. 26–32.

[372] Brereton, C. J., Yao, L., Davies, E. R., Zhou, Y., Vukmirovic, M., Bell, J. A., Wang, S., Ridley, R. A., Dean, L. S. N., Andriotis, O. G., Conforti, F., Brewitz, L., Mohammed, S., Wallis, T., Tavassoli, A., Ewing, R. M., Alzetani, A., Marshall, B. G., Fletcher, S. V., Thurner, P. J., Fabre, A., Kaminski, N., Richeldi, L., Bhaskar, A., Schofield, C. J., Loxham, M., Davies, D. E., Wang, Y., and Jones, M. G., 2022, "Pseudohypoxic HIF Pathway Activation Dysregulates Collagen Structure-Function in Human Lung Fibrosis," Elife, **11**, pp. 1–28.

[373] Faller, D. V., 1999, "Endothelial Cell Responses to Hypoxic Stress," Clin Exp Pharmacol Physiol, **26**(1), pp. 74–84.

[374] Sedlakova, O., Svastova, E., Takacova, M., Kopacek, J., Pastorek, J., and Pastorekova, S., 2014, "Carbonic Anhydrase IX, a Hypoxia-Induced Catalytic Component of the PH Regulating Machinery in Tumors," Front Physiol, **4 JAN**(January), pp. 1–14.

[375] Liu, Y., Cox, S. R., Morita, T., and Kourembanas, S., 1995, "Hypoxia Regulates Vascular Endothelial Growth Factor Gene Expression in Endothelial Cells: Identification of a 5' Enhancer," Circ Res, **77**(3), pp. 638–643.

[376] Wulftange, W. J., Rose, M. A., Garmendia-Cedillos, M., da Silva, D., Poprawski, J. E., Srinivasachar, D., Sullivan, T., Lim, L., Bliskovsky, V. V., Hall, M. D., Pohida, T. J., Robey, R. W., Morgan, N. Y., and Gottesman, M. M., 2019, "Spatial Control of Oxygen Delivery to Three-Dimensional Cultures Alters Cancer Cell Growth and Gene Expression," J Cell Physiol, **234**(11), pp. 20608–20622.

[377] Brereton, C. J., Yao, L., Davies, E. R., Zhou, Y., Vukmirovic, M., Bell, J. A., Wang, S., Ridley, R. A., Dean, L. S. N., Andriotis, O. G., Conforti, F., Brewitz, L., Mohammed, S., Wallis, T., Tavassoli, A., Ewing, R. M., Alzetani, A., Marshall, B. G., Fletcher, S. V., Thurner, P. J., Fabre, A., Kaminski, N., Richeldi, L., Bhaskar, A., Schofield, C. J., Loxham, M., Davies, D. E., Wang, Y., and Jones, M. G., 2022, "Pseudohypoxic HIF Pathway Activation Dysregulates Collagen Structure-Function in Human Lung Fibrosis," Elife, **11**, pp. 1–28.

[378] Setty, B. A., Pillay Smiley, N., Pool, C. M., Jin, Y., Liu, Y., and Nelin, L. D., 2017, "Hypoxia-Induced Proliferation of HeLa Cells Depends on Epidermal Growth Factor Receptor-Mediated Arginase II Induction," Physiol Rep, **5**(6), p. e13175.

[379] Baird, N. A., Turnbull, D. W., and Johnson, E. A., 2006, "Induction of the Heat Shock Pathway during Hypoxia Requires Regulation of Heat Shock Factor by Hypoxia-Inducible Factor-1," Journal of Biological Chemistry, **281**(50), pp. 38675–38681.

[380] Martin, C., Uhlig, S., and Ullrich, V., 1996, "Videomicroscopy of Methacholine-Induced Contraction of Individual Airways in Precision-Cut Lung Slices," European Respiratory Journal, **9**(12), pp. 2479–2487.

Appendices

Appendix 1. Design drawings

a. Device v4 – Gas layer

b. Device v4 – Culture layer

c. Oxygen gradient generator

d. Clamp platform – top

e. Clamp platform – bottom

f. Chip holder – top

g. Chip holder – bottom

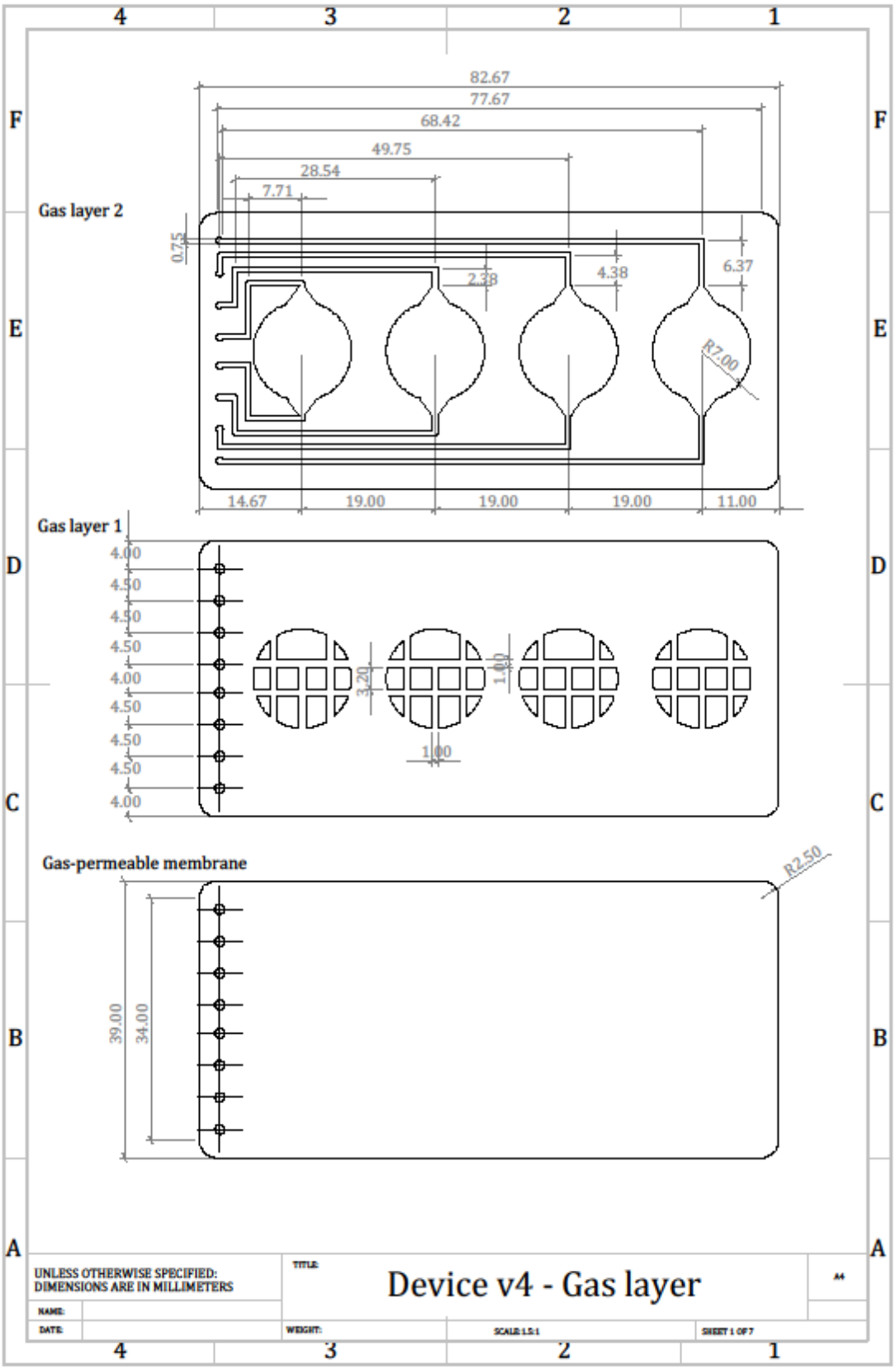
Gas layer 2
82.67
77.67
68.42
49.75
28.54
7.71
0.75
2.38
4.38
6.37
R7.00
14.67
19.00
19.00
19.00
11.00
Gas layer 1
4.00
4.50
4.50
4.50
4.00
4.50
4.50
4.50
4.00
3.20
1.00
1.00
Gas-permeable membrane
R2.50
39.00
34.00
UNLESS OTHERWISE SPECIFIED:
DIMENSIONS ARE IN MILLIMETERS
TITLE:
Device v4 - Gas layer
A4
NAME:
DATE:
WEIGHT:
SCALE: 1.5:1
SHEET 1 OF 7

1)

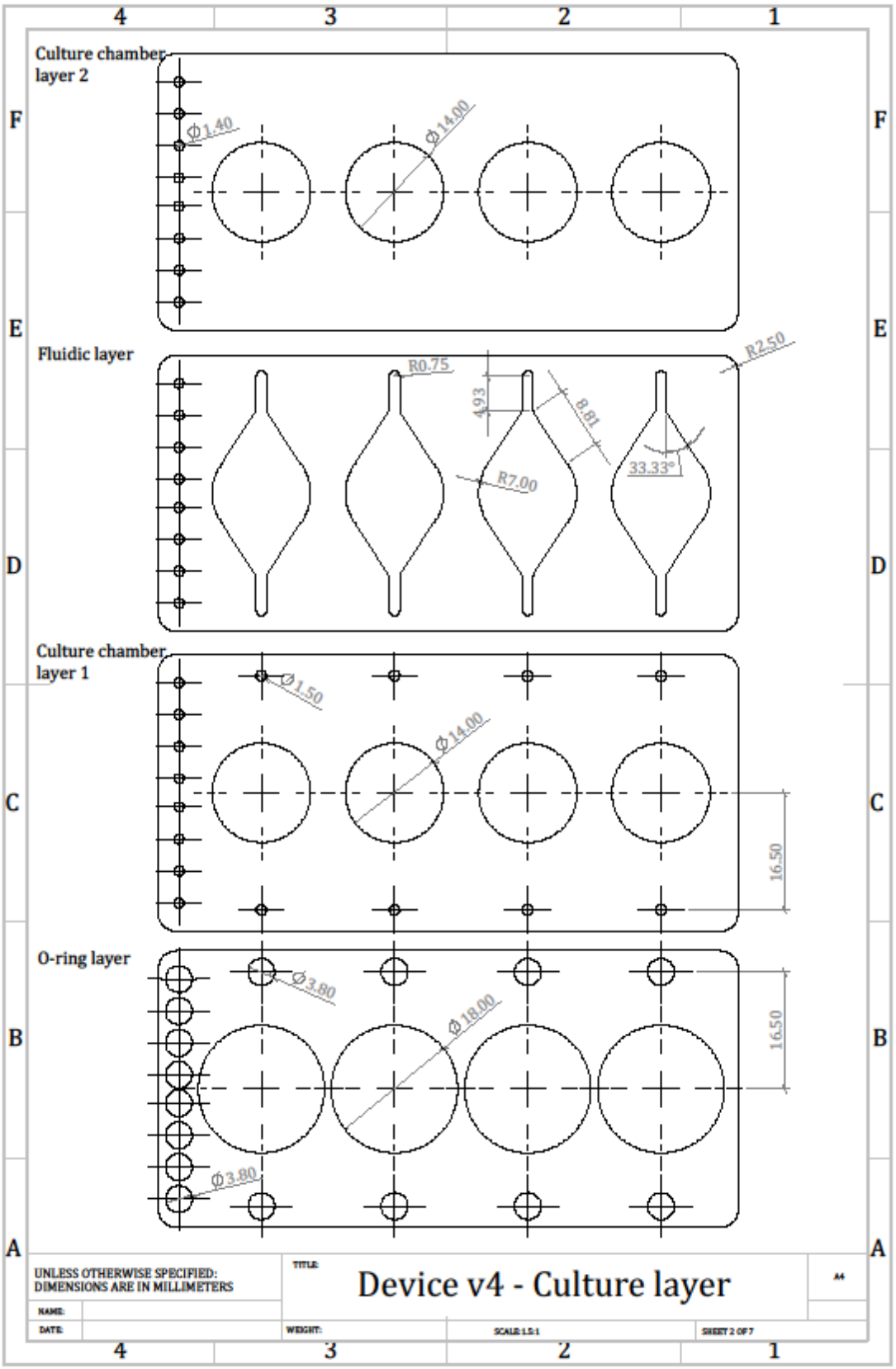
Culture chamber layer 2
Ø1.40
Ø14.00
Fluidic layer
R0.75
R2.50
4.93
8.81
R7.00
33.33°
Culture chamber layer 1
Ø1.50
Ø14.00
16.50
O-ring layer
Ø3.80
Ø18.00
16.50
Ø3.80
UNLESS OTHERWISE SPECIFIED:
DIMENSIONS ARE IN MILLIMETERS
TITLE:
Device v4 - Culture layer
NAME:
DATE:
WEIGHT:
SCALE: 1.5:1
SHEET 2 OF 7

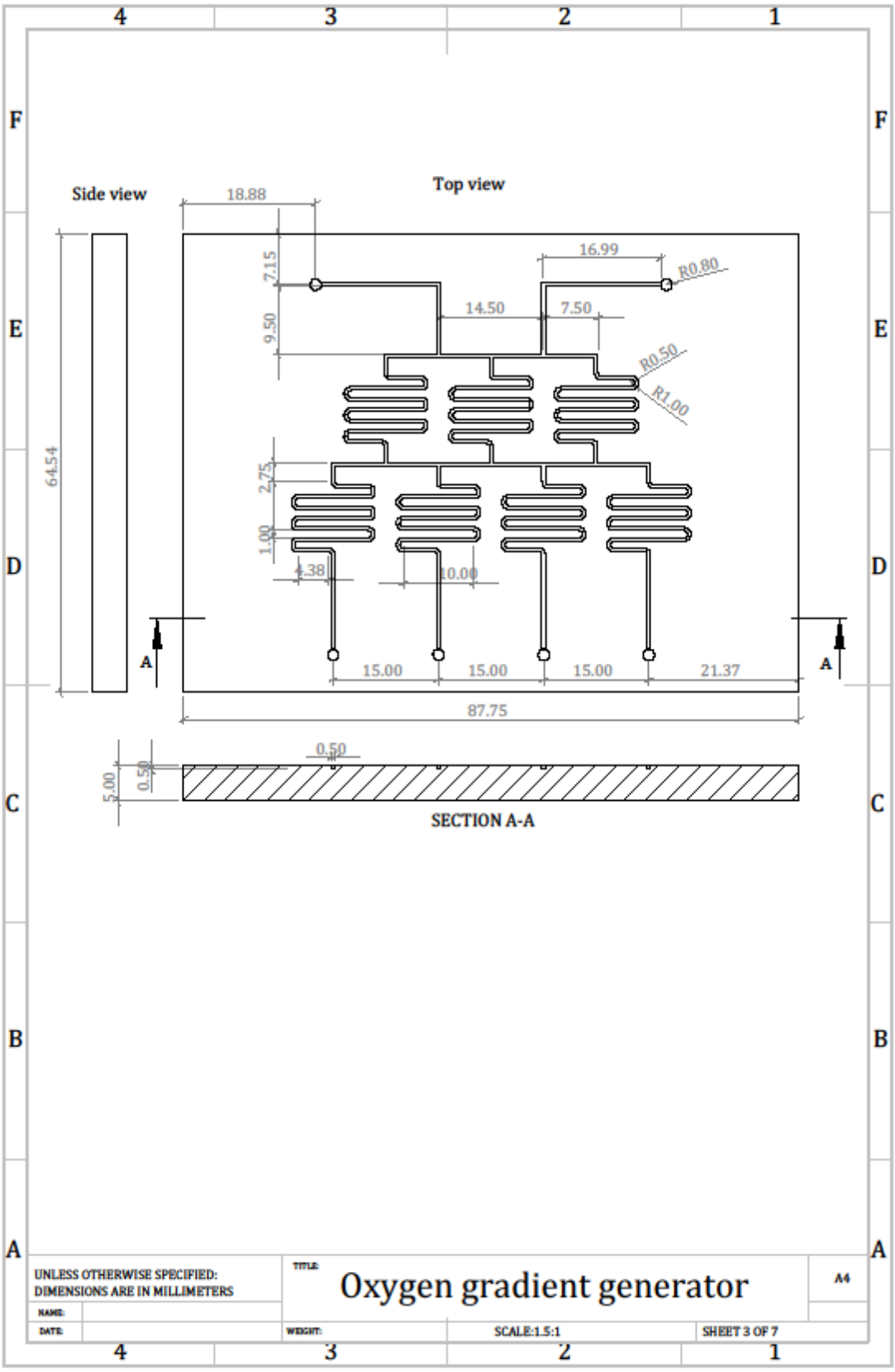
Side view
Top view
18.88
16.99
R0.80
7.15
14.50
7.50
9.50
R0.50
R1.00
64.54
2.75
1.00
4.38
10.00
A
A
15.00
15.00
15.00
21.37
87.75
0.50
0.50
5.00
SECTION A-A
UNLESS OTHERWISE SPECIFIED:
DIMENSIONS ARE IN MILLIMETERS
TITLE:
Oxygen gradient generator
A4
NAME:
DATE:
WEIGHT:
SCALE:1.5:1
SHEET 3 OF 7

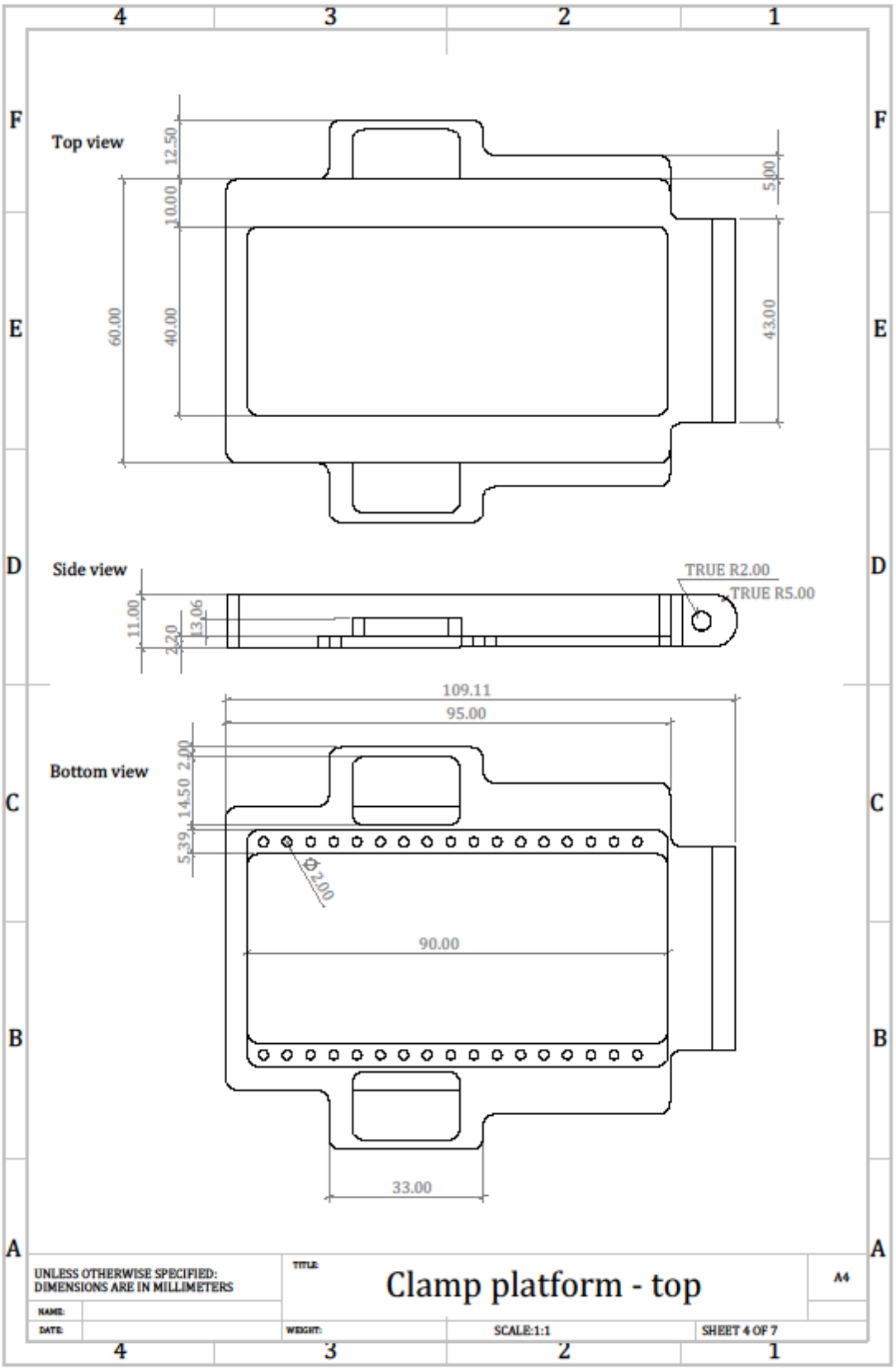
Top view
12.50
10.00
40.00
60.00
5.00
43.00
Side view
TRUE R2.00
TRUE R5.00
11.00
2.20
13.06
Bottom view
109.11
95.00
2.00
14.50
5.39
Ø2.00
90.00
33.00
UNLESS OTHERWISE SPECIFIED:
DIMENSIONS ARE IN MILLIMETERS
NAME:
DATE:
TITLE:
Clamp platform - top
A4
WEIGHT:
SCALE:1:1
SHEET 4 OF 7

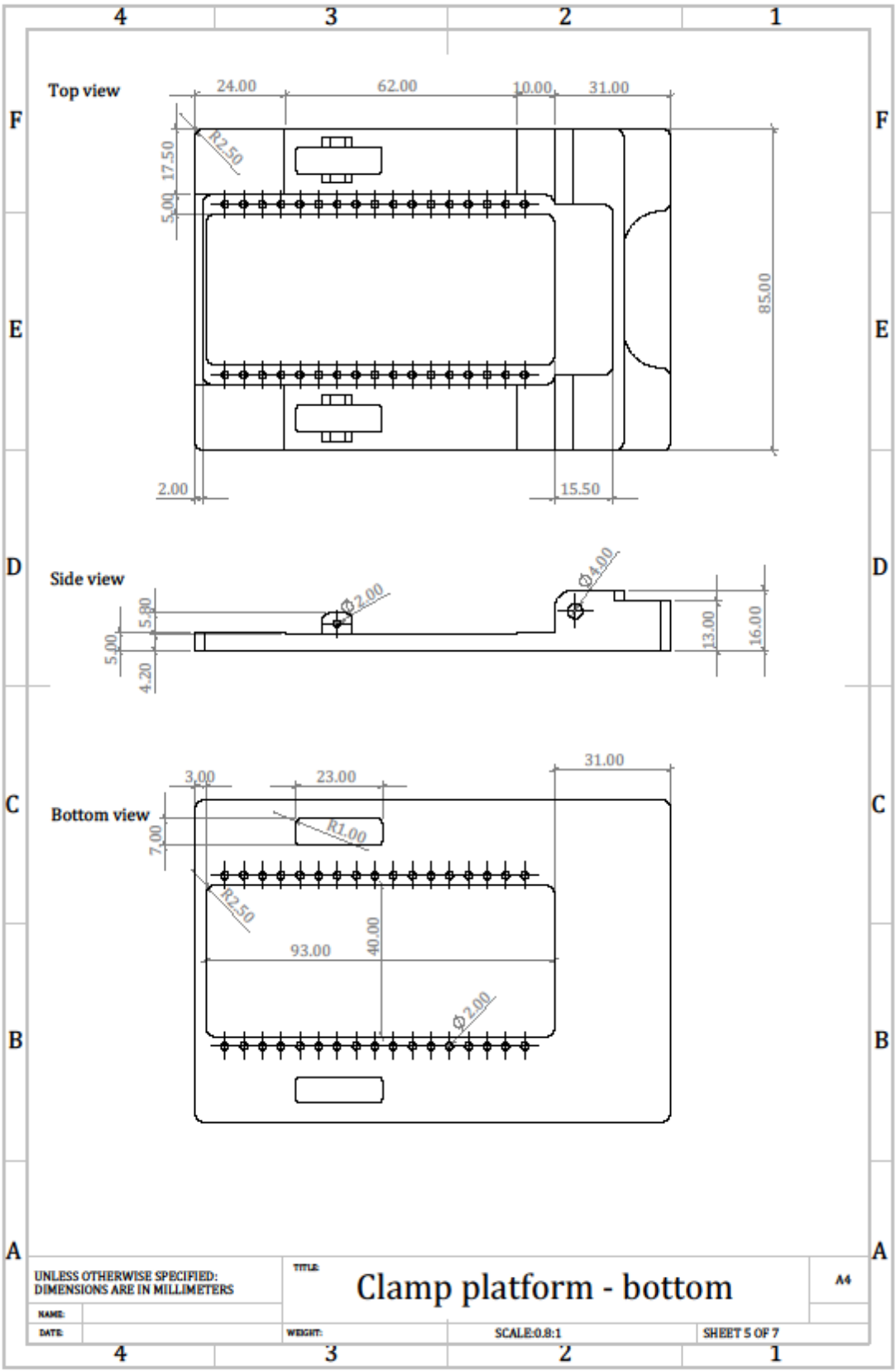
Top view
24.00
62.00
10.00
31.00
R2.50
17.50
5.00
85.00
2.00
15.50
Side view
Ø2.00
Ø4.00
5.80
5.00
4.20
13.00
16.00
Bottom view
3.00
23.00
31.00
R1.00
7.00
R2.50
40.00
93.00
Ø2.00
UNLESS OTHERWISE SPECIFIED:
DIMENSIONS ARE IN MILLIMETERS
TITLE:
Clamp platform - bottom
A4
NAME:
DATE:
WEIGHT:
SCALE:0.8:1
SHEET 5 OF 7

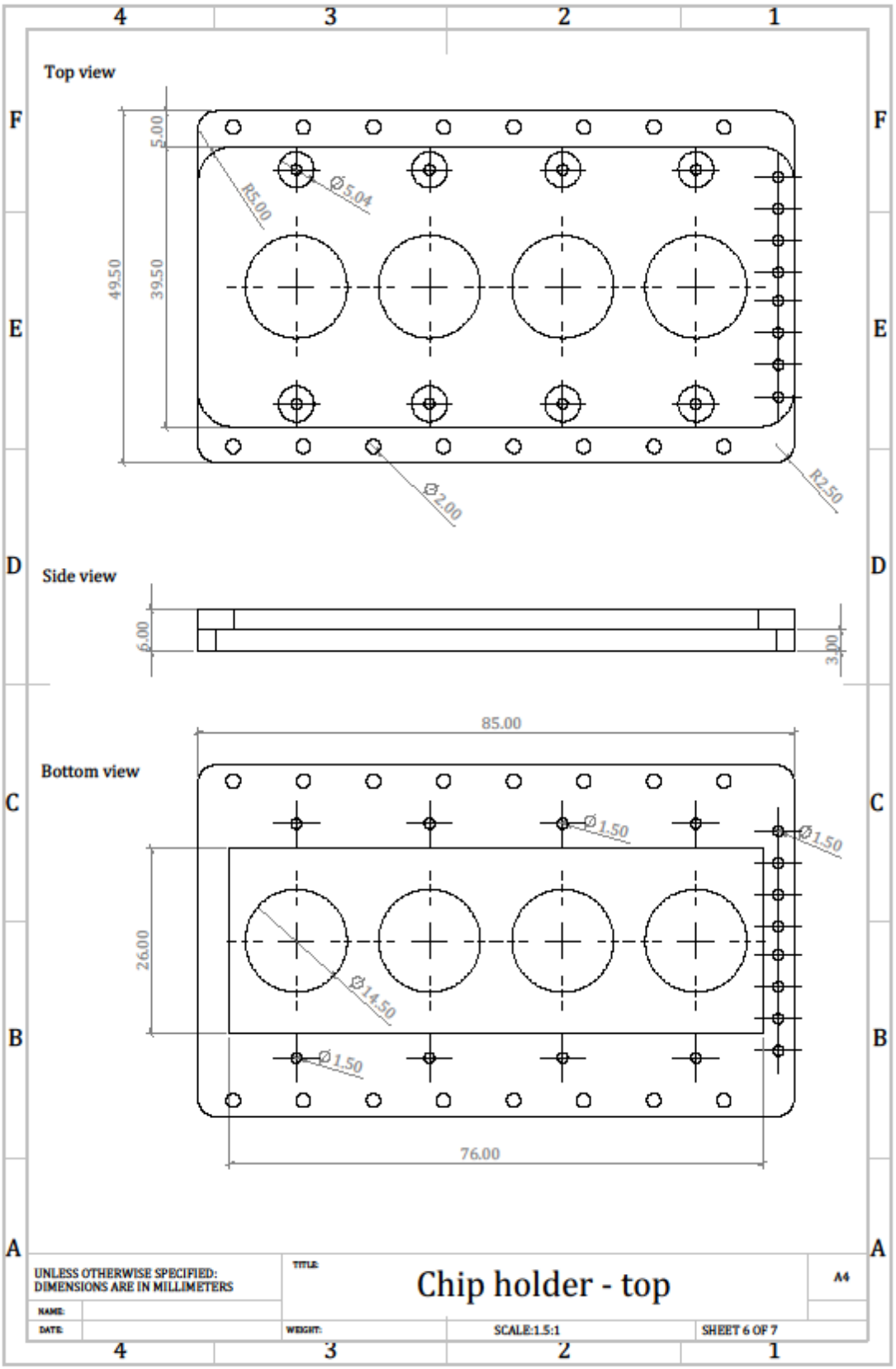
Top view
5.00
R5.00
Ø5.04
49.50
39.50
Ø2.00
R2.50
Side view
6.00
3.00
Bottom view
85.00
Ø1.50
Ø1.50
26.00
Ø14.50
Ø1.50
76.00
UNLESS OTHERWISE SPECIFIED:
DIMENSIONS ARE IN MILLIMETERS
NAME:
DATE:
TITLE:
Chip holder - top
A4
WEIGHT:
SCALE:1.5:1
SHEET 6 OF 7

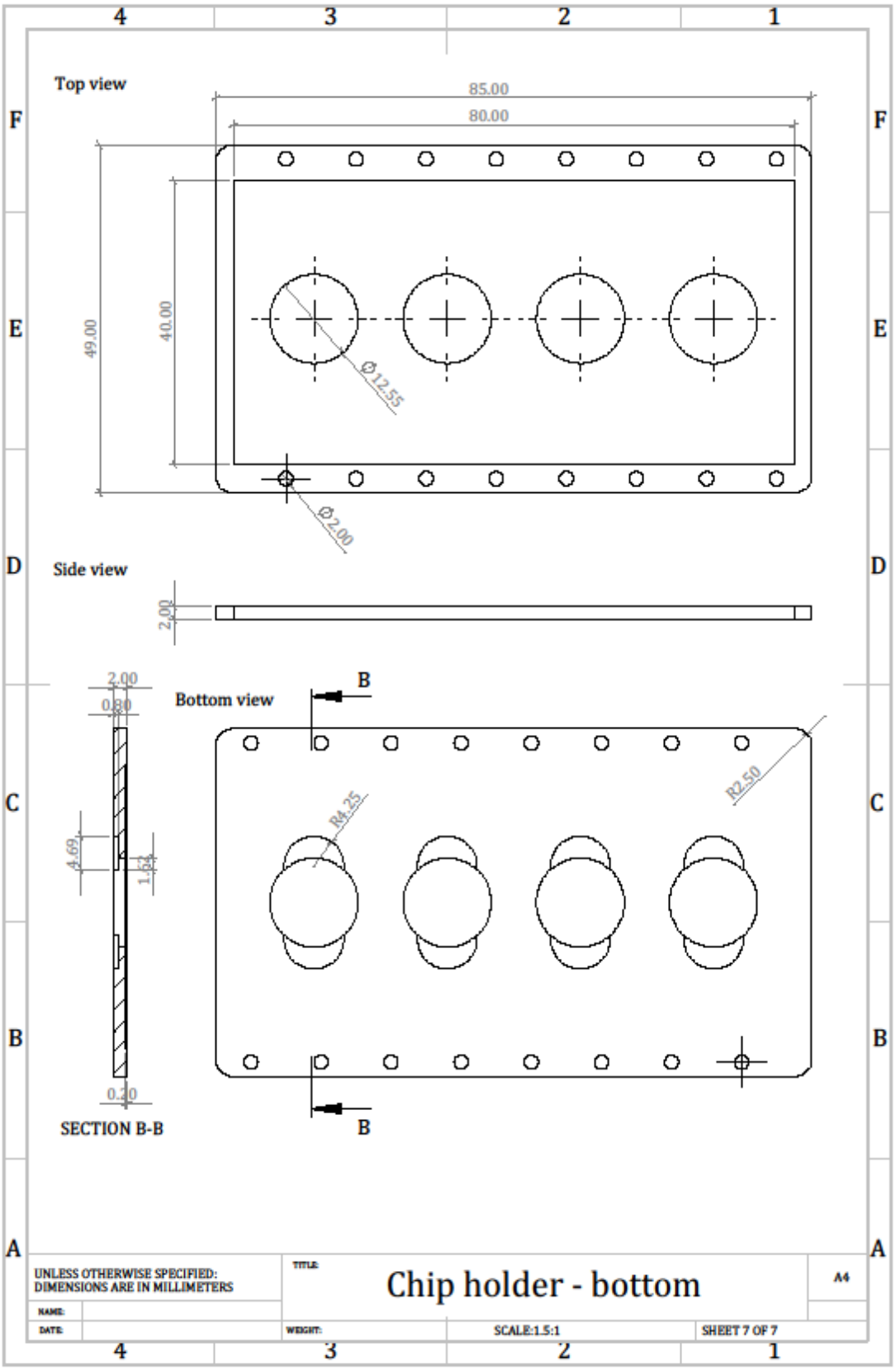
Top view
85.00
80.00
49.00
40.00
Ø12.55
Ø2.00
Side view
2.00
Bottom view
B
2.00
0.80
4.69
1.64
0.20
SECTION B-B
R4.25
R2.50
B
UNLESS OTHERWISE SPECIFIED:
DIMENSIONS ARE IN MILLIMETERS
TITLE:
Chip holder - bottom
A4
NAME:
DATE:
WEIGHT:
SCALE:1.5:1
SHEET 7 OF 7

Appendix 2. Oxygen sensing

a. Arduino script

```
#define inPin0 0
 #define inPin1 1
 #define inPin2 2
 #define inPin3 3
 #define inPin4 4
int led = 13; // the pin the LED is connected to
unsigned long previousMillis = 0;
const long interval = 600000;                    //measuring period
double pinRead0;
double pinRead1;
double pinRead2;
double pinRead3;
double pinRead4;
float DO1;
float DO2;
float DO3;
float DO4;

void setup() {
  Serial.begin (9600);
  pinMode (led, OUTPUT);
}

void loop() {
  analogWrite (led, 255);
  unsigned long currentMillis = millis ();

  if (currentMillis – previousMillis >= interval){
            previousMillis = currentMillis;
            analogWrite (led, 0);                          //turn LED on
     delay (4000);                                  //Excite for 4 s
     pinRead0 = analogRead (inPin0);          //read signal of each chamber
     pinRead4 = analogRead (inPin1);
     pinRead0 = analogRead (inPin0);
     pinRead2 = analogRead (inPin2);
     pinRead0 = analogRead (inPin0);
     pinRead1 = analogRead (inPin3);
     pinRead0 = analogRead (inPin0);
     pinRead3 = analogRead (inPin4);
     pinRead0 = analogRead (inPin0);
     analogWrite (led, 255);                                //turn LED off
     DO1 = pinRead1*5/1023;          //Transform reading into a voltage (0-5V)
     DO2 = pinRead2*5/1023;
     DO3 = pinRead3*5/1023;
     DO4 = pinRead4*5/1023;
            Serial.print (DO1); Serial.print (", "); //print on screen
            Serial.print (DO2); Serial.print (", ");
            Serial.print (DO3); Serial.print (", ");
            Serial.print (DO4); Serial.println ();
            }
}
```

b. Signal processing

Previous to each experiment, the sensors were calibrated by flushing N2 gas through the gas channels, and monitoring the signal collected from the sensors until it stabilised (Appendix 2). The maximum value was then attributed as the 0% DO and the background value as the 100% DO. Due to the linearity of the sensor in the range of interest (Figure 3.30, right), the Stern-Volmer equation is used to calculate the K_{SV} of each chamber, which is then used to transform the voltages collected by the Arduino into oxygen tensions. During the experiment, the flow of gas mixtures was started, and the DO detector was connected (Appendix 2.1, left). The signal collected was then filtered using a Gaussian filter to reduce the noise (Appendix 2.2, right), and transformed into an oxygen concentration using the K_{SV} calculated during the calibration step (Appendix 2.3).

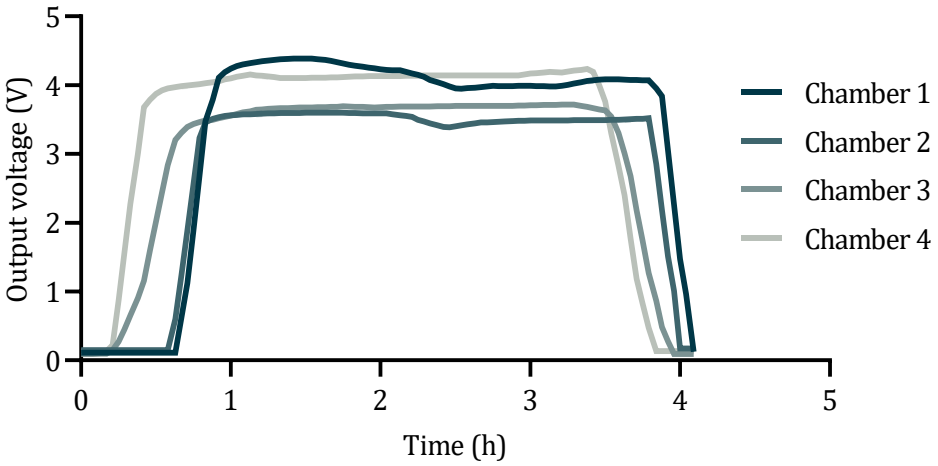

Appendix 2.1: Calibration of each individual chamber detector, showing the maximum and minimum signal to calculate the K_{SV}

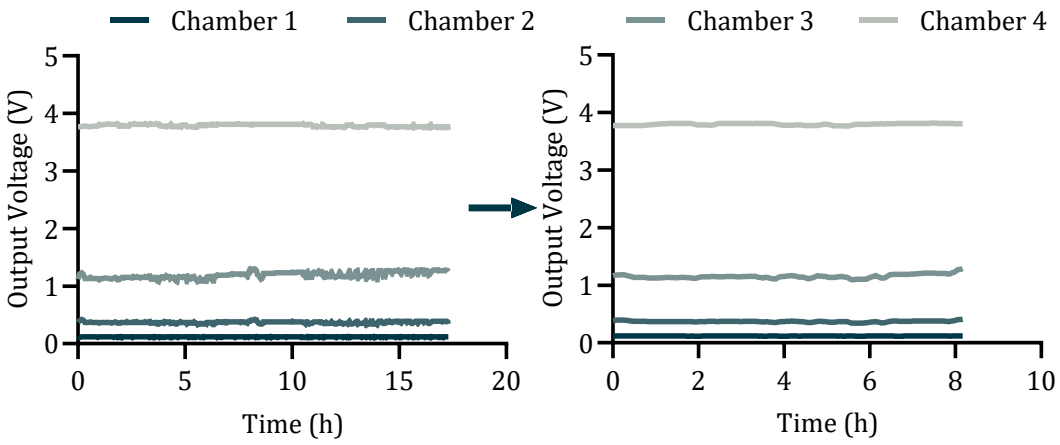

Appendix 2.2: Signal before and after filtering with a gaussian filter.

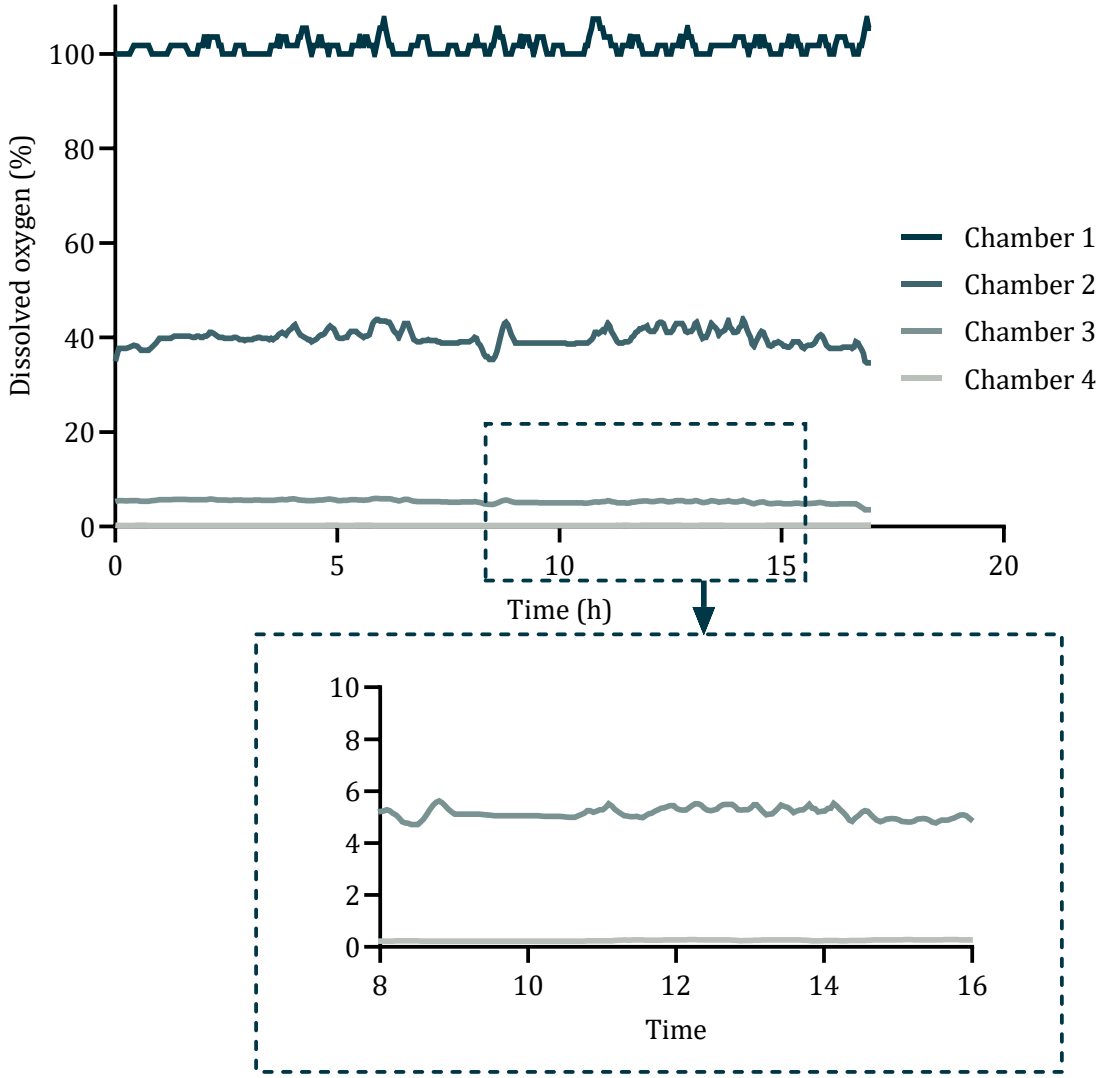

Appendix 2.3: Oxygen concentration in each chamber calculated by transforming the voltage using the Stern Volmer equation and the constant previously obtained during calibration. Below, detail of the lower different oxygen tensions in each chamber, stable over several hours.

Appendix 3. Media formulations

		DMEM	MEM	Leibovitz's L-15
Salts	*$CaCl_2.2H_20$*	0.2 (anhyd)	0.185	0.14 (CaCl2 (anhdyr))
	Ferric Nitrate	0.0001	-	-
	$MgCl_2$ (anhydr)	-	-	0.0937
	$MgSO_4$ (anhdyr)	0.09767	0.09767	0.09767
	KCl	0.4	0.4	0.4
	KH_2PO_4 (anhyd)	-	0.06	0.06 (KH2PO4)
	$NaHCO_3$	3.7	0.35	-
	NaCl	6.4	8	8
	Na_2HPO_4 (anhy)	0.125	0.048	0.19
	D-glucose	4.5	1	0.9 (D+ Galactose)
	Phenol Red	0.015	0.011	0.01
	D+ galactose	-	-	0.9
	sodium pyruvate	-	-	0.55
Amino acids	*Glycine*	0.03	-	0.2
	L-Alanyl-Glutamine	-	-	0.446
	L-Arginine hydrochloride	0.084	0.126	0.5 (L-arginine)
	L-Cystine	0.063	0.0313	0.12
	L-Histidine hydrochloride-H_2O	0.042	0.042	0.25 (L-histidine)
	L-Isoleucine	0.105	0.052	0.25
	L-Leucine	0.105	0.052	0.125
	L-Lysine hydrochloride	0.146	0.0725	0.075 (L-lysine)
	L-Methionine	0.03	0.015	0.075
	L-Phenylalanine	0.066	0.032	0.125
	L-Serine	0.042	-	0.2
	L-Threonine	0.095	0.048	0.3
	L-Tryptophan	0.016	0.01	0.02
	L-Tyrosine	0.104	0.04176	0.3
	L-Valine	0.094	0.046	0.1
	L-Alanine	-	-	0.225
	L-Asparagine	-	-	0.25
Vitamins	*Choline chloride*	0.004	0.001	0.001
	D-Calcium pantothenate	0.004	0.001	0.001
	Folic Acid	0.004	0.001	0.001
	Niacinamide	0.004	0.001	0.001
	Pyridoxal hydrochloride	0.004	0.001	0.001
	Riboflavin	0.0004	0.0001	0.0001
	Thiamine hydrochloride	0.004	0.001	0.001
	i-Inositol	0.0072	0.002	0.002